Natural graphite sheet heat sinks for power electronics

by

Martin Cermak

M.Sc., Brno University of Technology, 2013
B.Sc., Brno University of Technology, 2010

Thesis Submitted in Partial Fulfillment of the
Requirements for the Degree of
Doctor of Philosophy

in the
School of Mechatronic Systems Engineering
Faculty of Applied Sciences

SIMON FRASER UNIVERSITY
Summer 2020

Approval

Name:	**Martin Cermak**
Degree:	**Doctor of Philosophy (Engineering)**
Title:	**Natural graphite sheet heat sinks for power electronics**
Examining Committee:	**Chair:** Gordon McTaggart-Cowan Associate Professor
	Majid Bahrami Senior Supervisor Professor
	Rodney Vaughan Supervisor Professor
	Martin Ordonez Supervisor Professor University of British Columbia
	Patrick Palmer Internal Examiner Professor
	Mohamed Hamed External Examiner Professor Department of Mechanical Engineering McMaster University
Date Defended:	**June 4, 2020**

Abstract

In this thesis, a multi-disciplinary investigation of using natural graphite sheet (NGS) for heat sink applications is presented with focus on thermal performance, electromagnetic performance, reliability, cost, energy efficiency, and environmental impact. NGS heat sinks are a promising alternative for weight-sensitive applications in which the heat sink is protected by a case. Contrary to the conventional metals, NGS is also predicted to be feasible at high temperatures or in corrosive environments. To provide the basis for the heat sink design, the thermal conductivity, thermal diffusivity, electrical conductivity, thermal emissivity, coefficient of thermal expansion, and compression behavior are measured and reported in an easy-to-use form. It is shown experimentally that the the thermal contact resistance at metal-NGS interfaces is comparable to metal-metal ones with thermal interface materials, and that the poor through–plane thermal conductivity can be mitigated by embedding heat pipes in NGS heat sinks. The conducted common-mode electromagnetic emissions cannot be reduced by using NGS heat sinks, but potential to reduce the radiated emission by 12 to 97 % was identified. Complex implications on reliability arising from replacing conventional metal heat sinks with NGS ones are discussed. The cost of NGS heat sinks produced in high volumes is predicted to be a double that of mass-produced conventional aluminum ones. The environmental impact of production, manufacturing, and end-of-life management of NGS is reviewed and compared to the conventional heat sink materials. A case-specific approach to evaluating the feasibility of using NGS heat sinks is recommended and the major steps are outlined. The technology is considered to be ready for a transfer to the industrial research and development stage. An audiovisual summary of the work is available at `https://www.youtube.com/playlist?list=PLaX55SIXaD20NQQ2JLP-7abmET7l-6LS4`.

Keywords: heat sinks, exfoliated natural flake graphite; material properties; experimental characterization of heat sinks; EMI/EMC; electromagnetic interference and compliance; environmental impact; cost; reliability

In hope to help the clean technology revolution

Table of Contents

List of Tables

List of Figures

Nomenclature

α_{in}	In–plane thermal diffusivity
α_{th}	Through–plane thrermal diffusivity
ϵ	Near-normal-hemispherical emissivity
ϵ_{λ}	Spectral emissivity
λ	Wevelength
ϕ	Average angle of graphite basal planes
ρ_{in}	In–plane electrical resistivity
$\rho_{th,b}$	Bulk electrical resistivity
$\rho_{th,eff}$	Effective electrical resistivity
ρ_{th}	Through–plane electrical resistivity
σ_{in}	In–plane electrical conductivity
σ_{th}	Through–plane electrical conductivity
θ	Phase of impedance
A	Area
A_{th}	Area for through–plane measurements
c_v	Volumetric heat capacity of graphite
C_{D-HS}	Device-to-heat sink capacitance
$c_{m,gr}$	Molar heat capacity of graphite
$c_{p,gr}$	Specific heat capacity of graphite
CTE_{in}	In–plane coefficient of thermal expansion

CTE_{th} Through–plane coefficient of thermal expansion

d Density

d_0 relaxed density

d_{gr} Density of graphite crystal

F Force

F_c Clamping force

I Electrical current

I_{CM} Common-mode current

K_d Density correction factor

k_{in} In–plane thermal conductivity

k_{th} Through–plane thermal conductivity

$L_{HS,CM}$ Heat sink inductance

P Porosity

p_c Clamping pressure

p_f Forming pressure

R Electrical resistance

R_{ECR} Electric contact resistance

$R_{HS,CM}$ Heat sink electrical resistance (commond-mode currents)

R_{thCS} Case-to-sink thermal resistance

R_{thDA} Device-to-ambient thermal resistance

R_{thDS} Device-to-sink thermal resistance

R_{thJA} Junction-to-ambient thermal resistance

R_{thJC} Junction-to-case thermal resistance

R_{thSA} Sink-to-ambient thermal resistance

R_{th} Thermal resistance

S Strain

S_v	Viscous strain
t	Thickness
T_A	Ambient temperature
T_D	Device temperature
T_S	Heat sink temperature
u	Uncertainty
V_{EX}	Excitation voltage
Z_G	Impedance of ground coupling

Executive Summary

Widespread electrification and a transition to renewable energy sources have been identified as one of the key solutions to reducing emissions and limiting the climate change. Power converters are used extensively in electrical systems, starting from generation (wind turbines, solar farms), through distribution (smart grid nodes), all the way to consumption (electric vehicles, chargers). In their cores, power semiconductors control the flow of electric current. Because no available material is a perfect electrical conductor, heat is generated as a result of passing electric current, and cooling systems are necessary to prevent failure and to guarantee a reliable long-term operation. The requirements for size, weight, performance, and cost of power converters have been pushing the limits of conventional air-cooled systems and made the thermal design one of the main challenges facing the power electronics industry.

Heat sinks are used to increase the cooling rate of power semiconductors by extending the area of the surface that is in contact with cooling air. Currently, the majority of heat sinks are made of thermally conductive metals such as aluminum or copper. Natural flake graphite is a relatively inexpensive material (1.36 USD/kg compared to 1.78 USD/kg of aluminum) which is mined from abundant deposits in Canada and worldwide, but can be also recovered from steelmaking waste known as kish. Natural graphite sheet (NGS), which is made by compressing exfoliated natural graphite, has the material properties that are desired in the power electronics industry, including: i) high thermal conductivity, up to 600 W $m^{-1}K^{-1}$ (300% of aluminum and 200% of copper) in a highly compressed state in the in-plane direction; ii) low weight, approx. 30% of aluminum and 17% of copper, iii) manufacturability into complex shapes at low cost; iv) lower electrical conductivity in comparison with metals; v) chemical, corrosion, and high temperature resistance; and vi) conformity to rough surfaces, which reduces thermal contact resistance and offers the potential to eliminate the need for thermal interface materials (TIM).

Despite the great suitability of NGS for electronics cooling, only a limited number of studies are available in the open literature, none of which consider applications in power electronics. In this PhD research, the feasibility of NGS heat sinks is assessed in a multi-disciplinary manner by considering their thermal performance, electromagnetic performance, weight, cost, environmental impact, integration, resiliency, and integration.

Objective

The objective of this research is to evaluate whether using NGS heat sinks in power electronic can offer an improvement in performance when compared to conventional aluminum and copper heat sinks. To do so, the following research questions are formulated:

(i) Does the anisotropy in thermal conductivity of NGS limit the thermal performance of NGS heat sinks?

(ii) How does the thermal contact resistance at the interface between the heat sink and semiconductor differ for NGS and metal heat sinks?

(iii) Can – and under what conditions – using NGS heat sinks lead to the elimination of thermal interface materials (TIM)? What is the impact on the reliability and overall cost of cooling systems?

(iv) Does the low electrical conductivity of NGS heat sinks impact the conducted and radiated emissions of power electronic devices?

(v) What are the implications on the reliability of power semiconductors after replacing metal heat sinks with aluminum ones?

(vi) Does the low mechanical strength of NGS impede the practical applications of NGS heat sinks?

(vii) What is the estimated cost of NGS heat sinks?

(viii) What weight reduction can be achieved by replacing metal heat sinks with NGS ones?

(ix) How do NGS and conventional heat sink materials compare in terms of the environmental impact?

Methodology

To achieve the research objective and answer the research questions, a systematic approach is adopted with the steps listed below and summarized graphically in Fig. 1.

- Proof-of-concept demonstration - prototype NGS heat sinks are built and the benefits and challenges are reviewed;
- Relevant material properties are identified, the available data is compiled, and the literature gaps are filled by carrying out measurements;
- Thermal performance of NGS heat sinks is evaluated with a focus on investigating the effect of the anisotropic material properties and the thermal contact resistance;
- Analytical and experimental methods are used to evaluate the potential reduction of electromagnetic emissions;
- Material cost is compared based on data from the available sources, and the heat sink cost is estimated through a collaboration with an industrial partner;
- The environmental impact of material production, manufacturing, and end-of-life management is reviewed for NGS and conventional heat sink materials;
- A holistic feasibility study is performed to summarize the benefits and challenges of NGS heat sinks;
- The necessary future steps are outlined.

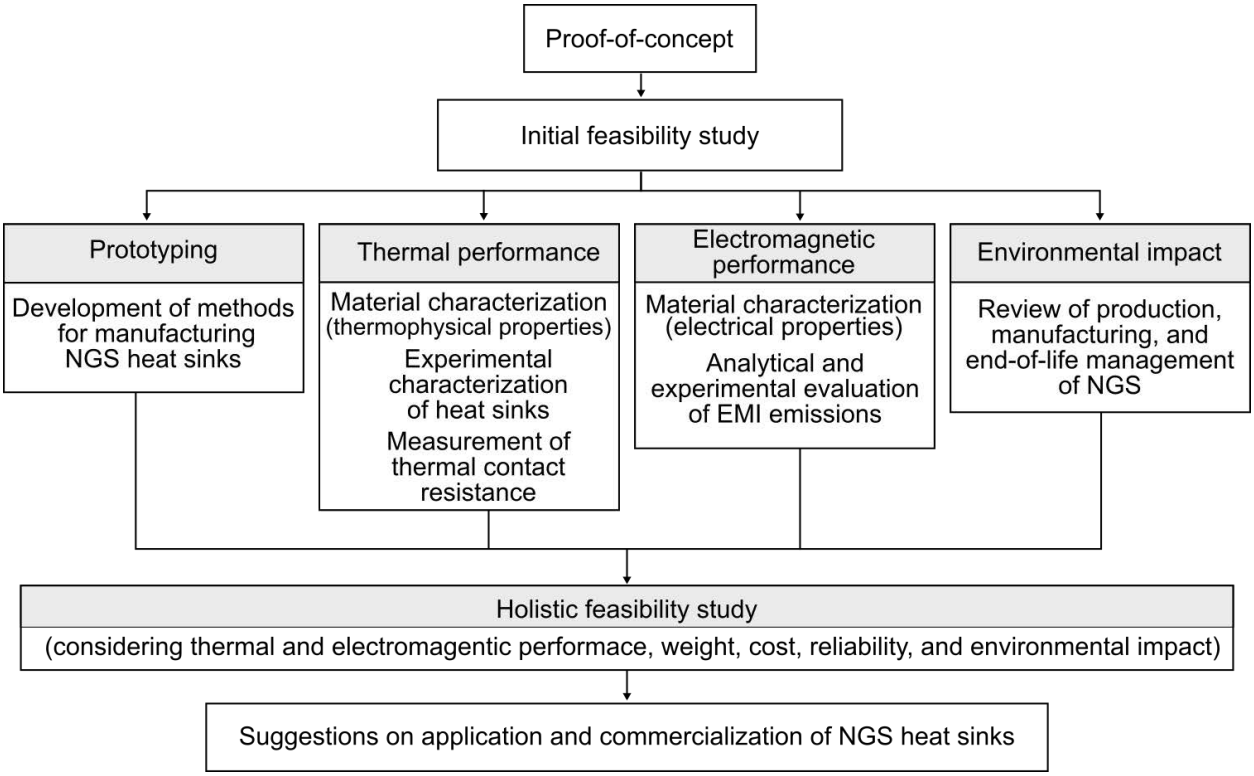

Fig. 1: Research roadmap

Outcomes

- Thermal conductivity, thermal diffusivity, electrical conductivity, thermal emissivity, coefficient of thermal expansion (CTE), and compression behavior are measured as a function of density and, where applicable, as a function of mechanical pressure. The results are compiled in an easy-to-use graphical summary [P5, P6, P7].

- The thermocouple and transient thermal methods for experimental heat sink characterization are compared and suggestions on their suitability are made [P2]. Small and large-scale prototypes of NGS heat sinks are manufactured and measured. For small-scale heat sinks whose width matches the heat source size, thermal resistance is shown not to be limited by the anisotropic properties and conclusions on the effect of clamping pressure and resin impregnation are made [P1]. For large-scale heat sinks, whose width is larger than the heat source size, the anisotropy of NGS limits thermal performance; in response, a novel concept of NGS heat sinks with embedded heat pipes is introduced and shown to mitigate the anisotropy drawbacks [P8].

- The thermal contact resistance (TCR) between stacked NGS and metal is measured for the first time. Its value is found to be comparable to metal-to-metal interfaces with thermal grease.

- The effect of the heat sink material on conducted common mode electromagnetic emissions is studied analytically and experimentally. It is shown that despite the four orders of magnitude lower electrical conductivity, a simple change of the heat sink material from aluminum to NGS cannot reduce common mode emissions. The potential for a reduction of radiated emissions is quantified to be 12 – 97 %. An attempt to measure permittivity is documented, and recommendations for the future work are offered.

- The cost of NGS heat sinks produced at high volumes is estimated to be double that of commercially available aluminum ones. Pathways to cost reduction are identified, and low-volume production is analyzed.

- The energy requirement of primary production of graphite flakes is shown to be lower than that of aluminum and/or copper [P4]. Recycling of NGS is found to be

challenging; however, recommendations for solutions aligned with the concepts of circular economy are suggested. An extensive life cycle assessment study is suggested, and the existing road blocks are reviewed.

- The feasibility of NGS heat sinks is evaluated with respect to the thermal performance, electromagnetic performance, cost, weight, reliability, resiliency, integration, and environmental impact. Weight-sensitive applications with large heat sources and no requirement for an electrical insulation are identified as the most feasible. A per-case approach to evaluating feasibility is suggested

- The need for further research is outlined with the major task being a development of a computational tool for optimizing the heat sink geometry. The optimization results are crucial for the case-dependent feasibility evaluation.

Publications

C = Conference, P = Poster, J = Journal

[C1] M. Cermak, J. Kenna, and M. Bahrami, "Natural-graphite-sheet based heat sinks," in *2017 33rd Thermal Measurement, Modeling & Management Symposium (SEMI-THERM)*, 2017, pp. 310–313.

Presented by M. Cermak

[C2] M. Cermak, W. J. He, and M. Bahrami, "A transient thermal tester as an alternative to thermocouples for characterizing heat sinks," in *2018 34th Thermal Measurement, Modeling & Management Symposium (SEMI-THERM)*, 2018, pp. 148–154.

Presented by M. Cermak

[C3] M. Cermak, M. Bahrami, and J. Kenna, "Natural graphite sheet heat sinks: A review of the material properties, benefits, and challenges," in *2018 34th Thermal Measurement, Modeling & Management Symposium (SEMI-THERM)*, 2018, pp. 55–62.

Presented by M. Cermak

[C4] M. Cermak, N. Perez, and M. Bahrami, "Thermal conductivity and diffusivity of natural graphite sheet", in The Second Pacific Rim Thermal Engineering Conference, December 13-17, 2019, Maui, Hawaii, USA.

Presented by M. Bahrami

[P1] M. Cermak, C. McCague, and M. Bahrami, "Graphite in clean technologies: the importance of availability of material production data", Conference poster presented at Resources for Future Generations, Vancouver, B.C., Canada, 2018.

Presented by M. Cermak

[J1] M. Cermak, M. Bahrami, “Compression behavior of natural graphite sheet,” in *SN Appl. Sci. 2*, 357 (2020). https://doi.org/10.1007/s42452-020-2075-y

Author contributions: M.C. identified the research needs, reviewed literature, planned and troubleshooted the experimental methods, prepared samples, collected data, analyzed results, prepared figures, and wrote the manuscript. M.B. initiated and supervised the project and secured funding.

[J2] M. Cermak, X. Faure, M. A. Saket, M. Bahrami and M. Ordonez, "Natural Graphite Sheet Heat Sinks With Embedded Heat Pipes," in *IEEE Access*, vol. 8, pp. 80827-80835, 2020, doi: 10.1109/ACCESS.2020.2988832.

Author contributions: M.C. identified the research needs, reviewed literature, planned and troubleshooted the experimental methods, analyzed results, prepared figures, and wrote the manuscript. X.F. prepared samples, collected data, and analyzed results. M.A.S. provided EMI noise expertise, collected data, and analyzed results. M.B. initiated and supervised the project and secured funding. M.O. Supervised the EMI portion of the work. All authors have reviewed the manuscript.

[J3] M. Cermak, N. Perez, M. Collins, and M. Bahrami, “Material properties and structure of natural graphite sheet”, Under review at the time of thesis submission, *Scientific reports*.

Author contributions: M.Ce. identified the research needs, reviewed literature, planned and troubleshooted the experimental methods, prepared samples, collected data, analyzed results, prepared figures, and wrote the manuscript. N.P. planned and troubleshooted the experimental methods, prepared samples, collected data, and analyzed the results. M.Co. planned and performed the emissivity measurements. M.B. initiated and supervised the project and secured funding. All authors have reviewed the manuscript.

Chapter 1

Introduction

This chapter aims to remind the role of power electronics in the changing world, provide the necessary background in power semiconductors and their thermal management, introduce the concept of natural graphite sheet (NGS) heat sinks, summarize the previous work, and state the goals of the present research. An audiovisual summary of the introductory topics is available at `https://www.youtube.com/watch?v=DCds3oiVYAY&list=PLaX55SIXaD20NQQ2JLP-7abmET7l-6LS4&index=1` and `https://www.youtube.com/watch?v=iidm7ffG6IM&list=PLaX55SIXaD20NQQ2JLP-7abmET7l-6LS4&index=2` [1].

1.1 The role of power electronics in the world

Widespread electrification and a transition to distributed renewable energy sources has been identified as one of the solutions to reducing greenhouse gas emissions and limiting climate change [1]. The electricity distribution network, industrial machines, and consumer electronics are becoming more complex, and an increasing number of semiconductor-based power electronic devices is used across the entire electrical system. Power converters are electronic devices that convert one form of electrical energy into another, for example, alternating current (AC) into direct current (DC), or low-voltage DC into high voltage DC. Figure 1.1 shows an illustration of the electrical system and highlights the ubiquitous presence of power converters. Multiple conversion steps are necessary to deliver electric energy from its source to the end user. An example can be given by following the power generated in a photovoltaic solar plant on its way the motor of an electric vehicle. One of the multiple possible scenarios includes:

i) DC-AC conversion from the photovoltaic panel to the grid,

ii) AC-DC conversion for the short-term energy storage in batteries,

iii) DC-AC conversion from batteries to the grid,

[1] The video files are also available in Appendix F

iv) AC-AC conversion in the step-up and step-down transformers in the long distance power transmission grid,

v) AC-DC conversion in the vehicle battery charger, and

vi) DC-AC conversion in the inverter that feeds the AC motor of the electric vehicle.

Each of the conversion steps is associated with losses. The power electronics industry puts large amount of effort into reducing the losses by increasing the power conversion efficiency.

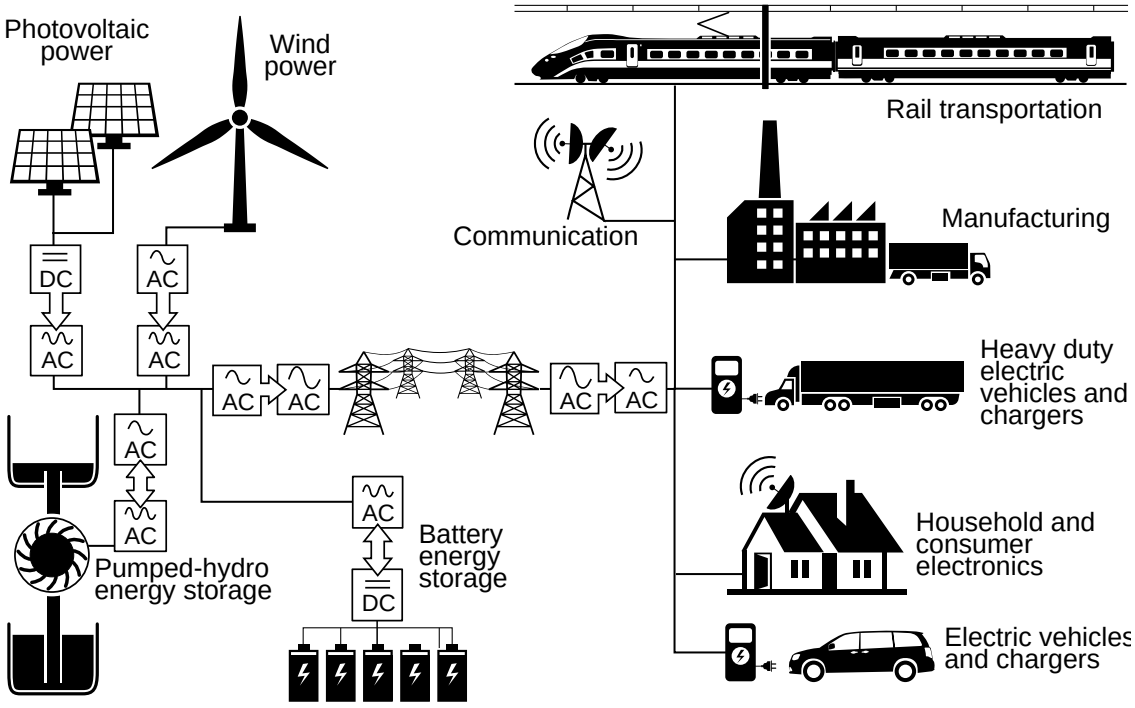

Figure 1.1: The electrical system with emphasized power conversion steps. The illustration uses freely available artwork from Macrovector, Freepik, and Vecteezy

1.2 Power semiconductors

Power semiconductors are the building blocks of virtually all modern electrical devices. The simplest semiconductor–a diode–allows the current to flow in one direction but blocks it in the other direction. A transistor allows modulation or on/off switching based on the input signal. From the thermal management perspective, it is not necessary to focus on the details of the electrical function of semiconductors, but the knowledge of the internal structure and heat generation mechanism is crucial.

To satisfy the needs of various industries, power semiconductors are available in many types of packaging that differ in size, number of chips, and mounting type (bolts, clamps, or solder). An example of a medium size diode in a discrete TO-247 packaging, which is

popular for its versatility and low cost, is shown in Figure 1.2. The semiconductor chip, which performs the diode function and is typically made of silicon, is attached to the lead frame by a solder or electrically conductive epoxy. Other names used to refer to the semiconductor chip are the junction or the die. While one of the leads is connected directly to the lead frame, the second one is connected to the top side of the die by a bond wire. The leads are used for attaching the device to a printed circuit board. The entire device is encapsulated in a molding compound (temperature-resistant plastic) that provides mechanical and environmental protection of the chip. The lead frame and terminals are typically made of tin-coated copper, while the bond wire is usually aluminum. The actual semiconductor accounts for only a small part of the the package.

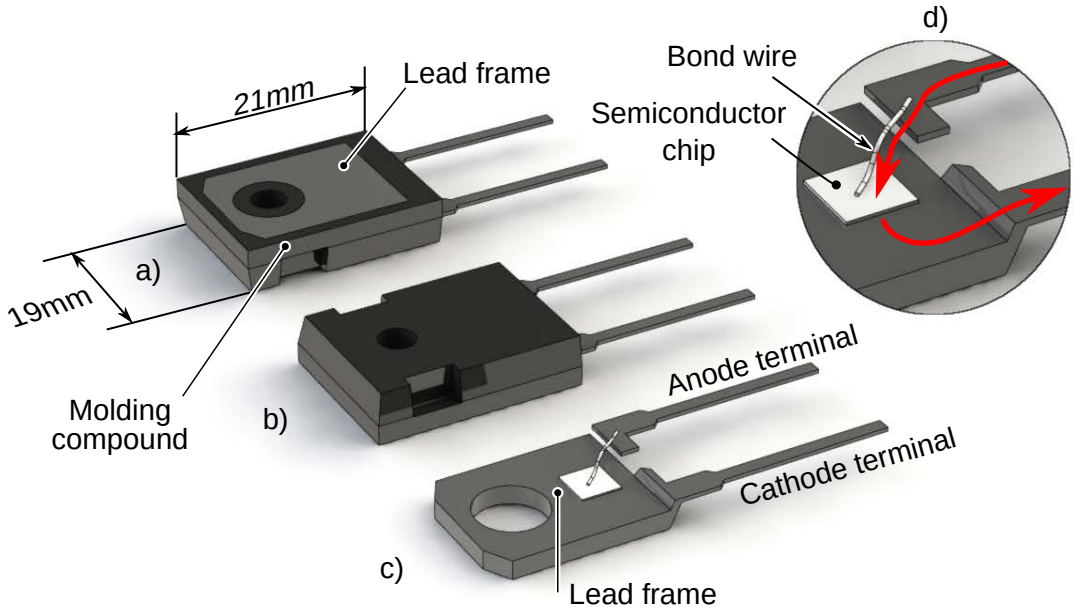

Figure 1.2: A diode in the TO-247 semiconductor packaging. In a) and b) the top and bottom of the package are shown. In c) the internal structure is exposed by hiding the molding compound, and in d) the an enlarged detail of the chip and bond wire is shown.

Heat generated in power semiconductors is an unwanted effect caused by the flow of electric current. As illustrated by the red arrow in Figure 1.2d, the current flows through the anode lead, wire bond, die, and then through the lead frame into the cathode lead. The main portion of the heat is generated in the semiconductor die. The metal parts also contribute to the overall heat generation, especially in sections with a small cross-sectional area, such as the leads or bond wires. Parts with higher resistivity (such as silicon) generate more heat than good conductors (copper) according to the Joule effect.

The example of a diode was chosen to illustrate the general structure of a power semiconductor. Modern application-specific semiconductor modules often integrate multiple chips,

electrical insulation, driving circuits, and temperature probes. Details about semiconductors and their packaging can be found in [2].

1.3 Cooling of semiconductors

The purpose of electronics cooling systems is to move the heat from the semiconductor into the ambient air or cooling liquid. Figure 1.3 shows a typical layout of an air-cooled heat sink assembly in which the device is mounted to the base of the heat sink using a bolt and a threaded hole. Depending on the application, the device can be mounted with an electrically insulating pad as shown in Figures 1.3b, or directly as shown in 1.3c. In case of direct mounting, the heat transfer from the device to the heat sink is limited only by the thermal contact resistance (TCR), which is caused by the surface imperfections of mating parts as is shown Figure 1.3d. The poor heat transfer through bare metal-to-metal contacts is typically improved by applying a thermal grease that fills the air gaps. When electrical insulation is used, the heat transfer from the device to the heat sink is dictated by the TCR at the device-insulator and insulator-heat sink interfaceces, as well as by the thermal conductivity of the insulator.

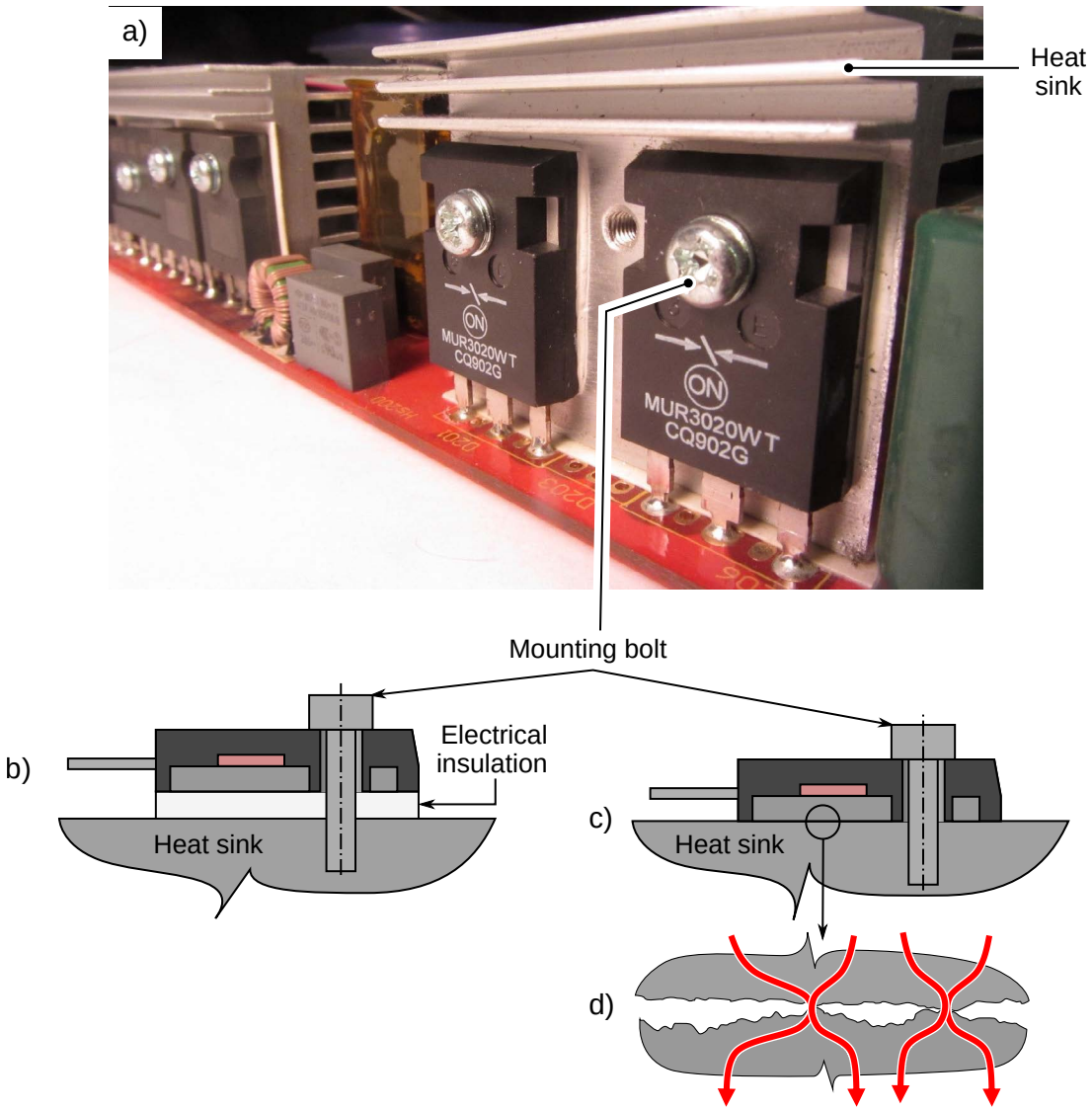

Figure 1.3: a) A typical heat sink assembly with TO-247 devices mounted on an aluminum heat sink with an electrically insulating layer. A section-view of the assembly with and withouth electrical insulatin is shown in b) and c), respectively. The detail of the imperfect contact at the device-sink interface with the heat flow lines in red is shown in d).

1.4 Basic heat transfer analysis

The most common thermal performance metric that is used widely in electronics cooling is the thermal resistance R_{th}, which is defined as the ratio of the temperature difference at the heat flow rate [3] as:

$$R_{th} = \frac{\Delta T}{\dot{Q}}, \tag{1.1}$$

where ΔT is the temperature difference, and $\dot{Q}$ is the heat flow rate. Thermal resistance can be interpreted as a quantity that determines what temperature difference is necessary

for transferring 1 W of heat between two locations on a one-dimensional heat transfer path under steady-state conditions. A summary of the most commonly used thermal resistances with the nomenclature according to the Joint Electron Device Engineering Council (JEDEC) [4] is given in Figure 1.4.

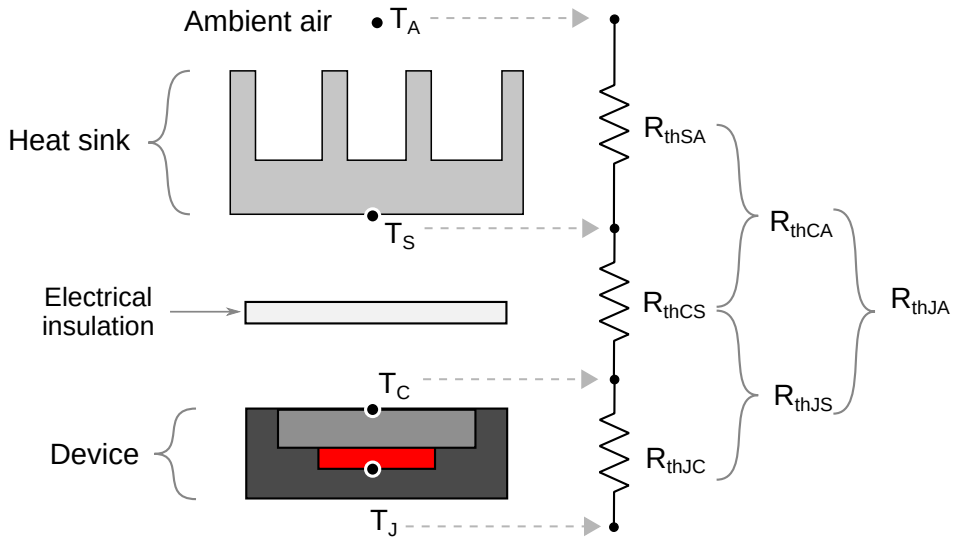

Thermal resistances		Temperatures	
Symbol	Description	Symbol	Description
R_{thJC}	Junction-to-case	T_J	Junction
R_{thCS}	Case-to-sink	T_C	Case
R_{thSA}	Sink-to-ambient	T_S	Sink
R_{thCA}	Case-to-ambient	T_A	Ambient
R_{thJS}	Junction-to-sink		
R_{thJA}	Junction-to-ambient		

Figure 1.4: A summary of the common thermal resistances with a definition of relevant temperatures

While the resistances described above are enough for designing electronic products, for heat sink development it is desirable to break down the sink-to-ambient resistance into partial resistances. By analyzing their magnitude and relative importance it is possible to identify the heat transfer bottlenecks and modify the thermal design accordingly to achieve a better performance. Figure 1.5 shows the partial resistances and lists the parameters that affect them. The notation does not follow the electronics standards, but it is typical for the heat transfer community.

The first resistance outside of the semiconductor package that the heat travelling from the chip encounters is the interface resistance. Its magnitude dependents on the TCR and, when electrical insulation is used, the thermal conductivity of the insulation material. The magnitude of TCR is a function of thermo-mechanical properties of mating materials (ther-

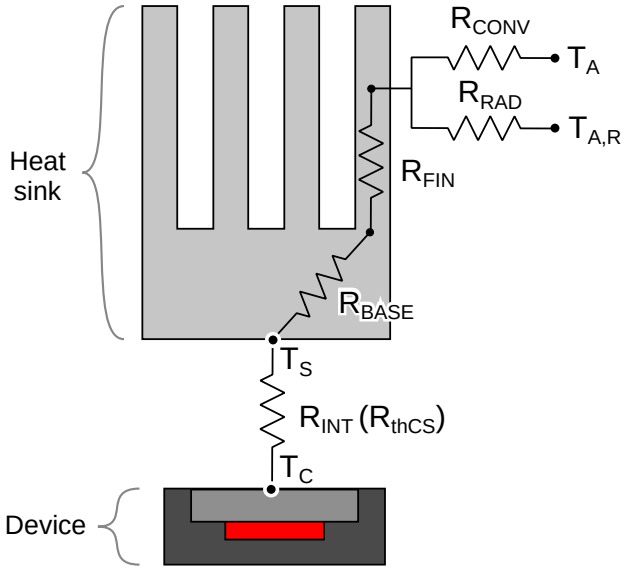

Symbol	Description	Function of:
R_{RAD}	Radiation resistance	• Material and surface properties of heat sink and surroundings • Heat sink material
R_{CONV}	Convection resistance	• Air flow characteristics • Heat sink geometry
R_{FIN}	Fin resistance	• Heat sink material • Heat sink geometry
R_{BASE}	Base (spreading) resistance	• Heat sink material • Heat sink geometry • Device geometry
R_{INT} (R_{thCS})	Interface (case-to-sink) resistance	• Contact pressure • Surface roughness and flatness • Thermo-mechanical material properties • Thermal interface material properties

Figure 1.5: A detailed breakdown of thermal resistances in a heat sink

mal conductivity, Young's modulus, hardness, and Poisson ratio) and their surface characteristics (roughness and flatness).

The quality of the heat transfer within the heat sink is typically described by the spreading and fin resistances whose magnitude is dictated by the geometry and thermal conductivity of the heat sink. From the surface of the heat sink, the heat is transferred to the surrounding air mostly by convection, but in some cases the radiation heat transfer to surrounding objects is also significant. The convection resistance is a function of the heat sink geometry and the flow field properties such as velocity or turbulence levels. The magnitude of the radiation resistance depends on the heat sink geometry and emissivities of the heat sink and surrounding objects. In Figure 1.5, the ambient temperatures for convection T_A

and radiation $T_{A,R}$ are separated because the convection resistance is related to the air temperature, while the radiation resistance is related to the temperature of the surrounding objects.

Networks of thermal resistances are beneficial for conceptual thinking and reduced-order modeling. In reality, the evaluation of individual resistances is often ambiguous due to a vague definitions of the relevant temperatures. In case of the junction-to-case resistance according to the JEDEC standards, the definition clearly states that the temperature of the junction and the temperature of the case beneath the semiconductor chip should be used. For other resistance, the standards are often not available and researchers typically choose the relevant temperatures based on their experience. Experimental investigation of partial resistances is complicated because installing temperature sensors at all the desired locations is often not possible.

1.5 Heat sink design considerations

Designing a cooling system is a complex task that has to take into account many constrains imposed by the application and operating conditions of power electronic products. During the heat sink selection step, the shape, material, and attachment method must be determined by considering the trade off between the thermal performance, cost, reliability, size, weight, electromagnetic compliance and interference, acoustic noise, energy efficiency, and ideally the relative environmental impact of the candidate materials. The following paragraphs include a brief summary of each of the consideration factors.

1.5.1 Thermal performance

Requirements for the thermal performance of cooling systems are typically given by the maximum allowed temperature of electronic components, and/or by the touch safety regulations that prescribe the maximum temperature of the heat sink or external surfaces. It is a common practice to quantify the requirements using the thermal resistance (Eq. 1.1).

1.5.2 Cost

The cost of cooling systems determines their commercialization success and market uptake. Solutions with simple manufacturing methods that use inexpensive materials are preferred. When evaluating the cost of multiple candidate solutions, it is important to consider not only the cost of the cooling system, but also the indirect costs such as the labor during the assembly process, or the maintenance cost during the product lifetime.

1.5.3 Reliability

Cooling systems affect the reliability of electronics directly by a failure of air movers or pumps [5, 6], and indirectly by determining the operation temperature of electronic devices.

The amplitude, mean, and frequency of the temperature variations have been shown to be correlated with the expected lifetime of power semiconductors [7, 8]. The failure mechanisms of power semiconductors arise from the different coefficients of thermal expansion (CTE) of materials used in the device packaging. The inducted stresses and deformations promote the degradation mechanisms such as micro-crack growth that eventually cause a failure [9]. The deformation of a semiconductor package during temperature cycling has been shown to cause the pump-out effect, which forces the thermal interface material (TIM) out of the device-heat sink interface and, in turn, degrades the thermal performance. As a result, the device temperature increases and the lifetime decreases [10, 11]. Besides the pump-out effect, a chemical degradation of thermal greases known as dry-out also threatens the reliability [12] especially in high-temperature applications [13]. The mechanical stiffness of a heat sink can also affect the reliability of large power modules because the deformation of the module is restricted by it being clamped to the heat sink [2].

1.5.4 Size and weight

The requirements on size and weight of cooling systems are determined by the application. The general miniaturization trend has been driving the research in cooling systems. The available space typically dictates whether simple air-cooled systems are still feasible, if or advanced liquid or two-phase ones are necessary. The low weight requirement is common in applications such as transportation, airspace, or satellites.

1.5.5 Electromagnetic Interference and compliance (EMI/EMC)

Heat sinks are typically made of electrically conducting materials and therefore they interact with electric fields within electronic products. Even though most heat sinks are electrically isolated from the circuitry, parasitic alternating currents can flow through them and disrupt the product operation or safety [14]. Devices such as CPU's, ASIC's[2], or modern power converters that operate at high frequencies can excite periodic current oscillations in heat sinks, which in turn generate electromagnetic waves [15]. The magnitude of the parasitic currents and electromagnetic waves is limited by regulating agencies such as ISO[3] or IEC[4]. Considering the contribution of the heat sink to the overall electromagnetic performance of a product is important for meeting the EMC[5] standards [16].

[2]Application specific integrated circuits

[3]International Organization for Standardization

[4]International Electrotechnical Commission

[5]Electromagnetic compliance

1.5.6 Energy efficiency and environmental impact

The energy efficiency of power converters and other electronic products is dictated by the ohmic loss in conductors and the energy consumption of fans and pumps in the cooling systems. The quality of the cooling system dictates the temperature of the device, which in turn affects the ohmic losses. An example of the resulting design trade-offs can be found in the study by Christen et al. [17] who compared the energy efficiency of forced and free convection cooling for high-efficiency power converters. While it is possible to state that the efficiency of a converter can be improved by using an energy-efficient cooling system, it is important to note that the overall product efficiency is the most suitable metric.

Besides the energy consumption during the operation of a product, the overall environmental impact is also affected by the manufacturing and end-of-life disposal of all the parts. By selecting materials and manufacturing methods with low environmental impact, and considering their position in the circular economy framework, high-level societal sustainability goals can be achieved [1]. The environmental impact of electronic products is often coarsely reflected in life cycle assessment (LCA) studies of larger systems. The practical examples include power converters in photovoltaic systems [18] or electric vehicles [19]. Where time-consuming LCA studies are not feasible, the concept of embodied energy is a useful tool for reflecting the energy demand during the entire lifetime in the calculations of the energy efficiency of a product. In cell tower and data center applications [20, 21], studies of embodied energy lead to a successful identification of factors that were previously not known to affect the energy efficiency.

1.5.7 Acoustic noise

Fans in cooling systems generate unwanted acoustic noise whose magnitude is given by the design of the fan, but also by the required flow rate and pressure drop [22]. Improvements in thermal resistance of cooling systems have been shown to lead to decreased acoustic noise [23]. From the heat sink design perspective, a shape optimized for low thermal resistance and low pressure drop will result in a lower acoustic noise, given that all the other good practices on mitigating fan noise are followed [24, 25, 26, 27].

1.6 Natural graphite sheet for heat sink applications

Natural graphite sheet (NGS) is a thin, compressible, porous, electrically and thermally conductive material that has been used primarily to make sealing gaskets because of its ability to conform to rough surfaces, recover after compression, withstand high temperatures, and resist corrosive fluids. NGS properties are also well aligned with the requirements for cooling systems summarized in section 1.5. A summary of the NGS properties alongside with those of aluminum and copper is given in Figure 1.6. The NGS properties are density

dependent and vary greatly in the in–plane and through–plane directions that are defined in Figure 2.3e.

The in–plane thermal conductivity was reported to range from $100\,\mathrm{Wm^{-1}K^{-1}}$ (which is a quarter that of copper and half that of aluminum) to $600\,\mathrm{Wm^{-1}K^{-1}}$ [28] (which is 1.5 times that of copper and 3 times that of aluminum). In the through–plane direction, the thermal conductivity was reported to be low in the range 1 to $15\,\mathrm{Wm^{-1}K^{-1}}$. The high in–plane thermal conductivity is desirable for heat sink applications, however, the low through–plane value poses a challenge. NGS has been considered to be used as a thermal interface material [29, 30, 31], which suggests that the TCR between the heat sink and heat source can be lower than in case of the conventional metals.

Based on the average prices of commodities in the United States ports [32], graphite flakes–which are the raw material in NGS production–are 95 to 99 % less expensive than copper, and 59 to 89 % less expensive than aluminum (Figure 1.6b). The weight of NGS is 79 to 94 % lower than that of copper, and 30 to 81 % lower than that of aluminum as shown in the comparison of densities in Figure 1.6c. As seen in Figure 1.6d, the electrical conductivity of NGS is two-to-four orders of magnitude lower than that of aluminum or copper, which is desirable for reducing the electromagnetic emissions of power electronics.

Based on the available information on NGS, it can be stated that it is a relevant candidate for a heat sink material.

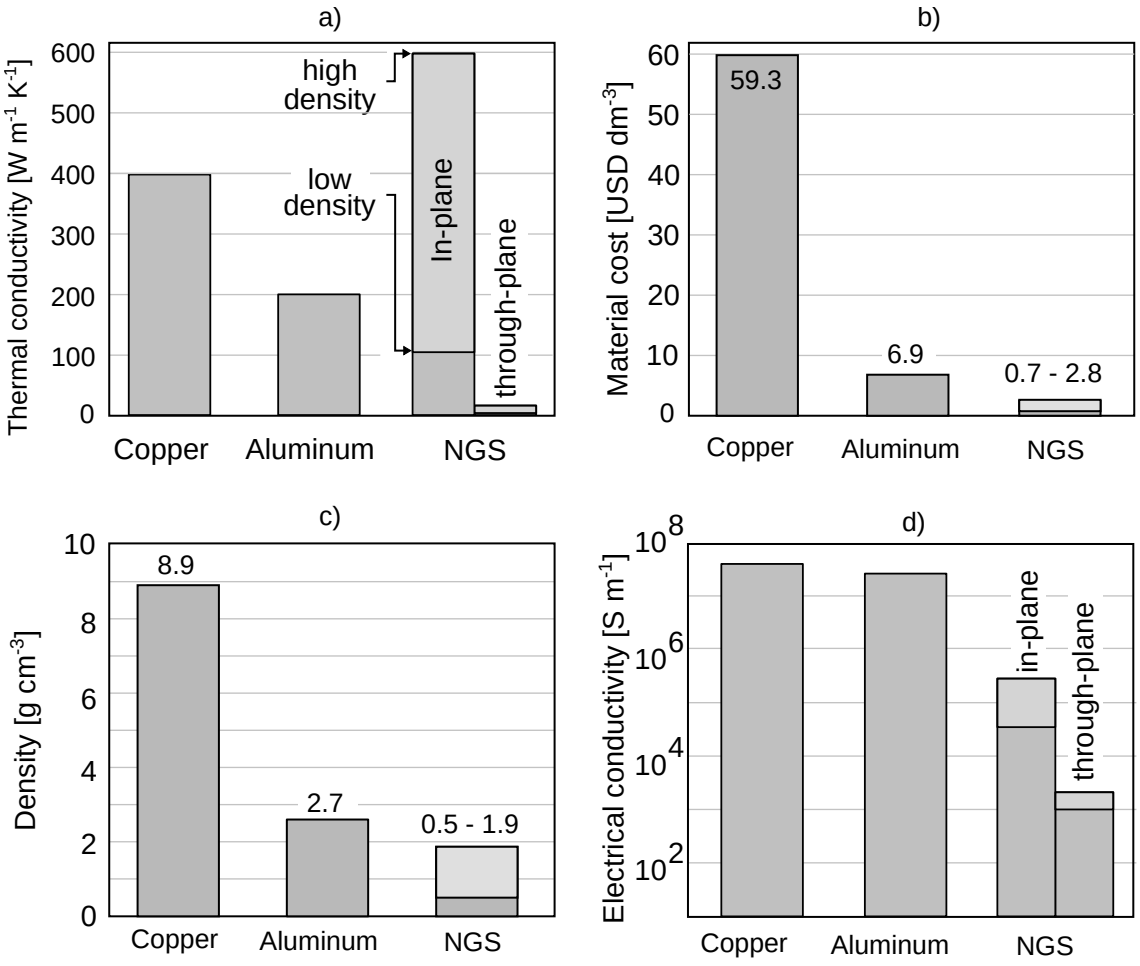

Figure 1.6: A comparison of a) thermal conductivity, b) material cost, c) density, and d) electrical conductivity of NGS, aluminum, and copper.

1.7 Literature review on graphite heat sinks

Norley et al. (2001) [33] first introduced the concept of natural graphite heat spreaders and heat sinks, and discussed two types of natural graphite based materials: i) laminate plate material, which is formed by chemically bonding individual sheets and subsequently machining the laminate into the final shape, and ii) compression molded graphite/epoxy composite, which is pre-formed by die-pressing or iso-molding. In case of complex shapes, the latter material is finished by machining. The material properties were reviewed, showing that the laminates offer thermal conductivities of $233\,\mathrm{Wm^{-1}K^{-1}}$ in the in–plane direction, $4.5\,\mathrm{Wm^{-1}K^{-1}}$ in the through–plane direction, and the density of $1.33\,\mathrm{gcm^{-3}}$. The properties of the graphite/epoxy composite can be modified by the amount of epoxy resulting in the in–plane thermal conductivity of 57 to $202\,\mathrm{Wm^{-1}K^{-1}}$, through–plane thermal conductivity of 7 to $71\,\mathrm{Wm^{-1}K^{-1}}$, and the density in the range from 1.5 to $1.9\,\mathrm{gcm^{-3}}$. Photographs of

prototype heat sinks are shown in the publication and were reprinted in Figure 1.7. The performance of the heat sinks was not discussed.

Figure 1.7: Photographs of products manufactured from compression molded graphite/epoxy composite. The figure has been reprinted from Norely at al. [33]. ©2001 IEEE.

Chen at al. (2003) [34] numerically evaluated heat sinks made of graphite/epoxy composites with an in-plane thermal conductivity of $376\,\mathrm{Wm^{-1}K^{-1}}$, through–plane thermal conductivity of $7\,\mathrm{Wm^{-1}K^{-1}}$, and density of $1.9\,\mathrm{gcm^{-3}}$. The effect of the orientation of the low through-plane conductivity on the heat sink performance was analyzed by modelling a large heat sink on a small heat source. The best case was when the low conductivity direction was aligned with the length of the heat sink. However, the graphite heat sink still showed 7.3 °C higher temperature in comparison with a geometrically identical copper heat sink, which was attributed to the poor spreading in the base. Expanding the heat source to cover the entire base led to a similar performance of graphite/epoxy and copper heat sinks. A hybrid heat sink composed of a copper base and graphite/epoxy fins was suggested to solve the poor spreading in the base, and the simulations showed that this design performs comparably to a copper heat sink.

Marotta et al. (2003) [35] built a parallel plate graphite/epoxy heat sink for high performance servers. The fins, spacers, and aluminum end plates (used for protecting the soft fins) were laminated and tie-rods were used to hold the laminate together. Steel inserts were mounted to the base to allow clamping of the heat sink to the heat source. The low sheet-to-sheet interface strength led to breaking, which was solved by using the metal parts of the heat sink for clamping. The details of the clamping design are unclear. The heat sinks were mounted on a heat source of a matching size using two types of a thermal interface material (synthetic oil and phase change material). Thermocouples installed in the

heat source, heat sink base, and in the ambient air were used to evaluate the resistance of the heat sink and the interface. The heat sinks were measured in cross flow and impinging flow configurations, and the results were compared to a geometrically identical aluminum heat sink. The graphite/epoxy heat sink showed a 27 % higher thermal resistance in comparison with the aluminum one. The interface resistance was not reported, but it can be calculated from the temperature drops and heat dissipation rate to be in the range of 34 to 194 $\mathrm{Kmm^2W^{-1}}$ for the graphite/epoxy heat sinks, and 24 $\mathrm{Kmm^2W^{-1}}$ for aluminum. The worse interface performance of the graphite/epoxy heat sinks was attributed to the poor flatness of the base. Subsequent grinding reduced the resistance to the lower bound of the given range.

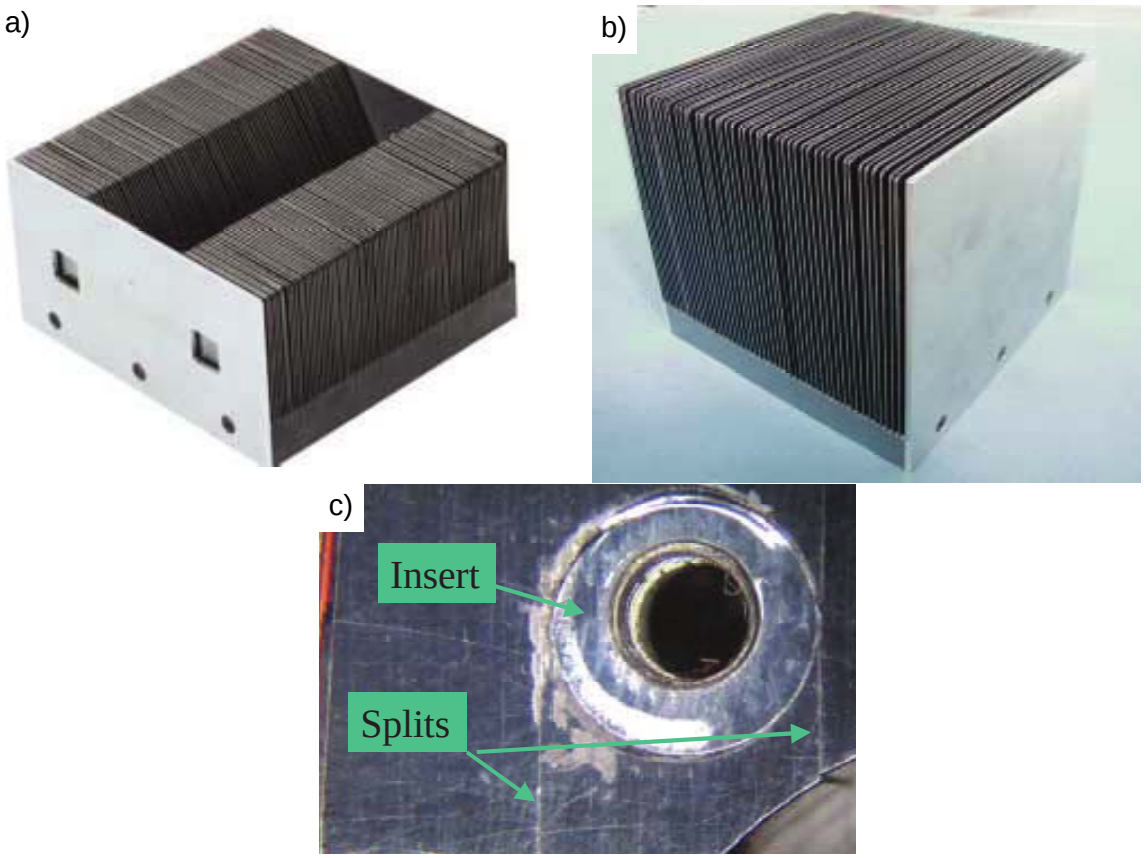

Figure 1.8: Photographs of the NGS heat sinks manufactured in the work by Marotta et al. [35]. a) impinging flow configuration, b) cross-flow configuration, and c) a illustration of cracks around the threaded inserts. The photographs were reprinted with permission from the publisher.

Shives el al. (2004) [36] realized the concept of a hybrid heat sink introduced by Chen at al. (2003) [34] by bonding graphite/epoxy fins to a copper base plate using a solder, conventional epoxy, and thermally conductive epoxy. The resulting heat sink consisted of $114 \times 98 \times 7.5$ mm base and 46 fins 0.5 mm thick and 30.6 mm long. A reference heat sink

was made by soldering copper fins to a copper base. During the tests in a wind tunnel, the heat sinks were mounted on a $37 \times 37\,\mathrm{mm}$ heat source and the air speed was varied from 1 to $3.2\,\mathrm{ms}^{-1}$. Among the hybrid heat sinks, the one bonded by the thermally conductive epoxy showed the best performance. However, its resistance was higher than the all-copper reference case by approximately $0.015\,\mathrm{KW}^{-1}$, which translates to a 5.6 % relative difference. The weight of the hybrid graphite/epoxy heat sink was reported to be 40 % of the reference all-copper heat sink.

Icoz and Arik (2010) [37] compared multiple lightweight materials for a vertical plate natural convection heat sinks. The considered materials were aluminum, carbon foam, plastic with a thermally conductive filler, and graphite with the in–plane thermal conductivity of $370\,\mathrm{Wm}^{-1}\mathrm{K}^{-1}$, through–plane thermal conductivity of $6.5\,\mathrm{Wm}^{-1}\mathrm{K}^{-1}$, and the density of $1.94\,\mathrm{gcm}^{-3}$. All tested heat sinks had a $50 \times 305 \times 3\,\mathrm{mm}$ base and 25 fins 2 mm thick and 30 mm long but the details about physical realization of the heat sinks are missing. Numerical simulations and an experimental measurements were performed and the performance was evaluated using the figure of merit (FOM), which was defined as:

$$FOM = \frac{1}{mR_{th}}\mathrm{Wkg}^{-1}\mathrm{K}^{-1}, \tag{1.2}$$

where m and R_{th} are the mass and thermal resistance of the heat sink, respectively. The comparison of the heat sinks showed that the carbon foam heat sink has four times higher figure of merit in comparison with the other materials. The possibility to use a low density NGS to design heat sinks with the FOM closer to that of the carbon foam ones was not considered. The thermal performance of the graphite heat sink was comparable to the one made of carbon foam.

A summary of the properties of all the heat sinks that have been built and reported in the literature is given in Table 1.1. Publications with marginal relevance are listed in the following paragraph.

Wang et al. [38] performed a broader literature review of heat sinks and heat exchangers made of carbonaceous materials and carbon matrix composites. Bouknadel et al. [39] carried out a numerical simulation of various heat sink geometries under natural convection and analyzed the performance of a graphitic material with the thermal conductivity of $1500\,\mathrm{Wm}^{-1}\mathrm{K}^{-1}$ in the in–plane and 50 to $60\,\mathrm{Wm}^{-1}\mathrm{K}^{-1}$ in the through–plane directions. Sabatino and Yoder [40] investigated using pyrolytic graphite for cooling of circuit boards, but the relevance to this thesis is low due to a different material and a different interpretation of the term heat sink.

	Icoz and Arik (2010) [37]	Marotta, Norley, et al. (2003) [35]	Shives, Norley, el al. [36]
Air flow	Natural convection	Forced convection, impinging flow	Forced convection
Heat sink type	Parallel plates	Parallel plates V-notch	Parallel plates
Base size mm (L x W x t)	305 x 50 x 3	113 x 113 x 10-15	114.3 x 98.0 x 7.6
Fin size mm (L x t)	30 x 2	45-50 x 0.64	30.6 x 0.5
Number of fins [-]	25	77	46
Density gcm^{-3}	1.94	1.94	1.94 (graphite), 8.89 (copper)
Material description	Graphite	Graphite/epoxy	copper base, graphite/epoxy fins
Thermal conductivity $Wm^{-1}K^{-1}$	370 in–plane 6.5 through–plane	370 in–plane, 6.5 through–plane	Graphite/epoxy: 370 in–plane, 6.5 through–plane; Copper: 387
Heat sink thermal resistance KW^{-1}	1.1 at 30 W	0.03 at 135 CFM	0.32 at $1\,ms^{-1}$ 0.17 at $3.2\,ms^{-1}$
Interface thermal resistance Kmm^2W^{-1}	N/A	5.1 to 194(phase change TIM)	N/A
Clamping pressure kPa	N/A	N/A	140
Heat source size mm	Full base	Full base	17 x 17
Photography in publication	no	yes	no

Table 1.1: Summary of the parameters of NGS heat sinks in the literature

1.8 Research motivation and goals

Despite the previous research on NGS heat sinks, the open literature does not contain clear conclusions on the feasibility of NGS heat sinks. The published work on server CPU cooling suggests that the low through–plane thermal conductivity and fragility of NGS pose a challenge for the thermal performance and heat sink mounting. However, the work considered heat sink geometries and clamping methods that are typical for isotropic metals, which can be considered irrelevant due to the different material properties of NGS. Further research is necessary for evaluating the feasibility in various applications such as computers, micro-electronic chips, or power electronics.

In power electronics applications, which are the focus of this thesis, the size and heat dissipation rate of heat generating components varies greatly. The variation is reflected in the cooling systems whose types range from large air-cooled natural convection heat sinks,

through compact fan-cooled heat sinks, to liquid-cooled cold plates. Despite the growing market share of liquid cooled systems especially in space-limited high-power applications such as electric vehicles, air cooled heat sinks are often preferred for their simplicity, reliability, low cost, and low weight. Technological innovations such as heat pipes or 3D printing keep on improving the achievable thermal performance of air cooled systems. The different material properties and manufacturing method of NGS offer a possibility to produce improved heat sinks with shapes that were previously impossible or cost prohibitive. Furthermore, manufacturing of the improved heat sinks without a cost penalty may be possible and additional benefits such as lower weight or better electromagnetic performance.

The primary goal of this PhD program is to evaluate the feasibility of using NGS heat sinks for power electronics cooling. An emphasis is placed on identifying the implications on the performance metrics of the entire system, rather than focusing on one of the subtopics such as thermal resistance. In scientific terms, the following hypothesis is tested: *Using natural graphite sheet heat sinks leads to improved power electronics products.*

The evaluation of feasibility as well as the subsequent design of heat sinks requires a detailed knowledge of material properties. NGS has been studied by material scientists, however, the understanding is incomplete and the data are scattered across many publications, poorly communicated, and often show high variability. Material characterization of NGS is a crucial pillar of the present work.

Based on the list of relevant parameters for heat sink design in section 1.5, the present research focuses on answering the fundamental questions about the thermal and electromagnetic performance, weight, cost, reliability, and environmental impact of NGS heat sinks. In particular, the research questions are:

- Does the anisotropy in thermal conductivity of NGS limit the thermal performance of NGS heat sinks? If yes, how can it be mitigated?
- How does the thermal contact resistance at the interface between a heat sink and heat source differ between NGS and metal heat sinks?
- Can – and under what conditions – using NGS heat sinks lead to an opportunity to eliminate thermal interface materials (TIM)? What will be the impacts on reliability, manufacturing, and overall cost of cooling systems?
- Does the low electrical conductivity of NGS affect the conducted and radiated emissions of power electronic devices?
- What are the implications on reliability of power semiconductors after replacing metal heat sinks with NGS ones?
- Does the low mechanical strength of NGS impede the practical applications of heat sinks?

- What is the estimated cost of NGS heat sinks?
- What weight reduction can be achieved by replacing metal heat sinks with NGS ones?
- How do NGS and conventional heat sink compare in terms of the environmental impact?

1.9 Overview of the thesis structure

The following chapter (Chapter 2) introduces the reader to the most common graphitic materials and elaborates on the NGS manufacturing process. In Chapter 3 a summary of the material properties and structure of NGS is first presented, and then a detailed description of all the measurements follows.

The manufacturing of NGS heat sink prototypes is described in chapter 4. Chapters 5, 6, 7, and 8 describe the tasks performed to investigate the thermal performance, electromagnetic behavior, cost, and environmental impact of NGS heat sinks. Chapter 9 uses all the findings from the previous chapters together with expanded analyses to evaluate the feasibility of NGS heat sinks for specific applications. Projections of the future development of NGS technology are given in chapter 10.

The structure of the thesis was optimized to allow a reader who is interested in a single particular part of the work to find the most of the relevant information in one place. Each of the chapters–and some sub-chapters–contains a brief introduction, a review of the relevant previous work, results, and the key conclusions.

Chapter 2

Graphite

Graphite is a form of carbon with the characteristic hexahedral layered atomic structure shown in Figure 2.1. Atoms within each layer are bonded by a strong covalent bond, while individual layers are bonded by weak van der Walls forces. It is common to denote the directions in the plane of graphite layers as ab, and the perpendicular direction as c. The difference in atomic bonds in ab and c directions is reflected in the anisotropy of graphite properties. For example, the thermal conductivity is estimated to be $2000\,\mathrm{Wm^{-1}K^{-1}}$ in the ab directions, and 6 to $9\,\mathrm{Wm^{-1}K^{-1}}$ in the c direction [41]. The high ab thermal conductivity attracts a significant amount of attention, but it is important to note that the value is relevant to a monolithic (single crystal) structure with no defects. In reality, all the graphite materials are polycrystalline, i.e., they consist of many crystals whose size and shape depends on the particular material. A general trend in developing graphitic materials for heat transfer applications is an effort to align the crystals in the same direction, which requires using thin sheets instead of standard shapes such as blocks, bars, or rods. If a polycrystalline graphitic material consists of large crystals whose a and b directions are aligned in the same direction direction, a high thermal conductivity can be achieved.

Graphite can be mined in its naturally occurring forms or manufactured from carbon-rich materials [43]. Both forms have significantly different properties and are suitable for different applications.

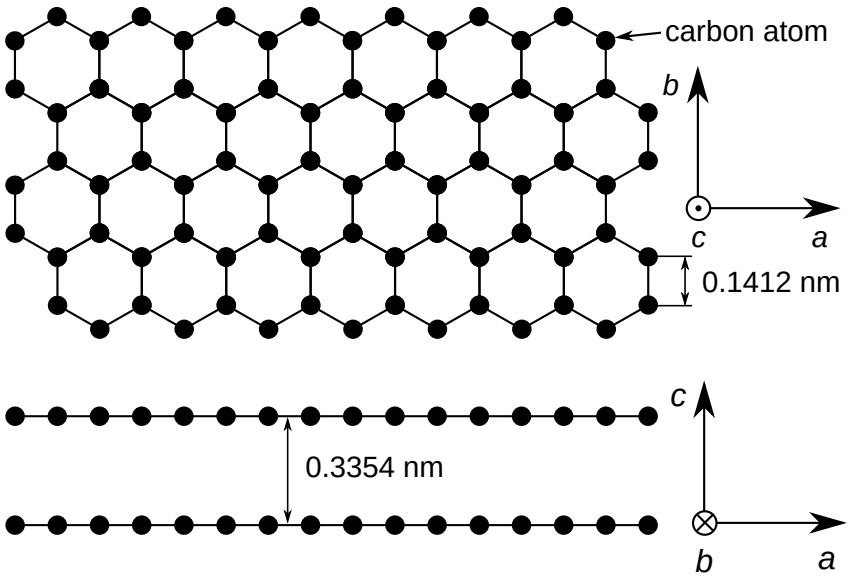

Figure 2.1: Atomic structure of graphite (The values of the spacing based on Inagaki (2014) [42]).

2.1 Synthetic graphite

The term synthetic graphite describes the family of materials that is manufactured from carbon-rich substances in gas, liquid, or solid phases. The most known synthetic graphite material, which has been used for decades in metal production and nuclear reactors, is referred to as polycrystalline or molded graphite. It is manufactured from petroleum coke and coal tar pitch in a process that involves heat treatment at high temperatures up to 3000 °C [43], and forming by extrusion or pressing. It is a relatively hard and strong material which is composed of mostly randomly oriented graphite crystals whose size depends on the starting material and the manufacturing process. The random crystal orientation results in isotropic material properties. For example, the thermal conductivity is 70 to 140 $\mathrm{Wm^{-1}K^{-1}}$ and the coefficient of thermal expansion is 3.5×10^{-6} to $6.5 \times 10^{-6}\,\mathrm{K^{-1}}$ [42]. To manufacture complex shapes, such as heat sinks, polycrystalline graphite stock has to be machined, which significantly increases the product cost and limits the applications to those where no other options exist.

Thin synthetic graphite films are manufactured from hydrocarbon gases such as methane, or from polyamide sheets such as Kapton. In the first case, a carbon-rich gas is deposited on a heated substrate and subsequently heat treated under pressure (1 MPa) at temperatures up to 3600 °C to obtain a tens or hundreds of micrometers thin film known as highly oriented pyrolytic graphite (HOPG) [42]. In the second case, a solid uncompressed polyimide film is heat treated at similarly high temperatures to form a pyrolytic graphite sheet (PGS[1]).

[1]Currently a trademark owned by Panasonic Corporation (Serial Number 75726644)

In both cases, the structure consists of large crystals aligned parallel to the film which results in the in-plane thermal conductivity very close to the theoretical limits of a single graphite crystal. Commercial products with the claimed thermal conductivities as high as 1950 $\mathrm{Wm^{-1}K^{-1}}$ are available [44]. The values are in agreement with the measurements in scientific literature [45]. PGS sheets are used as heat spreaders for their high in-plane thermal conductivity in applications such as handheld devices or screens.

2.2 Natural graphite

2.2.1 Raw forms of natural graphite

Natural graphite can be found in deposits around the world in various forms – amorphous (microcrystalline), flake, and vein. The main distinctions of the forms are the crystallinity and purity, both of which contribute to the material properties.

The form of natural graphite with the lowest crystallinity has been historically called amorphous, which is defined as "having no real or apparent crystalline form" [46]. Later, it was proven that the name is inappropriate because the material is composed of small (40 to 70 µm [47]) randomly oriented crystals (Figure 2.2a) and therefore a new name – microcrystalline graphite – was suggested [48]. Microcrystalline graphite is not suitable for thermal applications, but it has been used in refractory materials, lubricants, brake linings, or pencil lead.

The other two forms of graphite – flake and vein – have similar microstructure composed of relatively large crystals 1 to 25 mm [49], but their geological occurrence, mining practices, and quality are very different. Flake graphite (Figure 2.2b) is found as discrete flakes enclosed by soft or hard host rock. Vein graphite, which is also known as crystalline, chip, or lump graphite, occurs in a form of coherent lumps that contain high percentage of graphite with minimum impurities (Figure 2.2c). After extraction from surface or underground mines, vein graphite requires minimal processing and can be readily shipped as lumps or milled into vein graphite flakes. Flake graphite has to be separated from the host rock by crushing, milling, and flotation, which reduce the initial flake size into sub-millimetre sizes. The industry standards are: super jumbo >500 µm, jumbo 300 to 500 µm, large 150 to 300 µm, and medium/small 106 to 150 µm [50]. To achieve high purity, i.e. to increase the fixed carbon content and eliminate impurities such as sulfur, iron, quartz or clay, additional chemical or thermal treatment is used for both vein graphite and flake graphite [47].

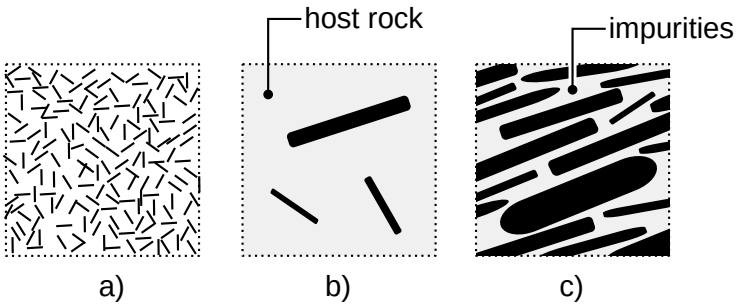

Figure 2.2: Schematics of a) microcrystalline, b) flake, and c) vein graphite

2.2.2 Natural graphite sheet

Loose graphite flakes can be formed into cohesive sheets in a process that does not require a binder [51]. First, the flakes (Figure 2.3a) are treated with an intercalation agent (most often sulfuric acid), which penetrates in between the graphite layers. This so-called graphite intercalation compound (GIC) or expandable graphite (EG) is then rapidly heated, which forces the intercalation agent to expand and push the individual carbon layers apart, and results in exfoliated natural graphite (ENG) particles known for their worm-like or accordion-like structure (Figure 2.3b). Compressing ENG particles using compression molds (Figure 2.3c) or calenders (Figure 2.3d) yields thin, cohesive sheets with graphite layers aligned perpendicular to the sheet thickness (Figure 2.3e). The nomenclature in this thesis uses the term *through–plane direction* to refer to the direction parallel to the compression direction. The term *in–plane direction* refers to the directions perpendicular to the through–plane direction. An illustration of the in–plane and through–plane direction is shown in Figure 2.3e.

In this thesis, the name natural graphite sheet (NGS) is used, but other names such as flexible graphite, compressed exfoliated natural graphite, or graphite foil have been used in the literature. Flexible graphite is the most common name, however, it can be misleading as thicker sheets are rigid and break easily when flexed by mere finger strength. Caution needs to be exercised to distinguish between NGS and PGS. The flexibility of highly-compressed thin NGS is closer to that of PGS, but thicker sheets, which are more relevant to the heat sink research, cannot be flexed, as is demonstrated in Figure 2.4.

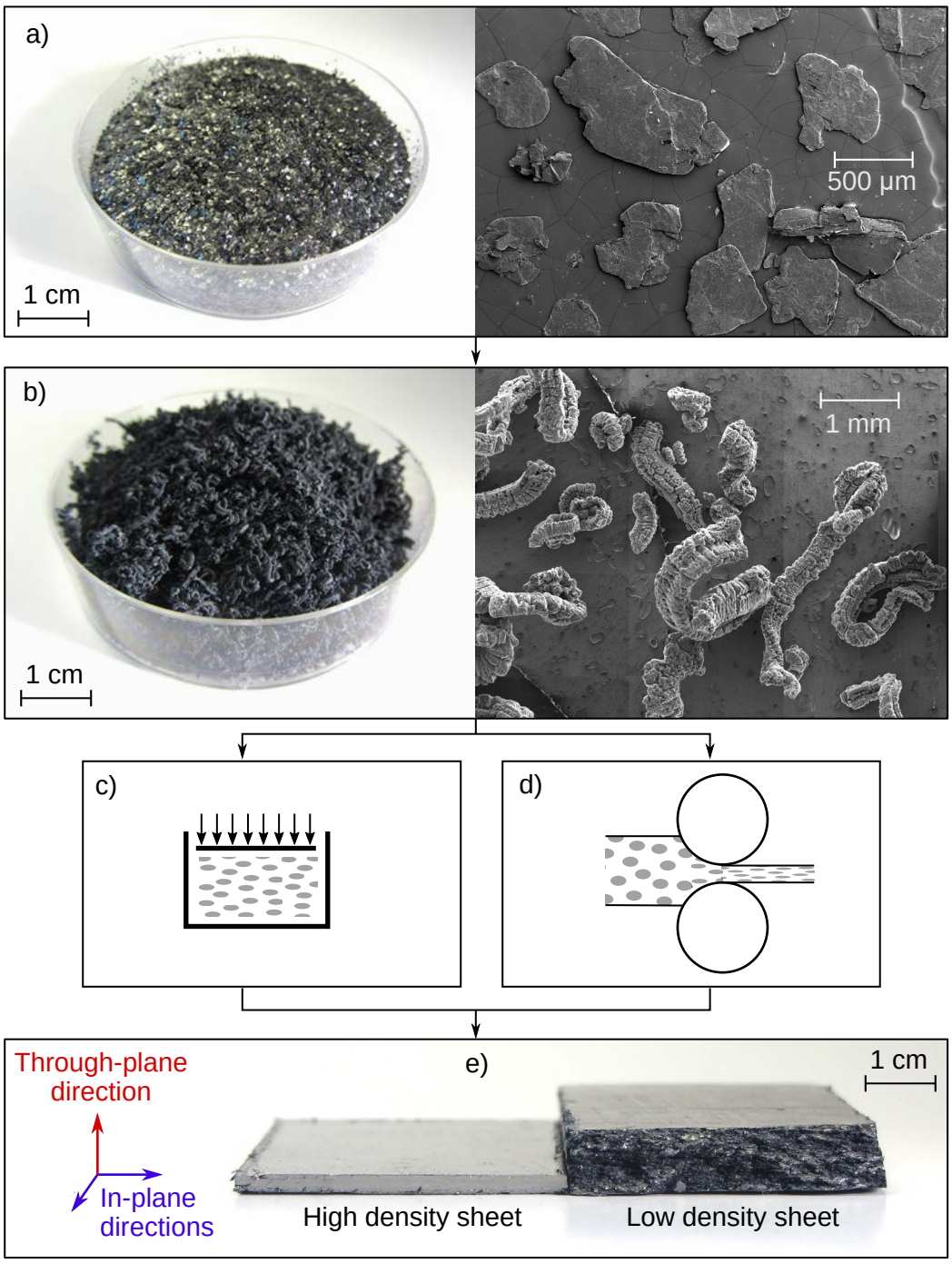

Figure 2.3: Illustration of production of NGS: a) natural graphite flakes, b) exfoliated natural graphite (ENG) particles, c) compression forming, d) calendering, and e) finished NGS.

Figure 2.4: An illustration of the flexibility of a) thick natural graphite sheet and b) pyrolytic graphite sheet.

2.3 Kish graphite

Kish graphite has the structure and properties similar to the natural flake graphite, but instead of mining, it is obtained as a by-product from the steel making process [52]. When molten steel cools down, it becomes supersaturated with carbon, which segregates into graphite flakes. The segregation of carbon in presence of liquid iron has been studied in laboratory conditions [53, 54, 55, 56] and the conclusions state that large, highly crystalline flakes can be produced at temperatures significantly lower than those required for production of synthetic graphites. The largest graphite crystal produced by cooling of an iron melt under controlled conditions was 30 mm long (a and b directions) and 0.06 mm thick (c direction) [57]. An SEM image of a commercially available kish graphite flake (Graphite Supermarket, grade 200, 2018) is shown in Figure 2.5.

Liu and Loper [58] investigated the crystallographic properties and the impurity content of kish graphite recovered from steel making process, and stated that despite a large tonnage of kish graphite being generated every day, it is not being used because the impurity content is expected to be high, and no suitable methods for recovering graphite flakes from steel making waste are available. It should be noted that the study was published in 1991 and may be obsolete. In the same study, sheets with the density of 1.1 g cm^{-3} and carbon content of 96 % were manufactured from thermally exfoliated kish graphite flakes, and their tensile strength, compressibility, and compression recovery were measured. The reported in–plane tensile strength is 30 % lower than that of NGS measured Gao et al. [59]. The thermal properties of kish graphite sheet have not been measured and conclusions on heat transfer applications cannot be made.

To the author's best knowledge, kish graphite sheets are not commercially available. However, an effort to commercialize the process is evident from the patent application by Klett et al. [60]. Frost [61] concluded that recovering kish graphite from steel making waste is economically feasible.

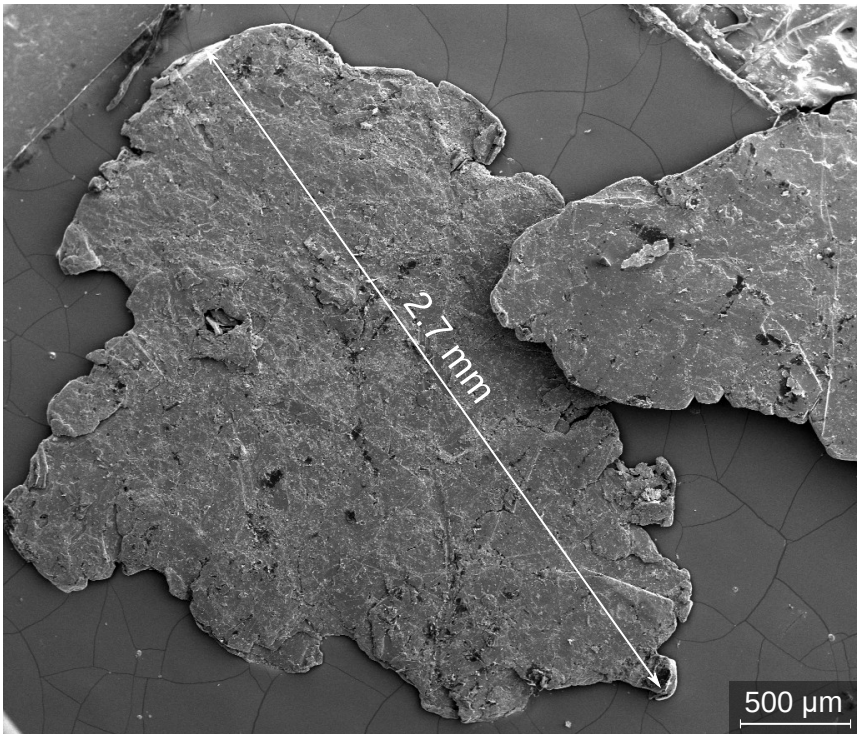

Figure 2.5: SEM image of commercially available kish graphite flake supplied by Graphite Supermarket. The production method was not confirmed by the supplier, but based on the flake size and research-focus of the supplier, it can be assumed that controlled environment was used and the flakes were not extracted from steel making waste

Chapter 3

Material properties of natural graphite sheet

In this chapter, the NGS material properties that have been identified to be relevant to heat sink applications are reviewed, and the literature gaps are filled by performing the necessary measurements. The thermal conductivity, thermal diffusivity, heat capacity, and emissivity dictate the steady-state and transient thermal performance of heat sinks, and they are considered essential for any future work on NGS heat sinks. The electrical conductivity is relevant to the electromagnetic performance of heat sinks, and reliable values are necessary for quantifying the conducted and radiated electromagnetic emissions of heat sink. The compression behavior is addressed to quantify the forming process and to provide the stress-strain data necessary for describing the change of the properties under compression. Assessing the potential reliability issues requires knowing the coefficient of thermal expansion (CTE) and stress-strain curves under compression. To provide explanations to the trends in the material properties, the structure of NGS is studied using microscope images.

In the greater context, the extensive material characterization study reported in this chapter is expected to offer the data for other applications such as fuel cells or flow batteries. An easy-to-use graphical summaries of the material properties and the forming process were prepared and included as Appendices A and B. Reduced size versions are shown in Figures 3.1, 3.2, and 3.3. The raw data, data processing scripts, results, and SEM images in high resolution are available in [62]. An audiovisual summary of the chapter is available at `https://www.youtube.com/watch?v=d9BnnHE9ywg&list=PLaX55SIXaD20NQQ2JLP-7abmET7l-6LS4&index=3` [1].

In many cases the standard nomenclature had to be substituted with alternative symbols; for example, even though the standard symbol for strain is ϵ, it was substituted with

[1] The video files are also available in Appendix F

S because ϵ was already reserved for emissivity. The reader is referred to the nomenclature for the complete list of symbols.

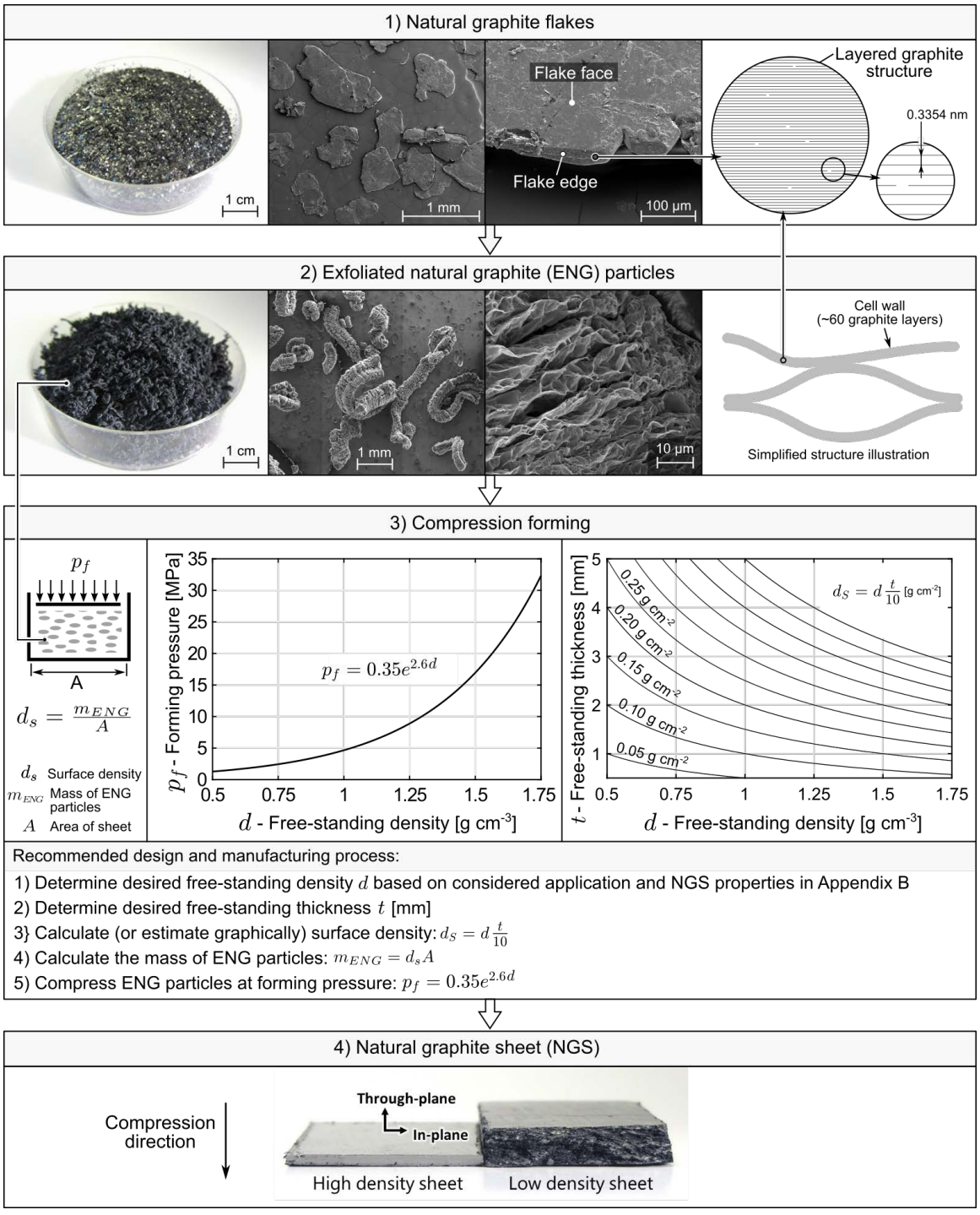

Figure 3.1: A graphical compilation of the NGS forming process. An enlarged high-resolution version is available in Appendix A.

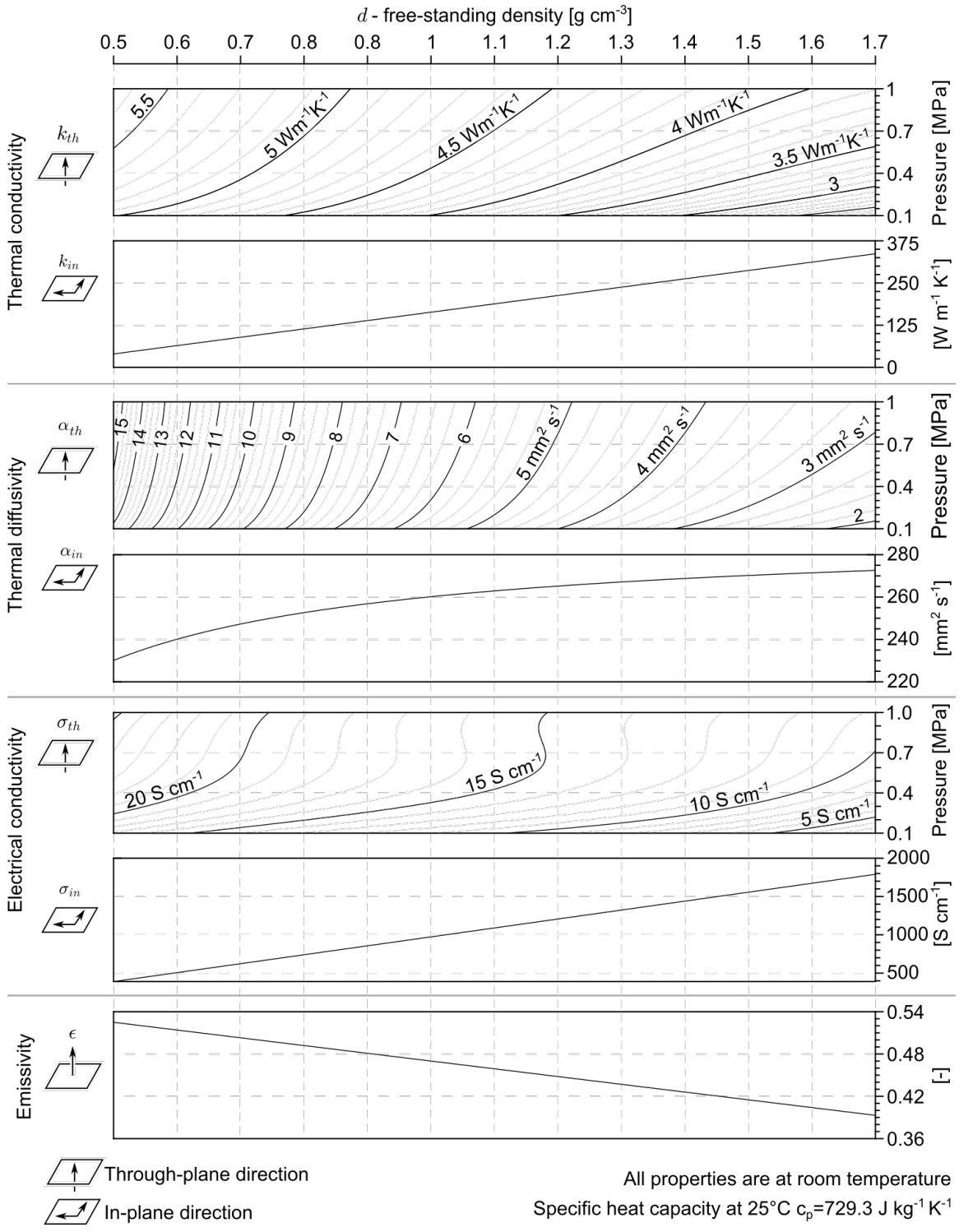

Figure 3.2: A graphical summary of thermal conductivity, thermal diffusivity, electrical conductivity, and emissivity of NGS. An enlarged high-resolution version is available in Appendix B.

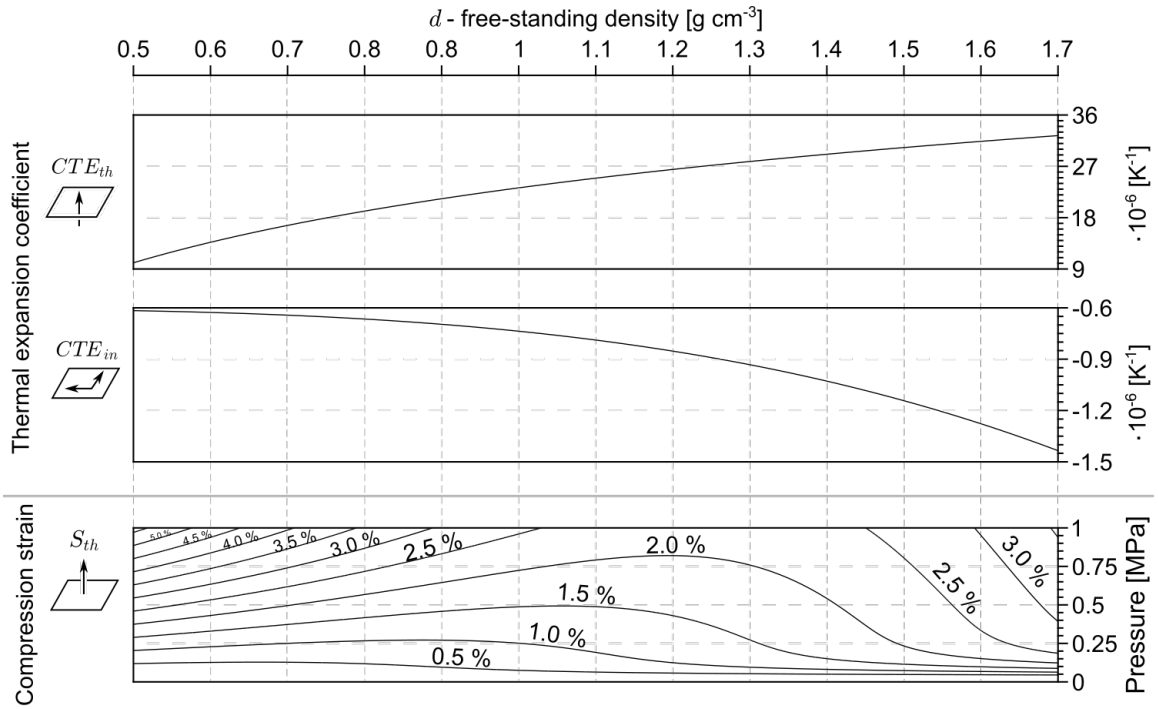

Thermal conductivity	↑	$k_{th} = (34.63 - 34.44d + 29.61d^2)p^{0.01015-0.0008422d} - 30.59 + 34.99d - 31.75d^2$	±0.4	[W m^{-1} K^{-1}]
	↗	$k_{in} = 212d - 22$	±15	
Electrical conductivity	↑	$\sigma_{th} = 2667 - 3806d + 4.111p + 2945d^2 - 1.795dp - 0.004019p^2 - 992d^3 + 0.9967d^2p - 0.0003251dp^2 + 1.877 \cdot 10^6p^3$	±150	[S m^{-1}]
	↗	$\sigma_{in} = 1.167 \cdot 10^5 d \ - 1.934 \cdot 10^4$	±10%	
Emissivity	↑	$\epsilon = -0.11d + 0.58$	±5%	[-]
Thermal expansion	↑	$CTE_{th} = -119d^{-0.151} + 142$	±18%	·10^{-6} [K^{-1}]
	↗	$CTE_{in} = -0.132d^{3.46} - 0.6$	±0.2	
Strain	↑	$S_{th} = (0.0026 - 0.014d + 0.0166d^2)(1 - e^{-(p-30)0.03d^{-1.6}}) + (0.00012 - 0.000147d + 4.8 \cdot 10^{-5}d^2)(p - 30)$	±0.004	[-]

d - density [g cm^{-3}], p - pressure [kPa], relationships valid for $0.5 \leq d \leq 1.7$ g cm^{-3} and $100 \leq p \leq 1000$ kPa

↑ Through-plane direction

↗ In-plane direction

All properties are at room temperature, CTE for the range 35 to 95 °C

Specific heat capacity at 25°C c_p=729.3 Jkg^{-1}K^{-1}

Figure 3.3: A graphical summary of CTE and through–plane compression strain of NGS. The best fit equations for all the measured properties are given in the table at the bottom. An enlarged high-resolution version is available in Appendix B.

3.1 Sample preparation

All samples in this work were prepared from a $0.2\,\mathrm{g\,cm^{-3}}$ NGS that was supplied by Nano Carbon Technology CO., LTD, Qingdao, China. The ordered surface densities were $70\,\mathrm{mgcm^{-2}}$, $140\,\mathrm{mgcm^{-2}}$, and $210\,\mathrm{mgcm^{-2}}$, which translates to the thicknesses of 3.5 mm, 7 mm, and 10.5 mm. The supplier stated that raw graphite flakes used for manufacturing the sheets had the fixed carbon content 99.27 % and size composition 81 % larger than 300 µm (50 mesh). The flakes were intercalated with an H_2SO_4+H_2O_2+$KMnO_4$ solution and exfoliated at 950 °C with 5 minutes residence time. The resulting exfoliated natural graphite (ENG) particles had the apparent specific volume of $250\,\mathrm{ml\,g^{-1}}$, which is equal to the apparent density d_{ENG} of $4\,\mathrm{mgcm^{-3}}$. The details about the compression of the ENG particles into the sheets were not provided by the supplier.

The $0.2\,\mathrm{g\,cm^{-3}}$ sheets were cut and further compressed using a calendering machine shown in Figure 3.4. The machine consists of two 93.5 mm cylinders that are kept at the set distance by a pneumatic system that imposes a 6.9 kN force. The calendered sheets were 100 mm wide, 300 mm long, and their density and thickness ranged from 0.5 to $1.7\,\mathrm{gcm^{-3}}$ and from 0.4 to 4.1 mm as shown in Figure 3.5. For each of the measurements, samples of the desired shape and size were cut from the calendered sheets. When calendering the high-density sheets ($1.7\,\mathrm{gcm^{-3}}$), the upper cylinder visibly lifted, which implies that the capacity of the calendering machine was reached.

Using sheets with varying surface density allowed preparing samples with matching density but different thickness. For example, a 1.2 mm thick sample prepared from the $140\,\mathrm{mgcm^{-2}}$ sheet has the same density as 0.6 mm thick sample prepared from the $70\,\mathrm{mgcm^{-2}}$ sheet. Samples with multiple thicknesses were desirable to study the effect of thickness, and investigating the thermal and electrical contact resistance in stacks of sheets.

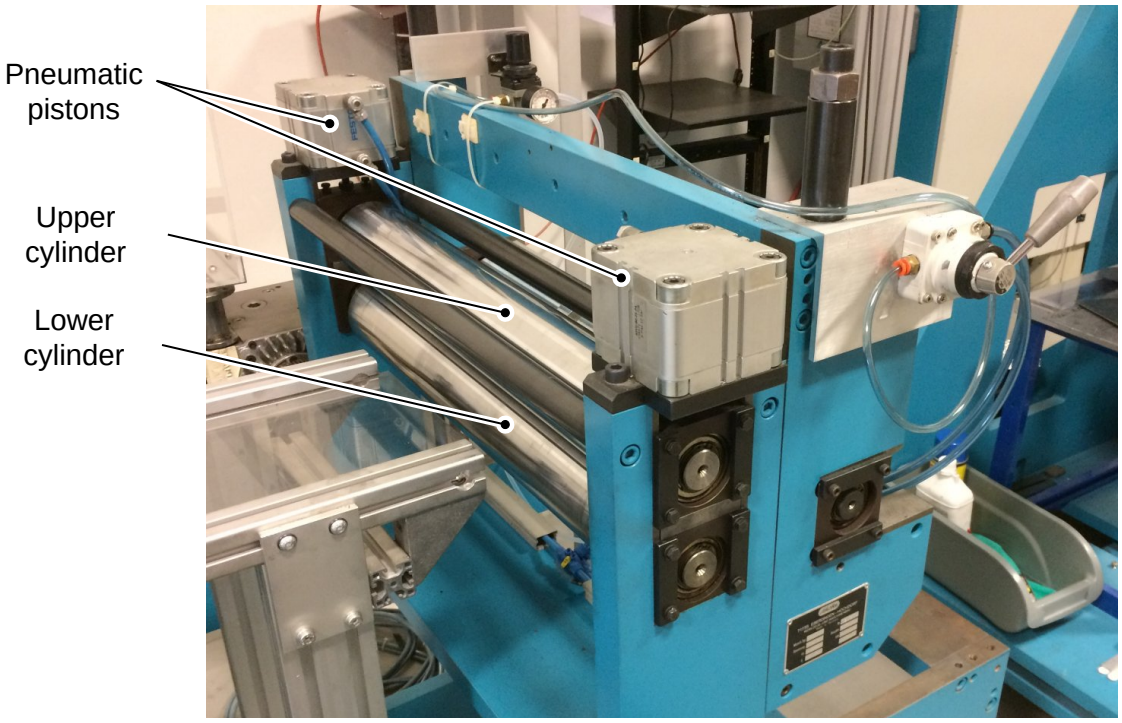

Figure 3.4: An image of the calendering machine that was used for sample preparation. The image was provided by John Kenna of Terrella Energy Systems.

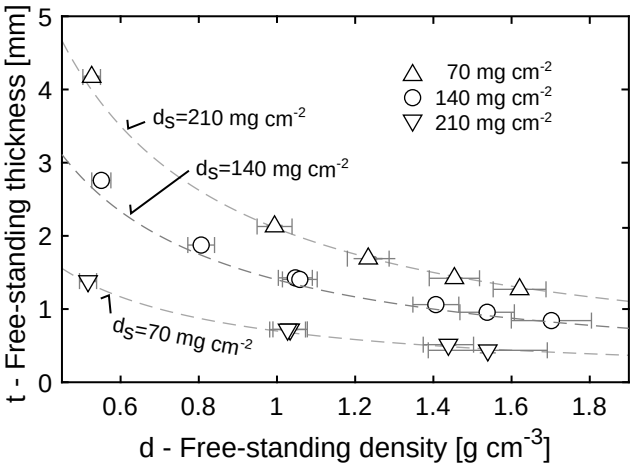

Figure 3.5: The thickness and density of the sheets used for the material characterization in this thesis. The dashed line symbolize the theoretical relationship between the free-standing density d, thickness t, and surface density d_s.

3.2 Density

The density of the calendered sheets was determined by measuring the weight, thickness, and diameter of discs that were cut using a 25 mm hole punch. The density was calculated as:

$$d = \frac{m}{tA} = \frac{m}{V}, \tag{3.1}$$

where m, t, A, and V are the disc mass, thickness, surface area, and volume, respectively. The weight was measured using an OHAUS AX124 scale and the dimensions by a Darson Instruments 0-1" 211-1313 analog micrometer. The uncertainty analysis is presented in section 3.11.1. The samples for measuring density were also used for measuring the through–plane electrical conductivity.

3.3 Structure

In this section, the structure of NGS is studied using a scanning electron microscope. The goal is to describe the structure and its change with density so that the trends in the measured material properties can be explained. The structure of ENG particles is also addressed because of its relevance to that of NGS.

3.3.1 Previous work

NGS is manufactured by compressing ENG particles with the apparent density in the range 2.6×10^{-3} to $7.5 \times 10^{-3}\,\mathrm{g\,cm^{-3}}$ [63] into sheets with the density ranging from 0.2 to $1.9\,\mathrm{g\,cm^{-3}}$. During the compression, the ENG particles deform, interlock, and form a cohesive object (NGS) without using a binder [63, 51]. The higher the forming pressure the higher is the density of the final sheet. The structure of ENG particles was reviewed in [51]. Before exfoliation, graphite flakes are highly crystalline with the density close to that of a theoretical graphite crystal ($2.26\,\mathrm{gcm^{-3}}$ [43]). During exfoliation, some graphite layers are pushed away but some remain in their original crystal configuration. The crystalline part of ENG particles is referred to as cell walls, and the same nomenclature is adopted in this thesis. A schematic and microscope images of ENG particle are given in section 3.3.3.1.

The literature contains multiple studies of NGS structure. Celzard et al. [63] manufactured a compression setup with a transparent wall to visually study the process of compressing ENG particles into sheets. While images are missing in the publication, the authors reported that at the beginning of the compression, the ENG particles rearrange spatially until contact points are made, and then start to deform and interlock. The authors defined the rigidity threshold – the density at which a block of compressed ENG particles becomes rigid and has a non-zero elastic modulus – to be in the range of 3×10^{-3} to $10 \times 10^{-3}\,\mathrm{g\,cm^{-3}}$. Additionally, a model to predict the intraparticle ENG density and the average disorientation of graphite basal planes was developed.

Dowell and Howard [64] studied the structure of NGS by microscope, X-ray diffraction, and porosity measurements. The samples for SEM microscope imaging were prepared by impregnating NGS in low viscosity epoxy in vacuum, polishing, and cathodic etching. Images of the surface of low density sheets ($0.2\,\mathrm{gcm^{-3}}$) showed that individual ENG particles are still distinguishable and were described as flattened sinuous tubes. Observing the fracture surface of a high density sheet that has been fractured under tension showed signs of interlocking of ENG particles. Wrinkling and interlocking was mentioned as the mechanism of joining individual ENG particles in NGS structure. The cross-section was described to have a cellular appearance consisting of wrinkled graphite plates approximately 1 µm thick, and voids 1 µm thick and several micrometers long. The density of the observed sheet was not explicitly specified. The thickness of the cell walls was estimated using three methods (X-ray diffraction, surface area, and SEM microscope) and its value ranged from 30 to 60 nm,

which is higher than the range 15 to 23 nm reported by Celzard et al. [65]. The difference can be explained by the fact that the thickness is most likely dependent on the quality of raw flakes and exfoliation method. The flake properties were not identical in the two studies.

To investigate the strength and quality of the interlocking of ENG particles, Dowell and Howard [64] positioned two ENG particles in an x-shape alignment, and compressed them. The subsequent intercalation and exfoliation did not change the region where the particles overlapped, but the rest of the particles re-gained a circular cross section. Repeating this process several times did not disconnect the joint and the authors therefore concluded that chemical bonding does not contribute greatly to the cohesion of the ENG particles.

Nitrogen adsorption measurements showed that the specific surface area of NGS decreases with increasing density. Since displacement in helium and kerosene yielded the same value of $2.25\,\mathrm{gcm}^{-3}$, the possibility of NGS containing closed pores was rejected. While a detailed description of the conclusion is missing, it is assumed that if NGS contains closed pores, helium or kerosene would not be able to access them and the trapped air would increase the buoyancy of the sheet, thus leading to a lower density reading.

The presence of impurities in raw graphite flakes was shown to reduce the tensile strength by limiting the number of bonds between individual exfoliated graphite particles. According to Dowell and Howard [64], the edges of raw graphite flakes contain oxide and silicate impurities, which can limit a proper exfoliation. While references or an explanation to support the claim are missing, it can be assumed that the chemical bond between an impurity and a graphite flake is stronger on the edges and weaker on the faces, which is analogical to the weak bonding of graphite layers in the c direction, but very strong cohesion within the layers in the ab directions.

Multiple authors focused on quantifying the average misalignment of graphite basal planes using x-ray diffraction measurements. A summary of the measured values is given in Figure 3.6. For the range of densities 0.5 to $1.7\,\mathrm{gcm}^{-3}$, which is the most relevant to the topic of this thesis, the average misalignment angle remains constant or slightly decreases. At the lowest relevant density of $0.5\,\mathrm{gcm}^{-3}$ it ranges from 9 to 20 deg. The data for the highest relevant density of $1.7\,\mathrm{gcm}^{-3}$ is not available, but at the highest measured density of $1.3\,\mathrm{gcm}^{-3}$ the misalignment angle ranges from 8.5 to 14 deg. To offer a comparison, pyrolytic graphite, which is known to have a superior highly-oriented crystalline structure, was reported to have the misalignment in the range 0.4 to 9.4° [64, 66]. Gu et al. [67, 59] also concluded that increasing the density does not result in all of the graphite basal planes being aligned perpendicular to the compression direction.

Toda et al. [69] studied the deformation of a single ENG particle during the forming process. They deposited a small tracing particles on the surface of the ENG particle, which was then placed in a 3 mm wide and 20 mm high cavity together with other ENG particles. Using the synchrotron X-ray micro tomography they observed the deformation of the marked ENG particle as a function of the compression of the entire sample. The deformation of the

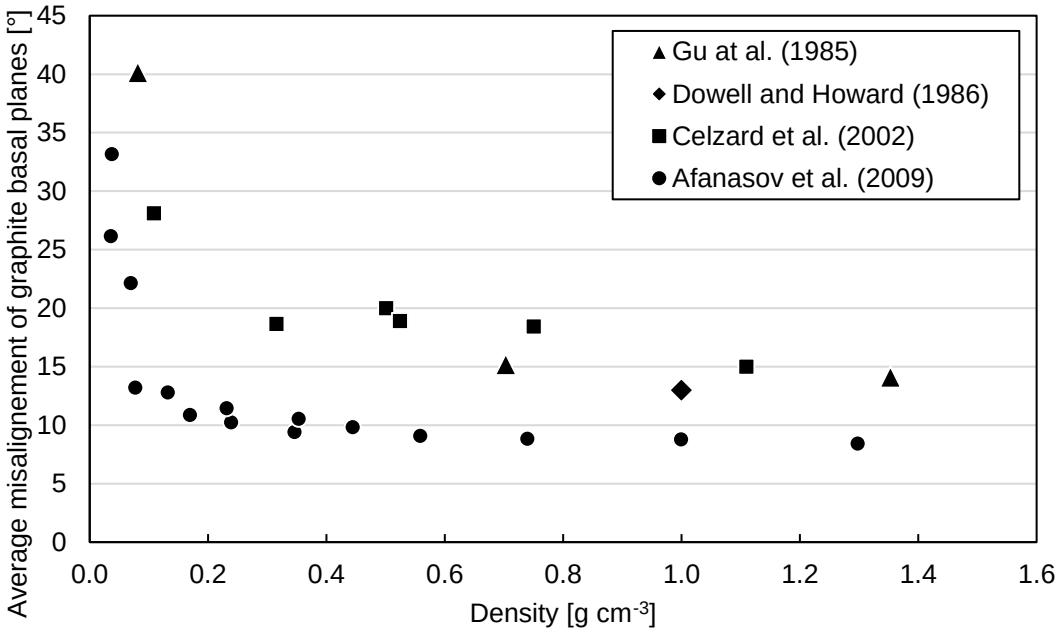

Figure 3.6: The average misalignment angle of graphite basal planes in NGS as a function of NGS density. The data were reported by Gu et al. [59]
, Dowell and Howard [64], Celzard et al. [63], and Afanasov et al [68].

marked ENG particle consisted of bending and thickness reduction. Bending was significant in the initial stages of the compression (i.e. at low sheet density) and thickness reduction became more pronounced at higher compression levels. During the unloading process the compressed ENG particle showed thickness recovery and transversal contraction.

Bonnissel [70] assumed that the density of NGS is non-uniform and varies in the thickness direction from $0.05\,\mathrm{gcm}^{-3}$ at the center of a sheet to $2.2\,\mathrm{gcm}^{-3}$ on the surface, following the relationship

$$d' = d(1-x)^{(\frac{2.2}{d}-2.2)-1} + 0.05, \tag{3.2}$$

where d' is the local density and x is the coordinate in the thickness direction normalized by the half-thickness value. The variation of density with thickness was not based on observing the structure and the validity was confirmed only by comparing the predicted thermal and mass transfer properties with the experimental data.

3.3.2 Preparation of samples for microscope imaging

NGS samples at four densities ($0.55\,\mathrm{gcm}^{-3}$, $1.05\,\mathrm{gcm}^{-3}$, $1.55\,\mathrm{gcm}^{-3}$, and $1.7\,\mathrm{gcm}^{-3}$) were cut from the calendered sheets whose preparation was described in section 3.1. Two approaches to sample preparation were used to observe the cross-section of NGS: polishing and tension fracturing, as is shown in Figure 3.7.

In the polishing approach, the four studied NGS samples were placed in a 30 mm diameter mold, which was then filled with an epoxy resin. Once cured, the epoxy resin blocks

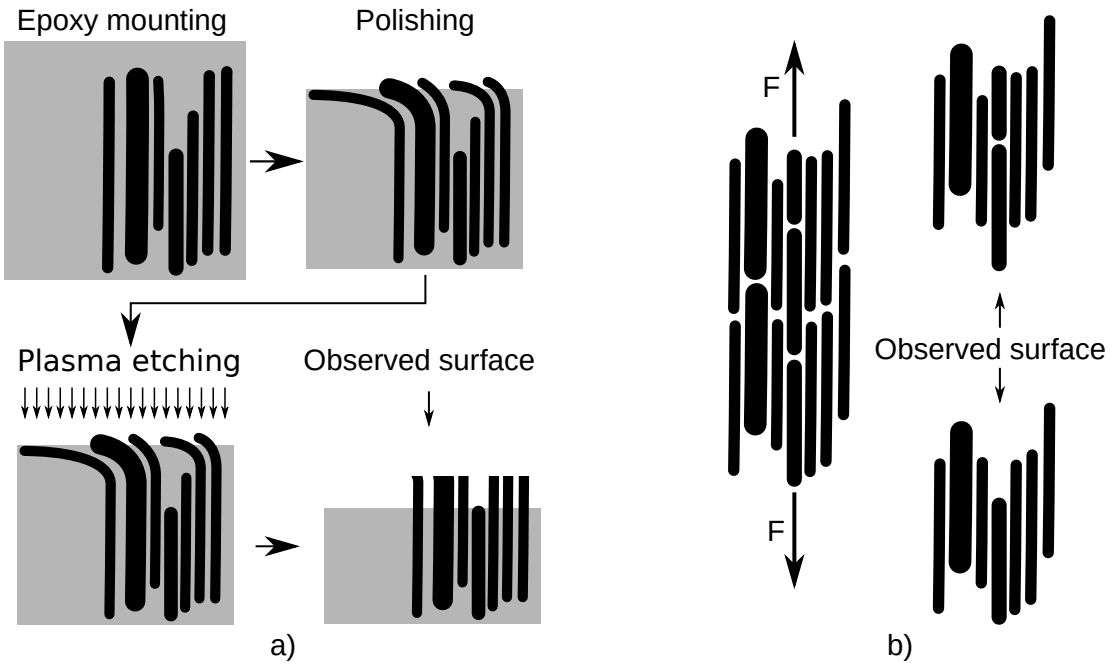

Figure 3.7: Illustration of the two sample preparation approaches: a) polishing and b) tension fracturing

were polished using a Struers Tegramin-20 polisher. The polishing process involved grinding the surface of the block to expose the NGS samples, and polishing to produce a uniformly flat analytical surface. Grinding of the block was done using a diamond-impregnated abrasive disc with an alcohol-based lubricant. A series of progressively finer grades of abrasive were used and ranged from 220 to 1200 grit until a uniform cross-section was achieved. The surface was then polished using diamond suspensions ranging from 3 to 6 µm. Given the very soft nature of the material, finer suspensions were not necessary. After each step of the process, the blocks were cleaned with denatured alcohol and checked for defects using an inverted microscope. Once polished, a thin carbon coating (25 Å) was applied on the surface of the sample to prevent charging in the SEM microscope. The sample preparation was done by SGS Canada Inc., Burnaby, B.C., Canada. A photograph of the mounted and polished sample is shown in 3.8a.

Initial observations of the polished cross-sections revealed smearing of the graphite layers as can be seen in Figure 3.9. To expose the true cross-section, oxygen plasma etcher was used as illustrated in Figure 3.7a. The etching was performed at 280 mTorr pressure, the power was 300 W, and the total etching time was 50 min. The conductive coating was renewed after the plasma etching step.

After the plasma etching step, bright artifacts were discovered on the observed surface as shown in Figure 3.10d. As shown in Figures 3.10a and 3.10b, it is assumed that the artifacts are a result of non-volatile contaminants that cannot be removed by plasma etching. Since

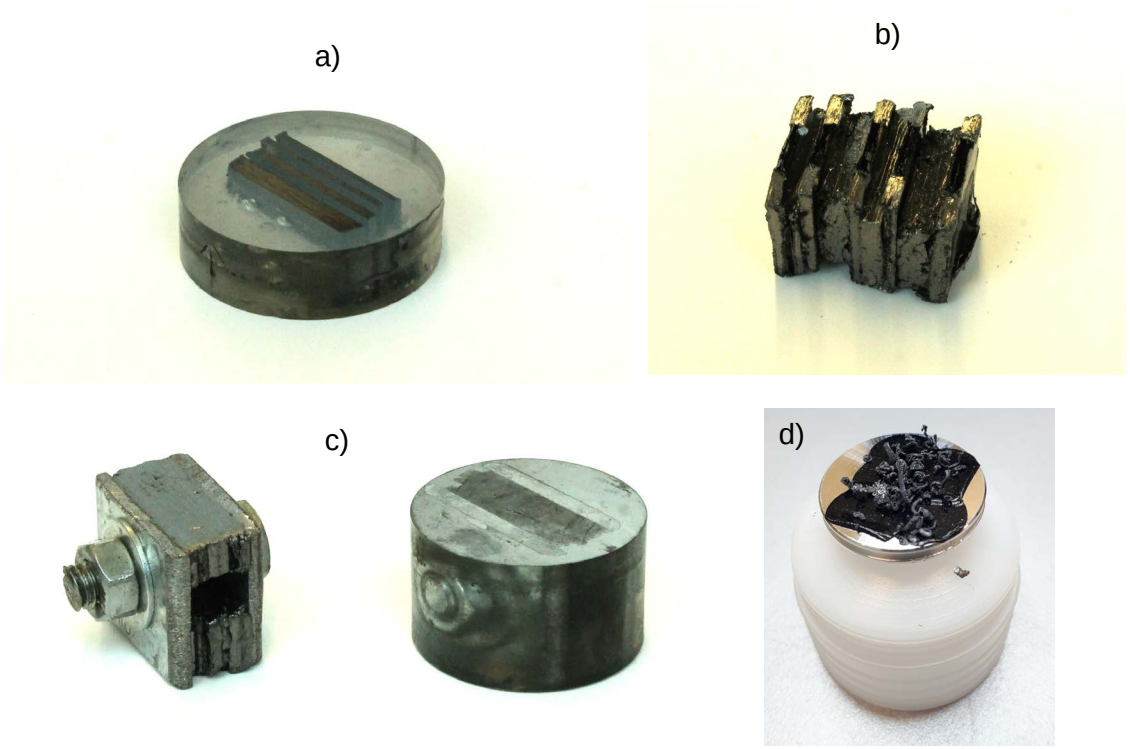

Figure 3.8: Photograph of a) four NGS samples mounted in an epoxy cylinder, b) a stack of five tension-fractured samples with spacers, c) a compressed stack of NGS sheets before and after mounting in resin, and d) ENG particles mounted on an SEM sample holder.

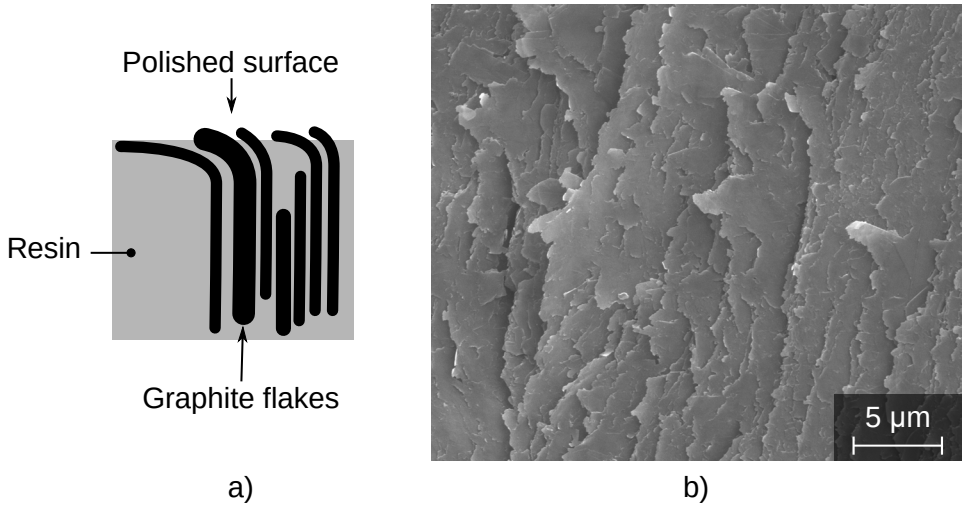

Figure 3.9: SEM image of smeared surface after polishing (right) and a simplified illustration of the smeared structure (left)

the artifacts are present on both NGS and on the mounting resin (3.10c), the contaminants are most likely the residue particles from the polishing process. The structure of NGS was

visible despite the artifacts and no further sample processing was done. It is likely that a sonication step can remove the non-volatile particles.

In the tension-fracturing sample preparation approach, the samples were fractured by applying a tension force, which resulted in breaking the interlocking of the ENG particles and exposing the cross-section structure as illustrated in Figure 3.7b. A photograph of the tension-fractured samples is shown in Figure 3.8b.

Besides cross-sections of a single sheet, the interfaces between stacked sheets under compression were of interest to support the understanding of the interfacial phenomena such as thermal or electrical contact resistance. A stack of six $1.05\,\mathrm{gcm}^{-3}$ sheets was compressed to 400 kPa using two metal brackets and a bolt. The assembly was then encapsulated in a resin and polished in the same way as the single NGS samples. The plasma etching step was not included. A photograph of the compressed stack of sheets before and after mounting in resin is shown in Figure 3.8c.

Samples of raw ENG particles were obtained from the supplier of NGS described in section 3.1. To observe the structure in an SEM microscope, the particles were mounted on a sample holder using a double-sided carbon tape as shown in Figure 3.8d.

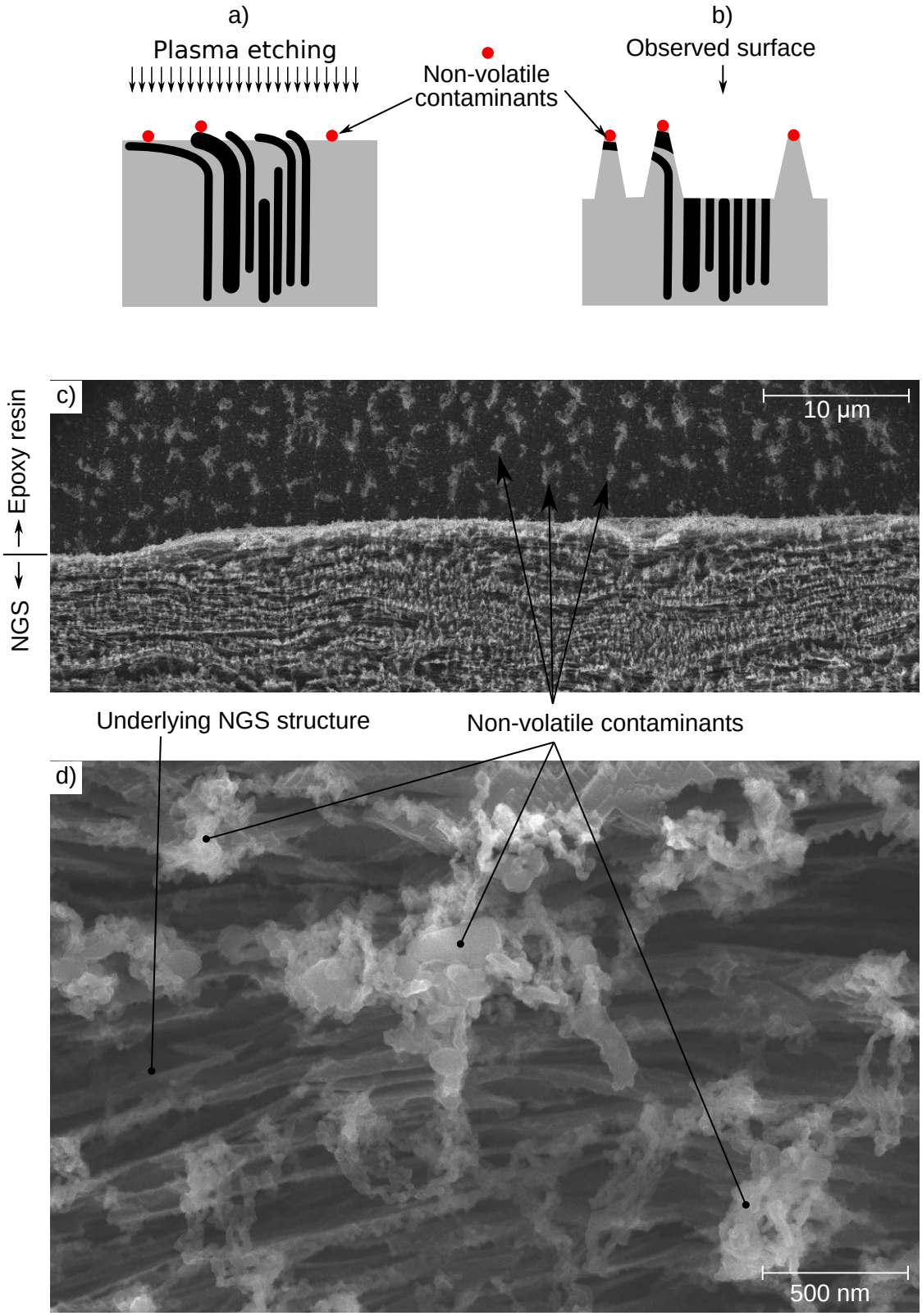

Figure 3.10: a,b) A schematic visualization of the formation of image artifacts due to non-volatile contaminants, and c,d) microscope images showing the artifacts.

3.3.3 Section results

3.3.3.1 Exfoliated natural graphite flakes

A compilation showing the images of ENG particles with a detailed view of one of the particles is shown in Figure 3.11. From the low-magnification image (Figure 3.11a) it is clear that the particles have a vermicular structure, and their size and shape varies widely. The diameter of the particles is related to the flake size before exfoliation (the dimension in the *ab* crystal directions). The length of the ENG particles is dependent on the thickness of the unexfoliated flake and the degree of exfoliation. The images at higher magnification (Figures 3.11b, 3.11c, and 3.11d) reveal that the structure at the scale of tens of micro meters is highly disorganized with signs of the original flake layering. The cohesive thin layered structures in 3.11d are considered to be the highly crystalline cell walls described in [51].

Comparing the images of ENG particles to the commonly known atomic structure of graphite (Figure 2.1) demonstrates the vast difference in the scale. The individual graphite crystals in the structure of cell walls consist of atoms organized in the layered hexagonal fashion, however, on larger scales, ENG shows different, highly random structure in which the cell walls are the building blocks. In Figure 3.12, a microscope image of an ENG particle (Figure 3.12a) is used as the reference for a simplified visualization of cell walls (3.12 b). Each of the cell walls was reported to be 15 to 60 nm thick [65, 64] and it consists of approximately 45 to 177 atomic layers with the characteristic spacing of 0.34 nm (Figure 3.12 d). Crystal defect was included in Figures 3.12c and 3.12d to symbolize that real world materials contain crystal imperfections [71].

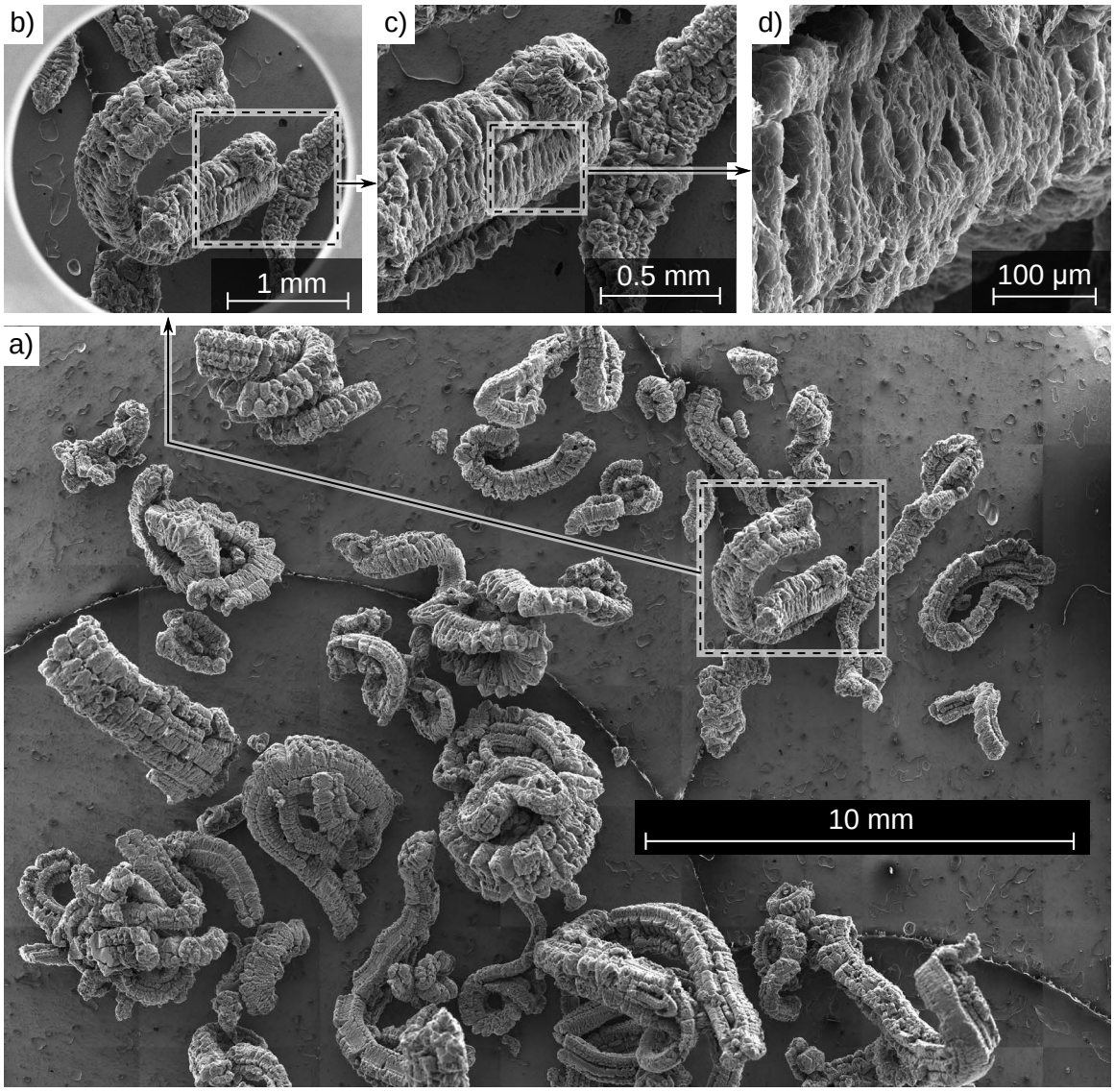

Figure 3.11: a) A low-magnification microscope image of multiple ENG particles. A high-magnification images of one of the particles are shown in b), c), and d). High resolution images are available in [62].

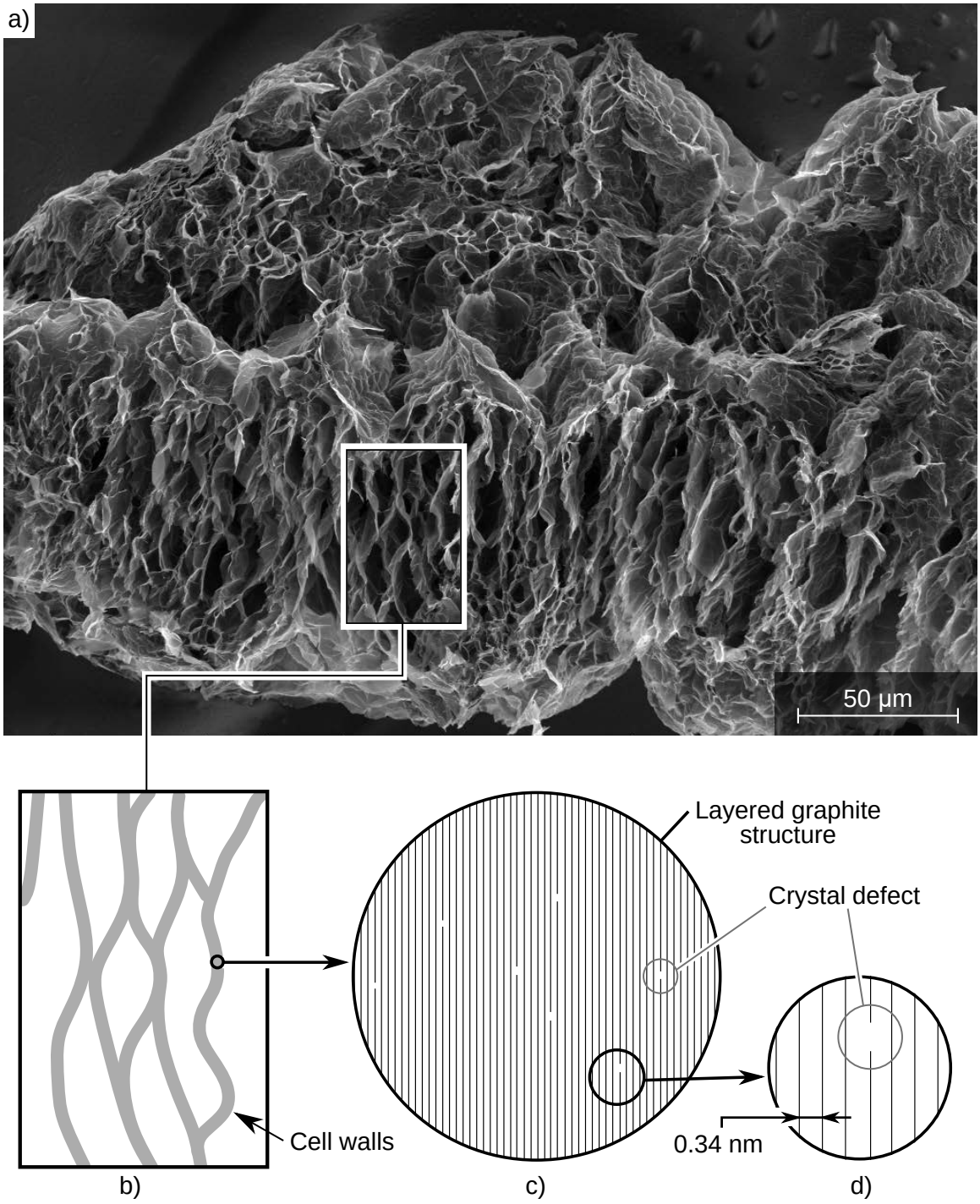

Figure 3.12: a) A microscope image of an ENG particle with a highlighted area that was used as a reference for b) simplified illustration of the cell walls. A schematic of the layered graphitic structure with the lines symbolizing the atomic layers is shown in c) and d).

3.3.3.2 Polished NGS cross-sections

Images of polished and etched NGS cross-sections at three levels of magnification are shown in Figure 3.13. The low and medium magnification images in Figures 3.13a and 3.13b reveal that polishing marks oriented diagonally from top left to bottom right are visible on the $0.55\,\mathrm{gcm}^{-3}$, $1.05\,\mathrm{gcm}^{-3}$, and $1.7\,\mathrm{gcm}^{-3}$ sheets. However, it is still possible to make conclusions about the structure.

At macro scale (hundreds of micrometers, Figure 3.13a), the structure becomes progressively more homogeneous with increasing density. The image of the lowest density sheet ($0.55\,\mathrm{gcm}^{-3}$) contains dark horizontal slit-shape areas, which were interpreted as large pores. Small pores were identified in the $1.05\,\mathrm{gcm}^{-3}$ sheet and no pores were seen on the high-density sheets.

The medium scale images (Figure 3.13b) confirm the observations made on the large scale images. By assuming that the bright linear features correlate with the angle of the cell walls, and in turn with the graphite basal planes, it is possible to qualitatively confirm the conclusions reported in [67, 68, 63, 64] stating that the average disorientation angle of graphite basal planes with respect to the sheet plane varies from 9 to 20° and its change with the sheet density is low at densities higher than $1\,\mathrm{gcm}^{-3}$. A quantitative analysis can be performed by applying feature recognition to the SEM images and statistically analyzing the angle distribution. However, such a study was beyond the scope of this work.

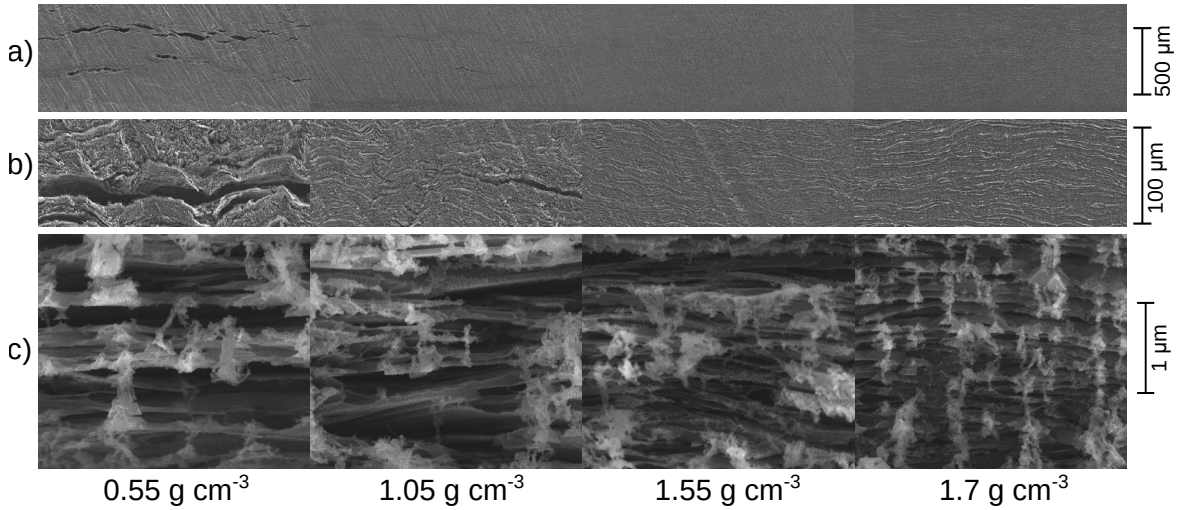

Figure 3.13: SEM images of cross-sections of polished and plasma-etched NGS samples at a) low, b) medium, and c) high magnification. High resolution images are available in [62].

On the micrometer scale (Figure 3.13c), the individual cell walls become visible and both their thickness and spacing decrease with increasing density. The images were rotated and cropped to allow an easy comparison of the thickness and spacing of the cell walls. In Figure 3.14, the raw non-rotated versions of the images at two random locations are shown.

The angle of the cell walls varies, no conclusion about the angle can be made as only two observations were made. The bright fuzzy features in the microscope images are the non-volatile impurities that are impossible to remove by plasma etching. Their formation was explained in the previous section.

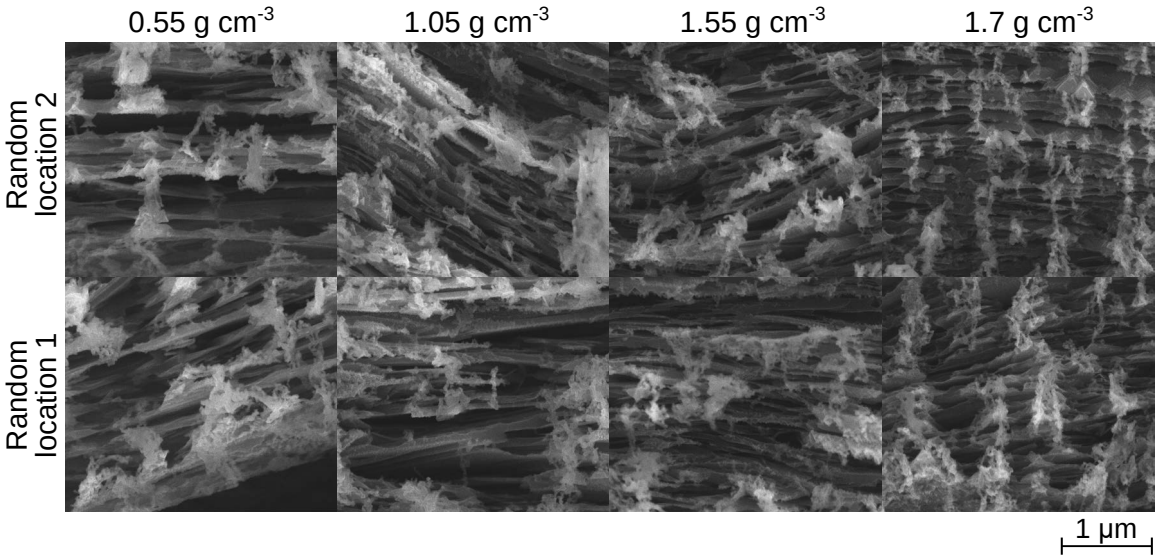

Figure 3.14: High magnification microscope images of NGS cross-sections at two random locations. High resolution images are available in [62].

In Figure 3.15, multiple raw images were combined to show the cross-section over the entire thickness of the sheets. No variation of the structure with the sheet thickness was observed and the conclusions based on Figure 3.13 made earlier therefore hold. The variation of the sheet density predicted by Bonnissel [70] was not seen in Figure 3.15.

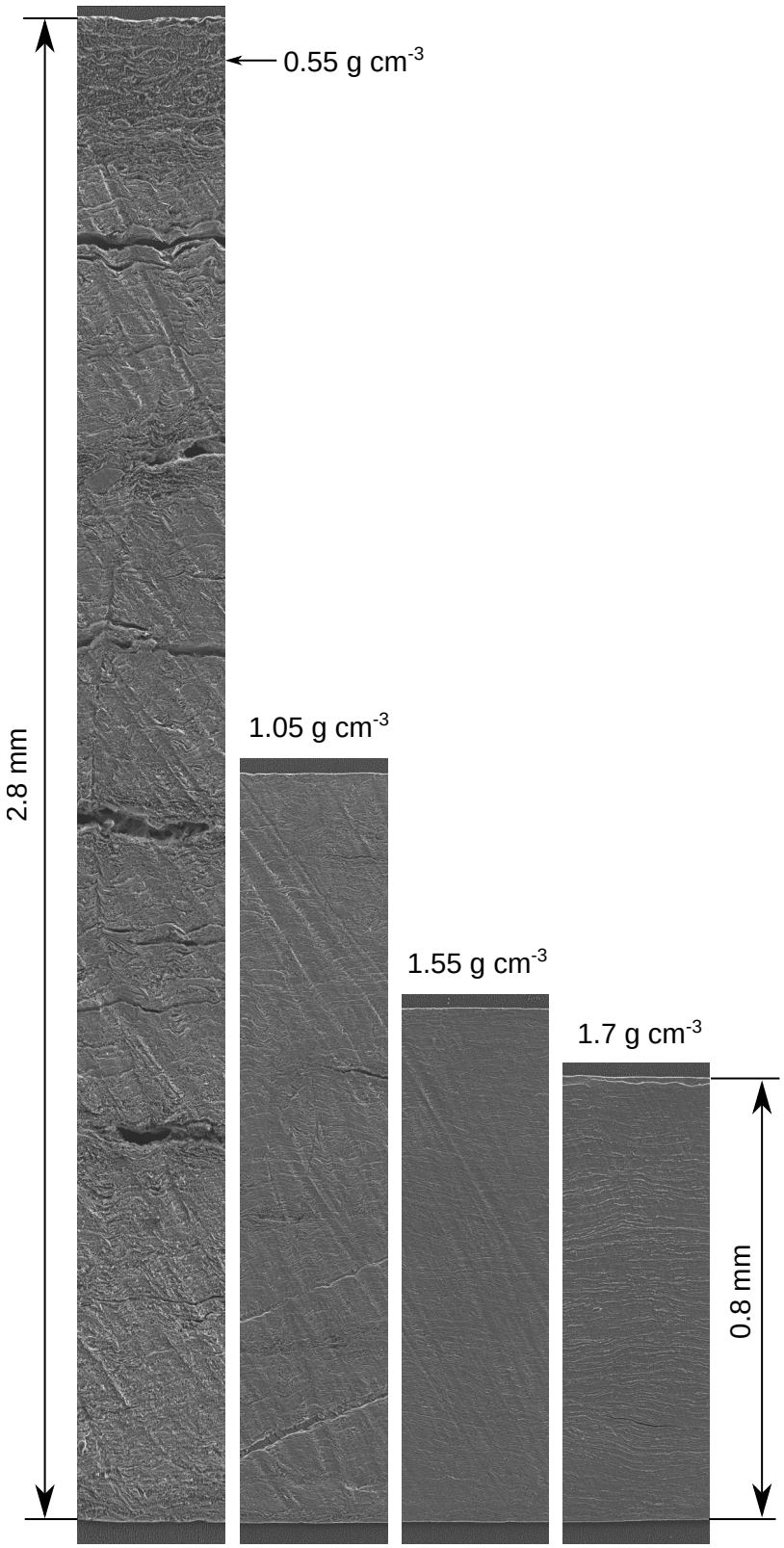

Figure 3.15: Composite images of NGS cross-sections. The images were created by merging multiple raw microscope image files using Image Composite Editor software. High resolution images are available in [62].

3.3.3.3 Tension-fractured NGS cross-sections

While it is a common practice to encapsulate samples of materials in resin, polish them, and observe the cross-sections, the idea of tension fracturing first introduced by Dowell and Howard [64] is a complementary method that offers an additional insight into the NGS structure. Low magnification images of tension-fractured NGS shown in Figure 3.16 confirm the platelet shape of compressed ENG particles that was well described and visualized by Toda et al. [69]. With increasing density the thickness of the platelets decreases, which correlates to the decrease in spacing and thickness of cell walls seen in Figure 3.13c.

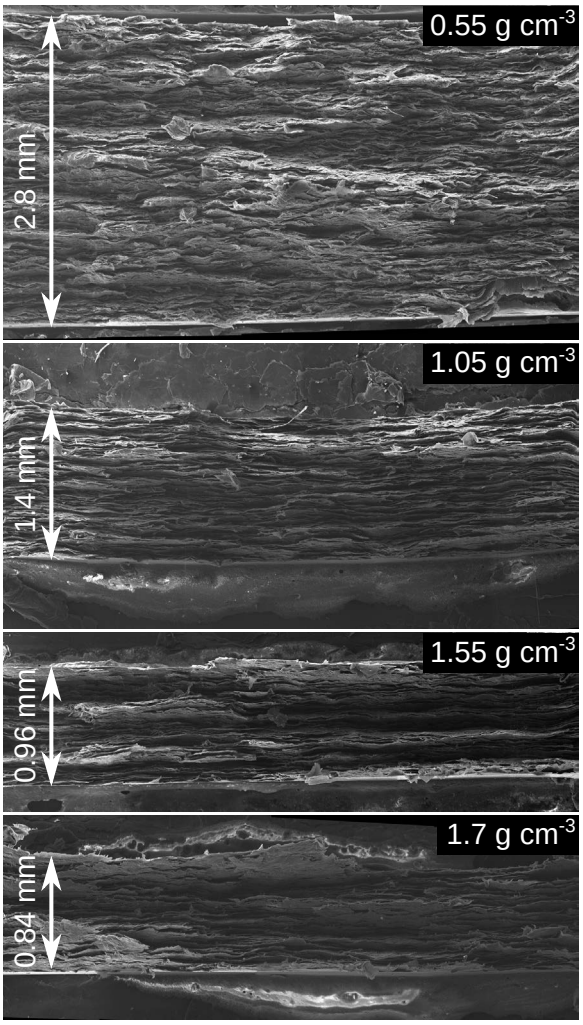

Figure 3.16: Low-magnification SEM images of the tension fractured samples. High resolution images are available in [62].

A comparison of the medium magnification images of the tension-fractured samples for the four measured densities in Figure 3.17 confirms not only the reduction of platelet thickness seen in previous images, but also confirms the concept of inter- and intra-particle porosity introduced in [63]. The intraparticle porosity, which arises from pores within ENG

particles, is visible in the image of the $0.55\,\mathrm{g cm^{-3}}$ sheet but disappears with increasing density,m and therefore it can be concluded that the intraparticle porosity decreases with density. Contrary to that, the relative amount of voids between the ENG particles is seen to increase, which can mean that the interparticle porosity increases with density. However, conclusions about porosity based on the images of tension-fractured samples are prone to error as the sample structure contains voids that were filled by platelets prior to the fracturing process, and the interparticle porosity can therefore appear significantly higher.

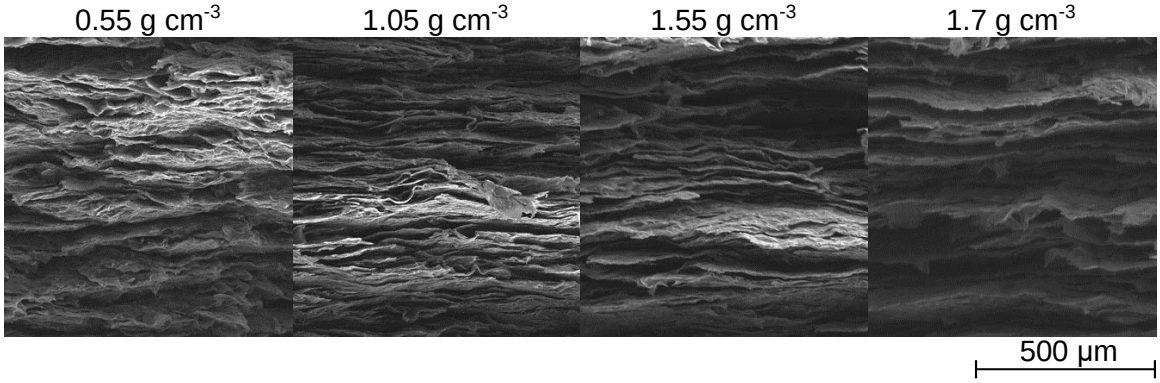

Figure 3.17: Medium-magnification SEM images of the tension fractured samples. High resolution images are available in [62].

3.3.3.4 Cross-sections of a compressed stack

In Figure 3.18, the image of the cross-section of the stacked sample is shown and the expected location of the sheet interfaces is marked by the arrows. Since no signs of the interfaces are visible in the image, it can be concluded that at 400 kPa compression pressure, the sheets coalesce and the interfaces are not visible. However, the surface structure can be distorted by the polishing process and the interfaces can be masked by smearing of the flakes. To make a reliable conclusions about the sheet interfaces, a plasma etching step should be added to the sample preparation process and the imaging should be repeated.

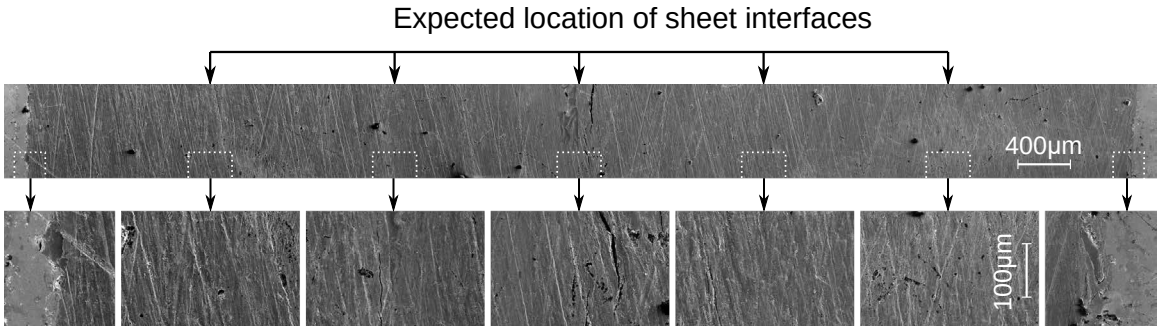

Figure 3.18: Low- (top) and medium- (bottom) magnification SEM images a stack of six $1.05\,\mathrm{gcm}^{-3}$ compressed at 400 kPa

3.3.3.5 Faces

Low and high magnification images of NGS faces are shown in Figures 3.19 and 3.20. The surface roughness decreases with increasing density. The boundaries of deformed ENG particles are visible in the low magnification image of the $0.55\,\mathrm{gcm}^{-3}$ (top-left in Figure 3.19).

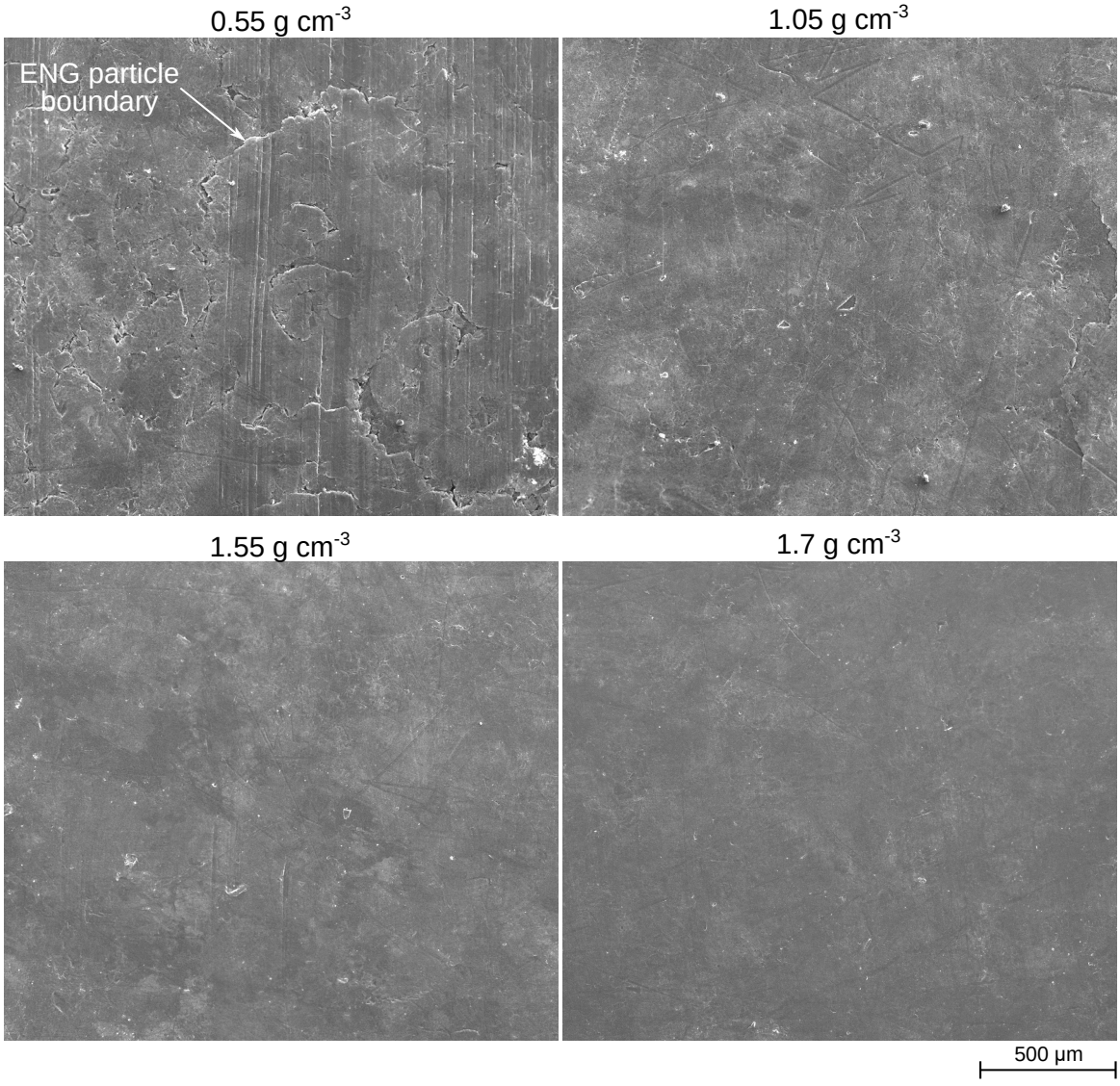

Figure 3.19: Low magnification microscope images of NGS faces. High resolution images are available in [62].

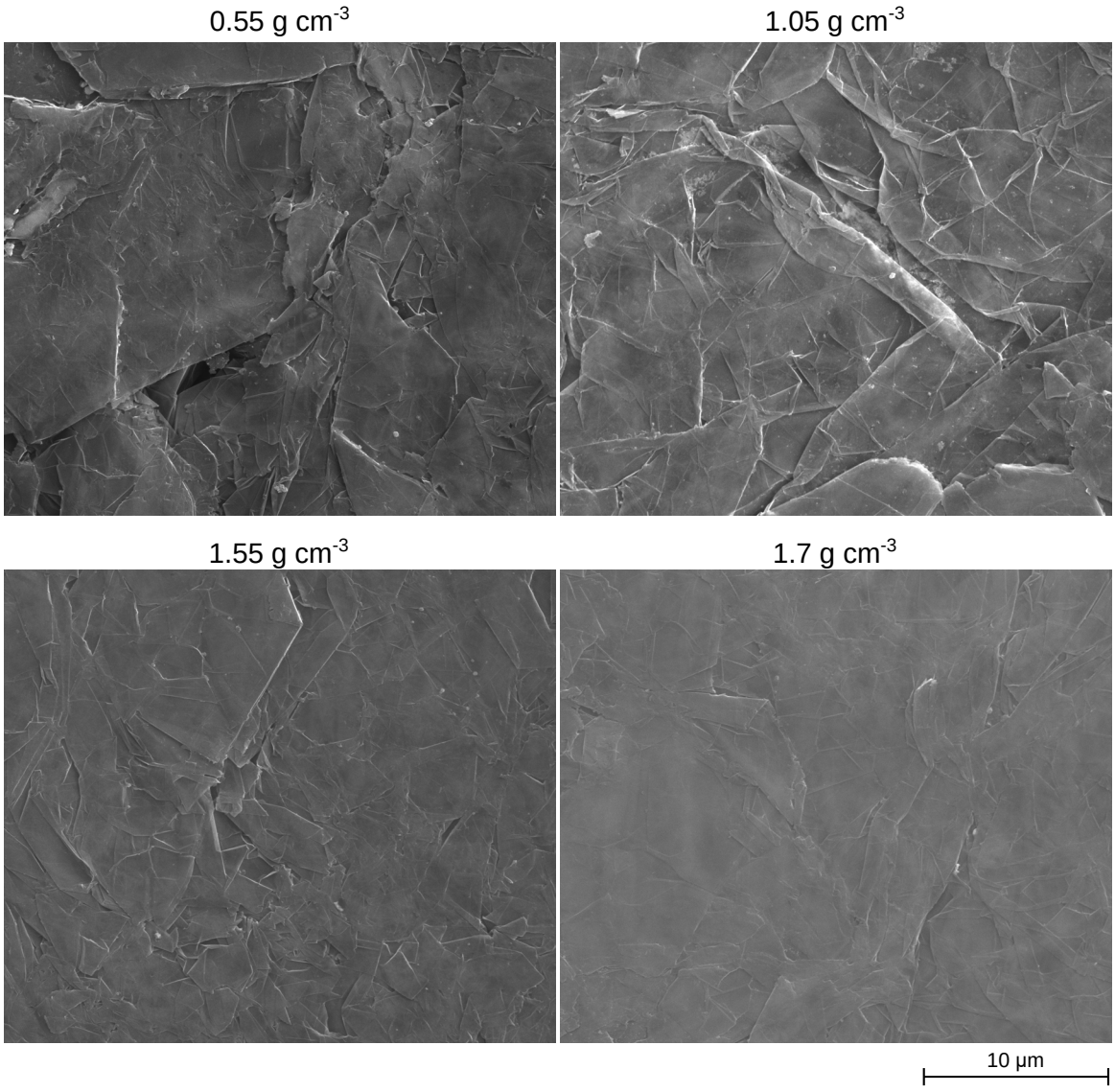

Figure 3.20: High magnification microscope images of NGS faces. High resolution images are available in [62].

3.3.4 Section conclusions

During the NGS forming process, vermicular ENG particles become thin platelets that consist of multiple highly crystalline cell walls separated by voids. The platelets are visible in the tension-fractured samples, but cannot be identified in the images of the polished samples. On a large scale, NGS heterogeneous at low densities, and becomes homogeneous at high densities. Macroscopic pores with the dimensions in the order of hundreds of micrometers in the in–plane direction and micrometers in the through–plane direction were identified in the cross-sections of the lowest density sheet ($0.55\,\mathrm{gcm}^{-3}$). At higher densities, the macroscopic pores reduce in size, and become invisible above $1.55\,\mathrm{gcm}^{-3}$. On a small scale, the thickness and spacing of cell walls decreases with increasing density and the spacing appears to be larger in comparison with the thickness. The thickness of the cell walls, which was reported to be in the range from 15 to 60 nm [64, 65], could not be verified because the achieved level of magnification did not give enough resolution for reliable measurements. However, the order of magnitude agrees. The cell walls are preferentially aligned perpendicular to the compression direction at all studied densities but the variation could not be studied. The non-uniform density distribution predicted by Bonnissel [70] was not seen in the composite images of NGS cross-section.

3.3.5 Future work

The clarity of the images of polished and plasma-etched samples can be improved by removing the layer of non-volatile residue that blocks the structure of the material. It is expected that a sonication could remove some or all of the residue. For observing the tension-fractured samples, Helium-ion microscope may results in a better images because of its higher depth of field. Also, tilting the sample could allow a better insight into the material structure. Studying the structure of NGS under compression could be beneficial for explaining changes of material properties with pressure. If the plasma etching and sonication steps are performed on the compressed stack samples, the variation of the cell wall spacing can be quantified as a function of pressure.

3.4 Porosity

Porosity was calculated from the density of NGS and the density of a graphite crystal as:

$$P = \frac{d_{gr} - d}{d_{gr}}, \tag{3.3}$$

where P is the porosity, d is the NGS density, and d_{gr} is the graphite crystal density of $2.26\,\mathrm{g\,cm^{-3}}$ [43]. This approach to calculate the porosity of NGS has been also used by Gu et al. [59] and Celzard [63]. For the range of densities 0.5 to $1.7\,\mathrm{gcm^{-3}}$, the porosity decreases from 76 to 25 %.

The literature sources do not agree on whether the pores in NGS are open or closed. Dowell and Howard [64] concluded that all pores are open while Toda et al. [69] claimed that 92 % of the pores are open.

3.5 Compression behavior

The work in this section is split into two parts:

i) forming of NGS at high pressures (up to 17 MPa in the present measurements and 31 MPa in the literature) during which the forming pressure is imposed on a low-density NGS to permanently increase its free-standing density, and

ii) low-pressure compression of formed NGS to pressures lower than the forming pressure, during which there is none or negligible permanent deformation.

Part i) is important for manufacturing NGS parts while part ii) is necessary for the in-situ performance of NGS parts as well as for the measurement of changes of NGS properties with compression pressure.

3.5.1 Previous work

Dowell and Howard [64] studied the compression behavior of NGS at high pressures. They loaded the sheets to a gradually increasing pressure and the subsequent relaxation revealed that the deformation of the graphite sheet consists of reversible and irreversible strain. When the sheet was compressed to the same pressure multiple times, the contribution of the irreversible strain diminished. The highest achieved free-standing density was $1.73\,\mathrm{g\,cm^{-3}}$ after a compression to 31 MPa. Increasing the pressure to 100 to 150 MPa resulted in a compression failure during which the sheets extruded from the loaded area. Heating the sheet to 2750 °C for one hour changed the compression behavior. Before the heating, the maximum density (current, not free-standing) at 27.6 MPa was $1.89\,\mathrm{g\,cm^{-3}}$. After the heating, it increased to $2.26\,\mathrm{g\,cm^{-3}}$, which corresponds to the theoretical density of a graphite crystal [43]. Contrary to the other studies in the literature, Dowell and Howard [64] concluded that the air in the pores has no effect on the overall compression behavior.

Wei et al. [28] prepared the samples for their material characterization in two steps. First, they compressed the exfoliated graphite flakes in a 100 mm-diameter mold to 3 to 5 mm thickness, and then they calendered the sheets to achieve the final density. The relationship between the forming pressure and the final free-standing density contradicts the findings of Dowell and Howard [64]. The forming pressures in the work by Wei et al. [28] are an order of magnitude higher that the values by Dowell and Howard [64], which is expected to be due to the the ambiguous definition of the compression area between two cylinders of a calendering machine. The data by Wei et al. [28] also suggest that by using ENG particles with lower apparent density d_{ENG} it is possible to achieve higher maximum sheet density. In particular, compressing ENG particles with d_{ENG} of $6.6 \times 10^{-3}\,\mathrm{gcm^{-3}}$ at 200 MPa yielded NGS with the free-standing density of $1.89\,\mathrm{g\,cm^{-3}}$, which was 9 % higher than that using particles with d_{ENG} of $1.85 \times 10^{-3}\,\mathrm{gcm^{-3}}$. The authors attributed the phenomenon to the higher elastic thickness recovery of NGS made of flakes with low d_{ENG}.

Toda et al. [69] studied the deformation of a single ENG particle during the forming process. They deposited a small tracing particles on the surface of the ENG particle, which was then placed in a 3 mm wide and 20 mm high cavity together with other ENG particles. Using the synchrotron X-ray micro tomography they observed the deformation of the marked ENG particle as a function of the compression of the entire sample. The deformation of the marked ENG particle consisted of bending and thickness reduction. Bending was significant in the initial stages of the compression (i.e. at low sheet density) and thickness reduction became more pronounced at higher compression levels. During the unloading process the compressed ENG particle showed thickness recovery and transversal contraction. In contrast to Dowell and Howard [64], Toda et al. [69] concluded that the air trapped in the pores is responsible for the recovery process. In a similar study using particle tracking and computer reconstruction of the structure, Kobayashi et al. [72] visualized the structural change of a small piece of NGS 0.5 mm wide, 0.8 mm long, and 0.5 mm thick under a compression to a 35.6 % strain. The reconstructed images show that the 1 g cm^{-3} sheet contains gaps between the structural units that closed at 31.3 % strain and did not appear after unloading. After complete unloading, the sheet did not recover to its original thickness, and the recovery ratio was 12.9 %).

Gu et al. [67] measured the compressibility and thickness recovery of NGS under compression at 32 MPa. At high densities, the thickness recovery was close to 100 % which was explained by the air pressure in the pores.

Only a very limited coverage of the low pressure compression of NGS is available in the literature. Luo and Chung [73] reported a reversible strain of 7 % at 0.42 MPa and 11 % at 0.81 MPa. At 4.12 MPa the strain kept increasing in each of the ten subsequent compression cycles. Density of the measured sheet was not reported. Afanasov et al. [68] measured the elasticity modulus of low-density sheets and reported the elastic modulus of 10 MPa at 0.2 g cm^{-3}.

Chen and Chung [74] studied the dynamic behavior of low-density sheets at 0.02 to 0.35 g cm^{-3} under compression, and observed a viscoelasctic behavior which was deemed to be useful for damping of vibrations. No data is available for higher sheet densities.

3.5.2 Experimental method

The present measurements were done using a Bose Electroforce 3300 Series II machine (Figure 3.21) in the configuration including circular, 50 mm diameter compression platens, and a 3 kN load cell (Figure 3.22a). For the forming tests, square samples 10 to 15 mm wide were cut from the 7 mm thick 0.2 gcm^{-3} low-density NGS (see section 3.1) using a conventional metal hand saw. The sample dimension was chosen so that the desired pressure can be achieved given the maximum force limitation of 2100 N. For the low-pressure tests, 32 mm diameter discs were cut from the calendered sheets using a hole punch. Images of the samples are shown in Figures 3.72 and 3.73. The details of the forming and low-pressure

tests are discussed separately in the following sub-sections. The raw data and processing scripts are available in [62].

Figure 3.21: a) A photograph of the equipment used for the measurements (Bose ElectroForce 3300 Series II).

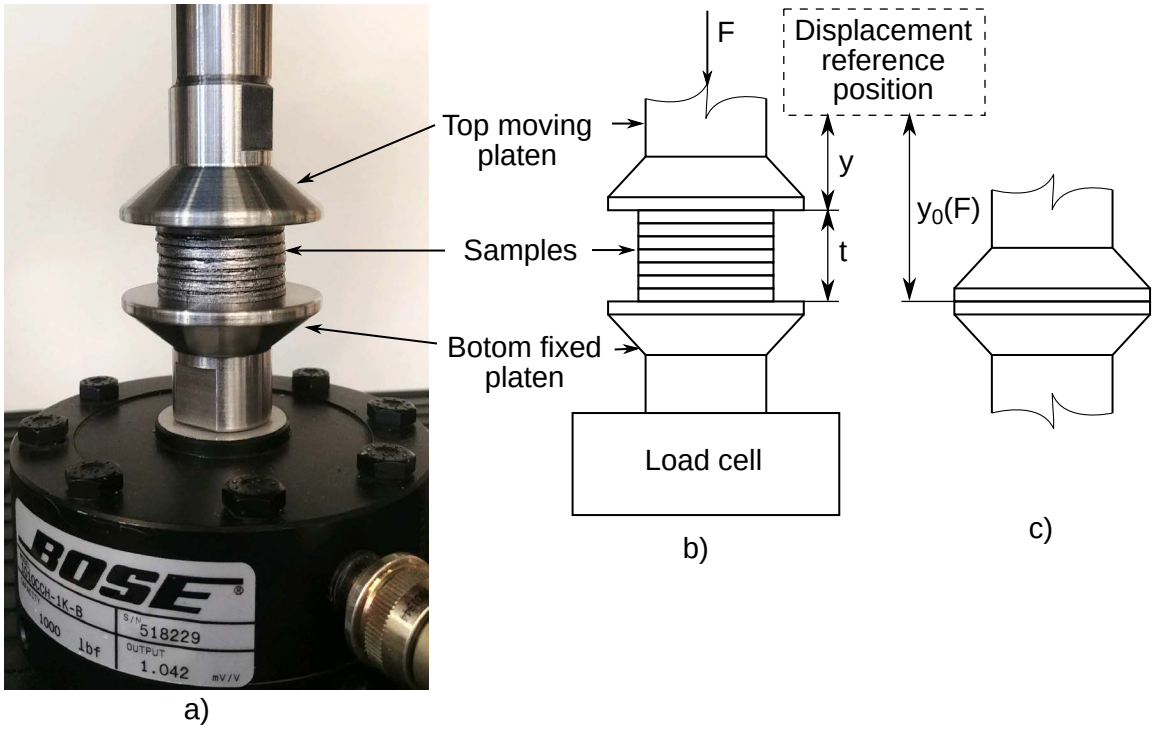

Figure 3.22: a) A photograph of the test section, b) a scheme of the measurement, and c) a scheme of the calibration run

3.5.2.1 Forming

The square samples were compressed by imposing the pressure profile shown in Figure 3.25b. After the first cycle, in which the forming pressure p_f was reached and the majority of the non-reversible deformation was done, an additional sequence consisting of three repetitions of cycles to $0.25p_f$, $0.5p_f$,$0.75p_f$, and p_f followed. The pressure was increased and decreased at the rate of $30\,\mathrm{kPa\,s^{-1}}$, and the peak pressure was held constant for 10 seconds. For each of the samples, the profile shown in Figure 3.25b was repeated seven times at a gradually increasing value of p_f.

3.5.2.2 Low-pressure compression after forming

The detailed compression behavior of the $0.55\,\mathrm{g\,cm^{-3}}$, $1.05\,\mathrm{g\,cm^{-3}}$, $1.54\,\mathrm{g\,cm^{-3}}$, and $1.7\,\mathrm{g\,cm^{-3}}$ sheets was studied by measuring stacks of the 32 mm circular samples. Stacking of samples was necessary because the dimension change of a single sheet at 1 MPa was in the order of the uncertainty of the thickness measurement. At least six measurements were performed for each of the four studied densities. After each of the measurements, the samples were dismounted and a different combination of all available samples was measured next. A single measurement consisted of loading to 1.06 MPa, 10-second hold, and unloading. The rate of pressure change was $1.58\,\mathrm{kPa\,s^{-1}}$.

3.5.3 Data reduction

The raw data files contained the time, force, and displacement readings. To obtain the thickness value and to account for the machine compliance, a calibration run in which there was no sample between the platens was necessary (Figure 3.22c). The no-sample displacement $y_0(F)$ was determined from a series of calibration runs. The thickness t was calculated as:

$$t = y_0(F) - y, \tag{3.4}$$

where y is the displacement as sketched in 3.22b. The reference thickness for the strain calculations (Figure 3.28) was taken at 30 kPa. The same pressure was used for determining the thicknesses t_f and t_n in Figure 3.22b. Although ideally the reference thickness should be measured in an unloaded state, any contact thickness measurement method requires a small compression pressure.

The tangent modulus was determined as the first derivative of the stress-strain curve. The derivative was found to be very sensitive to the noise in the data, and smoothing using a spline interpolation was necessary.

3.5.4 Section results

3.5.4.1 Forming

The free-standing density of the sheet after a single compression cycle to the forming pressure p_f is shown in Figure 3.23. With increasing density, the pressure required to further compress the sheet is increases exponentially following the relationship $d = 0.35e^{2.6p_f}$. The data are in a good agreement with those reported by Dowell and Howard [64] and Wang et al. [75]. Generating data points for pressures higher than 17 MPa was not possible in this study because the measurements would require samples smaller than 10 mm, which would cause a high uncertainty.

A viscous behavior was observed during the periods of constant pressure at the peaks of the compression cycles. Figure 3.24a shows that the thickness decreases in an exponential profile. The change in thickness was quantified using the viscous strain S_v, which is defined as:

$$S_v = \frac{t_{v,end} - t_{v,0}}{t_{v,0}}, \tag{3.5}$$

where $t_{v,0}$ and $t_{v,end}$ are the thicknesses at the beginning and the end of the constant pressure period, respectively. In Figure 3.24b, the magnitude of S_v was plotted against the forming pressure and a decreasing trend can be seen. At low forming pressures $p_f < 2$ MPa, which correspond to the free-standing densities less than $0.7\,\mathrm{g\,cm^{-3}}$, the thickness of the sheet reduces by 2 to 3 %. At higher pressures, S_v becomes negligible, and the dimension change is within the uncertainty of the measurement.

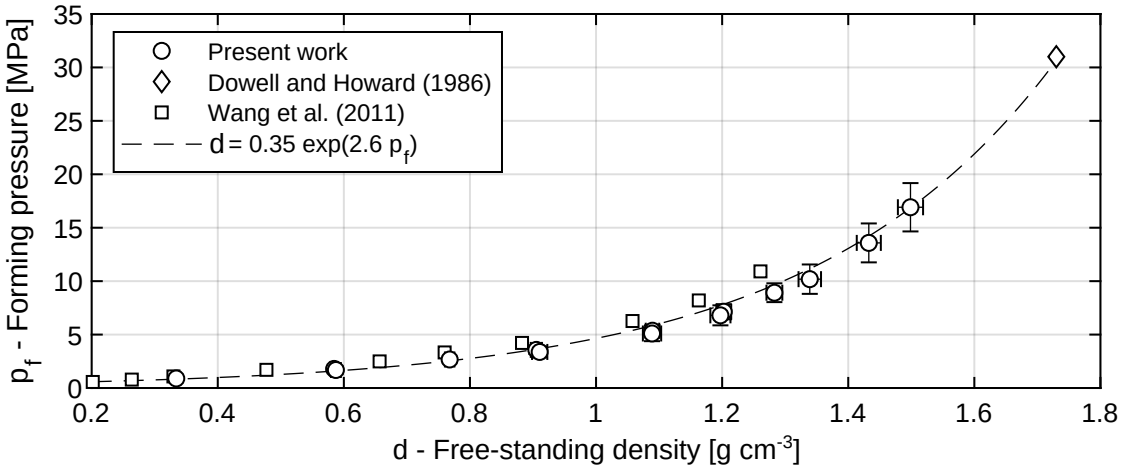

Figure 3.23: Free-standing density as a function of the forming pressure

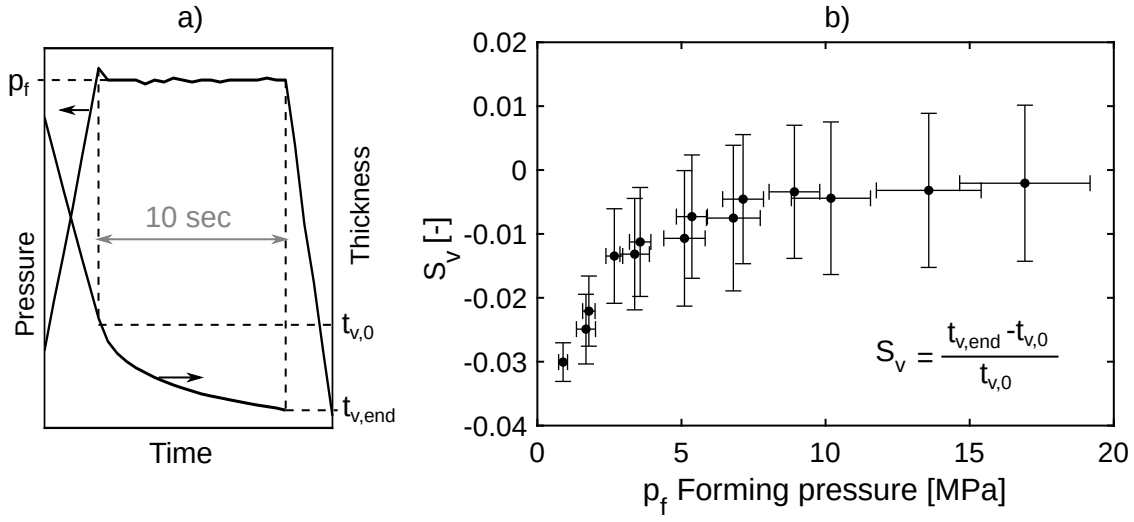

Figure 3.24: a) Illustration of the viscous behavior at constant pressure, b) Viscous strain as a function of the forming pressure

In Figure 3.25a, the strain at constant pressure S_v is plotted for each of the cycles in the test profile. Two measurements at the highest (16.9 MPa) and the lowest (0.9 MPa) forming pressure were included to show the variation of S_v. The two left-most data points in Figure 3.25a correspond to the minimum and maximum points in Figure 3.24b. The magnitude of S_v at the high forming pressure of 16.9 MPa remains low and within the measurement uncertainty for all the cycles. In the case of the low forming pressure of 0.9 MPa, it drops after the forming cycle, remains small during the $0.25p_f$ and $0.5p_f$ cycles, then slightly increases during the $0.75p_f$ cycles, grows in the first p_f cycle, and decreases again in the second and third p_f cycles.

The reduction in the free-standing thickness after each of the cycles is quantified in Figure 3.25c by plotting the ratio of the thickness after nth cycle t_n and the thickness after the forming cycle t_f. The thickness remains unchanged during the $0.25p_f$ cycles. In the subsequent $0.5p_f$ and $0.75p_f$ cycles a small reduction of thickness within 1 % of the original thickness is seen, however the change falls within the uncertainty of the measurement. Recompressing the sheet to the forming pressure p_f results in a significant thickness reduction that increases with every cycle and reaches 3 % after the third cycle. The 3 % decrease in thickness causes a 3 % increase in density.

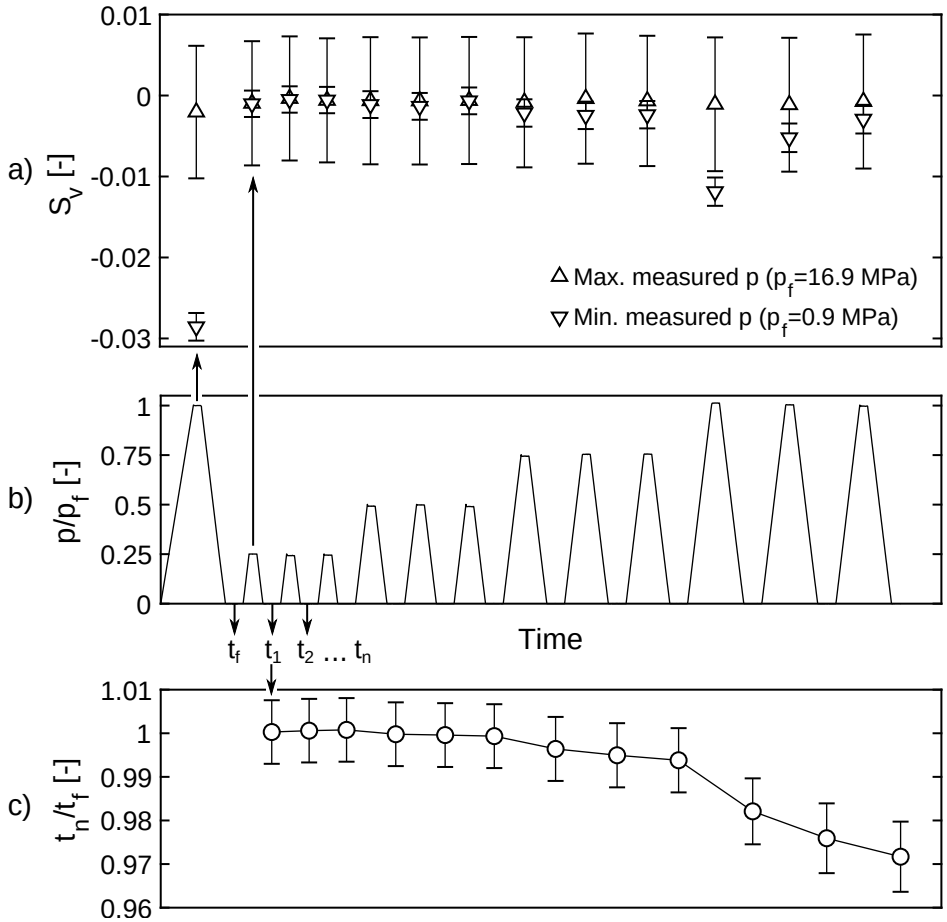

Figure 3.25: a) Viscous strain at the peak of the corresponding cycle, b) pressure profile used for the forming measurements, c) relative thickness reduction after the corresponding cycle

To investigate the thickness reduction after more than three cycles, one of the samples was left in the machine for 48 hours, and subsequently additional 19 cycles to the forming pressure p_f were performed. The results in Figure 3.26 are burdened with a high uncertainty of the measurement. However, they suggest a minor thickness increase after the wait period. During the additional cycles, the thickness reduced as expected. The rate of thickness

reduction decreased following an exponential decay and reached the value of 4 % after the last cycle. It should be noted that the three original cycles in Figure 3.26 do not correspond to the three last data points in Figure 3.25c because Figure 3.26 contains data for a single sample while Figure 3.25c shows the average of three samples.

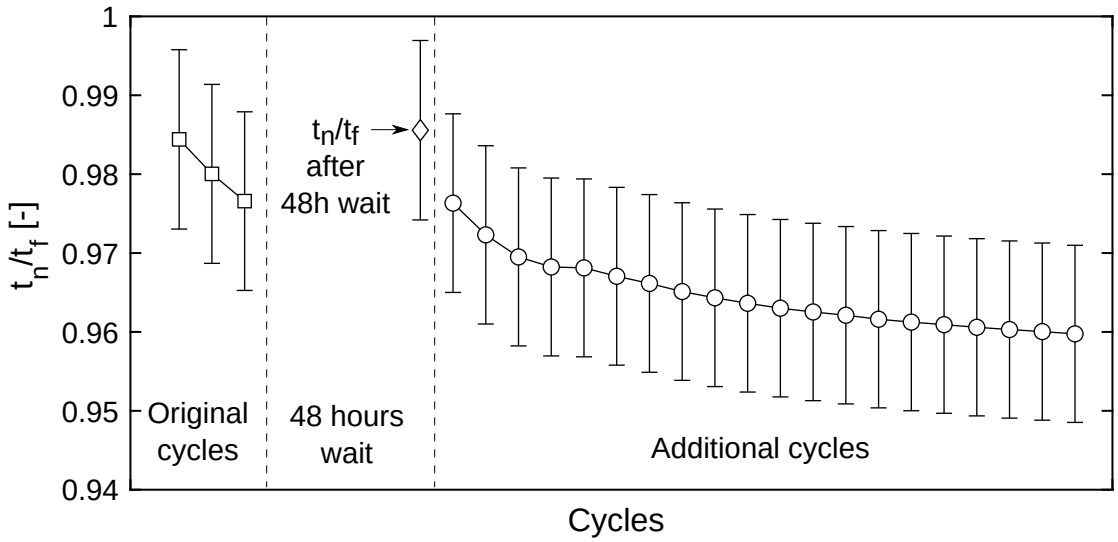

Figure 3.26: Relative thickness reduction after additional cycles

Figure 3.27 was created to analyze whether the the overall thickness reduction in a given cycle is related to the viscous thickness change at the peak of the cycle. The dashed line symbolizes the equality of the compared thickness changes. For points above the line the viscous thickness reduction is lower than the overall thickness reduction in the given cycle. While the interpretation of the most of the points in the upper-right corner is not viable due to the measurement error, the points in the middle and left part suggest that the viscous thickness reduction is always lower than the overall thickness reduction, which suggests that the permanent thickness reduction happens throughout the entire cycle and not only at its peak pressure.

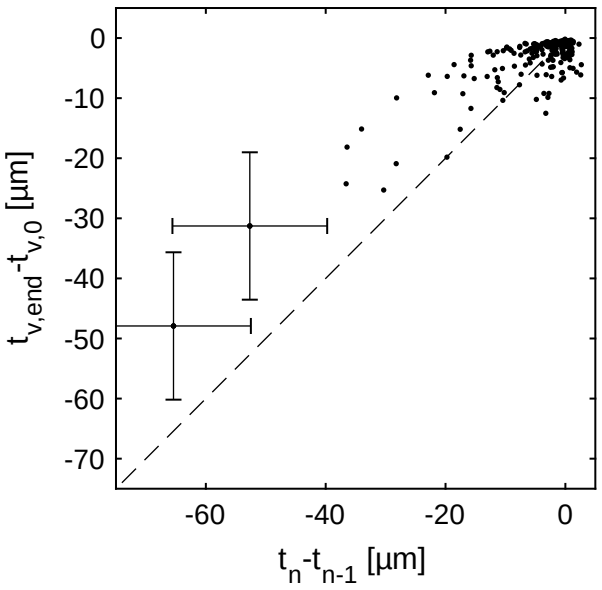

Figure 3.27: Correlation between the overall absolute thickness reduction after a compression cycle (horizontal axis) and the dimension change during the viscous deformation at the peak of the compression cycle (vertical axis). Only two error bars are shown to increase the clarity of the plot

3.5.4.2 Low-pressure compression after forming

The results in this section describe the compression behavior of NGS at low pressures up to p=1.06 MPa, which is lower than the forming pressure of any of the measured sheets. Based on the results of the forming process, the deformation is expected to have mainly an elastic character. For the lowest density, which requires the lowest forming pressure, the forming pressure is 1.45 MPa and thus the p/p_f ratio is 0.73. According to Figure 3.25, low permanent thickness reduction within 1 % is expected in this region. For the densities of 1.05 g cm^{-3}, 1.54 g cm^{-3}, and 1.7 g cm^{-3}, the forming pressures are 5.3 MPa, 18.8 MPa, and 28.3 MPa and the corresponding p/p_f ratios 0.21, 0.056, and 0.06, respectively, making the elasticity assumption to hold even stronger than that for the lowest density.

The stress-strain curves for each of the measured densities are compiled in Figure 3.28. Only the maximum and minimum measurements are shown to improve the readability of the figure. All the measurements that are not shown fall within the bounds given by the maximum and minimum measurements.

All the densities show hysteretic behavior that is the most pronounced for the lowest density sample, and decreases with increasing density. The shape of the stress-strain curves and the value of the maximum strain varies with density. The lowest measured density (0.55 g cm^{-3}) shows almost linear behavior during the loading cycle, but the unloading cycle is highly non-linear. For the higher densities, the loading cycle becomes progressively more non-linear and the curves flatten at high pressures.

The strain at the maximum pressure, which quantifies the overall stiffness of the sheet, does not show a monotonically increasing or decreasing dependence on the density. It is the highest for the lowest density (6 %) but then drops and remains in the range 2 to 3.5 % for all remaining densities. The strain value of 11 % at 0.81 MPa reported in [73] is higher than any strain measured in this work.

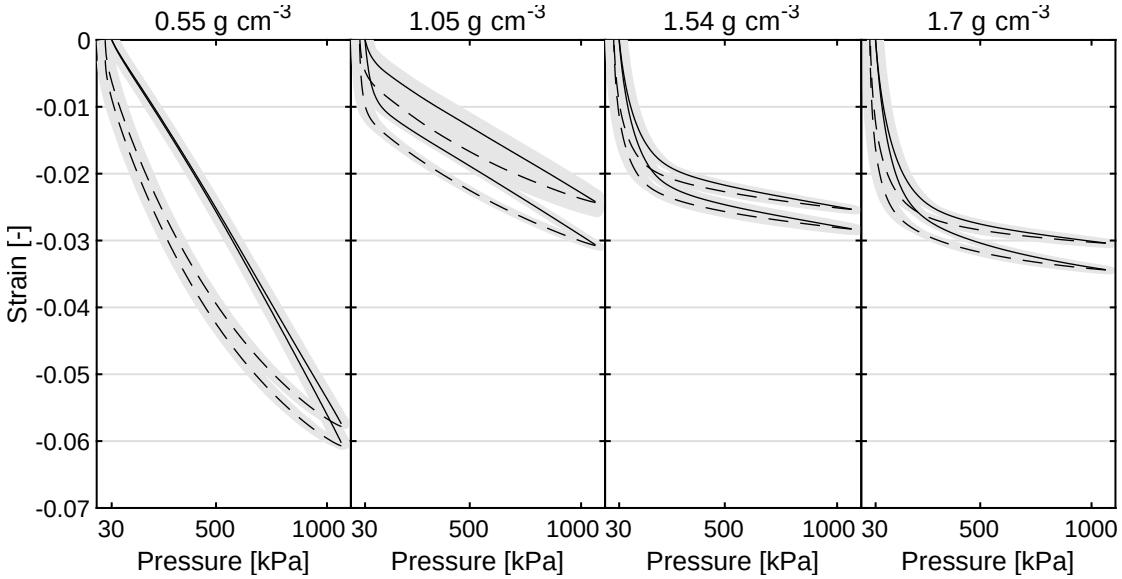

Figure 3.28: Low-pressure stress-strain curves of measured NGS samples. Loading and unloading is represented by the solid and dashed lines, respectively. For each of the plots only two measurements with maximum and minimum value of strain are shown to demonstrate the measurement variability.

To make the results easy to reuse by other researchers, an explicit compact mathematical relationship describing the loading portion of the stress-strain curves was sought. The best fit of the through–plane compression strain S_{th} as a function of pressure p and the free-standing density d was determined as:

$$\begin{aligned} S_{th} &= (0.0026 - 0.014d + 0.0166d^2)(1 - e^{-(p-30)0.03d^{-1.6}}) \\ &+(0.00012 - 0.000147d + 4.8 \cdot 10^{-5}d^2)(p - 30) \quad (error = \pm 0.004) \\ &d \in [0.5, 1.7]\mathrm{gcm}^{-3}, p \in [30, 1060]\mathrm{kPa}. \end{aligned} \tag{3.6}$$

A comparison of the fit with the collected data points for the measured densities of $0.55\,\mathrm{gcm}^{-3}$, $1.05\,\mathrm{gcm}^{-3}$, and $1.7\,\mathrm{gcm}^{-3}$ is shown in Figures 3.29, 3.30, and 3.31. For the lowest density $0.55\,\mathrm{gcm}^{-3}$, the fit is in a good agreement with the data at low pressures but diverges slightly at high pressures. The higher variability of the $1.05\,\mathrm{gcm}^{-3}$ data results in the measurements being scattered around the reported best fit value. The measured data for the $1.7\,\mathrm{gcm}^{-3}$ density are consistently lower than the best fit but within the reported error. The fitting process is a trade off between compactness of the relationship and its accuracy. While it is

possible to obtain a best fit that would follow the experimental data better, the resulting relationship would be significantly longer, and its practicality would be reduced.

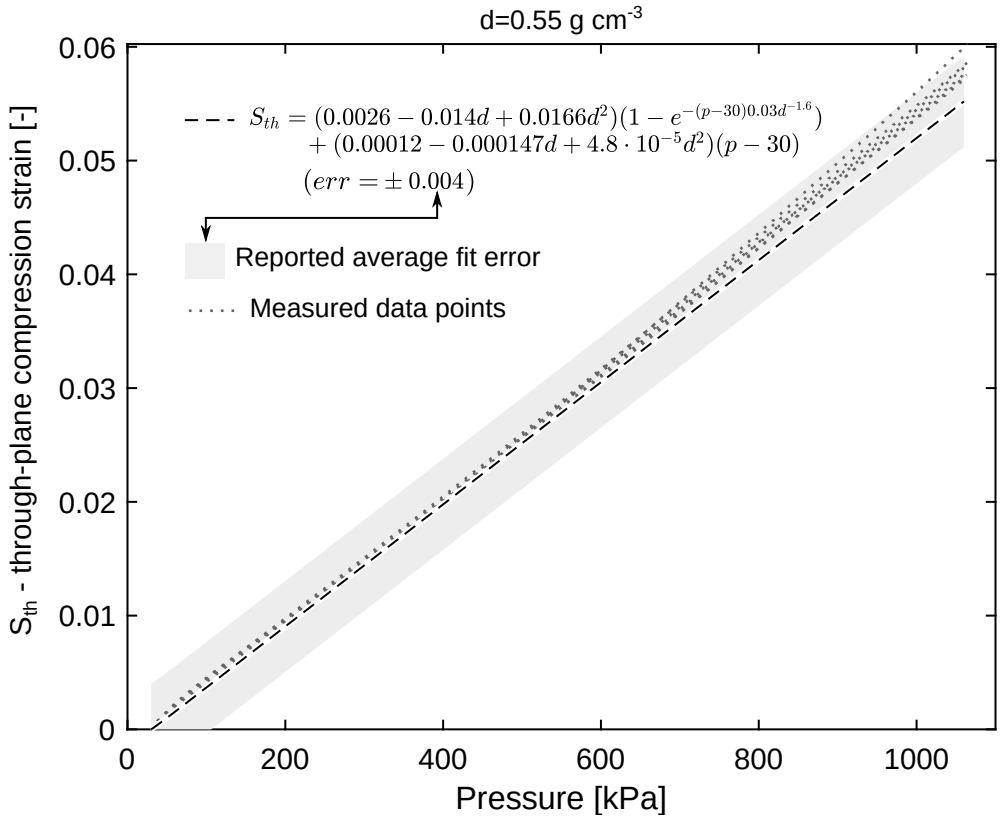

Figure 3.29: A comparison of the through–plane compression strain best fit with the measured data for the density $0.55\,\mathrm{gcm}^{-3}$.

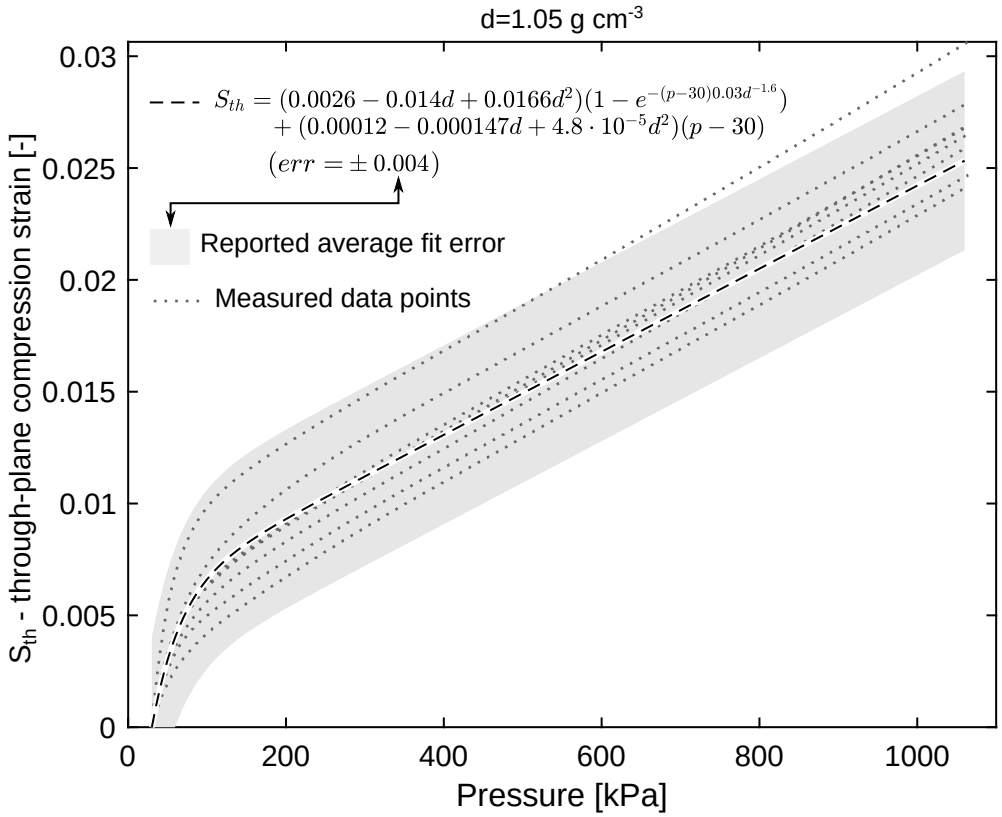

Figure 3.30: A comparison of the through–plane compression strain best fit with the measured data for the density $1.05\,\mathrm{gcm}^{-3}$.

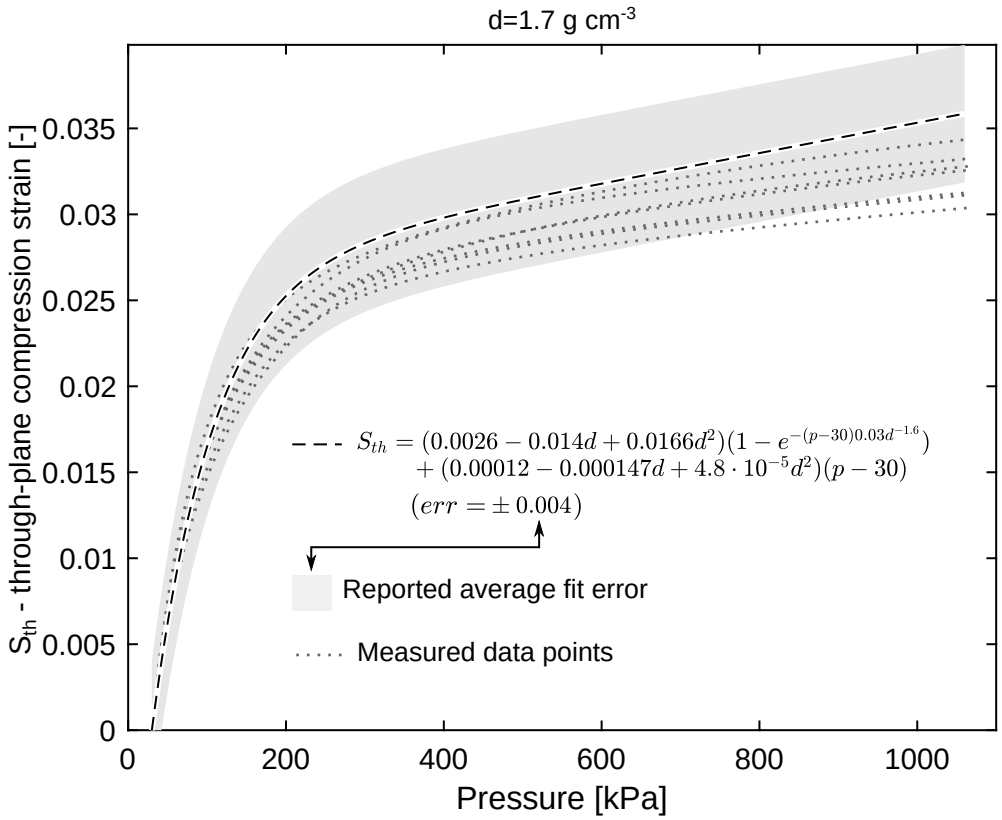

Figure 3.31: A comparison of the through–plane compression strain best fit with the measured data for the density $1.7\,\mathrm{gcm}^{-3}$.

The stiffness at any given pressure can be quantified by the tangent modulus. Figure 3.32 shows the average tangent moduli that were evaluated for the loading part of the compression cycle (i.e. the solid lines in Figure 3.28). The linear shape of the stress-strain curve during the loading cycle of the lowest density sample ($0.55\,\mathrm{g\,cm^{-3}}$) translates to the constant value of the tangent modulus of approximately 20 MPa, which is a value comparable to 10 MPa for a $0.2\,\mathrm{g\,cm^{-3}}$ sheet reported in [68]. The modulus of the $1.05\,\mathrm{g\,cm^{-3}}$ sheet shows a slight increase at low pressures and then stabilizes at 50 MPa. The modulus of the remaining two densities ($1.54\,\mathrm{g\,cm^{-3}}$ and $1.7\,\mathrm{g\,cm^{-3}}$) increases over the entire range of measured pressures and reaches 170 MPa and 220 MPa, respectively. The increase follows an s-curve trend with the inflection point at approximately 500 kPa.

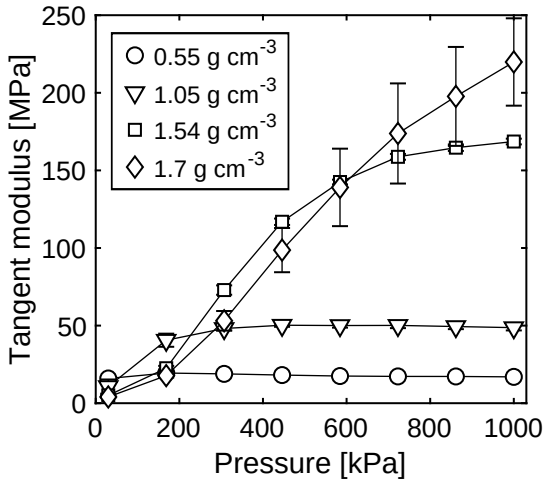

Figure 3.32: Tangent compression modulus during the loading part of the compression cycle

The viscous behavior at the constant pressure periods was analyzed in the identical way as in the previous section using the viscous strain, which is plotted in Figure 3.33. In comparison with the forming process, the viscous strain is approximately two orders of magnitude lower, but a similar trend of decreasing magnitude with increasing density can be seen. The error bars for each of the points in Figure 3.33 were omitted as the relative error reaches 500 %. Despite that, the trend of the results is expected to hold as the proximity of the data points suggests a good repeatability. The high uncertainty of viscous strain is due to the low change in thickness. The details are addressed in the discussion section.

To exclude the possibility of the viscous behavior being an artifact of the load cell, a control measurement with no sample between the compression platens was performed. The absolute dimension change during the constant pressure period of the control run was much lower than that of the the sample that shows the least viscous behavior (the dimension changes were 0.3 µm and 7.6 µm, respectively). The viscous behavior is therefore considered a real phenomenon.

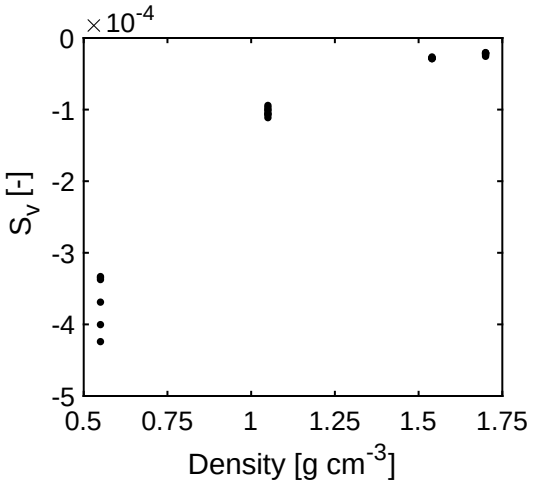

Figure 3.33: The viscous strain during the 10 second period of constant pressure (1.06 MPa) for each of the measured densities.

3.5.5 Section discussion

In the forming section of this work, the focus was to measure and summarize the properties that are crucial for a successful manufacturing of NGS parts and samples. The reader is referred elsewhere [64, 72, 69, 63] for the detailed description of the structural changes that happen during the forming process.

Compression of NGS increases its density, but it is not possible to achieve the free-standing density to be equal to the theoretical density of the graphite crystal ($2.26\,\mathrm{g\,cm^{-3}}$ [43]). The maximum achieved density varies from $1.73\,\mathrm{g\,cm^{-3}}$ at $p_f = 31\,\mathrm{MPa}$ [64] to $1.89\,\mathrm{g\,cm^{-3}}$ at $p_f = 200\,\mathrm{MPa}$ [28]. The drastic difference in the forming pressure is expected to be due to its unclear definition in the latter publication, which used calendering for manufacturing the sheets. The area used for calculating the pressure between two cylinders is ambiguous and was not stated. Moreover, the forming pressure of 200 MPa is above the failure stress of 150 MPa defined in [64].

Wei et al. [28] observed that the maximum NGS density is a function of the density of the ENG particles. Another similar trend can be observed when comparing the thickness of the sheets. While Dowell and Howard [64] reported that they tested stacks of sheets not less than 1.27 mm, the lowest value of thickness in Wei et al.[28] is 0.15 mm. It is likely that a higher maximum density can be achieved when the sheet thickness is low. For a reference, the thinnest sheet in the present work was 0.84 mm thick, its density was $1.7\,\mathrm{g\,cm^{-3}}$, and it was formed by rolling under a 6.9 kN compression force.

The viscous behavior of NGS observed in the present measurements is in agreement with Chen and Chung [74] who reported a decreasing viscous effect with increasing density over the density range 0.02 to $0.35\,\mathrm{g\,cm^{-3}}$. As seen in Figure 3.24 and 3.33, our data for higher densities (0.3 to $1.7\,\mathrm{g\,cm^{-3}}$) follow the same trend. Chen and Chung [74] attributed

the viscous behavior to the sliding of graphite layers at interfaces. While this theory is plausible, the viscous behavior can be also caused by the air in the pores. The porosity of natural graphite sheet ranges from 76 to 25 % for the densities of $0.5\,\mathrm{g\,cm^{-3}}$ and $1.7\,\mathrm{g\,cm^{-3}}$, respectively, and the pores have been reported to be all open [64] or 92 % open [69]. It is likely that upon compression, the air pressure in the pores increases, and the air starts flowing out through the constrictions formed by the material structure. Upon unloading, the stored elastic energy forces the sheet to increase the thickness, which lowers the pore pressure, and air is drawn into the pores from the surroundings. To confirm or reject this theory, measurements under vacuum are necessary. To offer further suggestions for potential future measurements, a set of measurements was performed on a stack of four $1.05\,\mathrm{g\,cm^{-3}}$ sheets. Increasing the rate of the load change from $1.6\,\mathrm{kPa\,s^{-1}}$ to $46\,\mathrm{kPa\,s^{-1}}$ (29 times more) was found to increase the viscous dimension change seven times.

The main source of uncertainty of the viscous strain S_v is the uncertainty of the thickness measurement, which is in the order of ± 5 to $\pm 10\,\mu\mathrm{m}$. The thickness difference in the numerator of S_v (Eq. 3.5) is calculated from the thicknesses at the end and the beginning of the constant pressure period. In this special case when all parameters are fixed and only the time change of the thickness is required, the absolute uncertainty of the thickness is not relevant and it may be possible to base the uncertainty analysis on the sensitivity of the displacement reading, which was reported by the manufacturer to be $\pm 1\,\mathrm{nm}$. However, to confirm this, a detailed understanding of the processing of the displacement signal is required. Further work was omitted due to its complexity and time requirements.

The magnitude of the viscous behavior is low and most likely negligible for the majority of the practical applications. From the material characterization perspective, the viscous behavior can become significant when measuring properties that are highly sensitive to minute changes in the material structure. For example, the electrical resistance of NGS was found to follow the same exponential decay as the thickness. This phenomenon may need to be addressed in high-accuracy measurements of electrical conductivity under compression. If a need to fully understand the viscous behavior of NGS arises, be it for the practical needs or to complete the scientific understanding of the phenomenon, an experimental setup capable of imposing pressures of up to hundreds of mega pascals and measuring micrometer displacements is suggested.

Measurements of the compression modulus can be biased by the barreling effect [76]. The highly anisotropic structure of NGS was considered to be prone to this behavior as the low shear stiffness in the in-plane direction (perpendicular to the compression direction) can allow high lateral displacement during the compression tests. The description of the compression failure in [64], during which the sheets displaced laterally, validates the expectation. The photographs of the stack of sixteen $1.54\,\mathrm{g\,cm^{-3}}$ sheets shown in Figure 3.34 did not reveal any lateral expansion at 1030 kPa, and the barreling theory was therefore rejected.

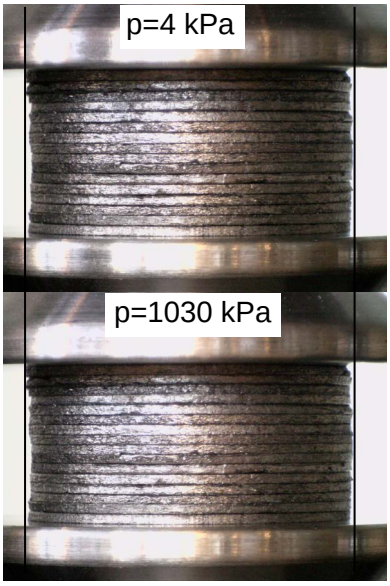

Figure 3.34: A photograph of a stack of sixteen $1.54\,\mathrm{g\,cm^{-3}}$ sheets at 4 kPa (top) and 1030 kPa (bottom). No lateral displacement was seen.

3.5.6 Section conclusion

The production of NGS parts involves compressing low-density NGS to the forming pressure to form a high-density sheet. The forming pressure required to achieve a given free-standing density was found to follow the relationship $d = 0.35e^{2.6p_f}$ where d is the free-standing density in $\mathrm{g\,cm^{-3}}$ and p_f is the forming pressure in MPa. Re-loading the high-density sheet to the forming pressure caused further increase in the free-standing density by up to 4 % after 23 cycles. The prediction of the maximum achievable free-standing density varies from 1.73 to $1.89\,\mathrm{g\,cm^{-3}}$. During the periods of constant forming pressure, NGS underwent a viscous deformation that was the highest at low forming pressures (3 % thickness reduction after 10 s at 0.9 MPa) and quickly decreases with increasing forming pressures. The forming pressure dwell time should be taken into account when designing methods for production of NGS parts, as it can affect the resulting free-standing density.

The detailed compression behavior of high-density sheets ranging from 0.55 to $1.7\,\mathrm{g\,cm^{-3}}$ was studied at pressures up to 1.06 MPa. All the sheets showed a hysteretic behavior that became less pronounced at higher densities. The stress-strain behavior was linear only during the loading cycle of the lowest-density sheet ($0.55\,\mathrm{g\,cm^{-3}}$), and non-linear for in all other cases. The non-linearity increased with increasing density. The strain at the maximum pressure (1.06 MPa) was 6 % for the $0.55\,\mathrm{g\,cm^{-3}}$ sheet and approximately 3 % for the $1.05\,\mathrm{g\,cm^{-3}}$, $1.54\,\mathrm{g\,cm^{-3}}$, and $1.7\,\mathrm{g\,cm^{-3}}$ sheets. The tangent modulus of the $0.55\,\mathrm{g\,cm^{-3}}$ sheet was 20 MPa, and that of $1.05\,\mathrm{g\,cm^{-3}}$, $1.54\,\mathrm{g\,cm^{-3}}$, and $1.7\,\mathrm{g\,cm^{-3}}$ sheets started from approximately 10 MPa at 30 kPa for all of the sheets, and increased to 50 MPa, 170 MPa,

and 220 MPa at 1 MPa, respectively. Small viscous deformation whose magnitude decreased with increasing density was detected during the periods of constant pressure.

3.5.7 Future work

Dowell and Howard [64] observed that heating of NGS causes its compression behavior to change. A detailed description of the phenomenon can be useful for determining the effects of a heat treatment on the properties of NGS. Similarly to steel that is heat treated to achieve different properties (e.g. hardness), heat treatment could be used during manufacturing of NGS parts to tailor the properties to the requirements given by various applications.

3.5.8 Expanded literature review

Additional data and observations with marginal relevance to the present work are summarized in the following paragraphs.

Dowell and Howard [64] used commercial graphite sheet ("Grafoil", Union Carbide Corporation, GTA grade with 0.1% of ash (per weight) or GTB grade with 5% - GTA used unless noted). For some tests they compressed the sheets themselves from thermally expanded graphite using a piston sliding in a cylinder. Samples for compression tests were discs 1.90 cm in diameter or squares 2.54cm on side stacked to at least 1.27mm. The compressive stress-strain curves were performed at $8.3 \times 10^{-4}\,\mathrm{s}^{-1}$ strain rate up to 31 MPa.

Based on microscope images of microstructure, Dowell and Howard [64] concluded that the irreversible strain is due to folding and interlocking of the basal planes that are highly misaligned with respect to the sheet plane while the reversible deformation is due to basal planes well aligned with the sheet plane. The Tangent compressive modulus at 6.9 MPa was found to be higher for samples with higher misalignment of the basal planes. The misalignment was determined by an X-ray diffraction measurement of 002 peaks.

Wang et al. [75] [77] used compression mold consisting of a 50.8 mm piston and a matching female counterpart to create cylinder shape samples. The surface density calculated from their data ranges from 46 to 642 mgcm^{-2}. The thickness of their sheets was higher than in the present work, ranging from 5 to 10 mm. The raw graphite contained 0.2 %. The information about the flake size is missing.

3.6 Heat capacity

In this section, the heat capacity of NGS is determined from the literature sources. In addition to the free-standing heat capacity, a relationship for evaluating the change of volumetric heat capacity with the compression pressure is developed.

3.6.1 Specific heat capacity

In this work, the specific heat capacity of NGS was assumed to be equal to that of pure graphite because the fixed carbon content of the NGS used in the present study was 99.27 % and the typical value is large than 95 %. The base for determining the heat capacity of NGS was the relationship by Spencer [78] reported in [71], which is:

$$c_{m,gr} = -5.293 + 58.998 \times 10^{-3} T - 43.225 \times 10^{-6} T^2 + 11.51 \times 10^{-9} T^3 \,[\mathrm{J\,mol^{-1}\,K^{-1}}], \quad (3.7)$$

where $c_{m,gr}$ is the molar heat capacity of graphite and T is the temperature in Kelvins. Using the molecular weight of carbon $M_{W,C} = 12.011\,\mathrm{g\,mol^{-1}}$ the specific heat capacity (per unit mass) is:

$$c_{p,gr} = -440.68 + 4.91T - 3.6 \times 10^{-3} T^2 + 9.58 \times 10^{-7} T^3 \,[\mathrm{J\,kg^{-1}\,K^{-1}}]. \quad (3.8)$$

The data predicted by Equation 3.8 are compared to the experimental data by Wang et al. [75] in Figure 3.35. It can be seen that the polynomial relationship by Spencer [78] predicts slightly higher values in comparison with the experimental data for NGS. However, the difference is low and therefore the relationship by Spencer [78] was considered valid, and the specific heat capacity of NGS in this work was determined by evaluating Equation 3.8 at 25 °C, which resulted in the value of $729.3\,\mathrm{J\,kg^{-1}\,K^{-1}}$.

Besides NGS, Wang et al. [75] also measured the specific heat capacity of aluminum and the data was included in Figure 3.35. At room temperature, the heat capacity of NGS is approximately 82 % that of aluminum. However, because the change of heat capacity with temperature is higher for NGS, the specific heat capacity of NGS and aluminum become equal at approximately 90 °C. Beyond this temperature, NGS shows a higher value of specific heat capacity.

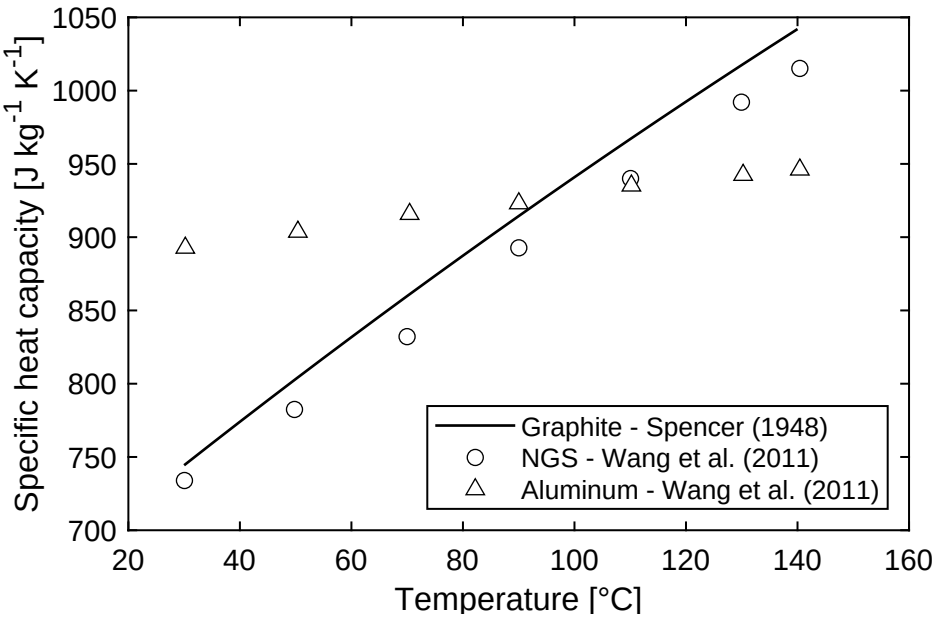

Figure 3.35: The specific heat capacity of graphite (Spencer [78], solid line), NGS (Wang et al. [75], circles), and aluminum (Wang et al. [75],triangles) as a function of temperature.

3.6.2 Volumetric heat capacity of NGS under compression

Volumetric heat capacity c_v is more practical for some of the comparisons of heat sinks described later in this thesis. Inputting c_v is also required for the measurement of thermal conductivity and diffusivity using the TPS method. It is defined as:

$$c_v = dc_p, \tag{3.9}$$

where c_v is the volumetric heat capacity, d is density of the material, and c_p is the specific heat capacity (per unit mass).

Since the thickness of NGS reduces significantly under compression, the change of density needs to be considered when evaluating the volumetric heat capacity of NGS at a compressed state. The density in the relaxed (uncompressed) state d is:

$$d = \frac{m}{tA}, \tag{3.10}$$

where m is the mass of the sample, t is the relaxed thickness, and A is the sample area. Density at a compressed state is:

$$d_p = \frac{m}{t_p A}, \tag{3.11}$$

where t_p is the thickness under compression. The thickness under compression can be calculated based on the strain at a given pressure S as:

$$t_p = t - St \tag{3.12}$$

Combining equations 3.10, 3.11, and 3.12 yields:

$$d_p = \frac{m}{tA(1-S)} = \frac{d}{1-S} = K_d d, \tag{3.13}$$

where the density correction factor K_d was defined as:

$$K_d = \frac{1}{1-S} \tag{3.14}$$

The volumetric heat capacity under compression is:

$$c_{v,p} = K_d d c_p = K_d c_v \tag{3.15}$$

The density correction factor K_d for four measured densities is shown in Figure 3.36. The values for other densities were calculated using linear interpolation.

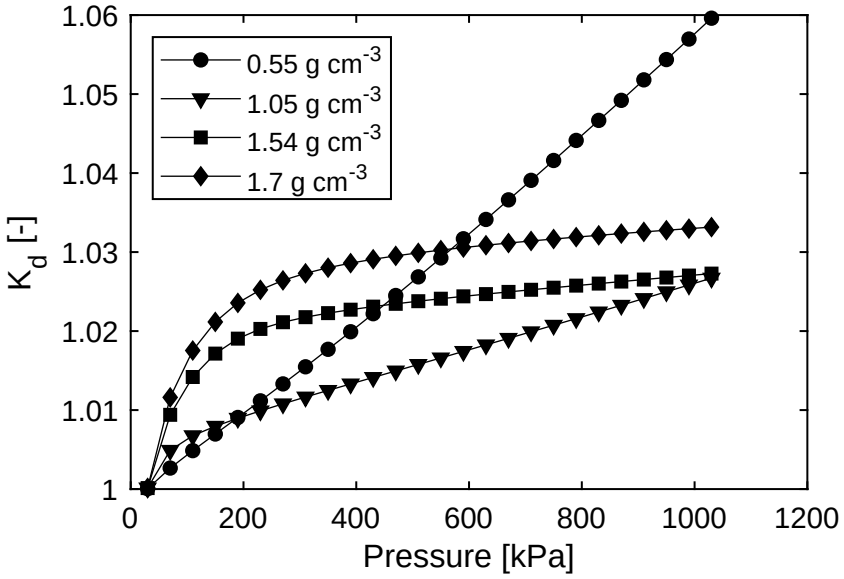

Figure 3.36: The density correction factor of the volumetric heat capacity as a function of the pressure

3.7 Thermal conductivity and diffusivity

In this section, the thermal conductivity and diffusivity of NGS are measured using the transient plane source method for the range of densities from 0.5 to 1.7 $\mathrm{gcm^{-3}}$ and pressures from 100 to 1080 kPa. The results are compared with the literature sources and recommendations for future measurements are made. The role of the sheet-to-sheet TCR in stacks of sheets is investigated. Lastly, the shortcomings of the TPS method are identified, and possible solutions are proposed.

3.7.1 Previous work

The available literature sources show that the thermal conductivity and diffusivity increase with density in the in–plane direction, and decrease with density in the through–plane direction. The explanations of the change of the thermal properties with density are consistent across the sources, and state that both the orientation of the highly anisotropic graphite cell walls and the contact resistance at their boundaries change with density and alter the overall bulk properties of NGS. Most of the studies [28, 79, 70, 68] were performed using the laser flash method, which is inherently not capable of measuring the dependence of the thermal properties on the uniaxial compression in the through–plane direction. Two relevant studies used the guarded heat flow meter method [75, 80], which requires the samples to be compressed to allow the heat to flow from the flux meters into the samples, but the pressure was not varied, and in one case its magnitude was not reported. Only one published article [81] focused on the thermal contact resistance (TCR) between the sheets, and the authors concluded that it is negligible at 100 kPa

Wei et al. [28] used the ASTM C714 laser flash method to measure the in–plane and through–plane thermal conductivity and diffusivity of NGS in the range of densities 0.55 to 1.89 $\mathrm{g\,cm^{-3}}$. They reported that the in–plane thermal conductivity is increasing with density while the through–plane thermal conductivity is decreasing. The authors argued that the change of the thermal conductivity with increasing density is due to the increase of the preferential orientation of the graphite basal planes and the decrease of porosity. In the in–plane direction, both factors cause an increased thermal conductivity. In the through–plane direction, the decreased porosity is expected to increase the thermal conductivity, but the increase in the preferential orientation is expected to decrease the thermal conductivity. The decrease of the through–plane thermal conductivity with density was explained by stating that the increase of the preferential orientation is dominant over the decrease in porosity. Besides the sheet density, the density of ENG particles d_{ENG} was found to have an effect on thermal diffusivity and conductivity. The thermal diffusivity of a 1.65 $\mathrm{g\,cm^{-3}}$ sheet manufactured from exfoliated graphite with the d_{ENG} of 6.25×10^{-3} $\mathrm{gcm^{-3}}$ was 330 $\mathrm{mm^2\,s^{-1}}$, which is 18 % higher than that of the sheet made of 3.4×10^{-3} $\mathrm{cm^3\,g^{-1}}$ flakes. The decrease was explained by the increased misalignment of graphite basal planes and by the fact that

the sheet made from flakes with lower d_{ENG} has more interfaces, which amplifies the contribution of the thermal contact resistance (TCR) between the cell walls to the overall thermal conductivity.

Liu et al. [79] measured the in–plane and through–plane thermal conductivity and diffusivity using the laser flash method, and their data closely follows the results of Wei et al. [28]. After observing the structure using an SEM microscope, the authors related density dependence to the orientation of the graphite basal planes, porosity, and the distribution of impurities. When comparing NGS to the conventional metals, the mode of heat transfer was deemed to be due to the phonon and electron diffusion for NGS, and only electron diffusion for copper and aluminum. Both the phonon and electron diffusion in NGS was claimed to be inhibited at the boundaries of the cell walls, which is in agreement with the TCR explanation in the other literature sources.

Bonnissel et al. [70] measured the in–plane and through–plane thermal conductivity and diffusivity, and the results are in agreement with Wei et al. [28] and Liu et al. [79]. The authors developed a model to relate the structure, thermal properties, and mass transfer properties. It was assumed that the density of NGS is not uniform and varies in the through–plane direction from $2.2\,\mathrm{gcm^{-3}}$ at the surface of the sheet to $0.05\,\mathrm{gcm^{-3}}$ at the middle of the sheet. However, the assumption was not based on observing the structure and its validity was confirmed only by comparing the predicted thermal and mass transfer properties with the experimental data. The thermal conductivity was expected to vary with thickness proportionally to the local density such that it is the highest at the surface and lowest at the middle of the sheet. The overall thermal conductivity was calculated as an integral of the local thermal conductivity over the thickness. If the assumptions about the structure of NGS by Bonnissel et al. [70] are correct, the thermal conductivity is expected to be a function of thickness, in which case sheets with equal density but different thickness would show different values of thermal conductivity.

Chen and Chung [80] measured the through–plane thermal conductivity of low density NGS ($<0.67\,\mathrm{g\,cm^{-3}}$) under compression (460 kPa) at 56 °C using the guarded hot plate method according to ASTM D5470. The samples were prepared from graphite flakes that were intercalated in sulfuric acid, exfoliated at 900 °C, and their resulting specific surface area was $40\,\mathrm{m^2\,g^{-1}}$. The measured values are lower than the other literature sources, and the trend does not show the inflection point at low densities that was reported by Bonnissel et al. [70] and Wang et al. [75]. Using the Hashin-Shtrikman and effective medium theory models, the authors concluded that within the given range of densities, 93.7 to 99.7 % of the heat transfer is in the *ab* directions of the graphite crystals.

Afanasov et al. [68] studied the effect of the intercalation agent and exfoliation method on the through–plane thermal conductivity of NGS. The standard intercalation method, which comprises of treating natural graphite flakes with a solution of sulfuric acid and an oxidizer, was compared to the anodic graphite oxidation in aqueous nitric acid solution. The

resulting intercalated graphite flakes were referred to as graphite bisulfate and graphite nitrate, respectively. The intercalated flakes were exfoliated in a furnace at 900 °C and 600 °C, respectively, and their d_{ENG} and specific surface area were measured to be $2.5 \times 10^{-3}\,\mathrm{gcm}^{-3}$ and $20\,\mathrm{m}^2\,\mathrm{g}^{-1}$, respectively, for the exfoliated graphite bisulfate, and $1 \times 10^{-3}\,\mathrm{gcm}^{-3}$ and $150\,\mathrm{m}^2\,\mathrm{g}^{-1}$, respectively, for the exfoliated graphite nitrite. The through–plane thermal conductivity of NGS prepared from the graphite bisulfate flakes was higher than that of the one prepared from the graphite nitrite flakes over the entire range of measured densities (0.02 to $1.2\,\mathrm{g\,cm}^{-3}$). For densities higher than $0.5\,\mathrm{g\,cm}^{-3}$, the difference in the thermal conductivity was $6\,\mathrm{W\,m}^{-1}\,\mathrm{K}^{-1}$. The difference was explained by the difference in the specific surface area, in particular by assuming that a higher surface area increases the TCR at the interfaces of cell walls, which is in agreement with Wei et al. [28]. Contrary to the other literature sources, the data by Avanasov et al. [68] show a slight increase of the through–plane thermal conductivity with increasing density.

Wang et al. [75] measured the through–plane and in–plane thermal conductivity of NGS using the guarded hot plate method according to ASTM E1530. While the preparation of the samples for the through–plane direction measurements was comparable to the other literature sources, the samples for the in–plane measurement were manufactured from ENG particles by pressing them in a tall narrow rectangular tube as shown in the related publication [77].

Smalc et al. [81] investigated the possibility of using NGS as a thermal interface material (TIM) for electronics cooling. They used sheets with the thickness of 0.13 mm and noted that at such low thicknesses, the impurities in NGS with dimensions higher than the sheet thickness can limit the conformity of graphite by not allowing the mating metal surfaces to be in contact. The purity of the NGS that was used for the study was low, with the typical impurity content of 5 %. Besides pure NGS, samples impregnated with synthetic and mineral polymers were studied. The thermal conductivity and TCR at the sheet-to-flux-meter interface was measured at 100 kPa using the guarded heat flow meter method according to ASTM D5470. To deconvolute the sheet-to-flux-meter TCR and the bulk thermal conductivity, the authors measured stacks of sheets and assumed that the sheet-to-sheet TCR is negligible. The assumption was confirmed by a measurement thermal resistance of a single 0.26 mm sheet and two 0.13 mm sheets that showed the same values. The reported thermal conductivity ranged from 4 to $6\,\mathrm{Wm}^{-1}\mathrm{K}^{-1}$. However, since density of the measured sheets was not reported, a comparison with other data sources is not possible. The samples impregnated with polymers showed slightly higher average thermal conductivity but the variation across the samples was large and the difference is likely not statistically significant (no statistical method was employed to judge the significance). The specific contact resistance at the interface between the sheet and the flux meter was $132\,\mathrm{mm}^2\mathrm{KW}^{-1}$ for the pure graphite sample and $59\,\mathrm{mm}^2\mathrm{KW}^{-1}$ and $67\,\mathrm{mm}^2\mathrm{KW}^{-1}$ for the samples impregnated with mineral and synthetic polymers, respectively. The results suggest that polymer im-

pregnation can reduce the TCR by approximately 50 %. The thermal resistance of a single 0.13 mm sheet was measured as a function of the through–plane compression pressure in the range from 50 to 1000 kPa and a decreasing behavior that was steep at low pressures and mild at higher pressures was seen. Whether the decrease was caused by the TCR or the change in the bulk thermal conductivity was not addressed.

3.7.2 Experimental method

All the measurements in this study were performed using the Hot Disk TPS 2500S machine, which is a commercial implementation of the transient plane source method [82, 83]. The method uses a sensor in the form of a nickel spiral. During the measurement the sensor is inserted between two identical samples, electric current is passed through it, and the generated heat penetrates the samples. The temperature increase of the sensor is recorded by measuring the current and voltage, and correlating it to the known resistivity of nickel. Based on the shape of the temperature-versus-time curve, the thermal properties can be determined. The TCR at the sensor-sample interface is excluded by discarding the initial section of the temperature-versus-time curve.

Pressure was imposed on the samples by manually turning a wheel attached to a threaded rod that lifts the sample table. The compression force was monitored by the Mark-10 M5-500 Series 5 force gauge. The measurement method and the sample size varied for the in–plane and through–plane directions.

3.7.2.1 In–plane direction

For the in–plane direction, the slab mode was used. 7 cm by 7 cm square samples were cut from the calendered sheets described in section 3.1. The measurement configuration consisted of the sensor, sample, insulation, and pressure spreader as shown in 3.37a. The sensor radius was 3.189 mm for all the in–plane measurements except for the samples at the lowest density and high thickness. In this case, the large thickness required using the 6.403 mm sensor to satisfy the slab mode criterion $0.03125 < h/a < 0.79836$ given in [84], where h is the sample thickness and a is the sensor radius. The heating power was in the range 0.4 to 1.8 W to achieve the total temperature increase given in [84]. The measurement time, which should be chosen so that the heat penetration depth is less than the available probing depth, was always set to the low limit of the machine (1 s) due to the high in–plane thermal diffusivity of NGS. Optimal measurement conditions would require lower measurement times or larger samples. The latter was not possible due to the limited size of the test section. The in–plane properties were measured under compression at 100 kPa. Additionally, an attempt to measure the pressure dependence of the in–plane properties was made. However, the insulation started deforming at pressures of approximately 500 kPa and other drawbacks were discovered. The drawbacks are addressed in the discussion section.

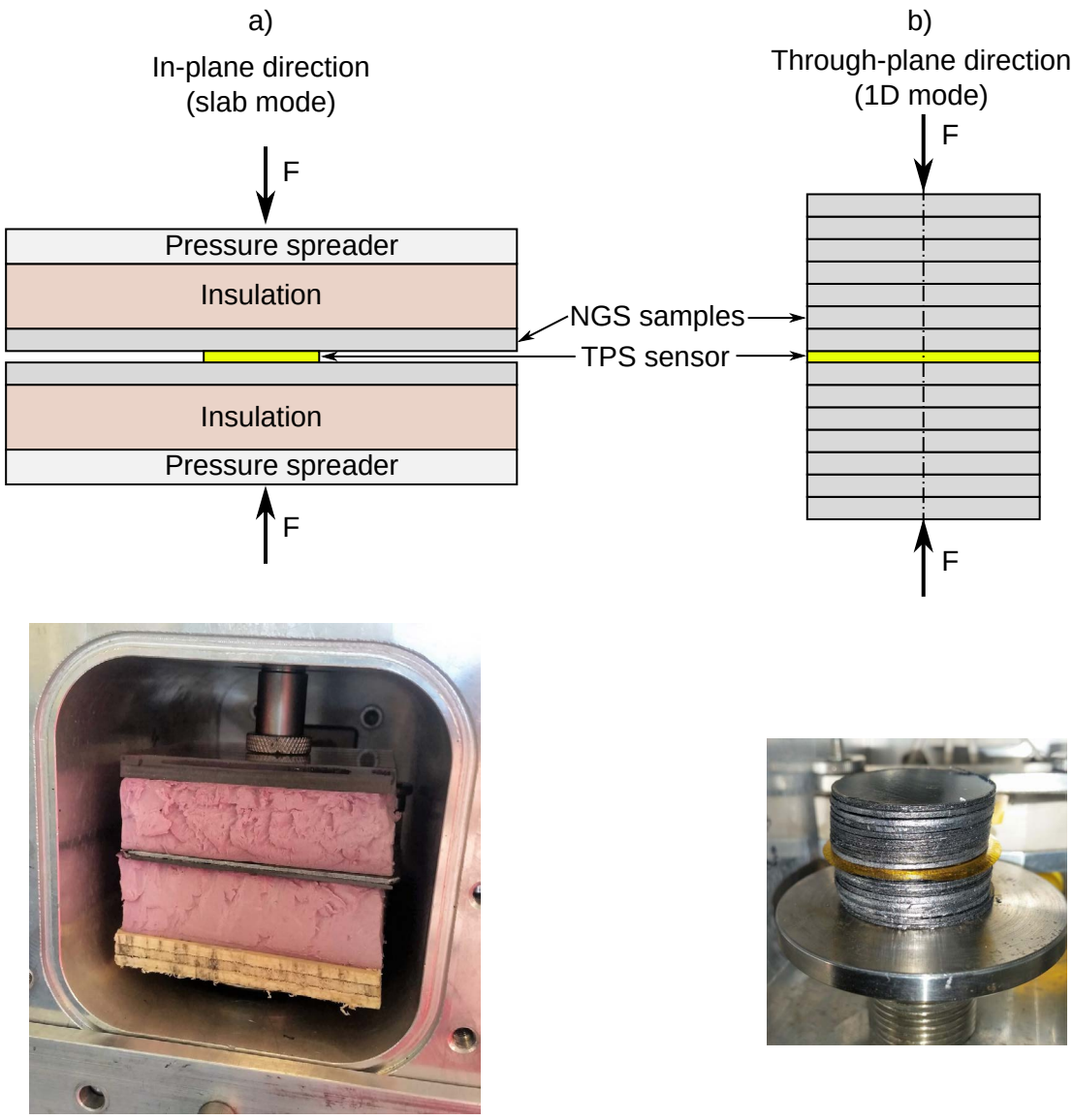

Figure 3.37: Schematics (top) and photography (bottom) of the thermal conductivity measurement

3.7.2.2 Through–plane direction

To measure the through–plane thermal properties, the one-dimensional mode was used. It requires the samples to match the sensor size, and therefore circular samples 32 mm in diameter were cut from the calendered sheet using a hole punch, and the measurements were performed using the 29.2 mm sensor. The difference between the sensor and sample diameters was within the requirements given in Ref. [84]. Stacks of sheets with the total height ranging from 6.7 to 27 mm were measured at pressures of 100 kPa, 200 kPa, 400 kPa, 800 kPa, and 1080 kPa. Measurements at no compression were attempted, however, the

repeatability was low and the results were not included in this text. The measurement time and the heating power were fixed to 2 s and 3 W, respectively. In all cases the penetration depth was smaller than the total height of the stack. Measurement of the through–plane properties of a single sheet was not possible as the required measurement times are much lower than the low limit of the machine.

3.7.3 Data processing

The data processing was done using the Hot Disk Thermal Constants Analyzer 7.3.12 software. While it is generally possible to determine the volumetric heat capacity using the TPS method, the modes used in this study required inputting it. The value of the volumetric heat capacity was calculated from the specific heat capacity of $729.3\,\mathrm{Jkg^{-1}K^{-1}}$ and the density. The density was corrected for the change with pressure as described in section 3.6. Both the raw data files and the implementation of data processing in Matlab are available in [62].

3.7.4 Section results

The results are summarized in Figure 3.38. While the in–plane thermal conductivity and diffusivity increase with the density, the through–plane properties decrease with density, which is in agreement with the data in the literature. The in–plane thermal conductivity increases linearly with density and can be approximated by the relationship $k_{in} = 212d - 22$. The thickness of the sheet, which is directly proportional its surface density, does not affect the in–plane thermal properties. The data points for the in–plane thermal diffusivity in Figure 3.38b are scattered and do not follow the expected trend $\alpha_{in} = 0.29 - 0.0301d^{-1}$ that was calculated from the thermal conductivity fit using the relationship between the thermal diffusivity and conductivity $\alpha = \frac{k}{dc_p}$. Since the values of the thermal conductivity and diffusivity were calculated using the proprietary software designed by the manufacturer of the TPS machine, further investigation of the scatter of the diffusivity data was not possible. Over the measured range of density, the in–plane thermal conductivity increases by approximately 250 % while the diffusivity increases only marginally by approximately 20 %, which likely makes the scatter in the data more pronounced.

No dependence of the in–plane thermal properties on pressure was seen. However, the pressure distribution may have been affected by the presence of the sensor between the samples as is explained later in the discussion section.

The through–plane thermal conductivity and diffusivity are a function of not only the density but also of the pressure. With increasing density, the through–plane thermal conductivity and diffusivity decrease non-linearly with the exception of the thermal conductivity at 100 kPa, which shows a linear decrease. Increasing the compression pressure results in an increased thermal conductivity and diffusivity for all the measured densities, but the

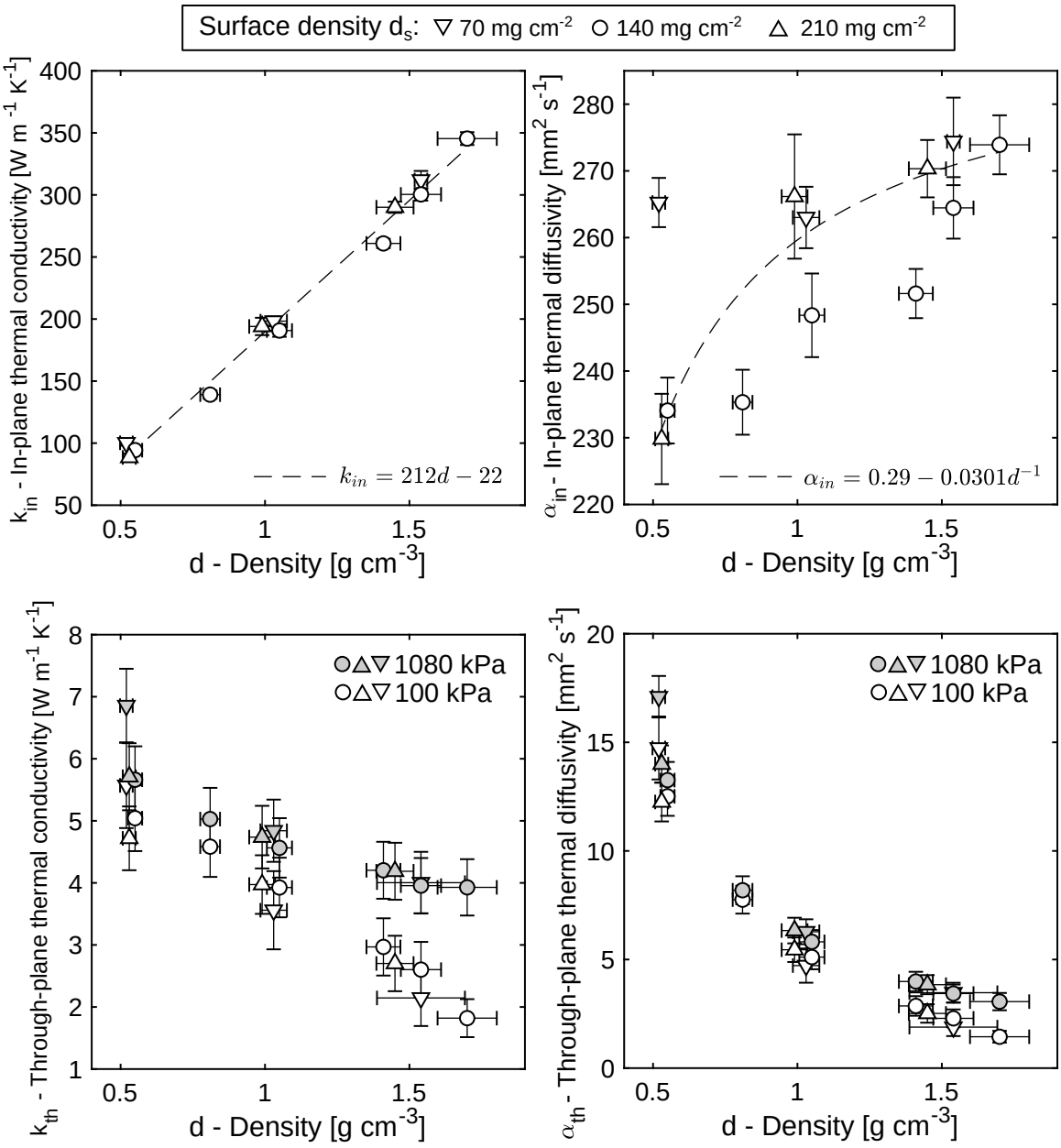

Figure 3.38: The results of the in–plane thermal conductivity (top left), in–plane thermal diffusivity (top right), through–plane thermal conductivity (bottom left), and through–plane thermal diffusivity (bottom right). The thickness of the samples is proportional to their surface density, which is distinguished by the triangle and circle symbols.

increase is more pronounced at higher densities as can be seen in Figure 3.39. After increasing the compression pressure from 100 kPa to 1080 kPa, the thermal conductivity and diffusivity of the 1.7 gcm^{-3} sheet increased by 116 % and 112 %, respectively, while that of the 0.55 gcm^{-3} sheet increased only by 12 % and 6 %, respectively. The change of thermal properties with pressure is linear at low densities and becomes non-linear with a logistic

profile at high densities. The repeatability of the measurements was better at higher pressures but this trend cannot be seen in Figures 3.38 and 3.39 as the overall uncertainty of the measurement is dominated by the 5 % accuracy of the machine given by the manufacturer [85].

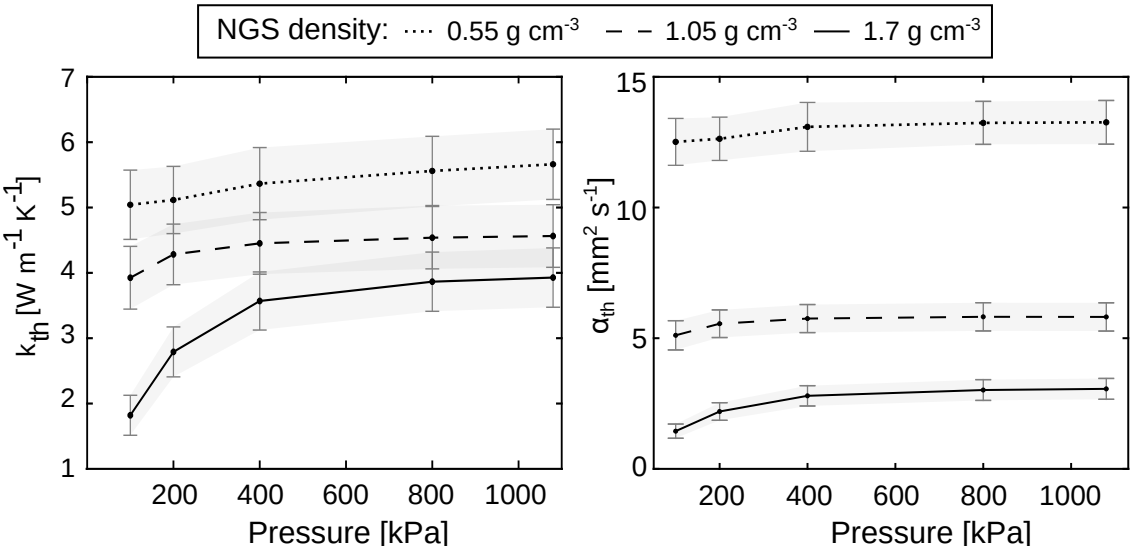

Figure 3.39: The pressure dependence of the thermal conductivity (left) and diffusivity (right) for the 140 mgcm^{-2} samples.

The through–plane conductivity and diffusivity and the in–plane diffusivity of the 0.5 gcm^{-3} 70 mgcm^{-2} sample deviate from the rest of the measurements. For the through–plane direction, the deviation is within the measurement uncertainty, and for the in–plane diffusivity, the deviation might be caused by the above mentioned scatter in the data. However, a similar trend was seen in the data by [28] and therefore the possibility of the low-density and low-thickness samples showing increased thermal properties cannot be rejected.

To make the results easy to reuse by other researchers, an explicit compact mathematical relationship between the measured properties and the relevant parameters was sought. The best fit of the in–plane thermal conductivity k_{in} as a function of the free-standing density d is a simple linear function that was determined as:

$$\begin{gathered} k_{in} = 212d - 22 \ [\mathrm{Wm^{-1}K^{-1}}] \quad (error = \pm 15\,\mathrm{Wm^{-1}K^{-1}}) \\ d \in [0.5, 1.7]\mathrm{gcm^{-3}}. \end{gathered} \tag{3.16}$$

A comparison of the k_{in} best fit with the measured data is shown in Figure 3.40.

In the through–plane direction, the thermal conductivity is also a function of pressure p and the best fit was determined as:

$$k_{th} = (34.63 - 34.44d + 29.61d^2)p^{0.01015-0.0008422d}$$
$$-30.59 + 34.99d - 31.75d^2\ [\mathrm{Wm^{-1}K^{-1}}] \quad (error = \pm 0.4\,\mathrm{Wm^{-1}K^{-1}}) \tag{3.17}$$
$$d \in [0.5, 1.7]\mathrm{gcm^{-3}}, p \in [100, 1080]\mathrm{kPa}.$$

A comparison of the k_{th} best fit with the measured data is shown in Figure 3.41.

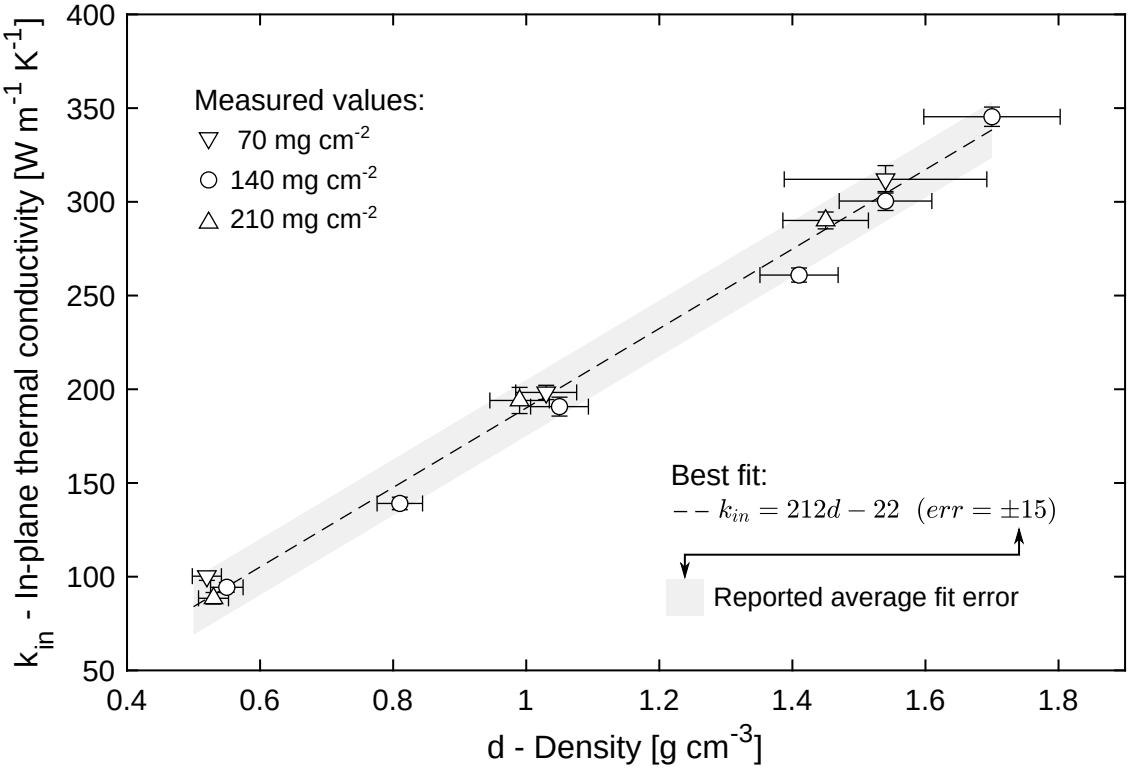

Figure 3.40: A comparison of the best fit of the in–plane thermal conductivity with the measured data.

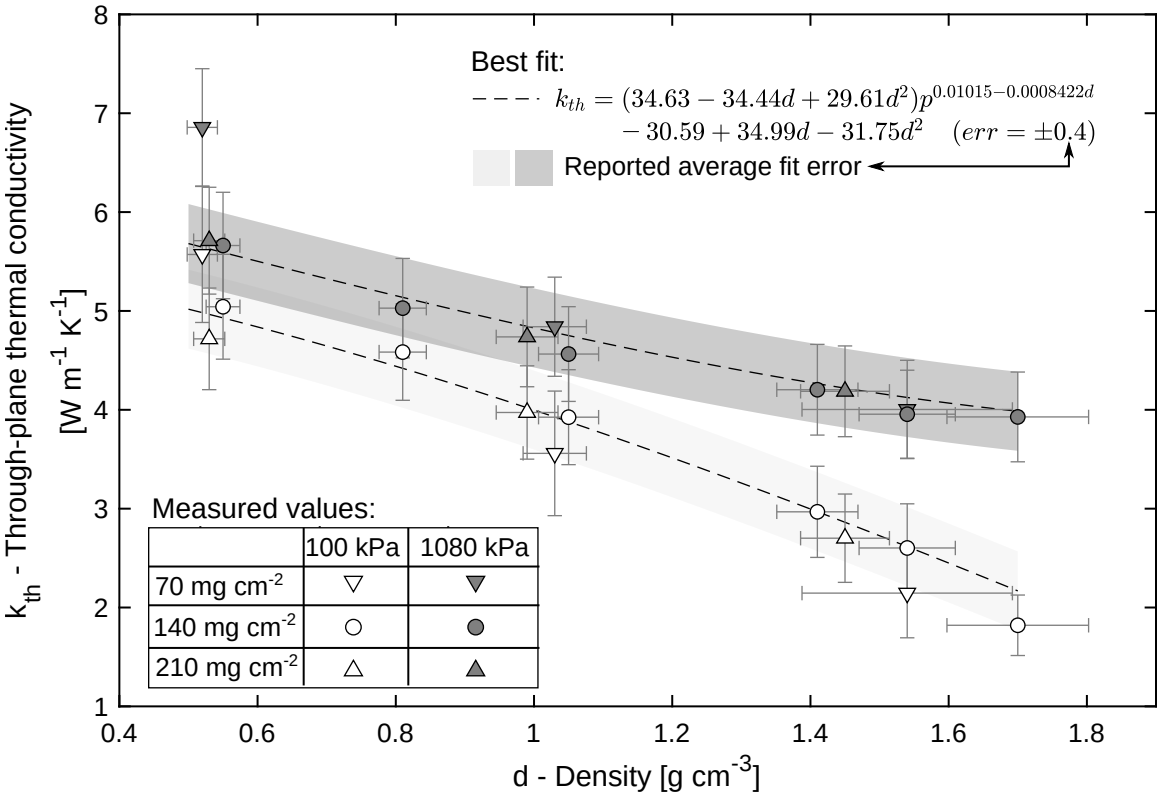

Figure 3.41: A comparison of the best fit of the through–plane thermal conductivity with the measured data.

Since stacks of sheets were measured, the sheet-to-sheet TCR is inherently included in the value of the through–plane thermal conductivity and diffusivity. Neither the TPS nor the guarded heat flow meter method are capable of deconvoluting of the sheet-to-sheet TCR. The importance of the sheet-to-sheet TCR can be estimated by comparing the results for stacks of sheets at different thicknesses. Figure 3.42 illustrates the theory employed to judge the importance of the sheet-to-sheet TCR. The surface density of the sheet dictates its thickness at the given density. A varying number of interfaces per stack height can be achieved by using stacks of low and high surface density sheets. If the sheet-to-sheet TCR is significant, the stack with more interfaces will show lower effective thermal conductivity. In practice, it was not possible to manufacture sheets at the same density because the calendering process did not allow a fine control of the final sheet thickness. Therefore, the sheets prepared for this measurement had a comparable but not identical density, as can be seen by the horizontal distance between the circular and triangular symbols in Figure 3.38. The results for the through–plane thermal conductivity and diffusivity in Figure 3.38 do not show the vertical stacking order outlined on the left side of Figure 3.42, and the contribution of the sheet-to-sheet TCR was therefore deemed to be negligible.

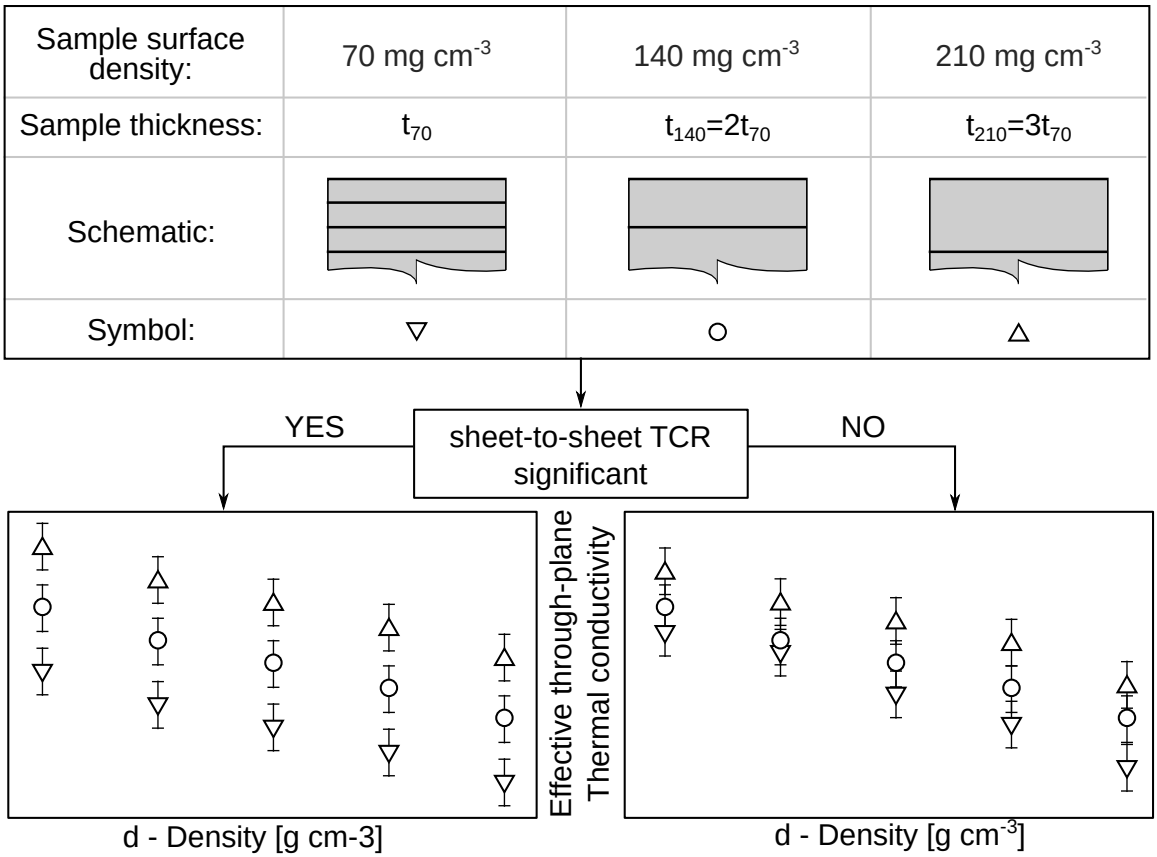

Figure 3.42: Illustration of the theory used for evaluating the importance of the sheet-to-sheet TCR

The theory for estimating the importance of the sheet-to-sheet TCR only holds if the through–plane thermal conductivity is not a function of thickness. Bonnissel et al. [70] stated that the local density of NGS varies across the thickness which can in turn cause a variation of the thermal conductivity between sheets with equal density but different thickness. If the low-thickness sheets have a higher bulk through–plane thermal conductivity, the decrease of the effective thermal conductivity caused by the added interfaces can be negated by the increased bulk thermal conductivity. Since the through–plane variation of local density was not confirmed based on the SEM images presented in section 3.3, the through–plane thermal conductivity was assumed to be independent of sheet thickness and the conclusion about the significance of sheet-to-sheet TCR is considered to be valid.

3.7.5 Section discussion

A comparison of the present and literature data with an extended legend that lists the relevant parameters is shown in Figure 3.43. The present data for the in–plane thermal conductivity are in a good agreement with the literature data at $0.5\,\mathrm{gcm}^{-3}$, but then start to deviate and become progressively lower. The same trend is seen for the in–plane thermal

diffusivity. The main source of the deviation is expected to be the mismatch in the value of the specific heat capacity. In the present study the value of $729.3\,\mathrm{J\,kg^{-1}\,K^{-1}}$ was used, which is smaller than $850\,\mathrm{J\,kg^{-1}\,K^{-1}}$ used by Wei et al. [28], Liu et al. [79], and Bonnissel et al. [70]. The value of $850\,\mathrm{J\,kg^{-1}\,K^{-1}}$ was referenced from the study by Wang et al. [75], in which the average for the temperature range 30 to 140 °C was reported. This temperature range is relevant to adsorption cooling systems but not for a measurement of thermal properties at room temperature.

Wang et al. [75] measured the in–plane thermal conductivity directly using the guarded heat flow meter method, which does not require inputting the heat capacity. Their data deviate from the other literature sources above $100\,\mathrm{Wm^{-1}K^{-1}}$, which was found to coincide with the upper limit of the used equipment [86] and the deviated data were therefore not considered valid.

Based on the table at the bottom of Figure 3.43, the density of ENG particles d_{ENG} used to prepare the samples does not correlate with the variation in the in–plane thermal properties. Other factors, such as graphite purity, sheet thickness, or the inherent inaccuracy of the measurement methods, can be responsible for the data mismatch between the present and literature data. Definite conclusions cannot be made because the parameters vary widely and some of them have not been reported.

Similarly to the in–plane properties, the through–plane thermal conductivity and diffusivity measured in this work are in most cases lower than the literature data. The scatter of the literature data for the through–plane thermal conductivity is high, reaching differences of approximately $8\,\mathrm{Wm^{-1}K^{-1}}$. The present data agrees the best with the data by Chen and Chung [80] which can be explained by the comparable compression pressure and thickness of the sheets. The data by Afanasov et al. [68] suggest a high dependence of the through–plane thermal conductivity on the density of ENG particles. However, the rest of the data sources do not confirm this trend as can be illustrated by the overlap of the data by Bonnissel et al. [70] and Wei et al. [28] who prepared the sheets from ENG particles with d_{ENG} of $1.7 \times 10^{-3}\,\mathrm{gcm^{-3}}$ and $6.25 \times 10^{-3}\,\mathrm{gcm^{-3}}$, respectively. Since Afanasov et al. [68] reported an increase in the through–plane thermal conductivity with increasing density, which is contrary to the other studies, it was concluded that their study is more likely to be inaccurate and the sensitivity to d_{ENG} may not be valid. Contrary to the in–plane thermal conductivity, the inconsistency in the value of the specific heat capacity cannot explain the lower values of the present through–plane thermal conductivity data, because the data by Wang et al. [75] were obtained using the guarded heat flow method, which measures the thermal conductivity directly and does not require inputting the specific heat capacity. The reason for the difference between the present and literature data for the through–plane properties could not be determined based on the available information.

During the measurements in the in–plane direction, the sensor covered only a part of the 7 cm by 7 cm sample, which causes a non-uniform pressure distribution, an in turn a non-

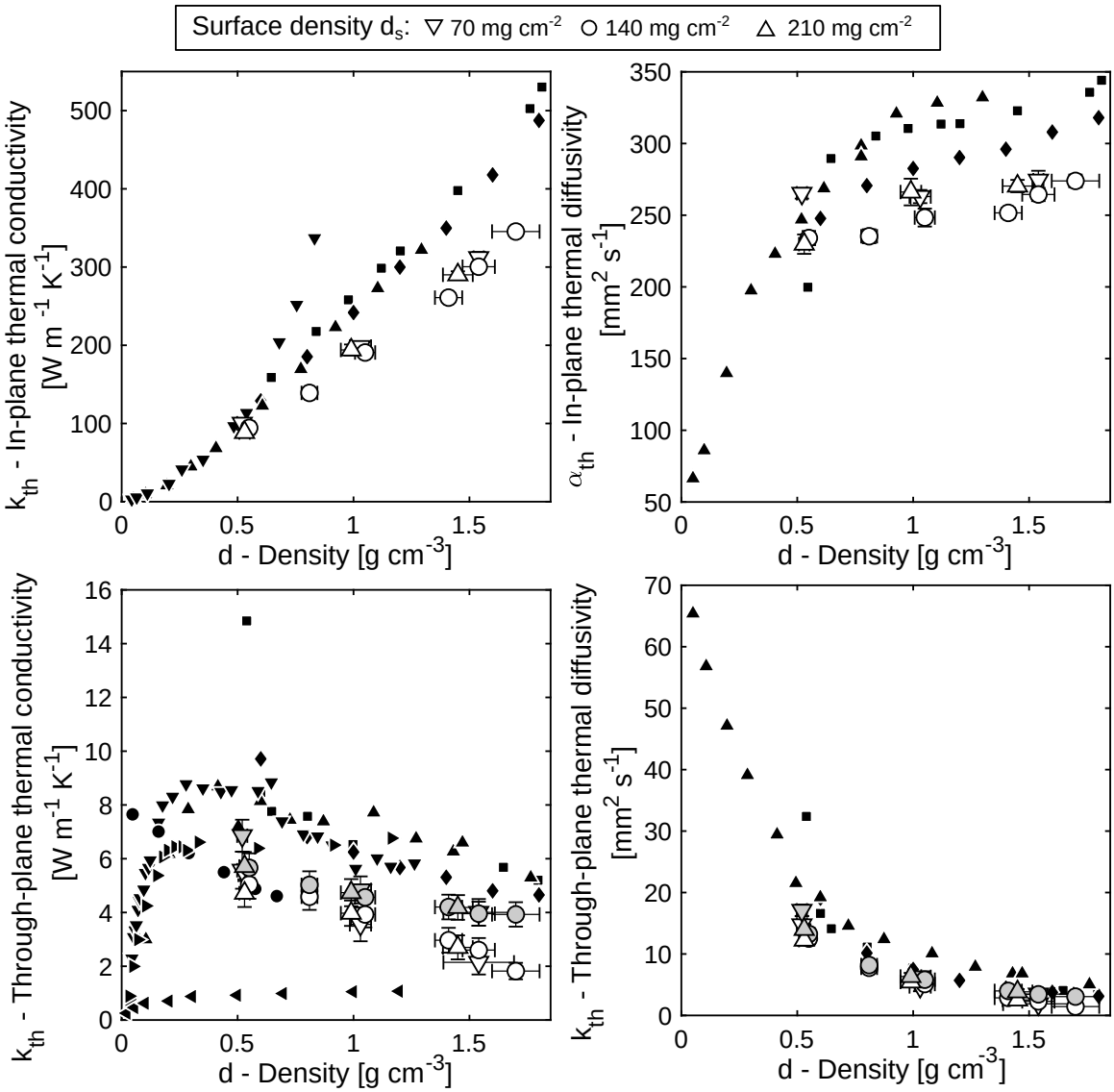

Symbol, data source	Method	Pressure [kPa]	c_p [J kg^{-1} K^{-1}]	Thickness [mm]	d_{ENG} [$\cdot 10^{-3}$ g cm^{-3}]
■ Wei et al. (2010)	LF	0	850	0.15-2	6.25
♦ Liu et al. (2013)				N/A	'moderate'
▲ Bonnissel et al. (2001)				N/A	1.7
▼ Wang et al. (2011)	GHFM	N/A	734	5 - 12	5-6
● Chen and Chung (2014)	GHFM	460	N/A	1.5-3.5	N/A
▶ ◀ Afanasov et al. (2009)	LF	0	711	1.3 - 1.5	2.5
					1
▽○△ ▽●▲ Present study	TPS	100 1080	729	0.4-4.1	4

LF=Laser flash, GHFM=Guarded heat flow meter, TPS=Transient Plane Source

Figure 3.43: A comparison of the present results of the thermal conductivity and diffusivity measurements with the relevant literature data.

uniform deformation as shown in Figure 3.44a and b. The importance of the non-uniformity can be estimated by comparing the half-thickness of the sensor $t_s/2$ to the difference between the uncompressed and compressed sheet thickness Δt. The two dimensions are sketched in Figure 3.44c. The thickness of the sensor t_s measured by a caliper is 0.05 mm. If $t_s/2$ is comparable to Δt then the sensor is expected to significantly affect the pressure distribution and distort the results. It is convenient to define the ratio of Δt and $t_s/2$ as:

$$\psi = \frac{\Delta t}{t_s/2}, \tag{3.18}$$

and use it for quantifying the importance of the pressure non-uniformity for the measured sheet densities. High values of ψ mean that the pressure non-uniformity is negligible, and values closer to and 1 and lower suggest that the pressure non-uniformity is significant. Based on the compression study in section 3.5, the thickness difference Δt associated with compressing the sheet to 400 kPa was calculated to be 0.054, 0.019, 0.02, and 0.024 for sheet densities 0.55 $\mathrm{gcm^{-3}}$, 1.05 $\mathrm{gcm^{-3}}$, 1.55 $\mathrm{gcm^{-3}}$, and 1.7 $\mathrm{gcm^{-3}}$, respectively, which translates to ψ of 2.16, 0.76, 0.80, and 0.96, respectively. It is therefore assumed that the non-uniformity is most likely negligible for the 0.55 $\mathrm{gcm^{-3}}$ but significant for higher densities.

Based on this analysis, it is recommended to conclude a study to verify the reliability of TPS measurements in the slab mode under compression for materials with the compression behavior similar to that of NGS. The shortcoming of the method can be potentially overcome by filling the low-pressure region (3.44b) with an additional material. It is important to keep the thickness of the additional material equal to the thickness of the sensor, and ideally use a material with similar mechanical properties as the sensor. Another potential improvement of the slab mode measurement is using an insulation material that can withstand high pressures and still provide a sufficient thermal insulation.

For the TPS measurements in the slab mode it is assumed that the thermal properties in the two perpendicular in–plane directions are identical, i.e. the measured material is orthotropic. Dowell and Howard [64] observed that the in–plane tensile strain of NGS at 4.9 MPa in the rolling direction is approximately half of the one in the direction perpendicular to the rolling direction. Similar difference may be seen in other material properties such as the thermal conductivity. Most of the conventional methods for measuring the thermal properties are not capable of measuring the difference in the directions parallel and perpendicular to the rolling direction. It is assumed that the TPS method can be used for measuring the difference if a rectangular sensor together with the one-dimensional mode are used as illustrated in Figure 3.45. Another option is to use the optical method developed by Pech-May et al. [87], which is capable of measuring the in–plane properties in two directions. Samples of NGS were sent to the authors of Ref. [87]. However, the measurement was not successful. It is likely that the upon further development of the method, it can become a desirable tool for thermal characterization of NGS and similar materials.

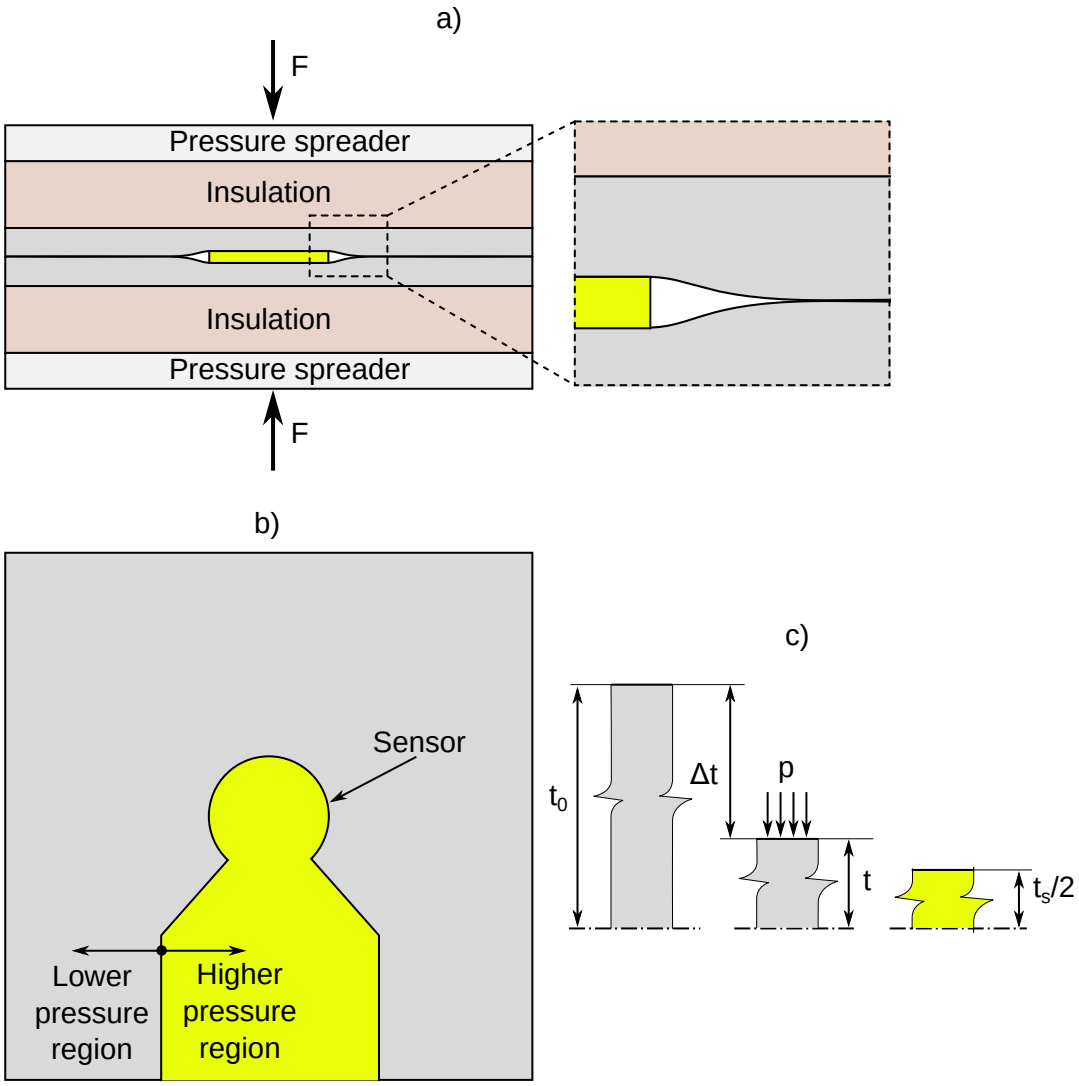

Figure 3.44: An illustration of the pressure and deformation non-uniformity during the slab mode TPS measurements. a) The section view of sheet deformation, b) a visualization of the low and high pressure regions on a measured sample, and c) comparison of thickness of the sensor and the sheet before and after compression.

Hot disk TPS2500S offers the anisotropic mode that is claimed to be capable of measuring the through–plane and in–plane properties simultaneously. Stacks of 7 cm by 7 cm sheets were measured, however, the results did not agree with those obtained from the slab and one-dimensional modes.

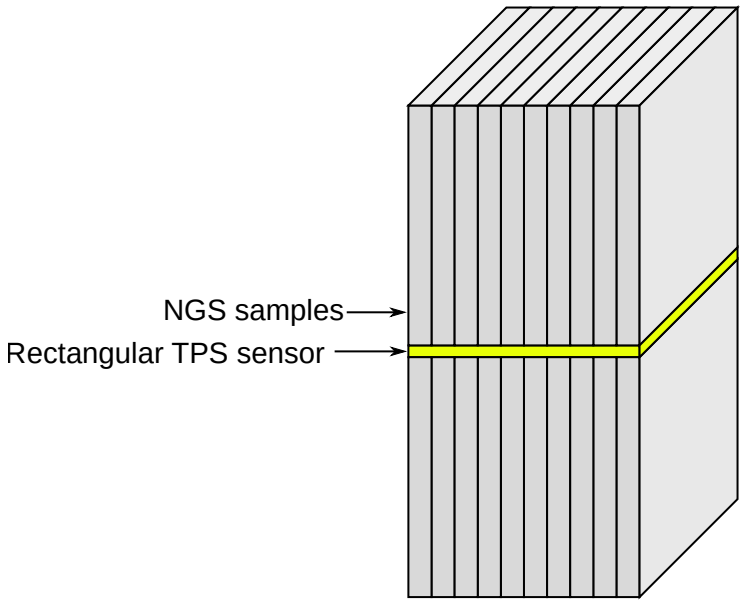

Figure 3.45: Illustration of measurement of in–plane thermal properties of NGS using the one-dimensional TPS method.

3.7.6 Section conclusions

The in–plane and through–plane thermal conductivity and diffusivity of NGS were measured at densities ranging from 0.5 to 1.7 g cm^{-1} and pressures from 100 to 1080 kPa. The in–plane thermal conductivity increases linearly with density from 100 Wm^{-1}K^{-1} at 0.5 g cm^{-1} to 350 Wm^{-1}K^{-1} at 1.7 g cm^{-1}. The in–plane thermal diffusivity increases non-linearly from 230 mm^{2}s^{-1} at 0.5 g cm^{-1} to 270 mm^{2}s^{-1} at 1.7 g cm^{-1}. The in–plane thermal properties are not a function of the compression pressure.

The through–plane thermal conductivity at 100 kPa decreases linearly from 5 Wm^{-1}K^{-1} at 0.5 g cm^{-1} to 2 Wm^{-1}K^{-1} at 1.7 g cm^{-1}. The through–plane thermal diffusivity at 100 kPa decreased non-linearly from 12 mm^{2}s^{-1} at 0.5 g cm^{-1} to 1.5 mm^{2}s^{-1} at 1.7 g cm^{-1}. The through–plane thermal properties increase with compression pressure. The increase is within the uncertainty limit for low densities but becomes significant at higher densities. The pressure dependence shows a logistic profile with a steeper increase at low pressures. At the highest measured pressure of 1080 kPa, the through–plane thermal conductivity and diffusivity increase by 116 % and 112 %, respectively, with respect to the 100 kPa values. The effect of the sheet-to-sheet TCR was considered negligible based on the measurements of sheets with varying thickness.

A comparison of the present results with the literature data showed significant differences, especially for the through–plane thermal conductivity. Factors such as the apparent density of ENG particles d_{ENG}, flake size, or the impurity content can influence the thermal properties and should be addressed in the future studies. The discrepancy between litera-

ture sources can also be due to different measuring methods (TPS, Laser flash, heat flow meter, Angstrom). To the best knowledge of the author, the open literature does not contain a study that clearly evaluates the suitability of the methods for measuring anisotropic materials.

All the data presented in this section were at room temperature. The thermal properties of graphite are dependent on temperature. For example, the thermal conductivity of crystalline graphite in *ab* directions was shown to be the highest at cryogenic temperatures of approximately $-150\,^{\circ}\mathrm{C}$, and decrease with increasing temperature [88]. Over the temperature range 25 to $300\,^{\circ}\mathrm{C}$ the *ab* thermal conductivity decreased from approximately $1400\,\mathrm{Wm^{-1}K^{-1}}$ to $600\,\mathrm{Wm^{-1}K^{-1}}$, which is a 57 % decrease. In the *c* direction, the thermal conductivity was also reported to decrease with temperature, halving over the temperature range from room temperature to $1000\,^{\circ}\mathrm{C}$ [43]. The trends in the temperature dependence of crystalline graphite cannot be directly translated to the thermal conductivity of NGS, and future work is necessary.

3.7.7 Future work

Besides the need to address the non-uniform pressure distribution in the slab mode measurements, another recommendation is to investigate the potential of combining the structure function approach used in thermal transient measurements (see section 5.1) with the hardware used for the TPS measurements. Evaluating the structure functions for stacked or layered materials could allow for a quantification of the TCR at the sample-to-sample or layer-to-layer interfaces.

3.8 Electrical conductivity

In this section, the electrical conductivity of NGS is measured for the range of densities and pressures identical to the thermal conductivity study presented in section 3.7. The terminology of the methods used for measurements of electrical conductivity is often ambiguous in the available literature. Within this text, the method names stated in [89] are followed and the term *four probe method* is used to refer to the methods identical or similar to the one described in ASTM C611. The term *four point probe method* is used to refer to the method in which small pins placed typically a few millimeters apart in a collinear configuration are used.

3.8.1 Previous work

The electrical conductivity of NGS is anisotropic and generally lower than that of metals by approximately two to four orders of magnitude. Wei et al. [28] measured the in–plane electrical conductivity of NGS using the four probe method according to the ASTM C611 standard. Celzard et al. [90], Luo and Chung [91], and Chen and Chung [80] measured the in–plane and through–plane conductivities using a variation of the four probe method in which the contact wires were attached to the samples using a silver paint. Qian at el. [92] measured the bulk electrical conductivity using the four point probe method, however, from their description it is not clear whether the anisotropy was taken into account. Literature sources that focus on the conductivity around the percolation threshold exist, but they were omitted from this review because of their marginal relevance to this work.

The available data for the in–plane electrical conductivity are in a good agreement across the literature sources, and the coverage is complete over the entire range of densities. An increasing trend with values reaching $3000\,\mathrm{S\,cm^{-1}}$ at high densities is seen. The available data for the through–plane conductivity vary widely across the sources, and values for higher densities are missing.

The goals of this section are to: i) measure the in–plane and through–plane electrical conductivity of NGS in the range of densities 0.5 to $1.7\,\mathrm{g\,cm^{-3}}$ to offer a reliable and comprehensive data source for designing or researching devices such as heat sinks or fuel cells, ii) expand the available data by exploring the effect of the compression pressure on the electrical conductivity, iii) investigate the role of electrical contact resistance (ECR) at the sheet-to-sheet interfaces of stacked NGS sheets, iv) determine if the thickness of NGS affects the electrical conductivity.

3.8.2 Experimental method

The measurements were performed using a Raytech Micro Junior 2 micro ohm meter that uses the four probe method to measure the resistance of the samples of interest. The resis-

tivity was calculated from the resistances based on the fundamental equation:

$$\rho = \frac{R}{t}A, \tag{3.19}$$

where ρ is resistivity, R is the electrical resistance, t is the sample thickness, and A is the sample cross-section. The measured resistance is a combination of the bulk resistance R_b and the probe-to-sample electric contact resistance $R_{ECR,p-s}$ as is shown on the left side of Figure 3.46. To deconvolute the contact resistance at the probe-sample interface, the two-thickness method is typically used as illustrated in Figure 3.46.

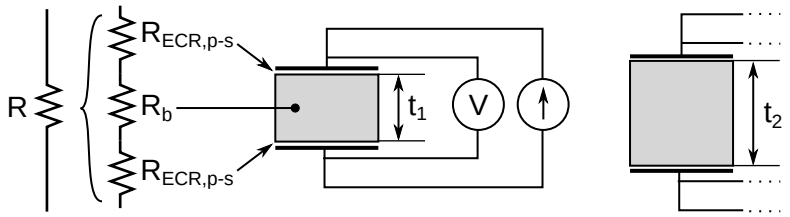

Figure 3.46: Illustration of the two-thickness method for measuring the electrical resistivity.

The bulk resistance R_b can be expressed in terms of resistivity and sample dimensions as:

$$R_b = \rho\frac{t}{A}, \tag{3.20}$$

and the total measured resistance is:

$$R = \rho\frac{t}{A} + 2R_{ECR,p-s}. \tag{3.21}$$

Evaluating Equation 3.21 for two thicknesses t_1 and t_2 and subtracting the two equations yields:

$$R_2 - R_1 = \rho\frac{t_2}{A} - \rho\frac{t_1}{A} + 2R_{ECR,p-s} - 2R_{ECR,p-s}, \tag{3.22}$$

which simplifies to:

$$R_2 - R_1 = \rho\frac{t_2 - t_1}{A}, \tag{3.23}$$

and the resistivity of the measured sample can be calculated as:

$$\rho = \frac{(R_2 - R_1)A}{t_2 - t_1} \tag{3.24}$$

The electrical conductivity can be calculated as the inverse of resistivity. If necessary the contact resistance $R_{ECR,p-s}$ can be calculated by using the resistivity value in Equation 3.21 as:

$$R_{ECR,p-s} = \frac{R}{2} - \frac{\rho t}{2A}. \tag{3.25}$$

In this study, the two-thickness method was extended by measuring more than two thicknesses. The accuracy of the $\frac{R_2-R_1}{t_2-t_1}$ term can be improved by substituting it with the slope of the linear fit of the resistance versus thickness data points. Due to the vast difference between the in–plane and through–plane properties, the measurement method and sample shape varied for the two directions. All the raw data files and the implementation of data processing methods can be accessed in [62].

3.8.2.1 In–plane direction

For the in–plane measurements, strips 210 mm long and 9 to 15 mm wide were used. The ohm meter terminals were attached to the samples using clips in a way showed in Figure 3.47. Each sample was measured at four nominal voltage terminal distances L_V of 50 mm, 100 mm, 150 mm, and 200 mm that were set by locking a caliper at the given distance, attaching it to the sample, and clipping the terminals next to the upper jaws. For each of the measured distances, the measurement was repeated at least three times. Before each of the repetitions, the clips were removed and re-attached again. The measurement current was 1 A.

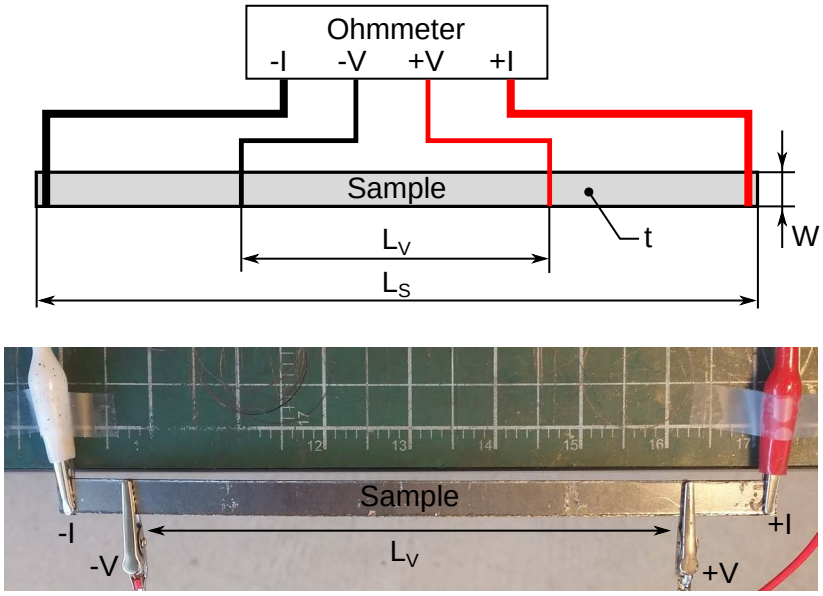

Figure 3.47: A scheme (top) and a photograph (bottom) of the in–plane electrical conductivity measurement. The length, width, and thickness of the sample are marked as L_S, W, and t, respectively. +I and -I are the current terminals and +V and -V are the voltage terminals. The distance between the voltage terminals is L_V.

For calculating the in–plane resistivity ρ_{in}, the general Equation 3.19 was modified to reflect the measurement configuration shown in Figure 3.47 as:

$$\rho_{in} = \frac{R}{L_V} A_{in}, \tag{3.26}$$

where R is the measured resistance, L_V is the distance between the voltage terminals, and A_{in} is the cross-section area for the in –plane measurements, which is defined as:

$$A_{in} = Wt, \tag{3.27}$$

where W and t_s are the sample width and thickness, respectively. For each of the samples, a line was fit thought the data points to obtain the slope a as illustrated in Figure 3.48. The fraction on the right side of Eq. 3.24 corresponds to the slope of the fitted line a and Eq. 3.26 can be therefore rewritten to:

$$\rho = aA_{in}. \tag{3.28}$$

The slope of the line a was obtained using the *fit* function in Matlab.

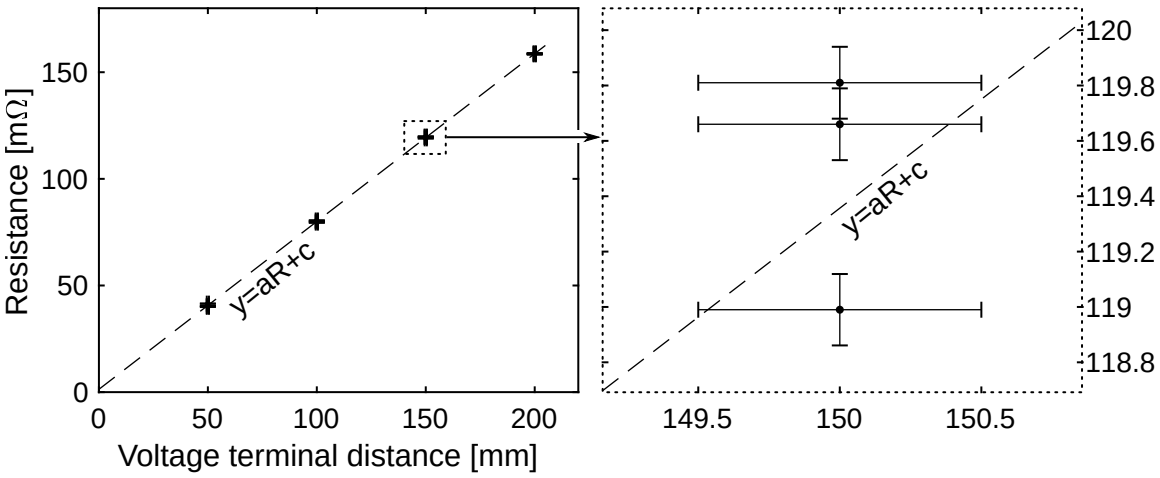

Figure 3.48: The measured data for the $1\,\mathrm{g\,cm^{-3}}$ $140\,\mathrm{mg\,cm^{-2}}$ sample. Left: the resistance data for the four measured voltage terminals distances. Right: a detail of the 150 mm terminal distance showing the variation of the data points and the measurement uncertainty.

3.8.2.2 Through–plane direction

For the though–plane direction, disc-shaped samples 24.7 mm in diameter were used and measured between gold-plated copper probes at pressures ranging from 100 to 1080 kPa as shown in Figure 3.49. The compression force was imposed using the same device as in the measurements of thermal conductivity (section 3.7). The measurement procedure consisted of mounting the samples between the probes, collecting the resistance readings at increasing values of pressure, and repeating the measurement for two random combinations of available samples.

In comparison with other materials such as metals, for which samples for the two-thickness method can be prepared by machining, preparing NGS samples at varying thickness and matching density requires the ability to control the compression in the forming

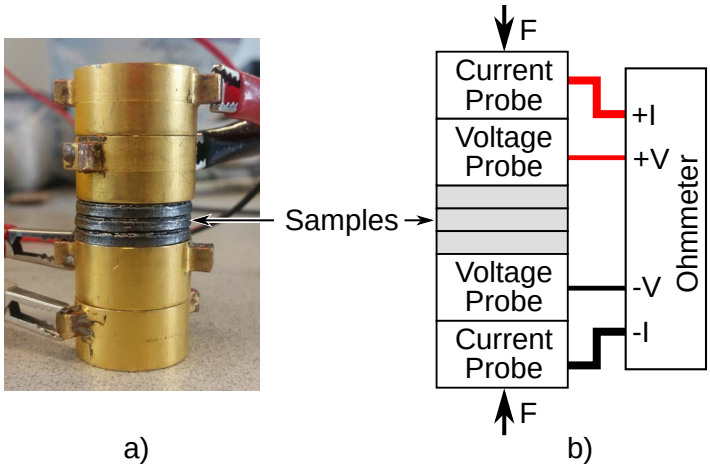

Figure 3.49: a) a photograph and b) a scheme of the through–plane electrical conductivity measurement. The compression device is not shown for clarity.

process at high accuracy. At the sheet thickness less than 1 mm, a 0.1 mm change in thickness can results in a 20 % increase in density. In this work, the accuracy required to prepare the samples for the two-thickness method was not achievable. Additionally, even if a different device was used for the forming process, it cannot be guaranteed that the bulk electrical conductivity is the same for thick and thin NGS samples. Based on the two drawbacks, using the two thickness method with two single-body samples was rejected, and stacks of samples were measured instead. This configuration introduces additional sample-to-sample (or sheet-to-sheet) contact resistances that need to be accounted for.

As illustrated in Figure 3.50, when a stack of sheet is measured, the total resistance R is a sum of the NGS bulk resistance R_b, probe-to-sheet contact resistance $R_{ECR,p-s}$, and the sheet-to-sheet contact resistance $R_{ECR,s-s}$. For the number of sheets n_s the total resistance is:

$$R = n_s R_b + 2R_{ECR,p-s} + (n_s - 1)R_{ECR,s-s}. \tag{3.29}$$

The bulk resistance R_b can be expressed as:

$$R_b = \rho_{th,b} \frac{t_s}{A_{th}} \tag{3.30}$$

where $\rho_{th,b}$ is the bulk through–plane resistivity, t_s is the sheet thickness, and A_{th} is the sample cross-section area relevant to the through–plane measurements. Substituting Equation 3.30 into 3.29 and rearranging the terms yields:

$$R = \underbrace{\left(\rho_{th,b} \frac{t_s}{A_{th}} + R_{ECR,s-s}\right)}_{a} n_s + \underbrace{2R_{ECR,p-s} - R_{ECR,s-s}}_{c}, \tag{3.31}$$

where the equation of the line $R = an_s + c$ outlined in Figure 3.50 can be identified. The slope of the line a is:

$$a = \rho_{th,b}\frac{t_s}{A_{th}} + \frac{r_{ECR,s-s}}{A_{th}}, \tag{3.32}$$

where specific contact resistance $r_{ECR,s-s}$ was used instead of $R_{ECR,s-s}$. Rearranging Equation 3.32 yields:

$$\frac{aA_{th}}{t_s} = \rho_{th,b} + \frac{r_{ECR,s-s}}{t_s}, \tag{3.33}$$

where the first term corresponds to the effective resistivity $\rho_{th,eff}$ and the equation can be therefore rewritten as:

$$\rho_{th,eff} = \rho_{th,b} + \frac{r_{ECR,s-s}}{t_s}. \tag{3.34}$$

It can be seen that the effective resistivity is a combination of the bulk resistivity of NGS, specific contact resistance at the sheet-to-sheet interface, and the thickness of the sheet. The contribution of the contact resistance decreases with increasing sheet thickness, which can be explained by fewer interfaces per unit length.

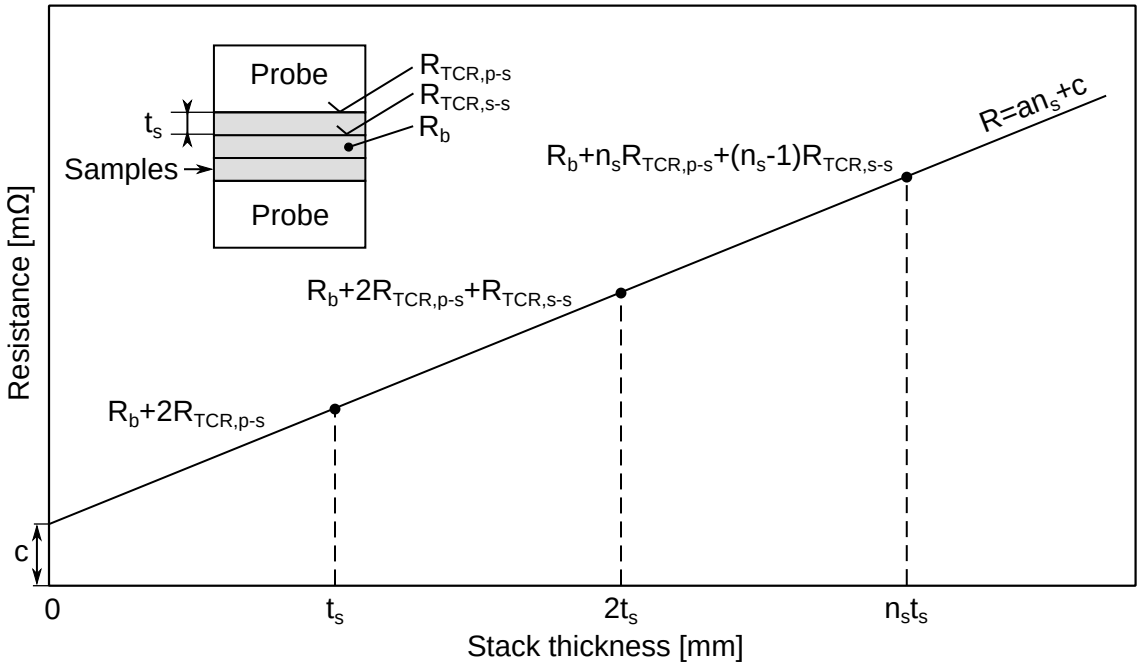

Figure 3.50: Illustration of the resistance of a stack of sheets during the four-probe measurement.

In the implementation of the theory, the slope of the line a was determined by fitting a line through the experimental data, and subsequently using it to calculate the effective resistivity as:

$$\rho_{th,eff} = \frac{aA_{th}}{t_s}. \tag{3.35}$$

In the two-thickness method, the contact resistance at the probe-to-sample interface can be determined from the intersection of the fitted line with the y axis, which was denoted c in the previous derivation. Equation 3.31 shows that in the case of stacks of samples, the intersect is not equal to the probe-to-sample contact resistance. Instead, it is reduced by the value of the sheet-to-sheet contact resistance. As illustrated in Figure 3.51, conclusions about the relative magnitude of the probe-to-sheet and sheet-to-sheet contact resistances can be made based on the magnitude and sign of the intersect. When the intersect is equal to zero, the sheet-to-sheet contact resistance is equal to double the probe-to-sheet resistance. Positive and negative values of the intersect mean that sheet-to-sheet contact resistance is smaller or larger than double of the probe-to-sheet contact resistance, respectively.

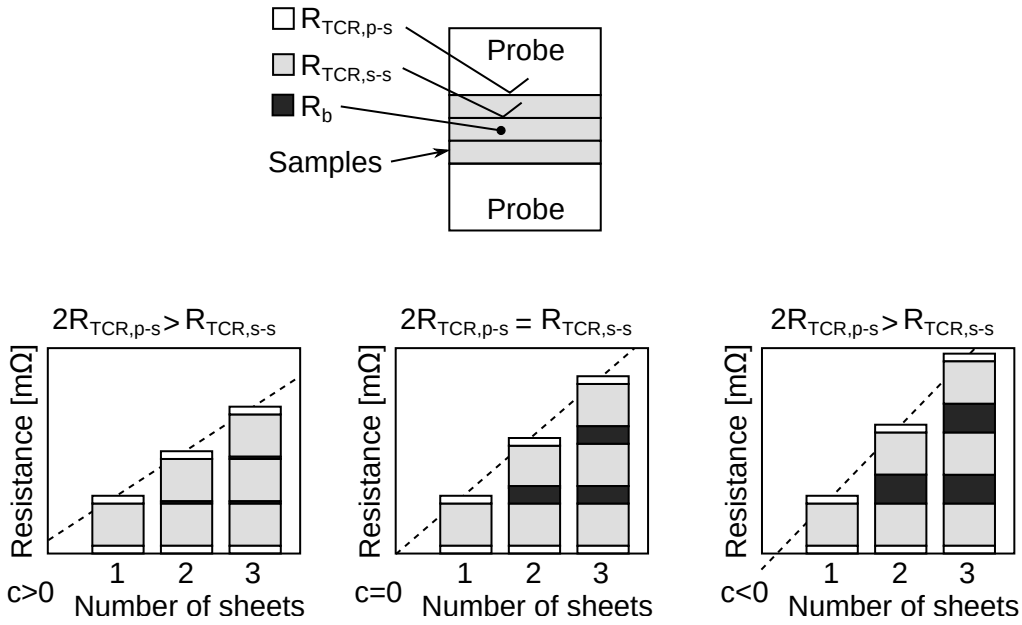

Figure 3.51: Illustration of the relationship between the intercept c and the relative magnitude of the sheet-to-sheet and probe-to-sheet contact resistances

At higher pressures, the thickness of the samples reduces, and the thickness value in Equation 3.35 should be therefore corrected to obtain reliable values. The relative increase in resistivity can be quantified as:

$$\frac{\rho_{th}}{\rho_{th,100kPa}} = \frac{\frac{aA_{th}}{(1-S)t_s}}{\frac{aA_{th}}{t_s}} = \frac{1}{1-S} = K_d, \tag{3.36}$$

where $\rho_{th,100kPa}$ is resistivity at the lowest reference pressure of 100 kPa, and S is the strain at the given pressure. In the last step in Equation 3.36, the term $\frac{1}{1-S}$ was identified to correspond to the density correction factor K_d, which was introduced in section 3.6. Figure 3.36 shows that the maximum value of K_d is approximately 1.06 for the 0.55 gcm^{-3} sheet at 1080 kPa, which means that correcting the values of resistivity for the change in thickness

would result in the maximum increase of 6 %. Since the relative uncertainty of resistivity for the $0.55\,\mathrm{gcm}^{-3}$ sheet at 100 kPa is 4 %, the correction was omitted as no significant improvement in the data quality can be achieved.

3.8.3 Section results

The results for the in–plane direction are shown together with the literature data in Figure 3.52. It can be seen that the present data agree with the literature except for the single data point by Qian at el. [92]. Based on the limited description of the method in [92], it is possible to assume that the anisotropy was not taken into account and the reported value is a combination of the through–plane and in–plane electrical conductivities. Over the measured range of densities 0.5 to $1.7\,\mathrm{g\,cm}^{-3}$ the electrical conductivity of NGS increases linearly with the density following the relationship $\sigma_{in} = 1167d - 193\,\mathrm{Scm}^{-1}$, where d is the sheet density in $\mathrm{g\,cm}^{-3}$. The present data are slightly lower than the literature data. The possible explanations are addressed later in the discussion section. Comparing the data for the three tested surface densities $70\,\mathrm{mg\,cm}^{-2}$, $140\,\mathrm{mg\,cm}^{-2}$, and $210\,\mathrm{mg\,cm}^{-2}$ does not reveal any trend and the through–plane electrical conductivity can be therefore considered independent of the sheet thickness. The data by Wei et al. [28] suggest that the in–plane electrical conductivity increases rapidly beyond $1.7\,\mathrm{g\,cm}^{-3}$ and does not follow the linear trend seen at the lower densities. Verification of this trend was not possible because the forming pressure required for manufacturing the high density samples exceeded the capacity of the equipment used in this work.

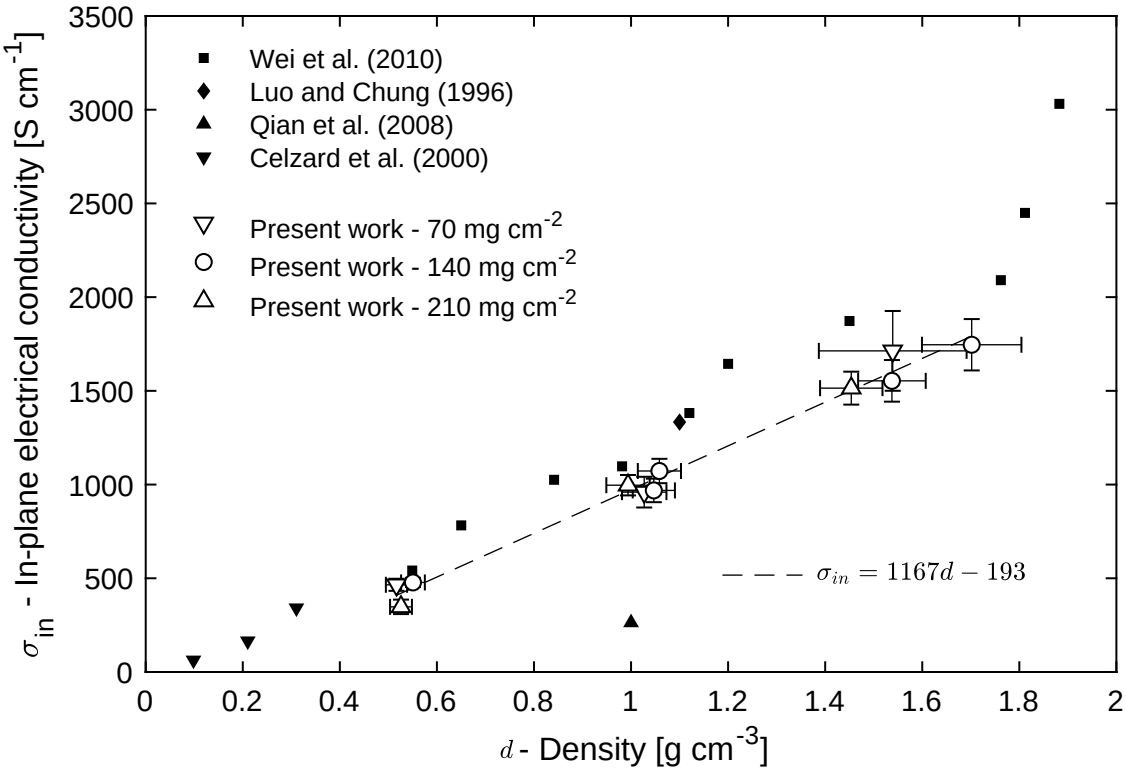

Figure 3.52: In–plane electrical conductivity as a function of density. The literature and present data are represented by solid and hollow symbols, respectively.

The present through–plane electrical conductivity data together with the literature data are shown in Figure 3.53. The through–plane electrical conductivity decreases with density and increases with pressure. The latter trend can be seen in Figure 3.54 where the through–plane electrical conductivity was plotted against the pressure. At 100 kPa the decrease with density is linear, while at higher pressures the trend is slightly convex. The increase in the through–plane electrical conductivity with pressure is higher at pressures below 400 kPa and lowers at higher pressures.

Since the data for different surface densities (and therefore various sheet thicknesses) do not show the distribution shown in Figure 3.42, the sheet-to-sheet contact resistance is not considered to significantly contribute to the effective conductivity. Analyzing the the intercept of the linear fits with the y-axis c showed values scattered between 0 mΩ and 5 mΩ, which suggests that the sheet-to-sheet contact resistance is comparable to, or lower, than the double of probe-to-sheet contact resistance.

The present data for through–plane electrical conductivity at 1080 kPa agree well with the data by Chen and Chung [80] at 460 kPa. The values by Celzard [90] at no compression show higher values than the data by Chen and Chung [80], which is contrary to the trends observed in this work, and it is therefore expected that the difference is either due to a measurement error, different sample material (impurity content, flake size, apparent density

of ENG particles d_{ENG}, etc.), or the measurement methods. The single data point by Luo and Chung [91] at 1.1 $\mathrm{gcm^{-3}}$ and no compression is approximately 15 $\mathrm{Scm^{-1}}$ higher than the present data at 100 kPa. The lack of measurement details in [91] prevents the explanation of the difference. Both Celzard [90] and Luo and Chung [91] did not explicitly report that the samples were measured at no compression. However, they used silver paint to attach the terminals to the samples, which is expected to make the measurement under compression impossible because the terminals would interfere with the compression platens. Since using silver paint for attaching the terminals is expected to eliminate the probe-to-sheet contact resistance, the higher values in [90] and [91] can be related to the inclusion of the contact resistance in [80]. The same argument does not apply to comparing the present data to Celzard et al. [90] and Luo and Chung [91] as the contribution of the contact resistance was eliminated by measuring stacks of sheets.

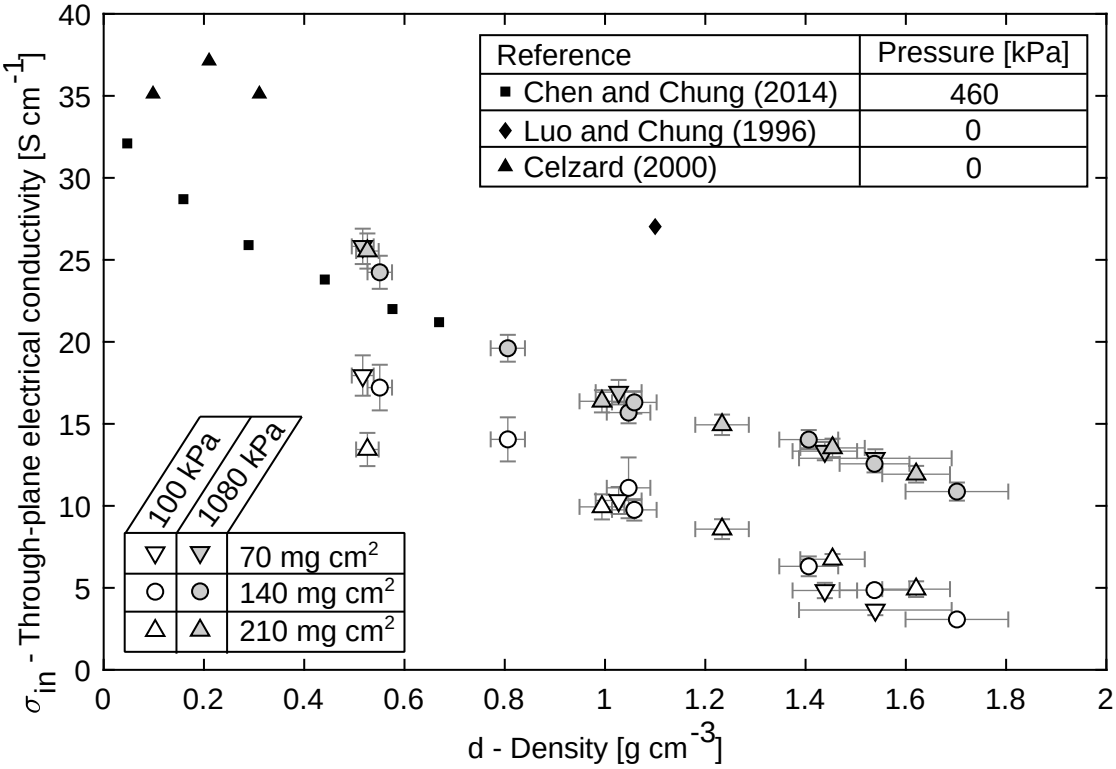

Figure 3.53: Through–plane electrical conductivity as a function of density. The literature and present data are represented by solid and hollow symbols, respectively.

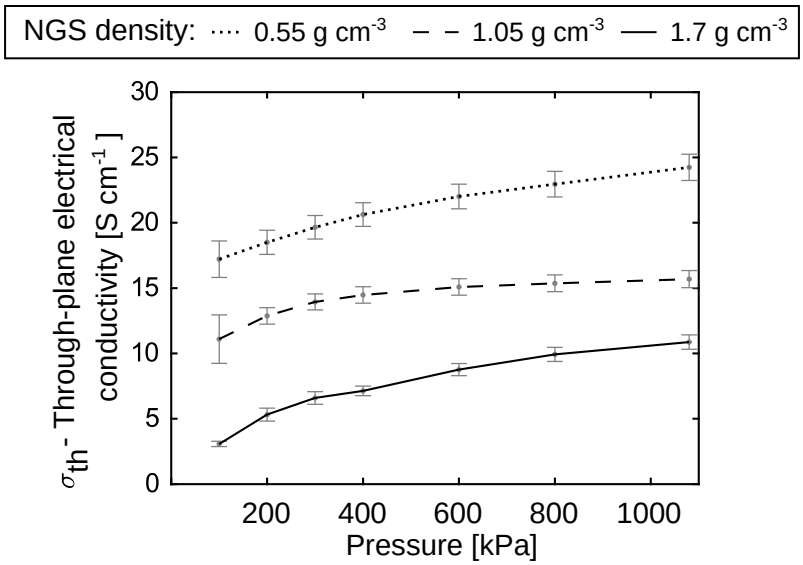

Figure 3.54: Through–plane electrical conductivity as a function of compression pressure

To make the results easy to reuse by other researchers, an explicit compact mathematical relationship between the measured properties and the relevant parameters was sought. The best fit of the in–plane electrical conductivity σ_{in} as a function of NGS density d is a simple linear function that was determined as:

$$\begin{gathered}\sigma_{in} = 1.167 \cdot 10^5 d - 1.934 \cdot 10^4 \ [\mathrm{Sm}^{-1}] \quad (error = \pm 10\,\%) \\ d \in [0.5, 1.7] \mathrm{gcm}^{-3}.\end{gathered} \tag{3.37}$$

A comparison of the σ_{in} best fit with the measured data is shown in Figure 3.40. In the through–plane direction, the thermal conductivity is also a function of pressure p and the best fit was determined as:

$$\begin{gathered}\sigma_{th} = 2667 - 3806d + 4.111p + 2945d^2 - 1.795dp - 0.004019p^2 - 992d^3 + 0.9967d^2p - \\ 0.0003251dp^2 + 1.877 \cdot 10^6 p^3 \ \mathrm{Sm}^{-1} \quad (err = 150\,\mathrm{Sm}^{-1}) \\ d \in [0.5, 1.7] \mathrm{gcm}^{-3}, p \in [100, 1080] [\mathrm{kPa}].\end{gathered} \tag{3.38}$$

A comparison of the k_{th} best fit with the measured data is shown in Figure 3.41.

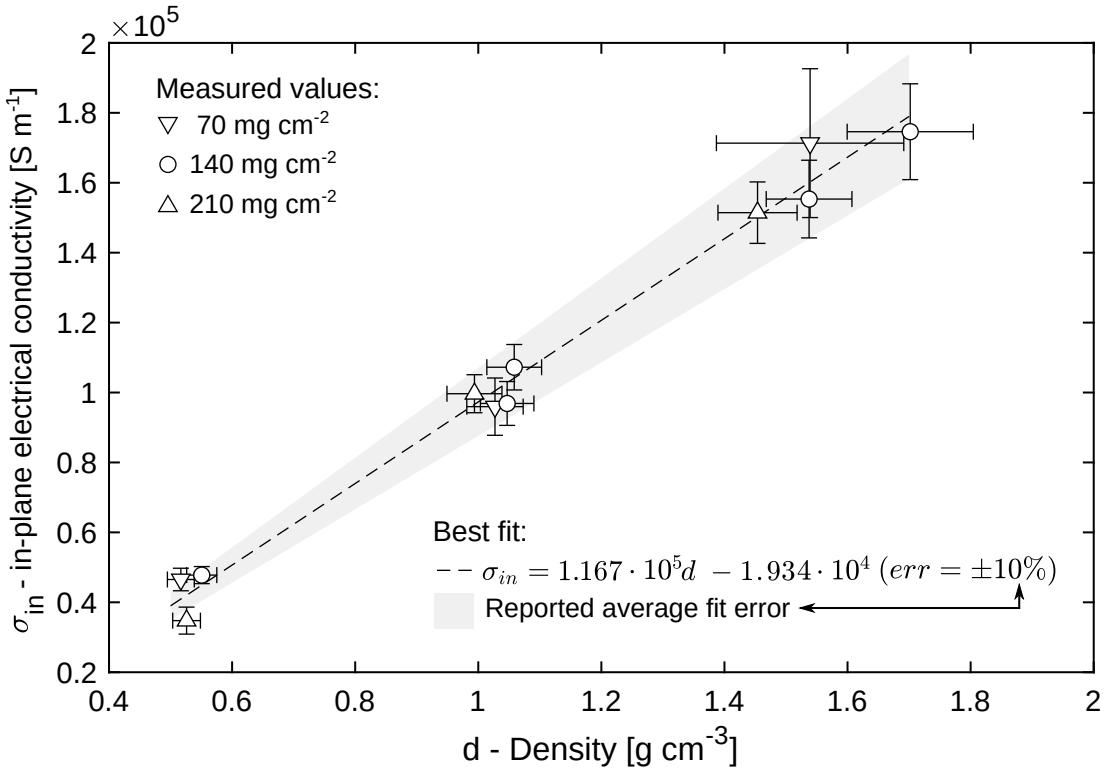

Figure 3.55: A comparison of the best fit of in–plane electrical conductivity with the measured data.

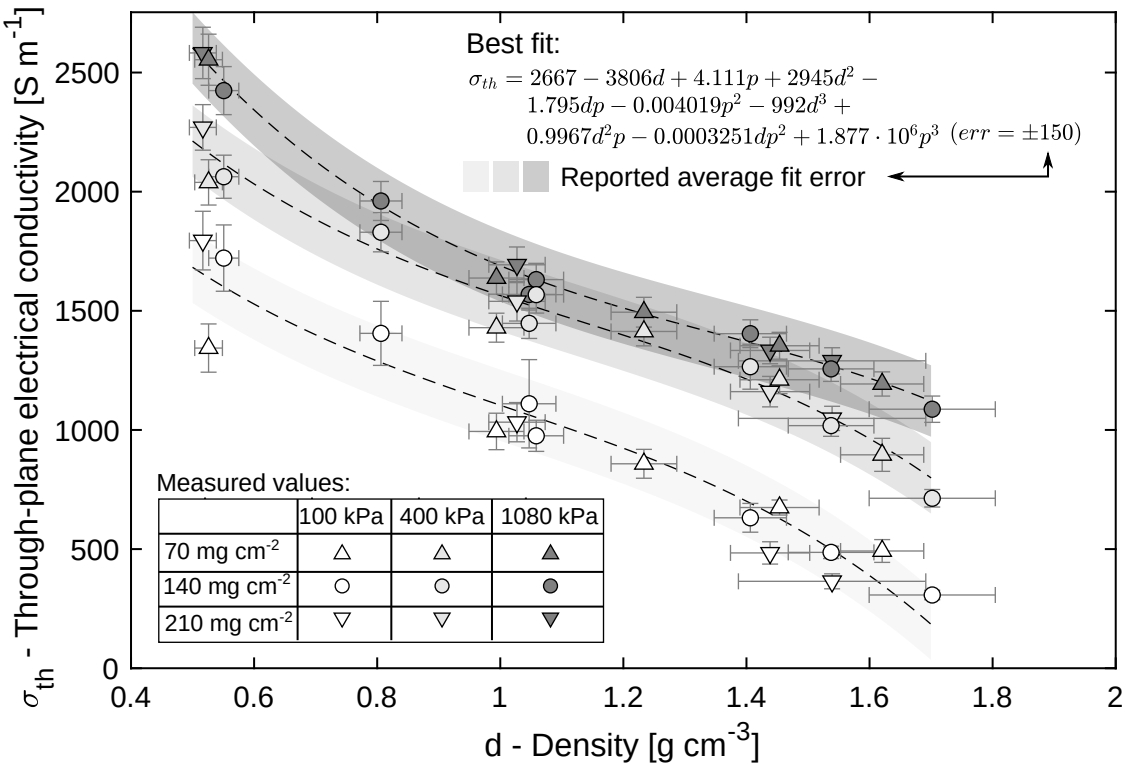

Figure 3.56: A comparison of the best fit of through–plane electrical conductivity with the measured data.

3.8.4 Section discussion

The trends in the measured data can be related to the structure of NGS, which was described in detail in section 3.3. The available literature sources generally relate the overall NGS electrical conductivity to the orientation of graphite basal planes, contact resistance between platelets, contact resistance between cell walls, and the electrical conductivity of cell walls. Because of the high crystalline structure of cell walls, their electrical conductivity approaches the theoretical conductivity of a graphite crystal, which was reported to be 12 500 to 26 000 Scm^{-1} in the *ab* directions, and 150 to 230 Scm^{-1} in the *c* direction [43, 71].

The measured values of the through–plane electrical conductivity of NGS are approximately one order of magnitude lower than that for a graphite crystal, which suggests that the contact resistance between the cell walls is significant. It should be also noted that the porosity of NGS varies from 76 to 25 % for the densities of 0.55 to 1.7 gcm^{-3} and the conduction path in both in–plane and through–plane directions is expected to be hindered by the pores filled with air. The SEM images in section 3.3 confirm that the cell walls are separated by voids and touch only at discrete locations. Additionally, macro-pores that are present in low-density sheets also limit the conduction, especially in the through–plane direction. With increasing density, the thickness and spacing of the platelets and cell walls decreases, which is expected to decrease the contact resistance between the cell walls and also between the platelets. However, since the through–plane electrical conductivity was seen to decrease with density, the decrease in the contact resistance is likely lower than the increased resistance caused by the change of the orientation of the cell walls.

By increasing the pressure, the spacing between the cell walls is expected to decrease even further, which in turn reduces the contact resistance and causes the through–plane conductivity to increase. A similar mechanism can cause the in–plane electrical conductivity to increase with pressure. However, the pressure dependence in the in–plane direction was not studied in this work. Considering the orientation of the cell walls and the fact that the in–plane thermal conductivity was found to be independent of the compression pressure, the pressure dependence of the in–plane electrical conductivity is expected to be low, or even negligible.

Attempts to measure the through–plane electrical conductivity at pressures as low as tens of kilo pascals have been made. The measurements showed very low repeatability and were not included in the results. Despite the low repeatability, the results suggest that the through–plane electrical conductivity at pressures imposed only by the weight of the copper probes can be up to one order of magnitude lower than at 100 kPa. The line fit intercept with y-axis *c* increased drastically at very low pressures, which suggests that the probe-to-sheet contact resistance was significantly higher than the sheet-to-sheet contact resistance.

The through–plane resistance of NGS was found to show hysteretic behavior, which is in agreement with the results of the compression tests in section 3.5. Increasing the compression

pressure causes the resistance to decrease in a non-linear manner. The decrease becomes smaller at higher pressures. Upon unloading, the resistance-versus-pressure curve does not follow the same path, and the resistance at any given pressure is lower than during the loading step. The difference between the loading and unloading steps is more pronounced at lower pressures. During the periods of constant pressure, the resistance drifted towards lower values, which can be partially explained by the viscous behavior of NGS under compression. However, after the initial exponential drop, the resistance was decreasing continually and did not reach a steady state even after one hour. A scale analysis ruled out the possibility of the decrease being due to the temperature increase cause by Joule heating. It was assumed that a relaxation at the probe-to-sheet interface can cause the resistance drift. This phenomenon was previously reported in the literature [93, 94, 95].

The complex behavior of the through–plane electrical conductivity at very low pressures requires an accurate measurement method to deconvolute all the competing factors. The four probe method is not expected to be able to offer the required accuracy. Instead, a modified version of the four point probe method is suggested for the future measurements. To account for the effect of pressure, the probes can be embedded in an electrically insulating compression platen. Methods for accounting for the anisotropy have been developed and experimentally validated [96, 97].

3.8.5 Section conclusions

The in–plane and through–plane electrical conductivity were measured in the density range from 0.5 to 1.7 $\mathrm{g cm^{-3}}$. In the in–plane direction, the conductivity increases with density linearly from approximately 400 $\mathrm{Scm^{-1}}$ at 0.5 $\mathrm{g cm^{-3}}$ to 1700 $\mathrm{Scm^{-1}}$ at 1.7 $\mathrm{g cm^{-3}}$ and can be approximated by the relationship $\sigma_{in} = 1167d - 193\,\mathrm{Scm^{-1}}$, where d is the free-standing NGS density in $\mathrm{g\,cm^{-3}}$. In the through–plane direction, the conductivity at 100 kPa compression pressure decreases from approximately 16 $\mathrm{Scm^{-1}}$ at 0.5 $\mathrm{g cm^{-3}}$ to 3 $\mathrm{Scm^{-1}}$ at 1.7 $\mathrm{g cm^{-3}}$, and by increasing the pressure to 1080 kPa it increases by 56 % at 0.5 $\mathrm{g cm^{-3}}$ and 263 % at 1.7 $\mathrm{g cm^{-3}}$. Based on the measurements of samples at three surface densities, the electrical conductivity of NGS was concluded to be independent of the sheet thickness. The contribution of the sheet-to-sheet ECR to the overall through–plane electrical conductivity was concluded to be negligible and its magnitude was deemed to be comparable or smaller than the double of the probe-to-sheet contact resistance. The unsuccessful measurements at very low pressures, which were not included in the report due to low repeatability, indicate that the free-standing through–plane electrical conductivity can be up to one order of magnitude lower than that at 100 kPa, and this trend should be investigated in the future work.

Both the density and pressure dependence arise from the changes in the structure of NGS. With increasing density, the cell walls–whose electrical conductivity is strongly anisotropic–become progressively more oriented in the direction perpendicular to the compression direction, which leads to an increase in the in–plane and a decrease in the through–

plane electrical conductivity. The increase in density also causes the spacing between the cell walls to reduce, which leads to a reduced contact resistance between the cell walls. However, the effect on the overall through–plane conductivity is most likely smaller in comparison with the change in the orientation because the through–plane electrical conductivity was seen to decrease with density. The increase of electrical conductivity with increasing compression pressure is due to the reduction of the contact resistance between the cell walls. The through–plane electrical conductivity of low-density sheets is also expected to be affected by the presence of macro pores.

The four probe method in the present configurations can be used to measure the in–plane electrical conductivity in the relaxed state, and the through–plane electrical conductivity at pressures higher than 100 kPa. To measure the pressure dependence of the in–plane electrical conductivity and the through–plane electrical conductivity at low pressures, it is suggested to investigate the possibility of modifying the four point probe method by embedding the pin probes into an insulating compression platen.

3.9 Coefficient of thermal expansion

In the context of thermal management of electronics, the coefficient of thermal expansion (CTE) is an important quantity for evaluating the reliability of the devices. When two parts made of materials with different CTE are attached to each other and periodically heated and cooled, the different dimension change results in stresses that cause a cumulative damage, and in some cases can lead to a failure of the component. The goal of this section is to measure and report the in–plane and through–plane CTE of NGS to provide a reliable data source for evaluating of the reliability of NGS heat sinks. In other applications such as fuel cells or flow batteries, the CTE data are necessary for addressing the thermomechanical stresses that arise from an expansion of the compressed stack.

Thermal expansion of a graphite crystal is anisotropic and temperature dependent [43, 71, 98]. In the *c* direction, the CTE increases drastically from zero at 0 K to approximately $25 \times 10^{-6}\,\mathrm{K}^{-1}$ at room temperature, and then further increases at a lower rate to approximately $37 \times 10^{-6}\,\mathrm{K}^{-1}$ at 2000 °C. In the *ab* directions, the CTE decreases from a near-zero negative value at 0 K to the minimum of $-1.8 \times 10^{-6}\,\mathrm{K}^{-1}$ after which it increases, intersects the zero axis at 400 °C, and reaches the value of $1.5 \times 10^{-6}\,\mathrm{K}^{-1}$ at 2000 °C.

3.9.1 Previous work

Mag-isa et al. [99] measured the in–plane CTE of a graphite crystal sample prepared from a natural graphite flake by mechanical cleaving. The sample was 40 nm thick, 110 µm long, and 67 µm wide. The measurement method involved mounting the sample in a bulged shape on a silicone substrate and measuring the change of the sample length using white light interferometry. The in–plane CTE varied from -1.8×10^{-6} to $-0.7 \times 10^{-6}\,\mathrm{K}^{-1}$ in the temperature range from 25 to 225 °C.

Many of the publications on NGS [51, 100, 39, 101] list the low thermal expansion coefficient as an advantage, or give a broad range of typical values. However, a comprehensive study of the thermal expansion of NGS is missing. NGS manufacturers reported values ranging from -0.4×10^{-6} to $0 \times 10^{-6}\,\mathrm{K}^{-1}$ in the in–plane direction, and 25×10^{-6} to $28 \times 10^{-6}\,\mathrm{K}^{-1}$ in the through–plane direction. Norley et al. [33] studied laminated and compression molded composites based on NGS. The reported value of the in–plane CTE for the laminated composites was $-0.77 \times 10^{-6}\,\mathrm{K}^{-1}$ and that for the compression molded composites was 3×10^{-6} to $24 \times 10^{-6}\,\mathrm{K}^{-1}$ in the in–plane direction and 9×10^{-6} to $41 \times 10^{-6}\,\mathrm{K}^{-1}$ in the through–plane direction. The reported values are a combination of the CTE of NGS and the polymer material used to make the composites.

3.9.2 Experimental method

The measurements were performed using a TA Instruments TMA Q400 thermo-mechanical analyzer shown in Figure 3.57a. For the in–plane measurements, rectangular samples 10 mm

wide and 15 to 29 mm long were cut from the calendered sheets described in section 3.1, and measured as shown in Figure 3.57b. For the through–plane measurements, square samples 10 mm wide were used and stacked to achieve the minimum recommended sample height of 5 mm as shown in 3.57c. Each of the measurement consisted of i) heating the sample to 100 °C at the rate of 4 °Cmin^{-1}, ii) keeping the temperature constant for 10 min, iii) cooling the sample to the room temperature at the rate dictated by natural convection from the chamber, and repeating the i)-iii) steps at least three times. An example of the raw data is shown in Figure 3.58. In some cases the measurements were left to run overnight or over weekends to measure as many cycles as possible. The probe compression force was set to 0.1 N, and nitrogen gas was introduced in the furnace at the flow rate of 50 mLmin^{-1}. The cooling rate in the measurements performed later in the study was increased by flowing compressed air on the outside of the furnace. This allowed reducing the measurement time, which was previously limited by the low heat transfer rate during the cooling phase.

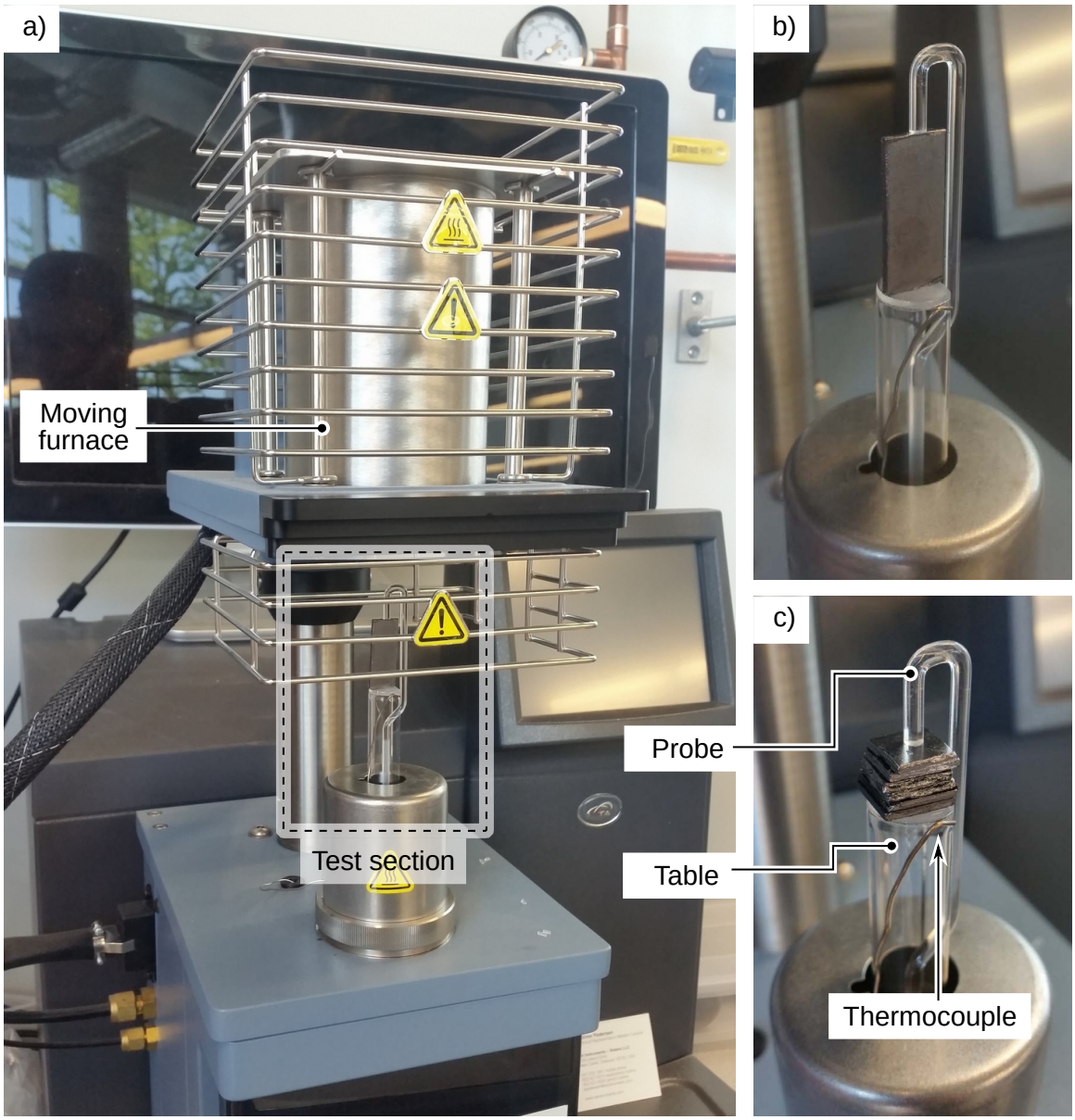

Figure 3.57: a) A photograph of the TMA Q400 machine with the test section highlighted by the dashed line. In b) and c) the test section is showed with the sample for in–plane and through–plane measurements, respectively.

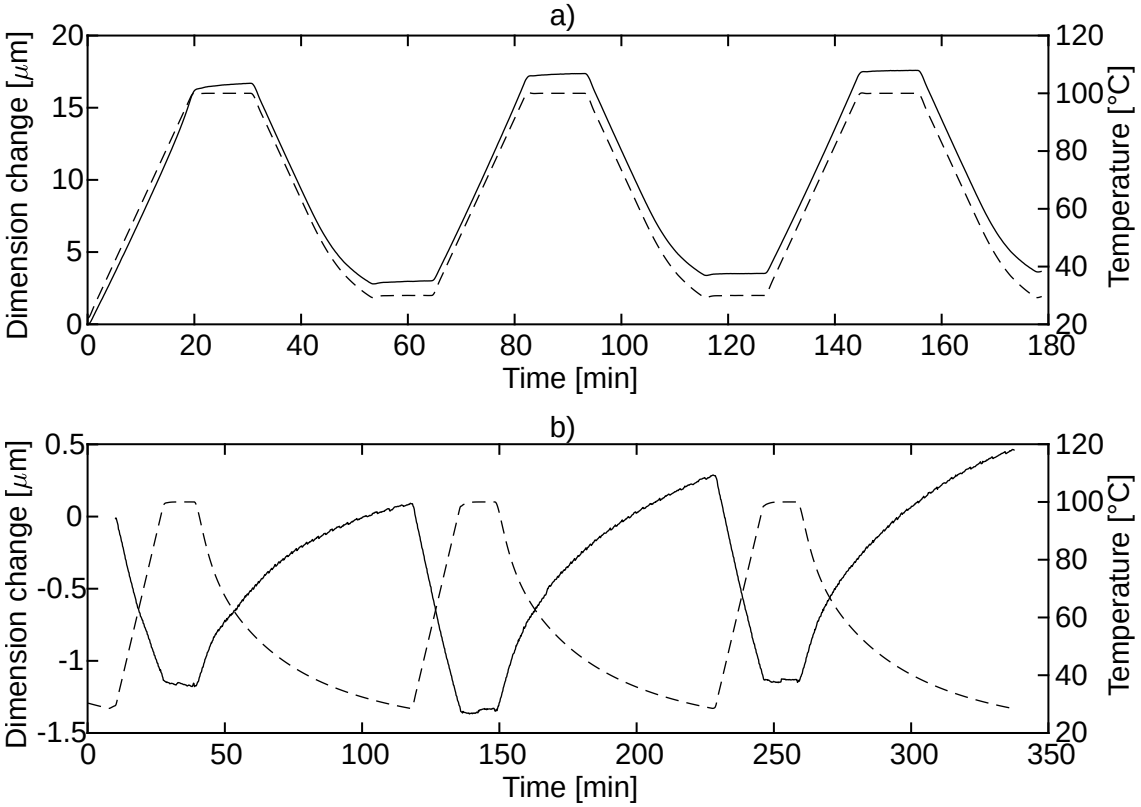

Figure 3.58: A sample of the raw data for the $1.05\,\mathrm{gcm}^{-3}$ $140\,\mathrm{mgcm}^{-2}$ sample in a) through–plane and b) in–plane direction. In a) the cooling rate was increased by flowing compressed air around the furnace to reduce the measurement time. The solid lines represent the dimension change, and the dashed lines represent the temperature.

3.9.3 Data processing

To obtain the CTE, the raw data were plotted in the dimension-versus-temperature plot as shown in Figure 3.59 and a line fit in the range 35 to 95 °C was determined for each of the cycles. The CTE values were calculated by dividing the slope of the line by the sample dimension. The final reported value of CTE is a mean value of all the cycles whose R^2 value is larger than 0.9. The criterion for the R^2 value was necessary to eliminate poor measurements arising from inevitable vibrations and other disturbances that occurred during the data collection period. The raw data files and the implementation of the data processing method is available in [62]

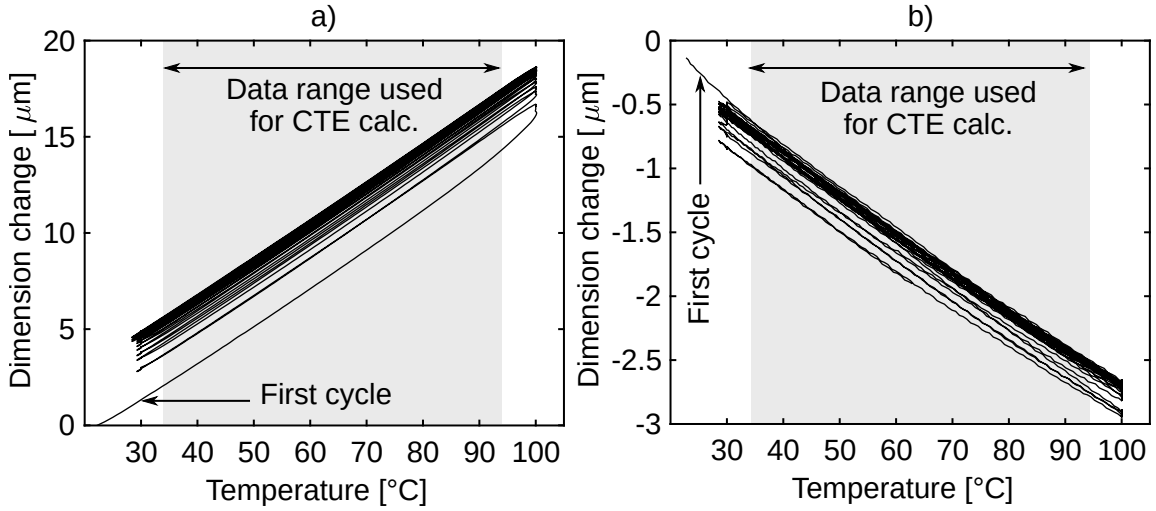

Figure 3.59: A plot of dimension change as a function of temperature for the 1.05 $\mathrm{gcm^{-3}}$ 140 $\mathrm{mgcm^{-2}}$ sample in a) through–plane and b) in–plane direction.

3.9.4 Section results

The results of the through–plane and in–plane CTE measurements are shown in Figures 3.60 and 3.61, respectively. Thermal expansion of NGS is anisotropic and density dependent. In the through–plane direction, CTE is relatively large, positive, and increases with density from approximately $10 \times 10^{-6}\,\mathrm{K^{-1}}$ at 0.5 $\mathrm{gcm^{-3}}$ to $33 \times 10^{-6}\,\mathrm{K^{-1}}$ at 1.7 $\mathrm{gcm^{-3}}$. The increase of the through–plane CTE is higher at low densities (0.5 to 1 $\mathrm{gcm^{-3}}$) and reduces beyond 1 $\mathrm{gcm^{-3}}$.

In the in–plane direction, CTE is very low, negative, and its magnitude increases with increasing density from approximately $-0.6 \times 10^{-6}\,\mathrm{K^{-1}}$ at 0.5 $\mathrm{gcm^{-3}}$ to $-1.4 \times 10^{-6}\,\mathrm{K^{-1}}$ at 1.7 $\mathrm{gcm^{-3}}$. Similarly to the through–plane direction, the rate of change with density appears to change at 1 $\mathrm{gcm^{-3}}$. However, the high uncertainty and spread of the low-density data, which arises from the very low dimension change, limits the strength of the conclusions.

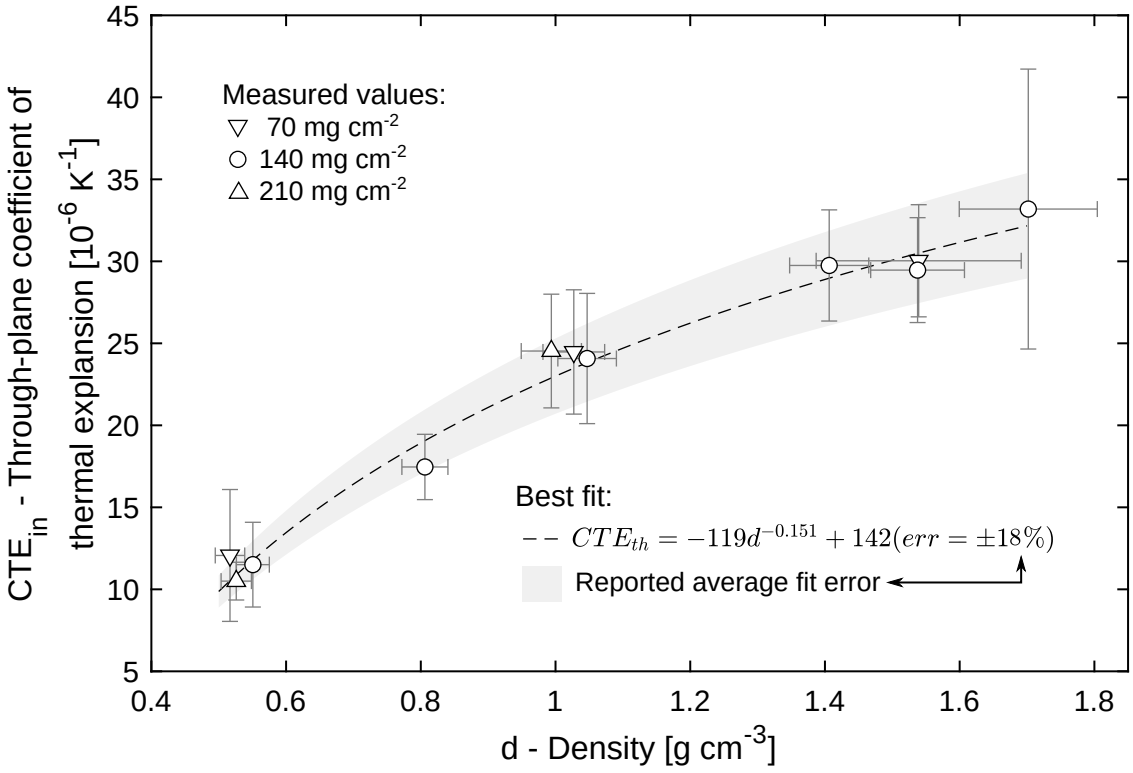

Figure 3.60: The results of through–plane CTE measurements.

The distribution of the circular and triangular symbols in Figures 3.61 and 3.61 is random, which suggests that the CTE is independent of the sheet thickness. It should be reminded here that the thickness of the sheet is proportional to the surface density, which was reported in all the figures.

The equations of best fits were calculated and shown in Figures 3.61 and 3.60 to allow other researchers to easily reuse the results. The through–plane CTE at a given density can be evaluated using the relationship:

$$\begin{gathered} CTE_{th} = -119d^{-0.151} + 142 \ \cdot 10^{-6} \ [\mathrm{K}^{-1}] \quad (error = \pm 18\,\%) \\ d \in [0.5, 1.7] \mathrm{gcm}^{-3}. \end{gathered} \tag{3.39}$$

The in–plane CTE can be evaluated using the relationship:

$$\begin{gathered} CTE_{th} = -0.132d^{3.46} - 0.6 \ \cdot 10^{-6} \ [\mathrm{K}^{-1}] \quad (error = \pm 0.2 \cdot 10^{-6} \mathrm{K}^{-1}) \\ d \in [0.5, 1.7] \mathrm{gcm}^{-3}. \end{gathered} \tag{3.40}$$

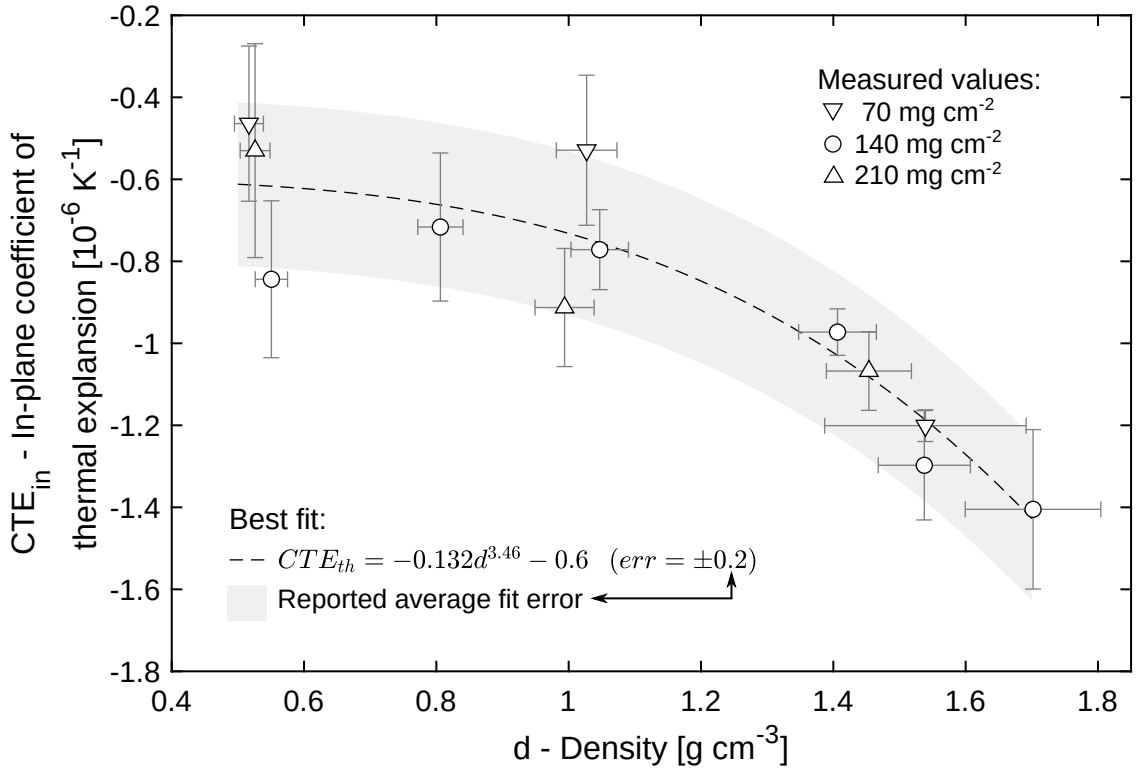

Figure 3.61: The results of in–plane CTE measurements.

3.9.5 Section discussion

The anisotropy and density dependence of the thermal expansion of NGS arises from the structure of the material. The orientation of graphite cell walls is expected to be the main factor for the overall CTE, but the size and spacing of cell walls are also relevant factors. At very low densities (less than $0.2\,\mathrm{gcm^{-3}}$), the CTE of NGS is assumed to be isotropic because of the random orientation of cell walls. With increasing density, the cell walls become oriented perpendicular to the compression direction, which makes the CTE anisotropic. At high densities, CTE is expected to approach the crystal properties.

A comparison of the measured values with the CTE of a graphite crystal is shown in Figure 3.62. At room temperature, the CTE of a graphite crystal is approximately $-1.8 \times 10^{-6}\,\mathrm{K^{-6}}$ in the *ab* directions and $26 \times 10^{-6}\,\mathrm{K^{-1}}$ in the *c* direction. The CTE of NGS at the highest measured density ($-1.5 \times 10^{-6}\,\mathrm{K^{-1}}$ at $1.7\,\mathrm{gcm^{-3}}$) is slightly higher (lower in magnitude) than the crystal value in *ab* directions, which confirms the expectation. In the through–plane direction, the CTE of the $1.7\,\mathrm{gcm^{-3}}$ sample is $33 \times 10^{-6}\,\mathrm{K^{-1}}$, which is $7 \times 10^{-6}\,\mathrm{K^{-1}}$ or 27 % higher that the crystal value in the *c* direction. However, the difference lies within the uncertainty limit. If future measurements confirm the values higher than the CTE of a graphite crystal the difference can be attributed to the expansion of the air in the pores, or the residual intercalation agent in the structure of graphite.

The possible contribution of the expansion of air in the pores to the overall through–plane CTE was estimated to be $74 \times 10^{-6}\,\mathrm{K}^{-1}$ (see Appendix C), which is much higher than the observed $7 \times 10^{-6}\,\mathrm{K}^{-1}$ difference. The calculation assumed an unconstrained expansion of the air, which is in reality limited by the stiffness of the surrounding NGS structure. The calculation also assumed that all pores are closed and the air remains in the pores. Since the pores were reported to be mostly open (see section 3.3), the latter assumption may be invalid, but the permeability of NGS must also be accounted for. Low permeability would result in the air not being able to escape the pores and the closed pores approximation would become relevant.

During the NGS manufacturing process, graphite flakes are treated with exfoliation agent whose molecules penetrate between the graphite layers. Upon exfoliation, most of the agent is removed, but a small amount may remain in the graphite structure and cause a change in the c direction CTE.

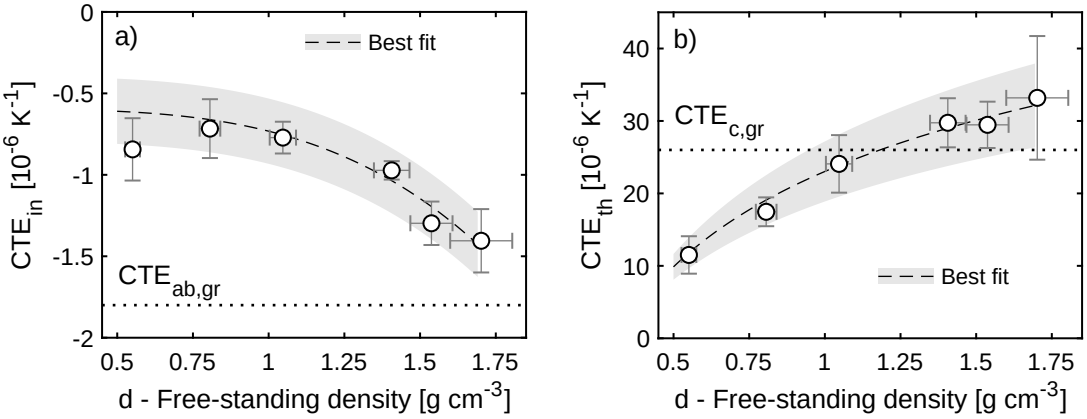

Figure 3.62: A comparison of the measured data with the CTE of a graphite crystal taken from [43, 71, 98]. Only the $140\,\mathrm{mgcm}^{-2}$ measurements are shown to improve the clarity of the plot

In practical applications, NGS is often impregnated with polymer materials to achieve better mechanical or sealing properties. Preliminary tests showed that impregnating a $1\,\mathrm{gcm}^{-3}$ NGS with Hernon HPS 991 sealant (Poly(methyl methacrylate)) increases the through–plane CTE from $24\,\mathrm{K}^{-1}$ to $106\,\mathrm{K}^{-1}$, and the in–plane CTE from $-0.8 \times 10^{-6}\,\mathrm{K}^{-1}$ to $1.6 \times 10^{-6}\,\mathrm{K}^{-1}$.

A comparison of the CTE of NGS with that of other materials that are common in the electronics cooling field is shown in Figure 3.63. The through–plane CTE of NGS is always higher than that of alumina (Al_2O_3), but for aluminum and copper it can be both larger or smaller depending on the density. At approximately $1\,\mathrm{gcm}^{-3}$, the through–plane CTE of NGS is identical to that of aluminum. For higher densities the through–plane CTE of NGS is higher and vice versa. For copper, the equivalency point is at approximately $0.7\,\mathrm{gcm}^{-3}$. The in–plane CTE of NGS is very low in comparison with all the materials included in Figure

3.63. Theoretically, NGS offers the possibility for the CTE to be tailored to match the other parts in the assembly. However, this is possible only for the through–plane direction, only if pure NGS is used, and only if other properties such as thermal conductivity at the given density are satisfactory for the thermal or other performance metrics.

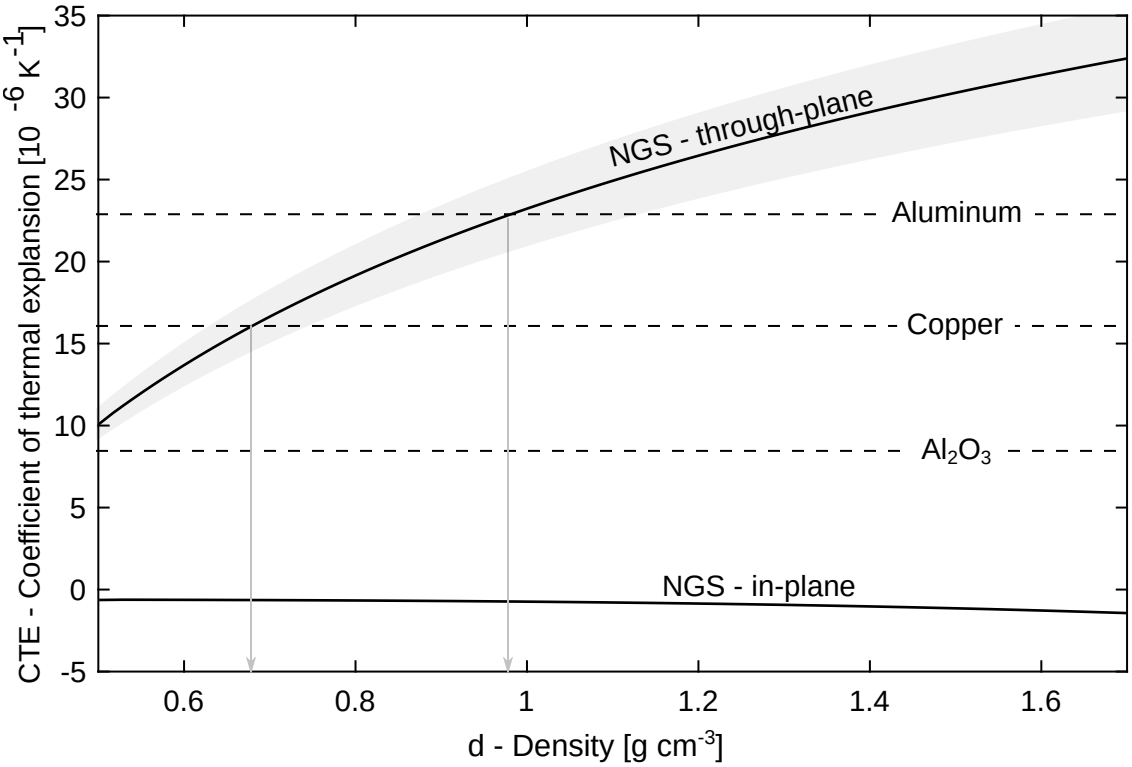

Figure 3.63: Comparison of the CTE of NGS and other materials

3.9.6 Section conclusions

The in–plane and through–plane CTE of NGS was measured in the range of densities from 0.55 to 1.7 $\mathrm{gcm^{-3}}$. In the through–plane direction, the increases with density from approximately $10 \times 10^{-6}\,\mathrm{K^{-1}}$ at $0.5\,\mathrm{gcm^{-3}}$ to $33 \times 10^{-6}\,\mathrm{K^{-1}}$ at $1.7\,\mathrm{gcm^{-3}}$, following the relationship $CTE_{th} = -118.8d^{-0.151} + 142$ where d is the free-standing density in $\mathrm{gcm^{-3}}$. In the in–plane direction, the CTE is negative, and its magnitude increases with increasing density from approximately $-0.6 \times 10^{-6}\,\mathrm{K^{-1}}$ at $0.5\,\mathrm{gcm^{-3}}$ to $-1.4 \times 10^{-6}\,\mathrm{K^{-1}}$ at $1.7\,\mathrm{gcm^{-3}}$ following the relationship $CTE_{in} = -0.132d^{3.46} - 0.6$. In comparison with aluminum and copper, the in–plane CTE of NGS is much lower, but the through–plane CTE is in the same order and can be higher or lower depending on the density of NGS. The anisotropy of the CTE in the in–plane and through–plane directions arises from the anisotropy of the graphite crystal in ab and c directions. The orientation of the cell walls in the NGS structure is expected to be the dominating factor dictating the overall CTE. Preliminary

results showed that by impregnating NGS with a polymer-based sealant, the through–plane CTE can increase by 340 %, and the negative in–plane CTE can become positive and double in magnitude.

3.9.7 Future work

Mounting the long in–plane samples in the way shown in Figure 3.61b is inherently unstable and prone to error. The TMA Q400 offers the possibility to use the tension sample holder, which is more appropriate for the in–plane measurements. However, the sample holder can only accommodate sample less than 1 mm in thickness, which only allowed measuring NGS at high density. The values obtained using the tension sample holder did not agree with those obtained using the standard expansion probe. For the future work, it is suggested to investigate the reason for the data mismatch and potentially modify the tension holder so that in can carry samples with thicknesses up to several millimeters.

3.10 Emissivity

In this section, the spectral and total hemispherical emissivity is measured for four samples of NGS. The change of emissivity with the sheet density is related to the surface structure and electrical conductivity.

3.10.1 Previous work

The scientific literature contains several studies of emissivity of graphitic materials, but emissivity of NGS has not been previously studied. Since graphite is often used in high temperature applications for its chemical stability, most of the available data is for temperatures of hundreds of degrees Celsius and higher, which is not relevant to heat sinks that typically operate at temperatures below 100 °C. Manufacturers of NGS reported the values of emissivity in the range of 0.4 at 400 °C [102] and 0.65 at 1500 °C [103].

Autio and Scala [104] studied the normal spectral emissivity of polycrystalline and pyrolytic graphite in the temperature range 800 to 1200 °C and observed a low temperature dependence. The authors discovered that the orientation of graphite crystals correlates with the normal spectral emissivity, and provided a qualitative explanation using the Hagen-Rubens equation (derived in Ref. [105]), which is given as:

$$\epsilon_\lambda = 4\sqrt{\frac{c}{\lambda\sigma}\pi\epsilon_0}, \tag{3.41}$$

where λ is the wavelength, σ is the DC electrical conductivity, c is the speed of light, and ϵ_0 is the permittivity of vacuum. The Hagen-Rubens equation suggests that with increasing electrical conductivity, emissivity decreases. The electrical conductivity of pyrolytic graphite is anisotropic, and its magnitude is dictated by the preferred orientation of the graphite basal planes [90, 91, 80]. The authors of [104] argued that the normal emissivity of a surface is affected by the electrical conductivity in the direction perpendicular to the normal vector as this direction coincides with the electric field vector of the electromagnetic wave leaving the surface. To prove the hypothesis, the authors prepared and measured samples of pyrolytic graphite that were cut in a crystal wafering unit so that the basal planes were aligned at varying angles with respect to the normal of the measured surface. The emissivity of the sample with the basal planes oriented parallel to the surface was lower than the one of the sample with the basal planes oriented perpendicular to the surface. The results supports the validity of the Hagen-Rubens equation. The higher electrical conductivity in the direction parallel to the surface results in a lower normal emissivity and vice versa. In all measurements of pyrolytic graphite the surface was mechanically polished, and the effect of the surface structure was not studied. The measurements of the polycrystalline graphite samples revealed that the polished surfaces had lower emissivity in comparison

with the rough ones. Another study by Wang et al. [106] also concluded that polishing of polycrystalline graphite resulted in lower values of emissivity.

Roh et al. [107] measured the thermal emissivity of a composite material consisting of graphite flakes and organic binder. The composites were manufactured by mixing graphite flakes with a binder, ball milling, compressing the samples at 80 MPa, and curing them at 1200 °C in a nitrogen atmosphere. Three samples with the alignment of graphite basal planes of 0°, 45°, and 90° were prepared and measured at 100 °C in a setup consisting of an infrared camera and a thermocouple. The sample surface was first polished using a sand paper and then using a 1 µm diamond polishing abrasive. The results showed a higher emissivity when the basal planes were oriented perpendicular to the surface, which is consistent with Autio and Scala [104].

3.10.2 Experimental method

In this study, four 5 x 5 cm samples with the density of 0.55 g cm^{-3}, 1.05 g cm^{-3}, 1.54 g cm^{-3}, and 1.7 g cm^{-3}, and the thickness of 2.76 mm, 1.43 mm, 0.96 mm, and 0.84 mm, respectively, were cut from the 140 mgcm^{-2} calendered sheets that were described in section 3.1. The measurements were made using the Surface Optics Corporation 400T Fourier Transform Infrared Reflectometer [108] (Figure 3.64) in accordance with the Method C of ASTM E408-13 Standard [109]. In the calibration process, the room was used as the black body, and a polished gold film as the reference for the spectral reflectivity (98 %). The samples were measured at room temperature and wavelengths ranging from 2 to 26 µm. Four measurements were made for each of the densities to capture the variation with the location and orientation of the sheet. The reflectometer outputs the near-normal-hemispherical spectral reflectivity at the accuracy of ±1 %. Both the raw and processed data are available in [62].

Figure 3.64: A photograph of a Surface Optics Corporation 400T Fourier Transform Infrared Reflectometer that was used for measuring the emissivity.

3.10.3 Section results

The total hemispherical emissivity integrated over the measured wavelengths (2 to 26 µm) decreases linearly from 0.52 at 0.55 g cm^{-3} to 0.39 at 1.7 g cm^{-3} as shown in Figure 3.65. The data can be approximated by the line fit:

$$\begin{gathered} \epsilon = -0.11d + 0.58 \quad (error = \pm 5\,\%) \\ d \in [0.5, 1.7]\mathrm{gcm}^{-3}, \end{gathered} \tag{3.42}$$

where d is the free-standing sheet density in g cm^{-3}.

The spectral emissivity shown in Figure 3.66 decreases with increasing wavelength and the rate of the decrease is higher at 2 to 6 µm wavelengths. The large error bars for the 1.05 g cm^{-3} sheet are due to the high variability in the measurements at different locations.

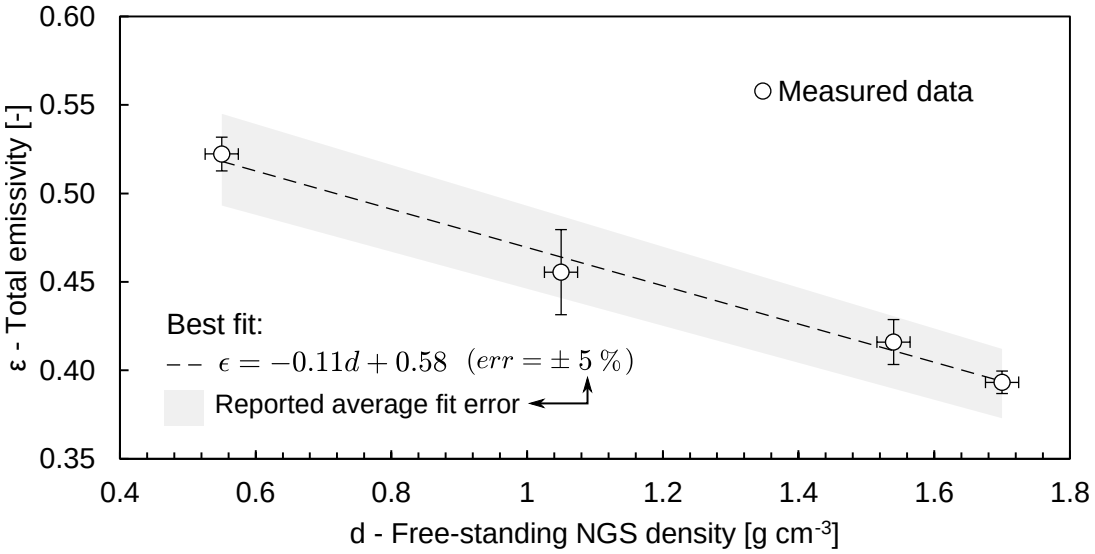

Figure 3.65: Total emissivity of four measured densities integrated over the 2 to 26 µm wavelength range.

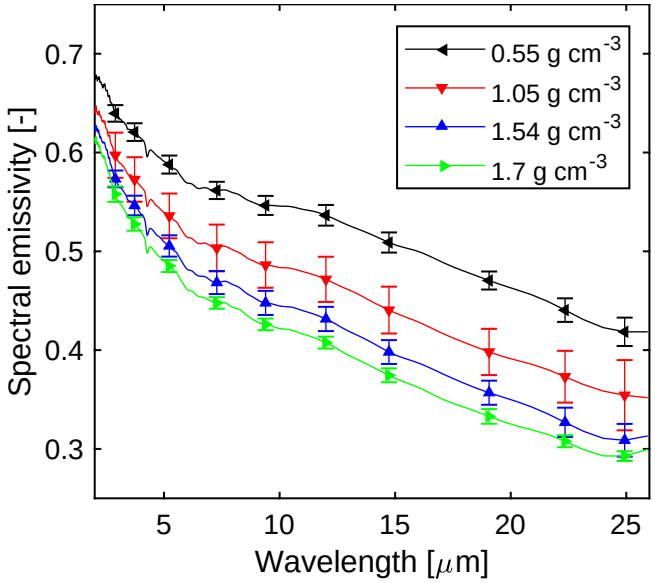

Figure 3.66: The average spectral emissivity of NGS at four measured densities. The symbols and error bars are shown only at several randomly selected locations. The shape of the curves is measured, not interpolated

The observed relationship between the emissivity and the density can be related to i) the electrical conductivity as suggested by Autio and Scala [104] and ii) the surface structure. According to the Hagen-Rubens equation (Equation 3.41) the emissivity is proportional to the square root of the inverse of the DC in–plane electrical conductivity ($\epsilon \propto \sqrt{\frac{1}{\sigma}}$). In Figure 3.67, this quantity is plotted against the density together with the emissivity data, and it can be seen that it follows the same decreasing trend. The in–plane electrical

conductivity of NGS was measured on samples that were prepared in the same batch as those for the present emissivity measurements, and it was found to follow the linear relationship $\sigma_{in} = 1167d - 193\,\mathrm{S\,cm^{-1}}$. The SEM images of the surface structure shown in Figure 3.67 reveal that the surface becomes progressively smoother with increasing density. The lowest density ($0.55\,\mathrm{g\,cm^{-3}}$) contains cracks and pores whose size is in the order of the measured wavelengths, and they can therefore act as small black bodies and increase the surface emissivity [104]. For the $1.05\,\mathrm{g\,cm^{-3}}$ density the cracks and pores appear to be mostly closed, and the two highest densities contain no pores or cracks. Based on the surface structure, the emissivity is expected to decrease with density, which is in an agreement with the measured data.

Both the increase in the in–plane electrical conductivity and smoothing of the surface correlate with the decrease of emissivity with increasing density. It is assumed that both factors contribute to the overall emissivity but quantifying their relative contribution was not within the scope of this work. It is possible to expect that the surface structure will have more pronounced effect at smaller wavelengths as the interaction of the electromagnetic waves with the surface is more complex.

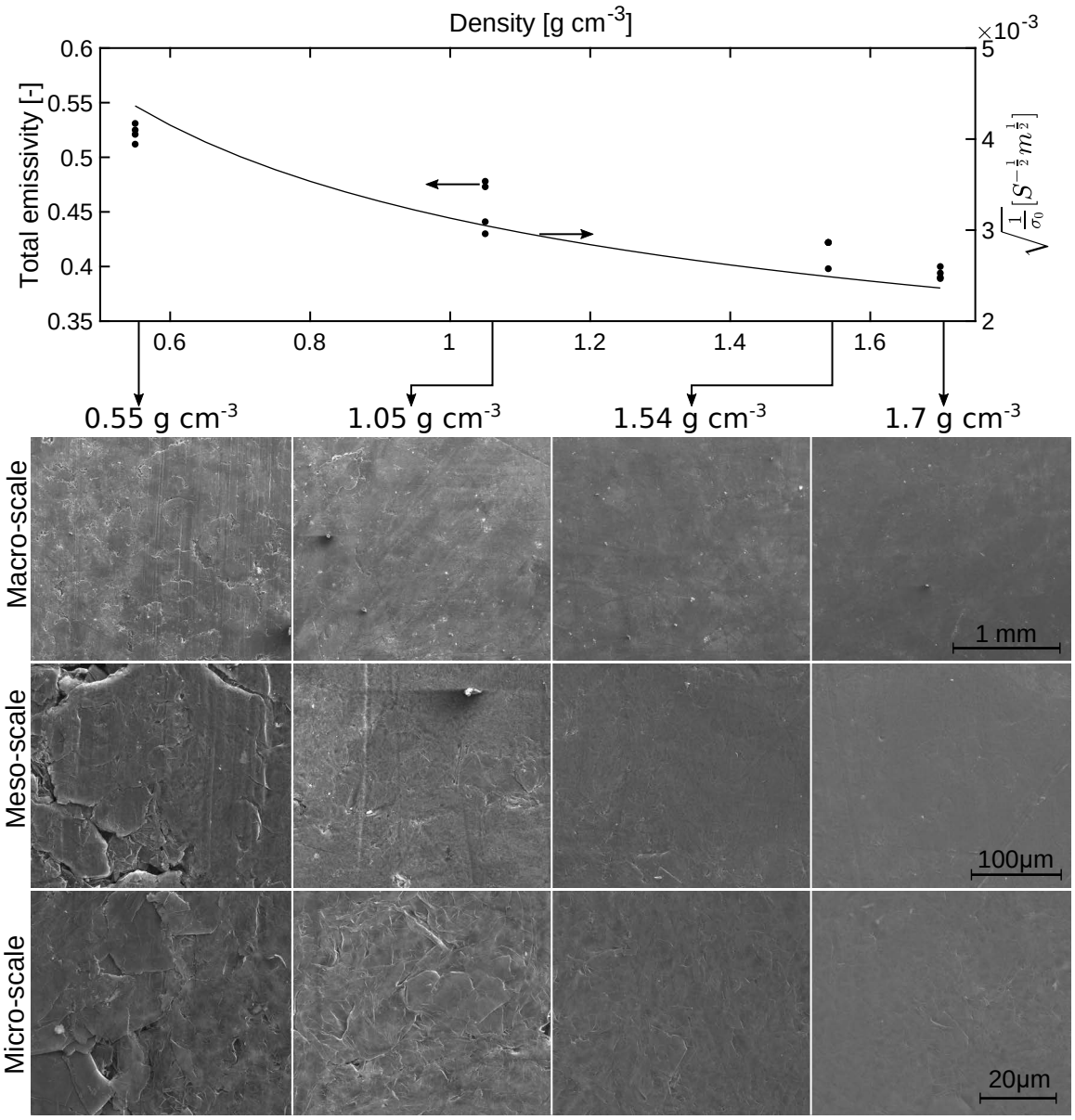

Figure 3.67: Top: A plot showing the measured total emissivity (solid circles, left axis) and the square root of the inverse of the in–plane electrical conductivity (solid line, right axis). Bottom: Microscope images of the surface structure. The high-resolution version of the microscope images is available in [62].

To further investigate the claim of Autio and Scala [104] who noted that for graphite the Hagen–Rubens equation holds only qualitatively, a comparison of the predicted and measured values of the spectral emissivity was compiled in Figure 3.68. The black and green dashed lines correspond to the predicted spectral emissivity that was calculated by evaluating Equation 3.41 using the in–plane electrical conductivity of the $0.55\,\mathrm{g\,cm^{-3}}$ and $1.7\,\mathrm{g\,cm^{-3}}$ samples. The predicted values match the experimental data only at high wave-

lengths for the 1.7 g cm^{-3} sheet. At wavelengths smaller than 3 µm, the emissivity prediction for the 0.55 g cm^{-3} sheet reaches non-physical values larger than one. At higher wavelengths, the Hagen-Rubens equation under predicts the measured values. The discrepancy between the predicted and measured values is expected because the Hagen-Rubens equation was derived for highly conductive isotropic metals [105].

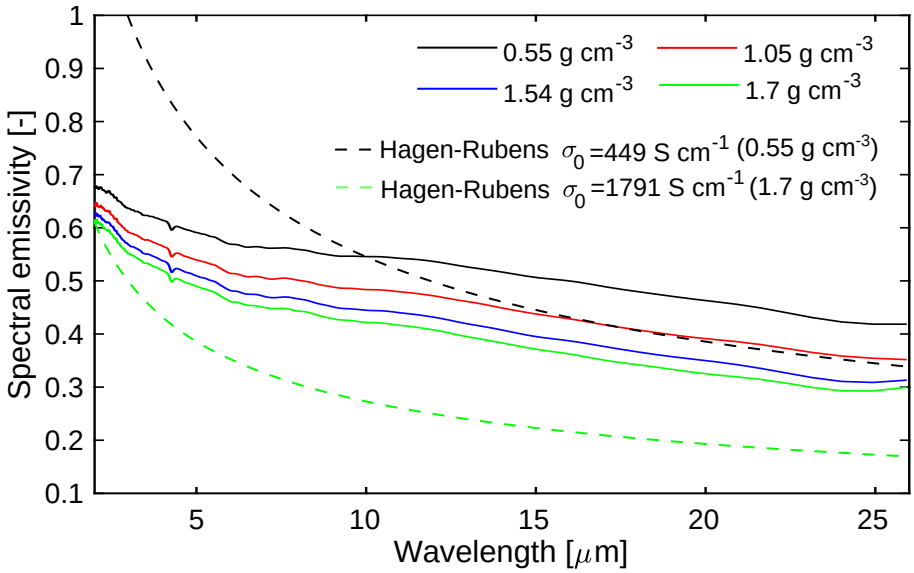

Figure 3.68: Measured (solid) and predicted (dashed) spectral emissivity as a function of density. The black and green dashed lines were calculated using the in–plane electrical conductivity of the 0.55 g cm^{-3} and 1.7 g cm^{-3} sheets, respectively.

A comparison of the present results with the two most relevant studies in the literature is shown in Figure 3.70. It is important to note that the materials, measurement methods, temperature, and surface finish of the samples in each of the studies were different which makes the comparison prone to inconsistencies. In both of the compared studies [104, 107], the authors prepared the samples so that the effect of the orientation of the graphite basal planes on the emissivity could be studied. In Figure 3.69, the average angle of the graphite basal planes ϕ is defined to unify the results. For polycrystalline graphite, ϕ is not relevant as the structure consists of randomly oriented graphite particles [43]. In the present study the orientation of the basal planes was inherently given by the calendering process and ϕ was always 0. It should be noted here that the average angle of graphite basal planes ϕ is not equivalent to the mean misalignment angle, which was reviewed and shown in Figure 3.6.

The spectral emissivity of NGS appears to be comparable to that of pyrolytic graphite at $15° < \phi < 90°$. The lowest and the highest values of emissivity shown in Figure 3.70 are those of the pyrolytic graphite at $\phi = 0°$ and polycrystalline graphite with rough surface, respectively. Pyrolytic graphite has the highest emissivity because of its high electrical conductivity (6250 S cm^{-1} [104]) and smooth surface. Polycrystalline graphite has the lowest

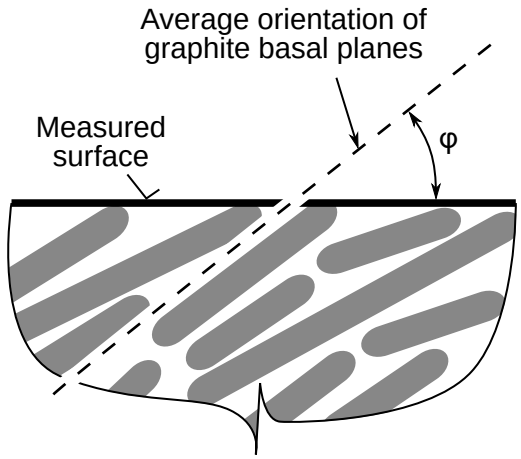

Figure 3.69: An illustration of the average angle of the graphite basal planes ϕ.

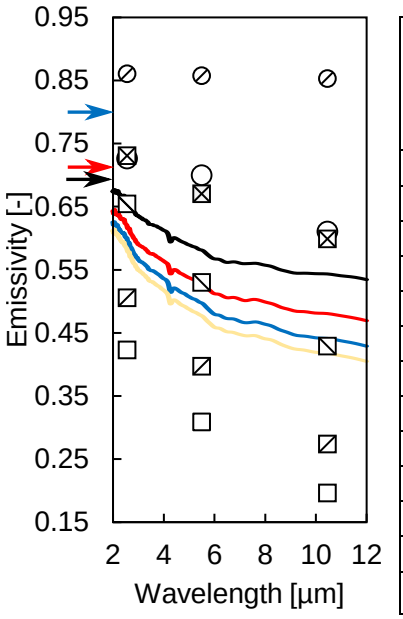

Symbol	Material	θ [°]	Surf. state	Temp. [°C]	Ref.
—	NGS 0.55 g cm^{-3}	0	calend	25	Present work
—	NGS 1.05 g cm^{-3}				
—	NGS 1.54 g cm^{-3}				
—	NGS 1.7 g cm^{-3}				
□	Pyrolytic	0	polish	1115	[6]
⊘		15			
⊠		35			
⊠		90			
○	Polycrystalline	-	polish	1174	
⊘		-	rough		
→	Natural graphite flakes w/ binder	0	polish	100	[12]
→		45			
→		90			

Figure 3.70: Comparison of the measured spectral emissivity with the data available in the literature. The extended legend on the right includes the material, average angle of the graphite basal planes ϕ (defined in Figure 3.69), surface state (calend = calendered), measurement temperature, and the reference number. The spectral data for [107] was not available therefore the arrows were used to symbolize the total emissivity.

emissivity because of its low electrical conductivity (328 to 1316 $\mathrm{S\,cm^{-1}}$ [104]) and rough surface.

The data for the natural graphite flake composite by Roh et al. [107] does not contain the spectral information. Therefore, only the total emissivity was shown using the arrows

on the left axis, and their position suggests that the emissivity is higher than that of NGS. The difference can be accounted to the effect of the binder.

3.10.4 Section conclusions

The total and spectral emissivity of NGS in the range of densities from 0.55 to 1.7 $\mathrm{g\,cm^{-3}}$ and wavelengths from 2 to 26 µm were measured at room temperature. The value of the total emissivity is decreasing with increasing density and can be approximated by the relationship $\epsilon = 0.11d + 0.58$ where d is the free-standing sheet density in $\mathrm{g\,cm^{-3}}$. The in–plane electrical conductivity and the surface structure were both found to be relevant factors affecting the emissivity, but their relative contributions could not be determined. Using the Hagen-Rubens equation with the value of the in–plane electrical conductivity cannot predict the spectral emissivity of NGS accurately.

While the reported data is expected to be satisfactory for designing heat transfer devices made of NGS, further work is necessary for a complete quantitative understanding of the surface emissivity of NGS. To provide a reliable comparison of the emissivity of various graphitic materials, a study using a single measurement method with well reported state of the sample surface is necessary.

3.11 Uncertainty

3.11.1 Density

The density was calculated as:

$$d = \frac{m}{tA} = \frac{m}{V}, \tag{3.43}$$

where m, t, A, and V are the sample mass, thickness, surface area, and volume, respectively. The uncertainty was calculated using the partial derivative method as:

$$u_d = \sqrt{\left(\frac{\partial d}{\partial m}u_m\right)^2 + \left(\frac{\partial d}{\partial V}u_V\right)^2} = \sqrt{\left(\frac{1}{V}u_m\right)^2 + \left(\frac{-m}{V^2}u_V\right)^2}, \tag{3.44}$$

where u_m and u_V are the uncertainties of mass and volume, respectively. The uncertainty of mass was determined as:

$$u_m = \sqrt{u_{m,d}^2 + \sigma_m^2}, \tag{3.45}$$

where $u_{m,d}$ is the scale accuracy of 0.0002 g [110], and σ_m is the standard deviation of the mass of the six measured samples. The uncertainty of the sample volume was calculated as:

$$u_V = \sqrt{\left(\frac{\partial V}{\partial t}u_t\right)^2 + \left(\frac{\partial V}{\partial A}u_A\right)^2} = \sqrt{(Au_t)^2 + (tu_A)^2}, \tag{3.46}$$

where u_t is the uncertainty of the sample thickness and u_A is the uncertainty of the sample area, where the former was determined as:

$$u_t = \sqrt{u_{t,d}^2 + \sigma_t}, \tag{3.47}$$

where $u_{t,d}$ is the micrometer accuracy of 0.0254 mm, and σ_m is the standard deviation of the thickness of the six measured samples. The uncertainty of the area was determined in the same way as described in section 3.11.2 using the burr size $b = 0.5$ mm.

3.11.2 Compression behavior

3.11.2.1 Thickness

The uncertainty of the thickness reading is a product of the subtraction of the two displacement values as seen in Equation 3.4. The uncertainty of the displacement reading is given by the manufacturer as :

$$u_y = \pm 5\,\mu\text{m}. \tag{3.48}$$

The base for determining the uncertainty of $y_0(F)$ was a set of calibration measurements during which no sample was in the mechanical tester. In Figure 3.71 the calibration measurements are represented by the gray curves. The overall uncertainty $u_{y_0}(F)$ is a combination of the machine accuracy u_y and the standard deviation of the values from the calibration

runs $\sigma_{y_0}(F)$. While u_y is a constant, the standard deviation of the calibration runs $\sigma_{y_0}(F)$ varies with the force, which can be seen by the varying vertical spacing of the gray curves in Figure 3.71 where the two sources of uncertainty were combined using the sum-of-squares method as:

$$u_{y_0}(F) = \sqrt{{u_y}^2 + \sigma_{y_0}(F)^2}, \tag{3.49}$$

and the result were plotted in Figure 3.71. The black solid line shows the value of $y_0(F)$ and the error bars show the uncertainty $u_{y_0}(F)$.

The uncertainty of the thickness was calculating according to the rules for addition of two random variables as:

$$u_t = \sqrt{(u_{y_0}(F))^2 + {u_y}^2} \tag{3.50}$$

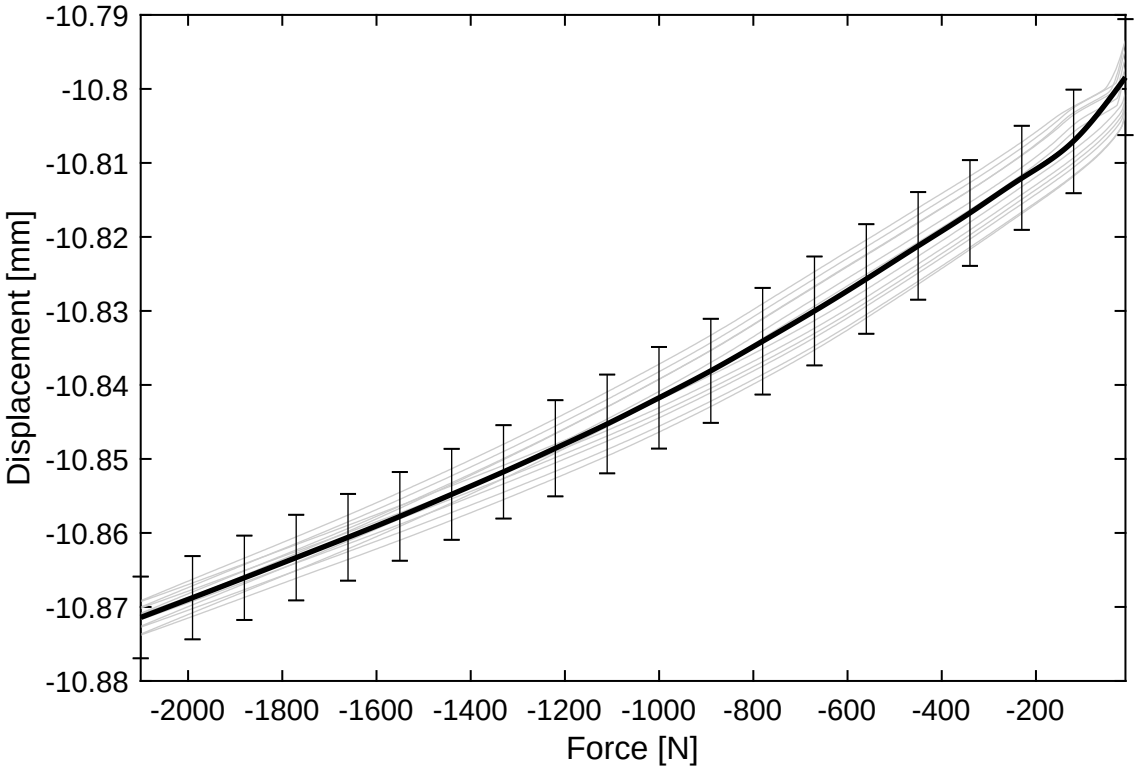

Figure 3.71: The gray lines are the multiple repetitions of measurements with no sample between the compression platens. The thick black line is the average value of displacement with no sample between the platens $y_0(F)$, and the error symbolize the magnitude of the thickness uncertainty.

3.11.2.2 Forming pressure

Forming pressure is defined as:

$$p_f = \frac{F_f}{A}, \tag{3.51}$$

where F_f is the forming force and A is the area of the shape to be formed. The uncertainty of forming pressure is

$$u_{p_f} = \sqrt{\left(\frac{\partial p_f}{\partial F_f} u_{F_f}\right)^2 + \left(\frac{\partial p_f}{\partial A} u_A\right)^2} = \sqrt{\left(\frac{1}{A} u_{F_f}\right)^2 + \left(\frac{-F_f}{A^2} u_A\right)^2}, \tag{3.52}$$

where u_{F_f} is the force uncertainty and u_A is the area uncertainty. The uncertainty of the force u_{F_f} is given by the load cell and its calibration. Due to a previous damage and subsequent repair, the load cell that was used for the measurement did not comply with the relevant ASTM E4 standard, and its accuracy was estimated by an application engineer to be $\pm 1\,\%$ of the full scale (3000N), which results in $u_{F_f} = \pm 30\,\mathrm{N}$.

The sample dimensions W and H were measured using a digital caliper prior to the measurement. Due to the lateral expansion that occurs as the result of compression the uncertainty of the area A had to be expanded to account for this phenomenon. The sample images (Figure 3.72) show that the sheet expands by approximately 0.5 mm on each side. This dimension is referred to as b. The nominal dimensions of the sample were set to be

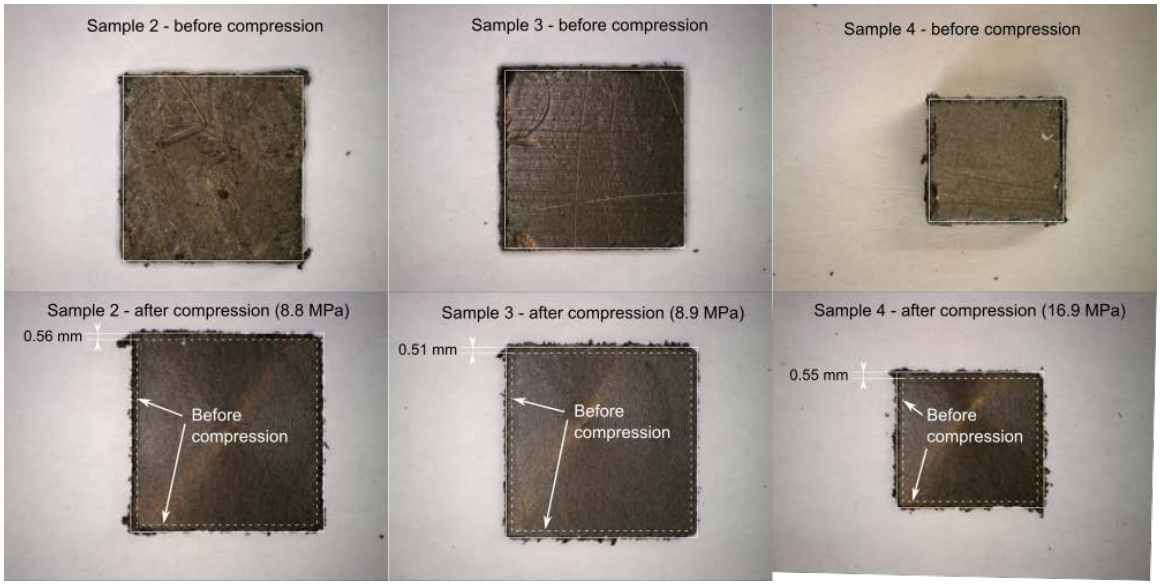

Figure 3.72: Images of the samples for the forming measurements before and after compression. The lateral expansion was included in the uncertainty of the results.

$$W' = W + b \tag{3.53}$$

$$H' = H + b \tag{3.54}$$

from which the nominal area is calculated as

$$A = W' \cdot H' \tag{3.55}$$

The uncertainty of the area was set to be

$$u_A = \frac{(W + 2b)(H + 2b) - WB}{2} \tag{3.56}$$

From Eq. 3.52 it was found that the dominating source of the pressure uncertainty is the sample area, which amplifies u_A. Increasing the sample area u_A would result in lower pressure uncertainty u_p, however, this would require increasing the compression force, which was already at the maximum limit of the machine (2100 N).

3.11.2.3 Pressure (in the low-pressure measurements)

The uncertainty of the pressure in the low-pressure compression part of this work was calculated analogically to the forming pressure. However, since the samples had a different shape, the parameters were adjusted. The size of the burr was estimated to be 0.5 mm. The uncertainty region of the samples is shown in Figure 3.73.

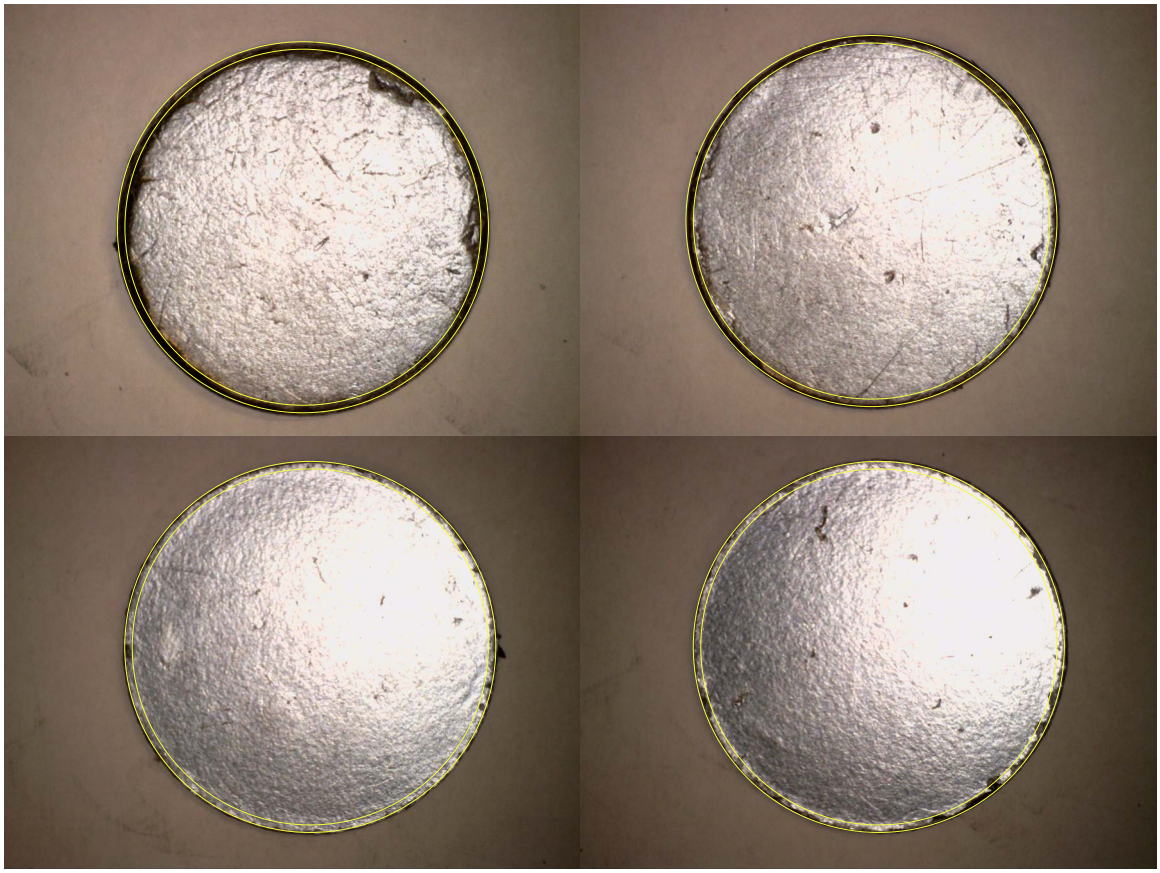

Figure 3.73: Photographs of the samples used for the low-pressure measurements with the area uncertainty region highlighted by the yellow circles. The density of the samples in the order top-left, top-right, bottom-left, bottom-right is 0.55 g cm^{-3}, 1.05 g cm^{-3}, 1.54 g cm^{-3}, and 1.7 g cm^{-3},respectively

3.11.2.4 Thickness ratio

In Figure 3.25c, the uncertainty of the average values of the t/t_0 ratio is a product of u_t and the standard deviation of the values σ_{t/t_0}, which arises from combining results for multiple samples and forming pressures. While the uncertainty of a single t/t_0 point is:

$$u_{t/t_0} = \sqrt{\left(\frac{1}{t_0}u_t(F)\right)^2 + \left(-\frac{t}{{t_0}^2}u_t(F)\right)^2}, \tag{3.57}$$

the uncertainty of the average value $\overline{t/t_0}$ was calculated as

$$u_{\overline{t/t_0}} = \sqrt{{\sigma_{t/t_0}}^2 + \left(\frac{1}{\overline{t_0}}u_t(F)\right)^2 + \left(-\frac{\overline{t}}{\overline{t_0}^2}u_t(F)\right)^2} \tag{3.58}$$

3.11.2.5 Strain

The uncertainty of both the viscous strain and the low-pressure compression strain was calculated using the same formula. The general definition of strain is:

$$S = \frac{t - t_0}{t_0} = \frac{\Delta t}{t_0}. \tag{3.59}$$

The two thicknesses in the numerator were considered to be independent random variables and the uncertainty of the numerator was therefore taken as the sum of variances, which translates to the following sum of squares expression:

$$u_{\Delta t} = \sqrt{{u_t}^2 + {u_{t_0}}^2}. \tag{3.60}$$

In the case of the viscous strain, in which the thicknesses in the numerator of Eq. 3.59 are evaluated at the same force, the uncertainty of t and t_0 are equal and Eq. 3.60 simplifies to:

$$u_{\Delta t} = \sqrt{2u_t^2}. \tag{3.61}$$

The final uncertainty is then calculated using the partial derivatives as:

$$u_{p_f} = \sqrt{\left(\frac{\partial S}{\partial \Delta t}u_{\Delta t}\right)^2 + \left(\frac{\partial S}{\partial t_0}u_{t_0}\right)^2} = \sqrt{\left(\frac{1}{t_0}u_{\Delta t}\right)^2 + \left(-\frac{\Delta t}{{t_0}^2}u_{t_0}\right)^2} \tag{3.62}$$

3.11.2.6 Compression modulus

The uncertainty of the tangent modulus at a given pressure p was determined in two steps. First the average value within the interval given by the load cell uncertainty $[p - \frac{u_F}{A}, p + \frac{u_F}{A}]$ was calculated for every measurement. The maximum and minimum values of the averages were then used to calculate the mean value and the error.

3.11.3 Thermal conductivity and diffusivity

The uncertainty of the thermal conductivity u_k was calculated as:

$$u_k = \sqrt{u_{k,m}^2 + \sigma_k^2}, \tag{3.63}$$

where $u_{k,m}$ is the measurement accuracy of the TPS machine and σ_k is the standard deviation of the measurements. The value of $u_{k,m}$ reported by the manufacturer is 5 % of the reading [85].

The uncertainty of diffusivity u_α was calculated identically to the conductivity as:

$$u_\alpha = \sqrt{u_{\alpha,m}^2 + \sigma_\alpha^2}, \tag{3.64}$$

where $u_{\alpha,m}$ was set to be 5 % of the reading. However, the equipment manual [85] does not specify the accuracy of the diffusivity. For a detailed analysis of the measurement uncertainty the implementation of the data processing within the Thermal Analyzer would have to be known. As this software is proprietary, an advanced uncertainty analysis was not performed.

The uncertainty of pressure u_p was determined as:

$$u_p = \sqrt{\left(\frac{\partial p}{\partial F} u_F\right)^2 + \left(\frac{\partial p}{\partial A} u_A\right)^2} = \sqrt{\left(\frac{1}{A} u_F\right)^2 + \left(\frac{F}{A^2} u_A\right)^2}, \tag{3.65}$$

where p is the pressure, F is the force, and A is the sample area. The uncertainty of the force gauge reading is given as 0.1 % of the full scale [111]. However, due to the viscous behavior of NGS, which was described in section 3.5, the uncertainty of the force reading was expanded to $u_F = 10\,\mathrm{N}$.

3.11.4 Electrical conductivity

The propagation of the uncertainty through the data processing steps starts with the line fitting. The uncertainty of the line slope u_a was determined from the confidence interval of the slope, which was calculated using the *confint* function in Matlab with which the confidence level was set to 68.27 %. The error of the resistance and voltage probe distance is not accounted for in the *confint* implementation. To calculate the uncertainty of the cross-section area, the uncertainty of the thickness and width were set to $u_t = 0.05\,\mathrm{mm}$ and $u_W = 0.5\,\mathrm{mm}$. The magnitudes were chosen based on the highest value of the standard deviation of the micrometer thickness measurements, and based on a conservative estimation of the dimension variation caused by the imperfect edges that are created when cutting NGS by a razor blade, respectively. The uncertainty of the cross-section area was calculated as:

$$u_A = \sqrt{\left(\frac{\partial A}{\partial W} u_W\right)^2 + \left(\frac{\partial A}{\partial t} u_t\right)^2} = \sqrt{(t u_W)^2 + (W u_t)^2}. \tag{3.66}$$

The uncertainty of the resistivity u_ρ was calculated as:

$$u_\rho = \sqrt{\left(\frac{\partial \rho}{\partial a} u_a\right)^2 + \left(\frac{\partial \rho}{\partial A} u_A\right)^2} = \sqrt{(A u_a)^2 + (a u_A)^2} \tag{3.67}$$

The electrical conductivity is the inverse of resistivity and therefore the uncertainty of electrical conductivity u_σ is:

$$u_\sigma = \sqrt{(\frac{\partial \sigma}{\partial \rho} u_\rho)^2} = \sqrt{(-\rho^{-2} u_\rho)^2} = \rho^{-2} u_\rho. \tag{3.68}$$

The uncertainty of the pressure was calculated in an identical way as described in section 3.11.3.

3.11.5 Coefficient of thermal expansion

The uncertainty of CTE was calculated by grouping the values from all the cycles and calculating the standard deviation. This approach does not reflect the accuracy of the device. The manufacturer reported 0.1 % precision of CTE measurement and 15 nm resolution of the displacement measurements [112]. However, the information on the absolute accuracy of the length measurement was not provided [113], which limited the possibility to perform an advanced uncertainty analysis. For this work the uncertainty arising from the standard deviation was considered dominating but the future work should verify this assumption.

3.11.6 Emissivity

The uncertainty of the total emissivity u_ϵ was calculated as

$$u_\epsilon = \sqrt{u_{\epsilon,m}^2 + \sigma_\epsilon^2}, \tag{3.69}$$

where $u_{\epsilon,m}$ is the measurement accuracy of the device (1 %) and σ_ϵ is the standard deviation of the four measurement repetitions. The 1 % measurement accuracy $u_{\epsilon,m}$ does not account for the propagation of the uncertainty through the spectral averaging process. The ASTM standards do not provide a clear guideline on how to address the propagation. It is likely that the error is amplified during the spectral averaging process, however, addressing this issue was out of the scope of this work.

Chapter 4

Design and manufacturing of NGS heat sink prototypes

In section 1.7 the published literature on NGS heat sinks was reviewed. The two most relevant previously reported approaches to building a parallel plate NGS heat sink are visualized in Figure 4.1a and 4.1b. In the approach by Marotta et al. [35] (Figure 4.1a), fins and spacers are stacked to form a heat sink made solely of NGS. In the approach by Shives el al. [36] (Figure 4.1b), NGS fins were bonded to a copper base with machined slots to form a hybrid heat sink. The copper base was used to improve the poor spreading due to the low through–plane thermal conductivity. All the heat sinks in this thesis were built by stacking L-shape sheets in an alternating fashion to form a staggered plate fin topology, as is shown in Figure 4.1c.

The design of the heat sinks in this thesis was aimed at a proof-of-concept demonstration. The goal was not to build a heat sink with an optimal performance. The topology was selected based on a qualitative evaluation of heat transfer, which is described below. The review of the previous work suggested that the low through–plane thermal conductivity of NGS may render NGS heat sinks not feasible for applications in which the heat source is smaller than the heat sink width. This possibility was reflected in the design by prioritizing the applications in which the heat source width matches that of the heat sinks. In the later stages of present research, the performance of large-scale heat sinks was investigated. Multiple uncertainties had to be reflected in the design. The significance of the poor spreading in the through–plane direction and the sheet-to-sheet TCR were not known and therefore a conservative approach was adopted, in which the contribution of the two phenomena was minimized.

Figure 4.2 shows a qualitative heat transfer analysis of the heat sink design in the previous and present work. In the design by Marotta et al. [35] (Figure 4.2a), the heat that enters the spacers must travel in the through–plane direction and cross the sheet-to-sheet interface, which can lead to an increased thermal resistance. Adopting a similar design in the present work was therefore not considered desirable. In the design by Shives el al. [36],

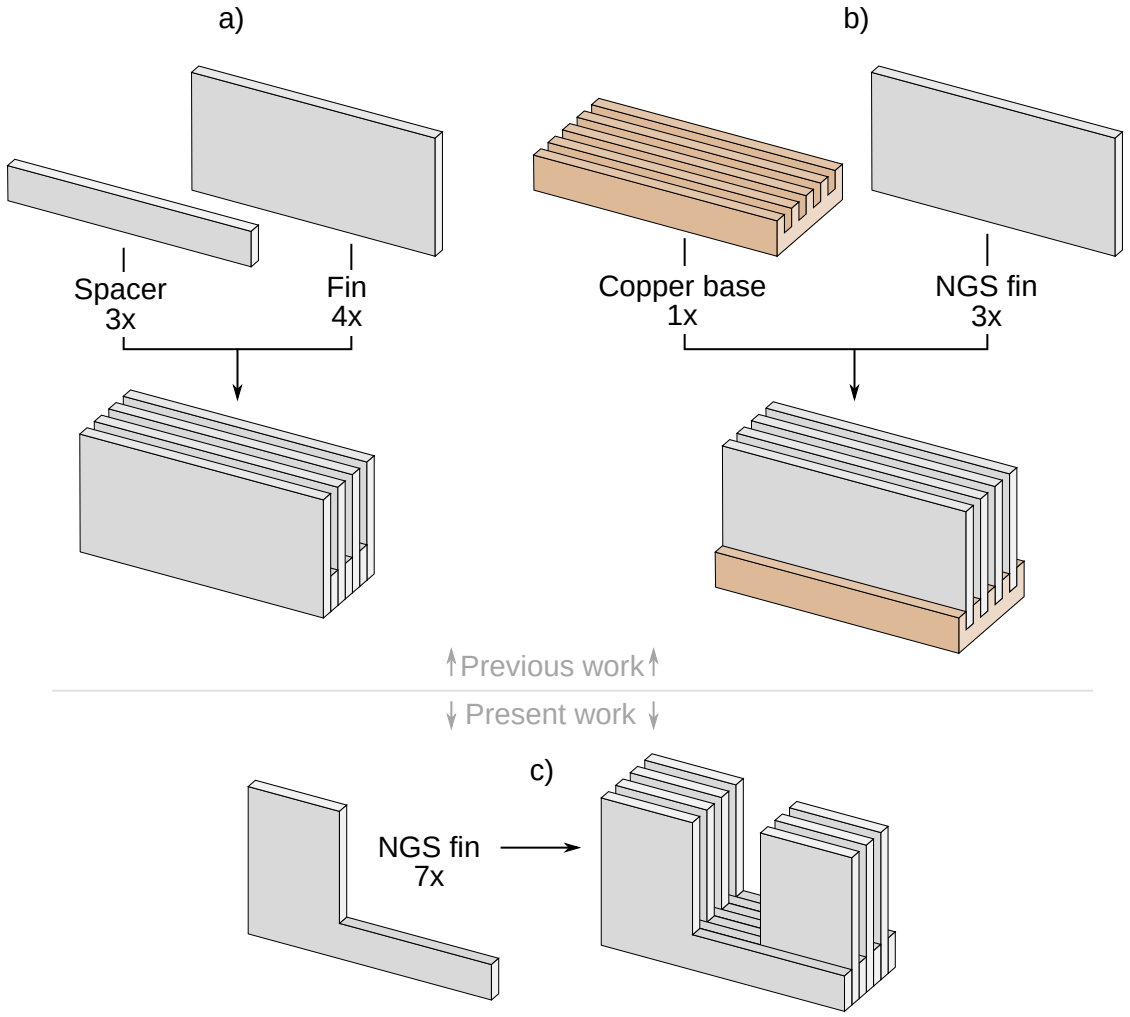

Figure 4.1: A visualization of a,b) previously proposed NGS heat sink designs, and c) the present design.

the dissipated heat must cross the copper-NGS interface, which poses an uncertainty for the thermal performance because the magnitude of the TCR at the interface has not been well studied. Moreover, additional cost, weight, and reliability concerns lead to rejecting the hybrid design for the purposes of this thesis. The cost of a hybrid heat sink was assumed to be high due to the complexity of the bonding process, and due to the high material cost of copper (Figure 1.6b). The density of copper is up to eighteen times higher than that of NGS, which was expected to lead to a higher heat sink weight, which would in turn hinder the usage in weight-sensitive applications. From the reliability perspective, the bonding interface may suffer from a long-term fatigue due to the mismatch in thermal expansion coefficient and resulting stresses. It should be noted that the advantages of the hybrid design are easy mounting using threaded holes and an improved heat spreading in the through–plane direction.

In the staggered-fin design that was used in this thesis, the heat travels only in the in–plane directions and does not need to cross any interfaces. It should be noted that the above statement holds only when the width of the heat sink and the heat source are the same. The gap between the fins allows for mounting without using threaded inserts or through-holes, but at the same time it reduces the available fin heat transfer area. However, interrupting the thermal boundary layer can lead to an improved heat transfer coefficient and the overall performance may be the same, or better, despite the lower fin area.

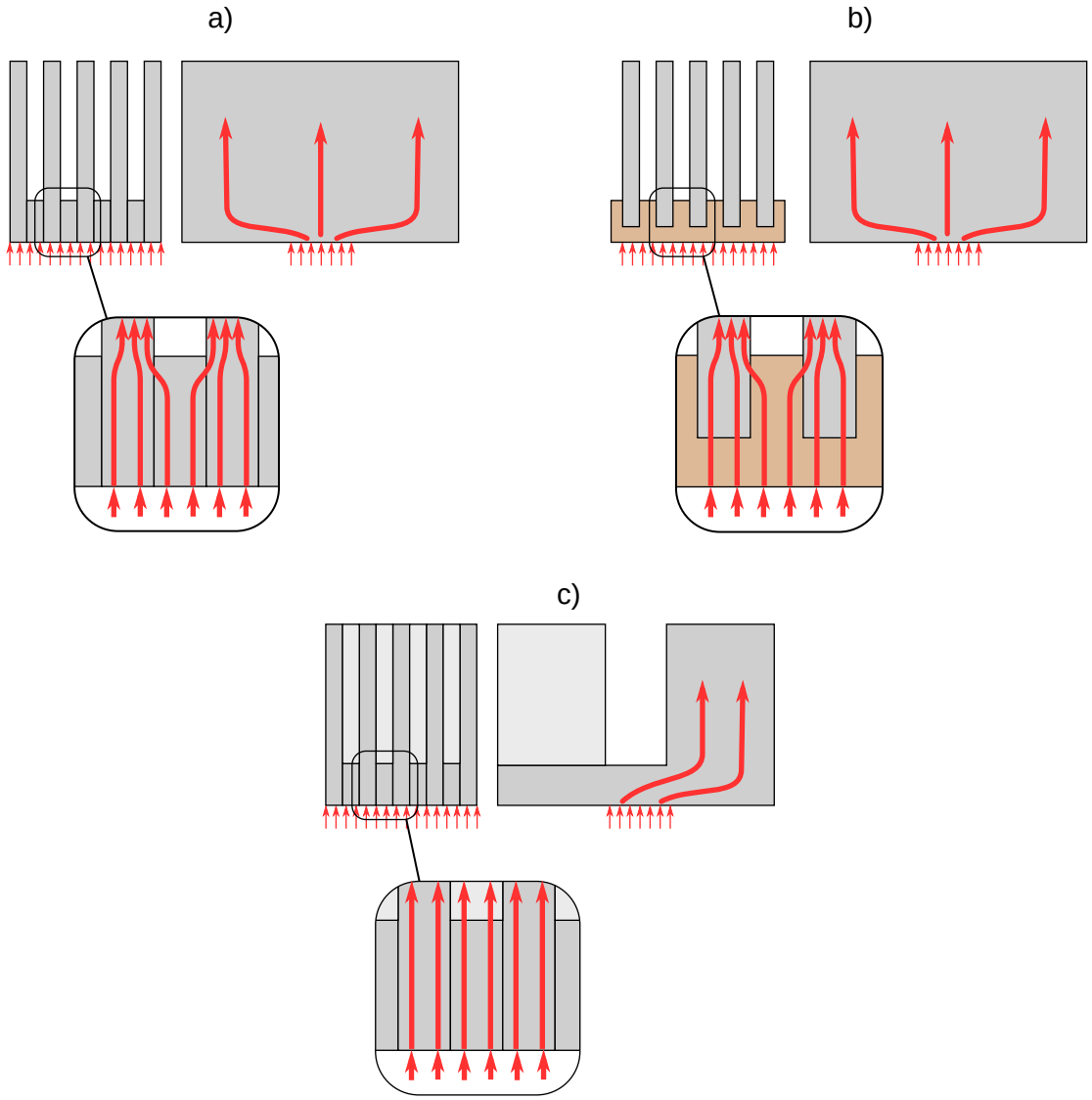

Figure 4.2: A Qualitative heat transfer analysis of multiple possible heat sink designs.

A simplified schematic of the manufacturing process is shown in Figure 4.3, and photographs of three stages of the process are shown in Figure 4.4. First, sheets in the shape shown in Figures 4.3a and 4.4a were die-pressed from the raw NGS described in section 3.1. The sheets were then glued together under compression (Figures 4.4b and 4.4c) to form

pairs (4.3b), which were assembled and glued in an alternating fashion into stacks (4.3c). The final heat sinks were cut from the stacks using a band saw as shown in Figures 4.3d and 4.3e. A photograph of one of the final heat sinks is shown in Figure 4.5.

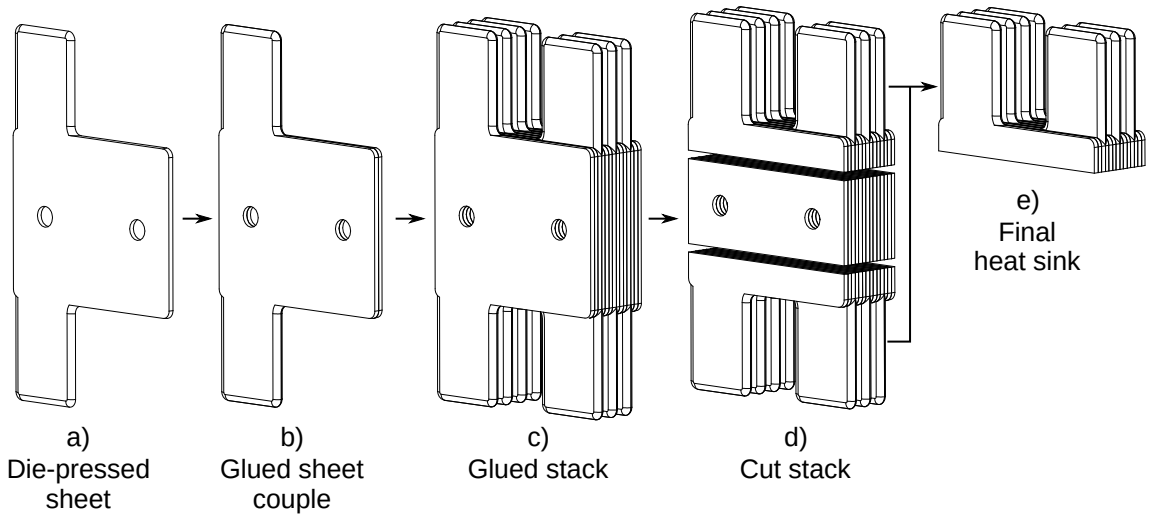

Figure 4.3: A schematic of the heat sink manufacturing process.

While only a general description of the manufacturing method is given here, the following chapters include details about the heat sinks used for each of the studies. It should be noted here that forming process of the sheets (Figure 4.3a) varied through out the course of the research work. While die-forming was eventually deemed to be the most suitable method, water jet cutting has been used too.

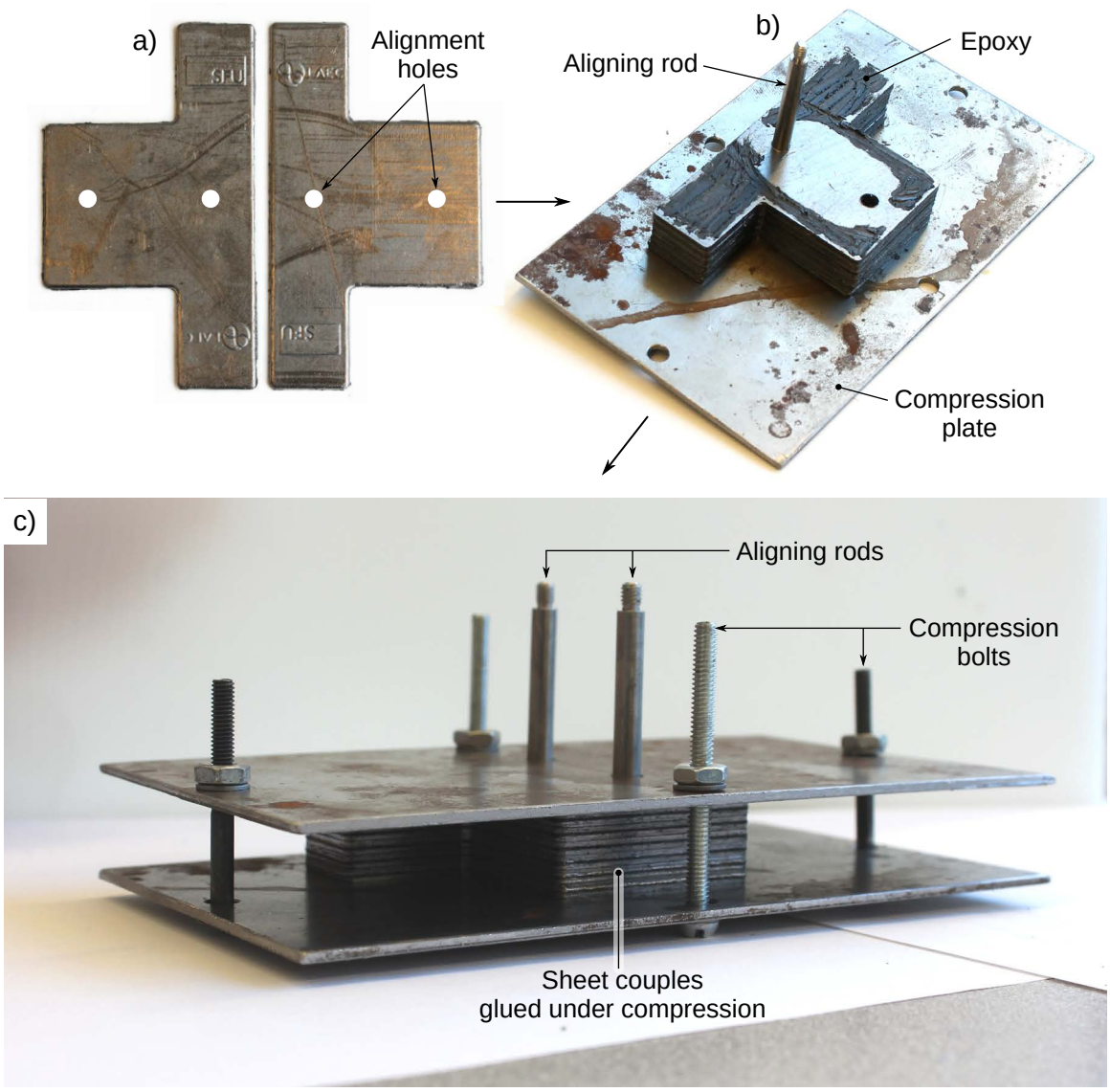

Figure 4.4: Photographs of a) NGS sheets, b) applying glue to sheet pairs, and c) compression of the glued pairs.

Figure 4.5: A photograph of a NGS heat sink produced within this thesis

Chapter 5

Thermal performance of NGS heat sinks

The thermal performance of NGS heat sinks is investigated here with the focus on comparing NGS and aluminum. In section 5.1, two methods for experimental characterization of heat sinks are analyzed and compared. The attention is focused on the possibility of measuring the TCR at the interface between a power semiconductor and a heat sink in an in-situ environment. Suggestions on the feasiblity of each of the methods are made. An audiovisual summary of the chapter is available at `https://www.youtube.com/watch?v=cxMcAGcPzAE&list=PLaX55SIXaD20NQQ2JLP-7abmET7l-6LS4&index=4` [1].

In sections 5.2 and 5.3 the thermal performance of small scale and large scale NGS heat sinks is measured. The small scale heat sinks are defined by their width being comparable the heat source width, as shown in Figure 5.1. Using the small scale heat sink in the first set of experiments allowed to reduced the complexity because the low through–plane thermal conductivity of NGS does not significantly affect the thermal performance. In addition, using small heat sinks also reduces the complexity and time requirement of the manufacturing process. The study of large scale NGS heat sinks in section 5.3 builds upon the small scale results and extends the focus on heat sinks whose thermal performance is limited by the low through–plane thermal conductivity.

[1] The video files are also available in Appendix F

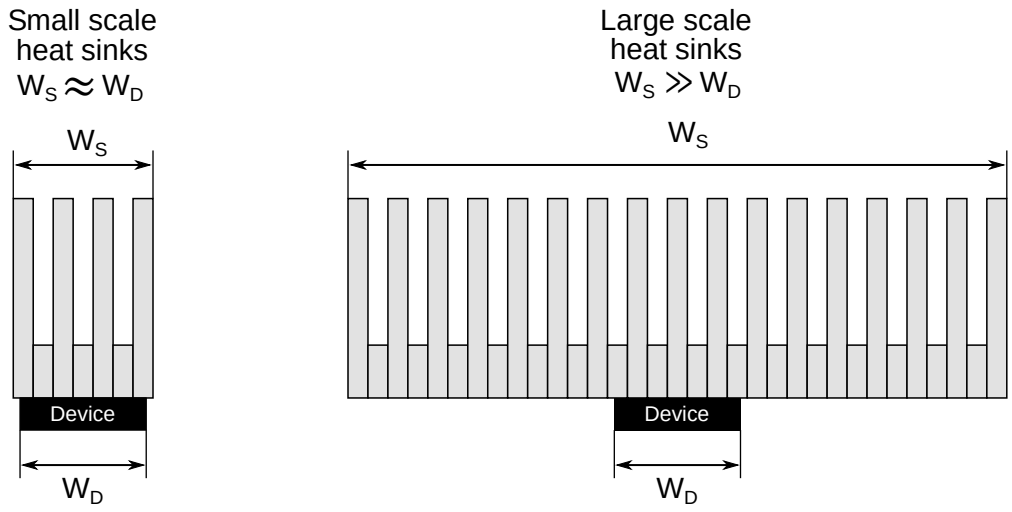

Figure 5.1: Illustration of the small scale and large scale heat sinks.

In section 5.4 the TCR at the interface between NGS and machined metals is studied using a standalone measurement device that eliminates the shortcomings of the methods used in sections 5.2 and 5.3. A comparison with the TCR at metal-to-metal interfaces with common thermal greases is provided.

5.1 Analysis of methods for experimental characterization of heat sinks

The performance of electronics cooling systems is typically expressed in terms of thermal resistance whose definition was given in section 1.4. In the design of commercial electronic devices, the overall juntion-to-ambient thermal resistance is typically the most valuable quantity because it relates the critical junction temperature to the ambient temperature. In research and development, a detailed knowledge of partial resistances that were summarized in Figures 1.4 and 1.5 is crucial for identifying the heat transfer bottlenecks and improving the cooling performance.

To evaluate the partial thermal resistances the relevant temperatures and heat fluxes must be measured. In electronics cooling, the heat flow through a heat sink is typically assumed to be equal to the heat dissipation rate in the power semiconductor. Measuring the heat dissipation is simple as only current and voltage drop readings are necessary. The temperature measurement, on the other hand, is complex because sensors must be installed at carefully chosen locations. In some cases, the most desirable locations such as the semiconductor junction cannot be measured because installing a sensor would disrupt the functionality of the device under test. A typical practical workaround is installing the temperature sensor as close to the junction. The junction temperature can also be determined by measuring the variation of temperature sensitive electrical properties such as the forward voltage [114].

The following section describes a study aimed at comparing two methods for heat sink characterization: thermocouples and transient thermal testing. The goal is to determine which method can deliver more detailed information about the heat flow in a heat sink, and to review the practical aspects including ease-of-use, accuracy, measurement time requirement, and cost. Other methods for heat sink characterization exists, however, the two selected methods represent the two major directions: using temperature sensors versus the temperature sensitive property of semiconductors. The focus of the present measurements is to capture the thermal resistance at the device-heat sink interface in an in-situ configuration. Throughout the following text, the names *thermocouple method* and *transient thermal method* are adopted. To the best knowledge of the author, the names of the heat sink characterization have not been standardized, and it is therefore likely that different names for the same methods are used in other publications.

5.1.1 Thermocouple method

Installing thermocouples at multiple locations along the heat flow path allows determining the desired partial thermal resistances. However, since not all the locations are feasible, thermocouples must be installed at nearest available locations, which introduces a systematic error in the measurement. Installation of thermocouples is labor intensive and prone to

errors arising primarily from the imperfect contact between the thermocouple and the measured surface [115]. Attaching thermocouples with a tape is the simplest and fastest solution but the variation in the contact quality can become high. Alternatively, thermocouples can be attached using thermally conductive adhesives, which decrease the mounting uncertainty but reusing of thermocouples is typically not possible. Other complications may arise from the fatigue of thermocouple wires, or from a measurement noise due to interactions with electric fields in power electronics. Despite the drawbacks, the simplicity and low cost makes the thermocouple method most common in the majority of electronic cooling applications.

5.1.2 Transient thermal method

The transient thermal tester uses the semiconductor chip as the temperature sensor, and in principle, the method is a variation of the four-point resistance measurement. It consists of a DC power supply and a voltmeter as shown in Figure 5.2a. The temperature of the chip is determined based on the forward voltage or other temperature sensitive property. The relation between the forward voltage and the temperature is obtained in the calibration process, during which the device under test (DUT) is clamped to a controlled temperature source (aluminum plate with internal liquid channels) and the relationship between forward voltage and temperature is captured.

The measurement starts with the heating phase, in which a heating current I_H is passed through the DUT until it reaches steady-state. The dissipated power is determined by measuring the voltage and current through the DUT and multiplying the two values. The current is then lowered to the measuring current I_M, which results in the DUT gradually cooling down. The transient temperature profile of the chip is recorded and deconvoluted into a curve called a structure function, from which the thermal resistances can be determined. While the details of the deconvolution are complex [116], the basic idea is to numerically generate an equivalent one-dimensional resistor-capacitor thermal network (Figure 5.2b) whose transient response is identical to the experimentally obtained response of the measured system. The structure function is a graphical visualization of individual resistor and capacitor pairs with the resistance on the horizontal axis and the capacitance on the vertical axis (Figure 5.2c). The differential structure function is a derivative of the capacitance with respect to resistance.

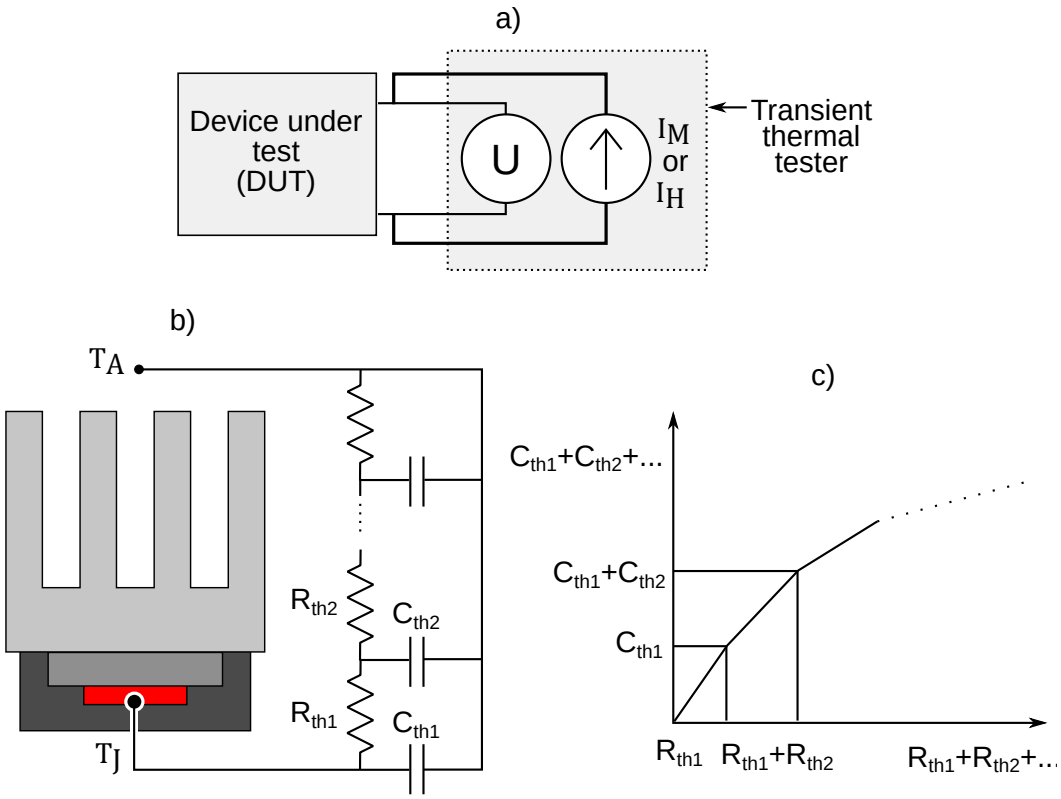

Figure 5.2: a) A schematic of the transient thermal tester, b) Equivalent 1-D RC thermal circuit, and c) illustration of the structure function

5.1.3 Experimental method

The experimental setup, which is shown in Figure 5.3a and 5.3b, was designed to allow a simultaneous measurement using thermocouples (Extech SDL200 thermometer) and the transient thermal tester (Mentor graphics T3ster with a 50A-30V Booster). It consisted of an acrylic wind tunnel with 4cm axial fan (JMC 4028-12) and a mounting plate (Figure 5.3c and 5.3d) with a plastic frame, printed circuit board, and the IXYS DSEI 30-06A diode whose structure is shown in Figure 5.4a and 5.4b. The current probes of the transient thermal tester were connected using three-pin connectors while the voltage probes were attached directly to the device terminals using test leads. The heat sinks were attached to the mounting plate using a 2 mm thick insulated metal bracket and two M3 bolts tightened to 0.05 Nm resulting in a contact pressure of approximately 0.5 MPa. Bending of the metal bracket was not observed. CAD files showing the geometry of the wind tunnel are available in the corresponding dataset [117].

Both heat sinks had the same geometry (Figure 5.5a) consisting of seven fins in the staggered configuration with the fin thickness of 2.4 mm, fin spacing of 2.4 mm, fin height of 24.1 mm, fin length of 19.1 mm. The base plate height was 7.6 mm and the total heat sink length, width, and height were 50.8 mm, 16.8 mm, and 31.7 mm. The aluminum heat

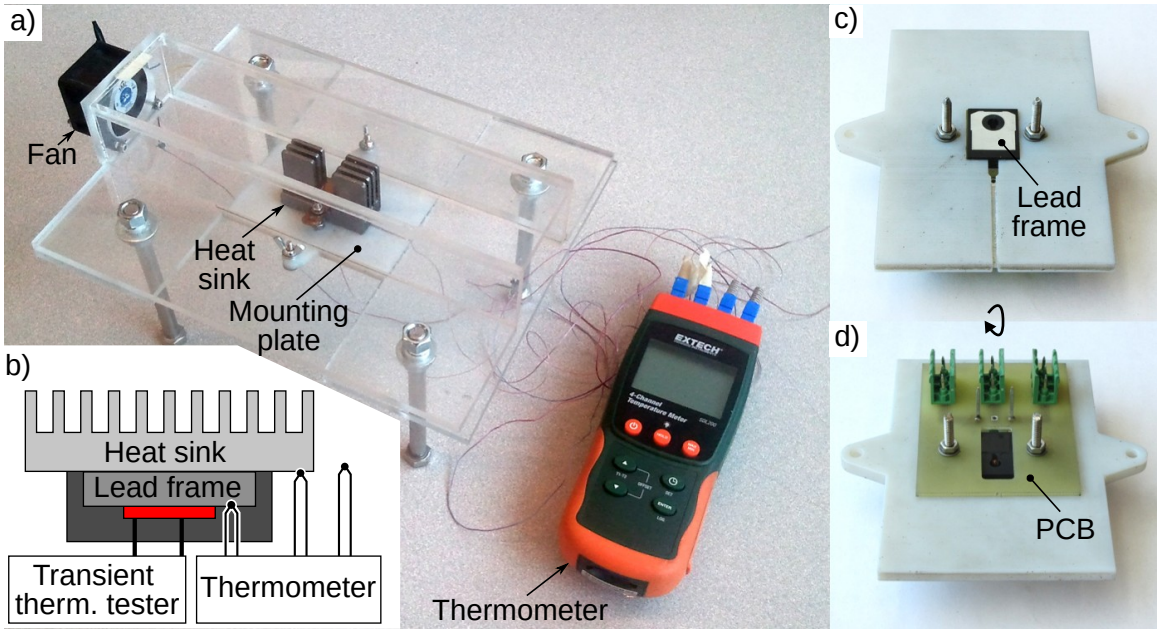

Figure 5.3: Experimental setup. a) a photograph of the whole setup (the transient thermal tester is not shown), b) scheme showing the two measurement methods, c) detail of the mounting plate and d) bottom of the mounting plate (rotated by 180°)

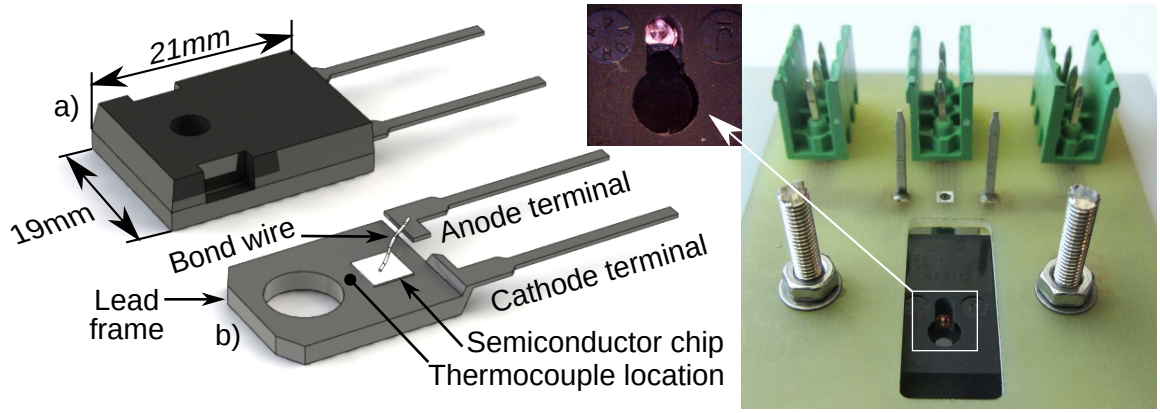

Figure 5.4: a 3D CAD visualization of a) the device (diode) and b) its internal structure. Right: The device mounted on the printed circuit board with the detail of the thermocouple location (picture before attaching the thermocouple)

sink was manufactured by CNC machining and the surface was anodized. The NGS heat sink was manufactured from a 1.2 mm thick sheet with the density of $0.58\,\mathrm{gcm}^{-3}$, which translates to the through–plane and in–plane thermal conductivity of $5\,\mathrm{Wm}^{-1}\mathrm{K}^{-1}$ and $100\,\mathrm{Wm}^{-1}\mathrm{K}^{-1}$, respectively. CAD files showing the geometry of the heat sinks are available in the corresponding dataset [117].

Four thermocouples (Omega 5SRTC, T-type, 36 AWG) were used to measure the temperature of the device T_D^{TC}, heat sink T_S^{TC}, inlet air T_A^{TC}, and outlet air $T_{A,out}^{TC}$. The location

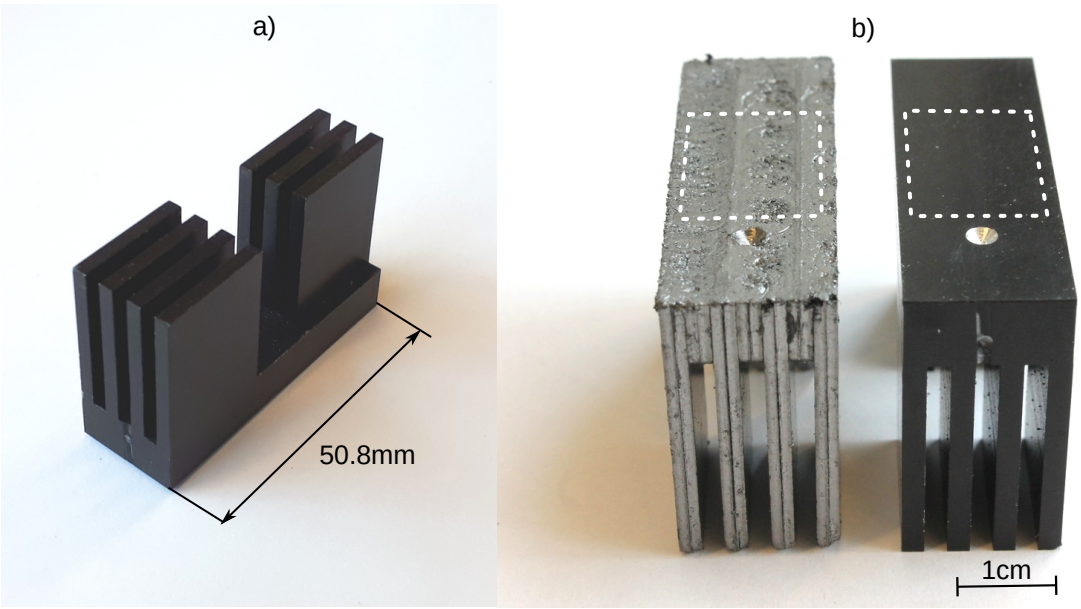

Figure 5.5: a)A photograph of the aluminum heat sink, b) Mounting dent for the heat sink thermocouples, the dashed lines show the position of the device.

of the device thermocouple shown in Figure 5.4 was chosen to be as close to the chip as possible while minimizing the risk of damaging the bond wire. The copper lead frame of the diode was exposed by machining off a portion of the molding compound, and a small dent 1 mm in diameter was drilled in the lead fram. A thermocouple was then inserted into the dent and secured using the J-B Weld two-part epoxy. The heat sink thermocouple was mouted identically and the location is shown in Figure 5.5b.

As illustrated in Figure 5.6, a single measurement started by the heating phase, in which the transient thermal tester ran the heating current I_H through the device. When steady-state was reached, the thermocouple readings were recorded and subsequently the heating current I_H was reduced to the measuring current I_M and the cooling curve of the device junction was recorded. Three configurations were measured: i) aluminum heat sink without thermal grease, ii) aluminum heat sink with the Shin-Etsu G751 thermal grease, and iii) NGS heat sink without thermal grease. Each configuration was tested at 5 A, 7 A, and 10 A heating currents, which translates to the disipated power of approximately 5.3 W, 7.5 W, and 11 W. The free-stream air velocity was $3.5\,\mathrm{ms}^{-1}$, and it was calculated from the vane anemometer flow rate measurement at the outlet of the wind tunnel. Each of the measurements was repeated three times and the heat sink was dismounted and re-mounted in all the repetitions.

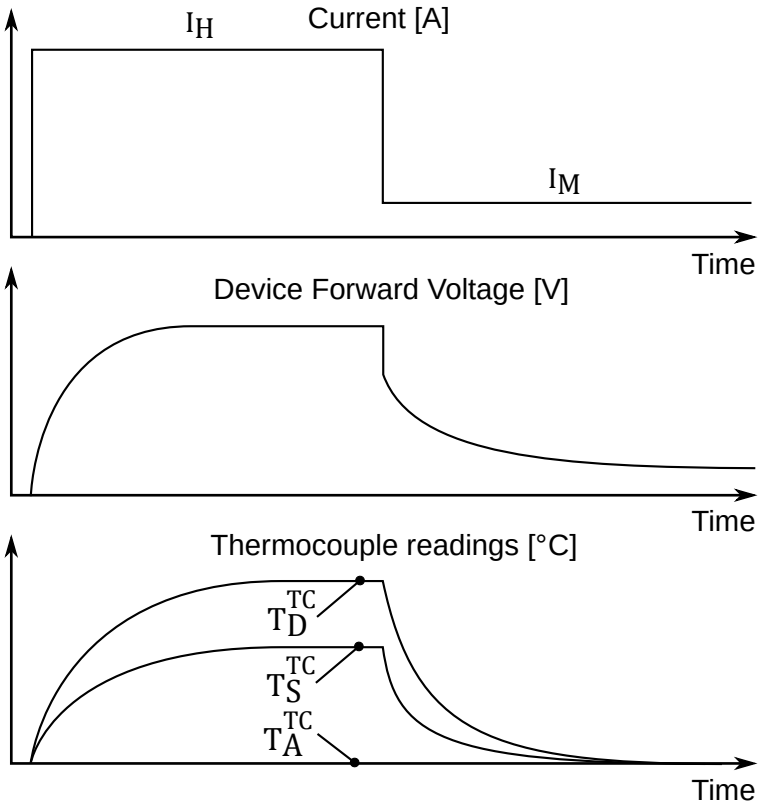

Figure 5.6: A visualization of the temporal profile of the current through the device (top), device forward voltage (middle), and thermocouple readings (bottom).

5.1.4 Data processing

The raw data for a single measurement included the thermocouple readings (device temperature T_D^{TC}, heat sink temperature T_S^{TC} and inlet ambient air temperature T_A^{TC}), dissipated power $\dot{Q}$, and the cooling curve. For the thermocouple method, the device-to-sink R_{thDS}^{TC} and sink-to-ambient R_{thSA}^{TC} thermal resistances were calculated as:

$$R_{thDS}^{TC} = \frac{T_D^{TC} - T_S^{TC}}{\dot{Q}}, R_{thSA}^{TC} = \frac{T_S^{TC} - T_A^{TC}}{\dot{Q}}. \tag{5.1}$$

The cooling curves obtained from the transient thermal tester were processed using the T3ster Master software to get structure functions (SF's) and differential structure functions (DSF's). As illustrated in Figure 5.7 in which one randomly selected SF and DSF for each of the measured configurations were plotted, by identifying the C (Case) and S (Sink) points it is possible to determine the junction-to-case R_{thJC}^{TR}, case-to-sink R_{thCS}^{TR}, and sink-to-ambient R_{thSA}^{TR} thermal resistances. R_{thJC}^{TR} is typically obtained using the Transient Dual Interface Method (TDIM) [116, 118, 119], which requires measuring the device on a cold plate with and without a thermal grease. The principle of the method is that when an identical device is measured under different boundary conditions, the initial parts of the structure functions,

which describe the heat flow within the device, will overlap and only when the heat has reached the device case, they will diverge. Thus, the divergence point (C point in Figure 5.7) is used for determining R_{thJC}^{TR}. Since the heat sink measurements performed in this work also provide three different boundary conditions, there were two options of determining the R_{thJC}^{TR}: i) from heat sink measurements, and ii) from a standalone measurement of the device on a cold plate using the TDIM. The data were collected for both and plotted in Figure 5.8. The curves diverge slightly sooner for the TDIM method. For the purposes of this work a graphically determined R_{thJC}^{TR} value of 0.6 K/W was used, however, a more rigorous approach should be implemented in the future to assure consistent results from different operators. To determine the magnitude of the case-to-sink resistance R_{thCS}^{TR}, the work of Poppe et al. [120] was followed and the point S (Figure 5.7) was assumed to be at the local maximum of the DSF, which demarcates the left limit of the flat section of the SF. The raw data and the implementation of the analysis method are available in the corresponding dataset [117].

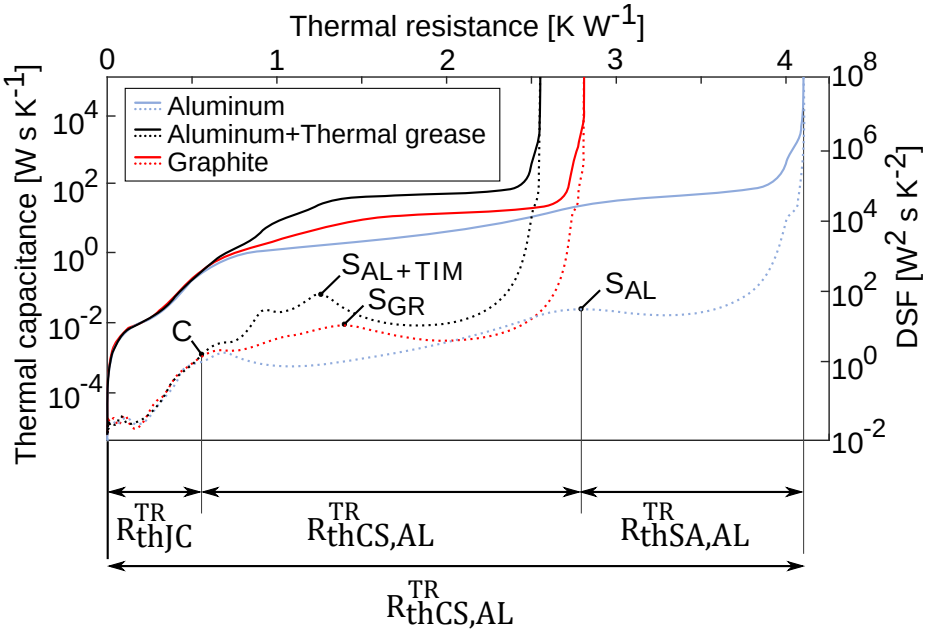

Figure 5.7: A single SF (solid lines) and differential DSF (differential structure function) for each of the measurements at 5 A heating current and 0.2 A measuring current.

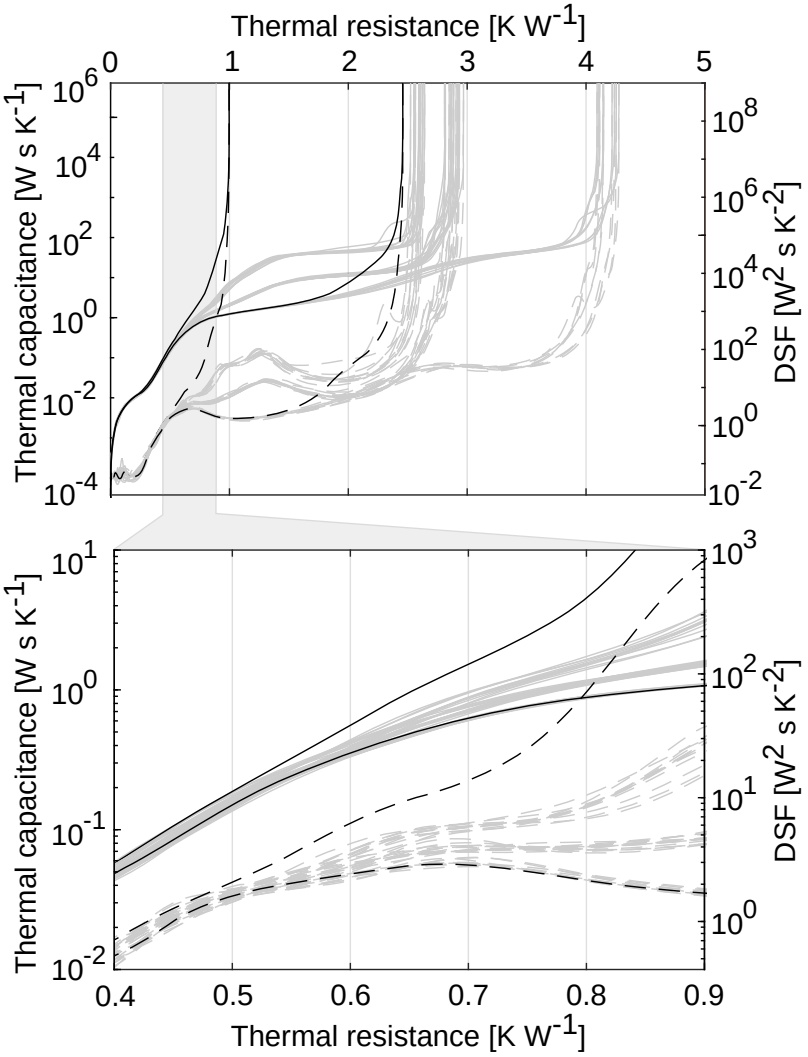

Figure 5.8: Compilation of all SF's (solid lines) and DSF's (dashed lines). Grey – measurements with heat sinks, black – measurements on a temperature controlled plate. The bottom figure is a detail of the top one.

5.1.5 Results

Figure 5.9 shows a summary of all the measured thermal resistances, where the height of the bars corresponds to the average values and the error bars show the maximum variation in the collected data. The major conclusions are: i) using thermocouples leads to underpredicting the total resistance due to inability to capture the true junction temperature, ii) if used for relative comparison of the heat sinks, both method result in the same conclusions (i.e. the aluminum heat sink with thermal grease shows the lowest total resistance followed by NGS and aluminum without thermal grease), iii) the average sink-to-ambient resistances (darkest gray bars) measured by the two methods are in a good agreement, iv) the average device-

to-sink resistance measured by thermocouples corresponds to the case-to-sink resistance measured by the transient thermal tester.

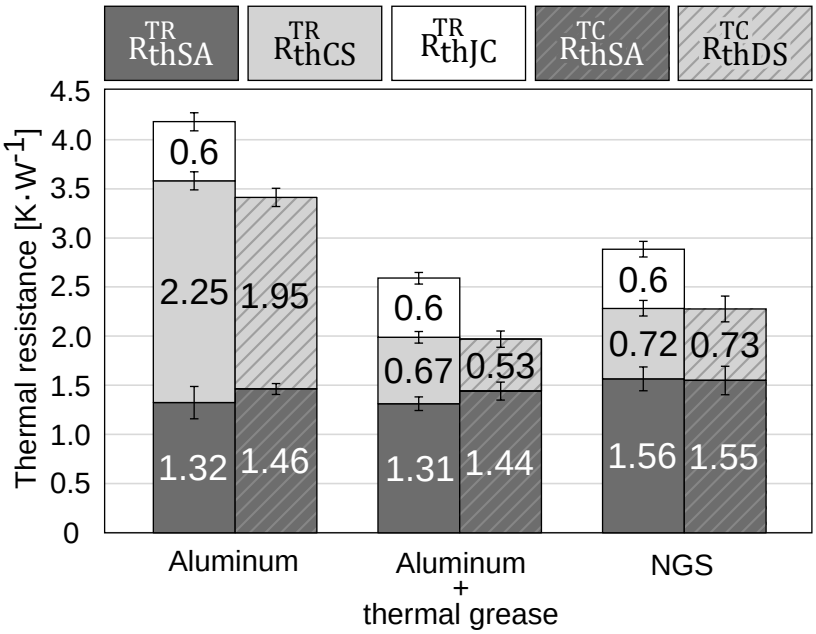

Figure 5.9: Comparison of the thermal resistances measured by thermocouples (hatched bars) and the transient thermal tester (solid fill)

The absolute difference between the average sink-to-ambient resistances (R^{TR}_{thSA} and R^{TC}_{thSA}) measured by the two methods is $0.14\,\mathrm{KW}^{-1}$, $0.13\,\mathrm{KW}^{-1}$, and $0.02\,\mathrm{KW}^{-1}$ for the aluminum without thermal grease, aluminum with thermal grease, and NGS heat sinks, respectively, which corresponds to the relative difference of 10 %, 10 %, and 1 %, respectively. All the relative differences reported in this thesis use the transient thermal tester values as the reference value. Analyzing the data on the individual measurement basis instead of the averages, which is relevant because the data was gathered at the same time using the same testbed, reveals the maximum absolute difference between the method to be $0.25\,\mathrm{KW}^{-1}$, $0.20\,\mathrm{KW}^{-1}$, and $0.17\,\mathrm{KW}^{-1}$, which translates to the maximum relative difference of 20 %, 15 %, and 11 %, respectively. The comparison suggests that the methods agree better in the case of the NGS heat sink.

The absolute difference between the average case-to-sink resistance measured by thermocouples R^{TR}_{thCS} and the average device-to-sink resistance measured by the transient thermal tester R^{TC}_{thDS} is $0.31\,\mathrm{KW}^{-1}$, $0.15\,\mathrm{KW}^{-1}$, and $0.01\,\mathrm{KW}^{-1}$ for the aluminum without thermal grease, aluminum with thermal grease, and NGS heat sinks, respectively, which corresponds to 14 %, 22 %, and 1 % relative difference. Performing the comparison for individual measurements instead of the averages yields the maximum absolute differences between R^{TC}_{thDS} and R^{TR}_{thCS} to be $0.39\,\mathrm{KW}^{-1}$, $0.22\,\mathrm{KW}^{-1}$, and $0.35\,\mathrm{KW}^{-1}$, which corresponds to 17 %, 31 %,

and 49 % relative difference, respectively. The scatter of the data is much higher than in the case of sink-to-ambient resistance.

5.1.6 Discussion

To further understand the differences between the two investigated methods, a numerical simulation of the aluminum heat sink with thermal grease was performed using the finite volume solver Ansys Fluent R19.2. The geometry of the diode shown in Figure 5.10a was simplified into the shape shown in Figure 5.10b. The size of the simulation domain matched the size of the wind tunnel. The inlet velocity was set to $3.5\,\mathrm{ms}^{-1}$, which is the value measured by a vane anemometer. The solver was set to the laminar flow mode. The TCR at the diode-heat sink interface was set to $17\,\mathrm{Kmm}^2\mathrm{W}^{-1}$ based on the manufacturer's data sheet [121]. The dissipation power was 11 W in accordance with the highest power measured experimentally. It should be noted here that the purpose of the simulation was to provide a qualitative insight into the temperature field of the heat sink, not to accurately predict the heat sink performance. Validation, mesh dependency study, and detailed description were therefore omitted.

The temperature field of the lead frame and the heat sink base plate at the mid-plane cross-section was visualized in Figures 5.10c and 5.10d. In Figure 5.10e the surface temperatures of the lead frame and the heat sink were plotted as the function of length (y coordinate). In all cases the relative temperature difference with respect to the maximum temperature of the lead frame (58 °C) is presented.

The simulation results in Figure 5.10 show a highly non-isothermal temperature distribution in both the lead frame and the heat sink. The location of the device and heat sink thermocouples (T_D^{TC} and T_S^{TC}) was outlined in Figures 5.10d and 5.10e. The device temperature measured by the thermocouples T_D^{TC} is approximately 5 °C lower than the maximum temperature of the lead frame, which confirms that the thermocouple method fails to capture the real junction temperature. The experimentally obtained average difference between the junction temperature measured by the transient tester and the device temperature measured by thermocouples in the case of aluminum with thermal grease is 6.4 °C, which is higher than the observed 5 °C due to the die attach resistance which was not captured in the simulation. Dividing the simulated 5 °C temperature drop by the dissipation power of 11 W yields the thermal resistance of $0.45\,\mathrm{KW}^{-1}$, which agrees with the constant $0.6\,\mathrm{KW}^{-1}$ offset between the methods seen in Figure 5.9, and it can be therefore concluded that the offset is caused by the fact that the device thermocouple does not capture the true junction temperature. For engineering purposes, the offset can be accounted for in the heat dissipation calculations, however, it should be noted that the heat spreading in the lead frame and the base is non-linear with the dissipation power, and the magnitude of the offset is expected to change for the values of dissipation power significantly higher or lower than the measured ones.

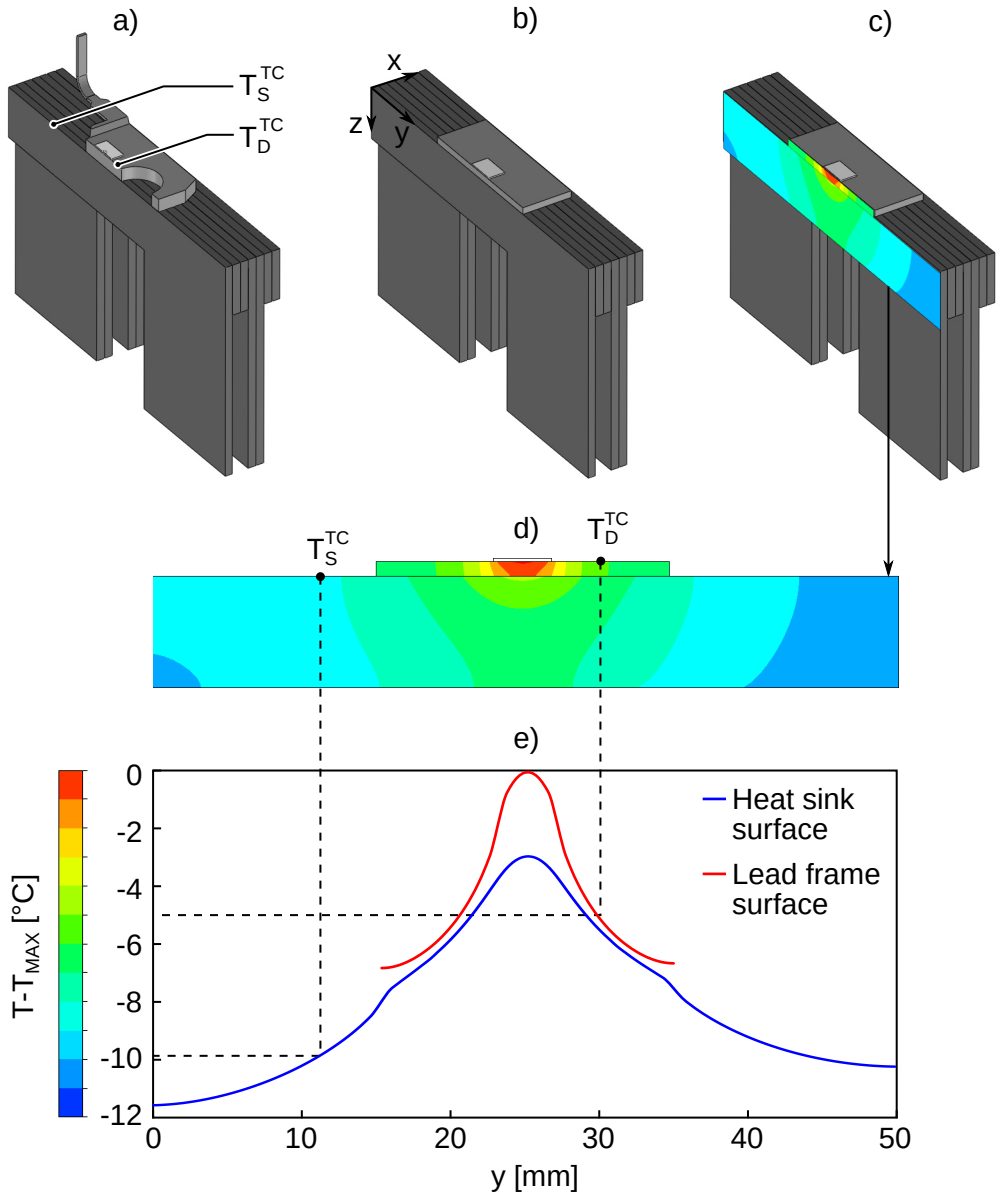

Figure 5.10: Simulation geometry a) before and b) after simplification, c) the temperature field and d) its enlargement, e) the temperature at the surface of the heat sink and the lead frame.

For the purposes of heat sink development, it is desirable to capture the TCR at the device-sink interface during the experimental characterization of heat sinks. While other standalone methods for measuring the TCR between two materials exist, in-situ measurements are preferable because they reduce the research and development time and include the effect of real surfaces as opposed to idealized samples clamped at uniformly distributed pressure. In the context of NGS heat sinks, an in-situ measurement of the device-sink TCR ($R_{thTCRDS}$) is relevant for investigating the effect of the low material hardness, which is expected to decrease the TCR. For the measured case of aluminum with thermal grease,

the theoretical value of $R'_{thTCRDS}$ can be calculated from the specific TCR given by the thermal grease manufacturer ($17\,\mathrm{Kmm^2W^{-1}}$ [121]) and the the interface area ($314\,\mathrm{mm^2}$), which results in the value of $0.05\,\mathrm{KW^{-1}}$. The device-to-sink resistance measured by thermocouples R^{TC}_{thDS} and the case-to-sink resistance measured by the transient tester R^{TR}_{thCS} were expected to capture the TCR at the device-sink interface; however, comparing the two ($0.53\,\mathrm{KW^{-1}}$ and $0.67\,\mathrm{KW^{-1}}$, respectively) to $R'_{thTCRDS}$ reveals an order of magnitude difference.

For the thermocouple method, the explanation of the difference between $R'_{thTCRDS}$ and R^{TC}_{thDS} can be made based on the simulation results in Figure 5.10d and 5.10e. From the temperature field in Figure 5.10d it is clear that the temperature difference $T^{TC}_D - T^{TC}_S$ used for calculating R^{TC}_{thDS} contains not only the temperature drop due to the device-to-heat sink TCR, but also the temperature drop that arises from the spreading of heat, where the latter is a function of the thermal conductivity and geometry of the device and heat sink. In Figure 5.10e it can be seen that the relevant temperature difference to evaluate the contact resistance is the vertical distance between the red and blue curves; however, even if a measurement of this temperature difference was possible, the total dissipated heat $\dot{Q}$ cannot be used for calculating $R_{thTCRDS}$ as the heat flux distribution is non-uniform. To conclude, the device-to-sink thermal resistance measured by thermocouples R^{TC}_{thDS} does not correspond to the device-to-sink TCR and includes a parasitic component that arises from the location of the thermocouples. Despite this short coming, the values of R^{TC}_{thDS} obtained for the three configurations measured in this work follow the expected trend because the TCR of aluminum without thermal grease is significantly higher than the aluminum with thermal grease and NGS cases. The thermocouple method is deemed to be sufficient for a relative comparison of the quality of the heat transfer through the device-sink interface. However, a further numerical work to understand the effect of the thermocouple location on the measured resistance is suggested.

In the case of the transient tester, the difference between R^{TR}_{thCS} and $R'_{thTCRDS}$ is expected to be due to the method used for determining the S point on the structure functions. The complexity of the transient thermal method does not allow for a simple analysis as in the case of the thermocouple method. However, the most plausible explanation is that the local maximum of the DSF used for determining the point S corresponds to portion of the 1-D R-C network that is associated with the heat wave reaching the fins of the heat sink. To verify this hypothesis, it is suggested to perform a numerical work that would explain the relationship between the shape of the structure function and the heat sink parameters such as shape, thermal conductivity, and TCR.

The error bars in Figure 5.9 reflect only the repeatability. The equipment error was not considered because the propagation of uncertainty through the complex calculation of structure functions was beyond the scope of this work. The equipment error for the thermocouple measurements was not included to keep the meaning of the error bars the

same when comparing the two methods. Some portion of the dissipated heat leaves the heat source through the leads and the circuit board. Accounting for this heat loss in the transient measurements was beyond the scope of this work. To keep the measurements comparable, the heat loss was neglected for the thermocouple method. However, measurements with a block of insulating material mounted instead of the heat sink showed that the losses are in the order of $\dot{Q}_{Loss} \approx 0.04\Delta T_{DA}[W]$, where ΔT_{DA} is the temperature difference between the device and the ambient air. The daily fluctuations in the laboratory ambient air temperature may have affected the results by disturbing the steady state, or by altering the cooling conditions during the recording of the cooling curves. The relevant temperature drift was estimated to be in the order of 1 to 2 °C per hour. All of the above points should be addressed in the future measurements.

Suitability of the methods for various applications is given by many factors. The thermocouple method is inexpensive and well known, but the installation of the thermocouples is time consuming and comes with challenges related to mounting and heat leakage through the thermocouple. The cost of a transient thermal tester is significantly higher, but it can be offset by other advantages: the need for an intrusive installation of thermocouples is eliminated. Additionally, other information describing the heat sink such as its heat capacity or the location of heat transfer bottlenecks can potentially be extracted from the shape of the structure functions. However, the extraction methods need to be developed. A promising, already documented method, is using the structure functions to calibrate a 3D numerical thermal model [122]. However, to the author's best knowledge, a study on how much information about a heat sink can be inferred using this approach is not available in the literature.

5.1.7 Section conclusion

The thermocouple and transient thermal methods for experimental characterization of heat sinks were compared using a setup that allowed a simultaneous measurement using the two methods. Both methods agree on the relative performance of the heat sink and can be therefore used for comparative studies of heat sinks. The thermocouple method fails to capture the true junction temperature which leads to under predicting the total junction-to-ambient thermal resistance.

Neither of the methods is capable of measuring the TCR at the device-sink interface. The values of the device-to-sink resistance measured by thermocouples and the case-to-sink resistance measured by the transient tester are a combination of the device-sink TCR and a parasitic resistance arising from the imperfection of the methods. Despite this, judging the relative quality of the heat transfer through the device-sink is deemed viable. However, caution should be practiced as the values are dependent on the dissipated power, thermal conductivity, and geometry of the system.

To decide which of the methods is practical for a given application, a complex trade-off has to be considered. The thermocouple method is simple and inexpensive but labor intensive and offers only a limited information about the thermal performance. The transient tester is complex and costly, but more time efficient and the results include more information such as the transient behavior and detailed insight into the heat flow in the measured system.

5.2 Small-scale prototype NGS heat sinks

Two studies of the thermal performance of small-scale NGS heat sink are presented in this section. First, the difference between geometrically identical NGS and aluminum heat sink is addressed. Then, the results of a detailed study of the effect of density, clamping pressure, and polymer impregnation on the thermal resistance of NGS heat sinks are reported.

5.2.1 Comparison of aluminum and NGS heat sinks

The results in the previous section (5.1) were used to draw conclusions about the methods for experimental characterization of heat sinks. Here, the same dataset is used to evaluate the performance of the NGS heat sink in comparison with the aluminum one. In Figure 5.11 the data from Figure 5.9 were reduced, rearranged, and the relative differences between the NGS and aluminum heat sink were annotated.

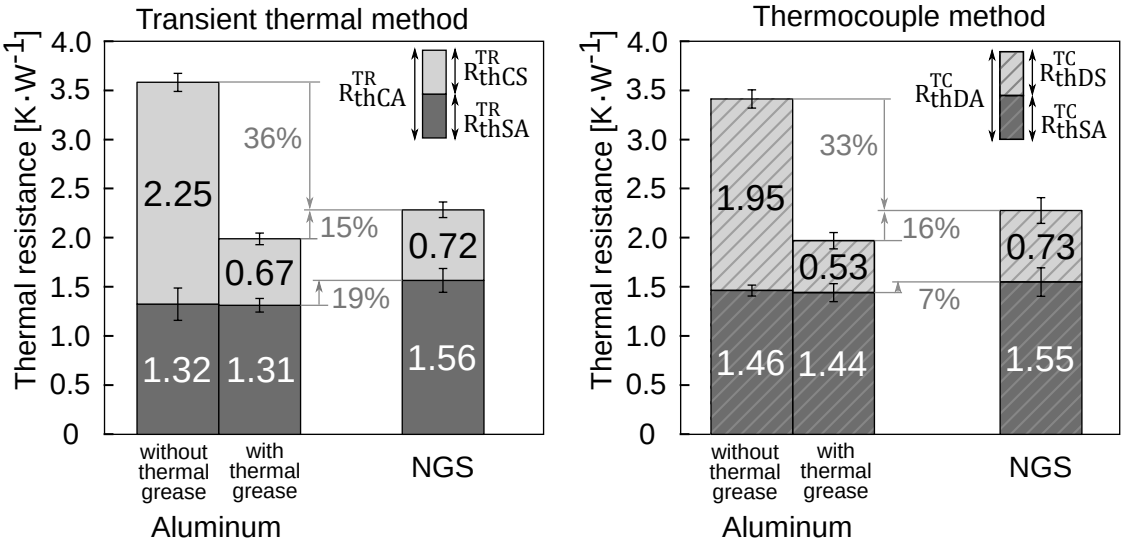

Figure 5.11: Results of thermal resistance measurements of small scale heat sinks. Left: case-to-sink (R^{TR}_{thCS}) and sink-to-ambient (R^{TR}_{thSA}) thermal resistances measured by the transient thermal method. Right: device-to-sink (R^{TC}_{thDS}) and sink-to-ambient (R^{TC}_{thSA}) thermal resistances measure by the thermocouple method.

As was explained in detail in the previous section, the physical meaning of the measured thermal resistances is inherently uncertain. To be able to draw conclusions about the aluminum and NGS heat sinks based on the results from both methods, a simplified terminology is used here. The case-to-sink (R^{TR}_{thCS}) and device-to-sink (R^{TC}_{thDCS}) resistances are both considered to reflect the quality of heat transfer through the device-sink interface, and they are referred to as the interface resistance. The sink-to-ambient resistances (R^{TR}_{thSA} and R^{TC}_{thSA}) are referred to as the sink resistance. The sum of interface and sink resistances, which corresponds to the total height of the bars in Figure 5.11, is referred to as the total resistance.

The total resistance of the NGS heat sink is 33 to 36 % lower than that of aluminum without thermal grease, and 15 to 16 % higher than that of aluminum with thermal grease. The sink resistance (dark gray portion in Figure 5.11) of the aluminum heat sink does not change significantly in cases with and without thermal grease, which confirms the validity of the measurement. The sink resistance of the NGS heat sink is 7 to 19 % higher than that of aluminum heat sink, however, the difference is not statistically significant because of the overlapping error bars. For the thermocouple method, the error bar of the NGS sink resistance overlaps with those of both the aluminum with and without thermal grease. For the transient thermal method, the error bar of the NGS sink resistance overlaps only with that of aluminum without grease. Based on these observations, the difference in the sink resistance between the NGS and aluminum heat sinks is not considered statistically significant. Nevertheless, a physical explanation for the difference exists. The thermal conductivity of the NGS heat sink was 5 $\mathrm{Wm^{-1}K^{-1}}$ in the through–plane direction and 100 $\mathrm{Wm^{-1}K^{-1}}$ in the plane in–plane direction, which is lower than 200 $\mathrm{Wm^{-1}K^{-1}}$ of the aluminum heat sink.

To make conclusions about the interface resistance, the light gray portion of the bar chart in Figure 5.11 was plotted separately in Figure 5.12. The stacked bar chart in Figure 5.11 is not suitable for taking the uncertainty into account.

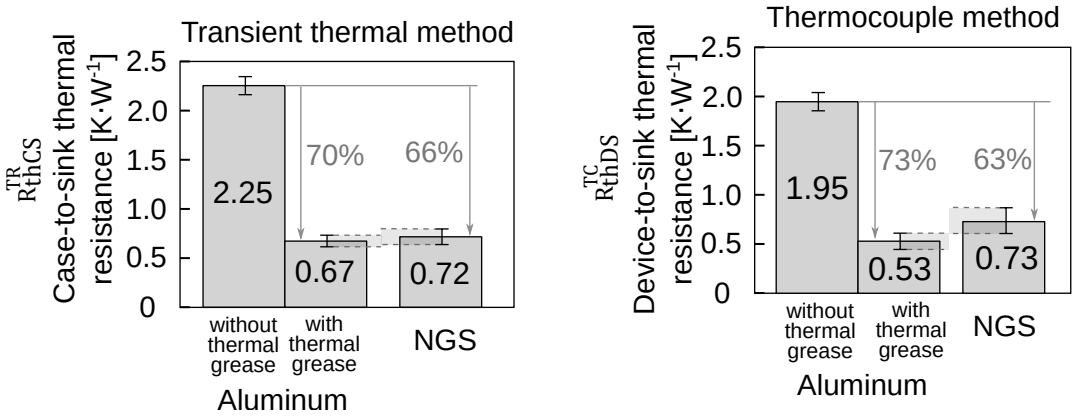

Figure 5.12: Left: case-to-sink thermal resistance (R^{TR}_{thCS}) measured by the transient thermal method. Right: device-to-sink thermal resistance (R^{TC}_{thDS}) measured by the thermocouple method.

The interface resistance of the aluminum heat sink dropped by 70 to 73 % when the thermal grease was used at the device-sink interface. The interface resistance of the NGS heat sink is 63 to 66 % lower than that of aluminum without thermal grease. From the average values it appears that the interface resistance of the NGS heat sink is higher than that of the aluminum heat sink with thermal grease, however, since the error bars are overlapping, a definite conclusion cannot be made.

5.2.2 The effect of density, clamping pressure, and polymer impregnation

Here, an experimental study is designed to resolve the effect of NGS sheet density, clamping pressure, and polymer impregnation on the thermal performance of NGS heat sinks. The clamping pressure affects the magnitude of the TCR at the device-sink interface, which in turn affects the total thermal resistance of the system. Understanding the pressure dependence is necessary for determining the adequate clamping pressure. A polymer impregnation is a technique used to improve the poor mechanical properties of NGS. During the impregnation process, NGS is immersed in a liquid polymer under vacuum, which forces the polymer to fill the pores. The subsequent thermal treatment solidifies the liquid polymer. Since the porosity of NGS ranges from 76 to 25 % for the densities $0.5\,\mathrm{g\,cm^{-3}}$ and $1.7\,\mathrm{g\,cm^{-3}}$, the amount of polymer in the pores is significant, and it can affect the mechanical and thermal properties, which in turn affect the TCR at the device-sink interface.

5.2.2.1 Previous work

Smalc et al. [81] used the guarded heat flow meter method to measure the through–plane thermal conductivity and TCR at the interface between the flow meter and NGS samples. Cases with and without polymer impregnation were considered. The reported thermal conductivity ranged from 4 to $6\,\mathrm{Wm^{-1}K^{-1}}$ but the density of the measured sheets was not reported. The samples impregnated with polymers showed slightly higher average thermal conductivity, but the variation was large and the difference is likely not statistically significant. The specific TCR at the interface between the sheet and the flux meter was $132\,\mathrm{mm^2KW^{-1}}$ for the non-impregnated samples. The polymer-impregnated samples showed values of $59\,\mathrm{mm^2KW^{-1}}$ for mineral polymers and $67\,\mathrm{mm^2KW^{-1}}$ for synthetic polymers, which leads to a conclusion that the polymer impregnation can reduce the TCR by approximately 50 %.

5.2.2.2 Experimental method

The measurement was perfomed using the transient thermal method in a setup that was derived from the one described in section 5.1. To improve the noise-to-signal ratio, the IXYS DSEI 30-06A diode was replaced with the Infineon AUIRGPS4067D1 transistor. The air flow velocity was lowered from $3.5\,\mathrm{ms^{-1}}$ in the original setup to $3.3\,\mathrm{ms^{-1}}$. The geometry of the heat sinks was kept the same, however, the sheets where manufactured using a water jet cutter instead of a compression mold. The raw data, implementation of the analysis method, and CAD files of the heat sink geometry are available in the corresponding dataset [117].

The effect of density was addressed by manufacturing heat sinks out of NGS at $0.79\,\mathrm{gcm^{-3}}$ and $1.25\,\mathrm{gcm^{-3}}$. For each of the densities, heat sinks with and without polymer impregnation (Hernon HPS 991) were prepared. To include the manufacturing variability in the

study, two heat sinks were prepared for each of the measured configurations, which resulted in a total of eight heat sinks. Figure 5.13 shows an image of all the heat sinks and a table summary of the parameters.

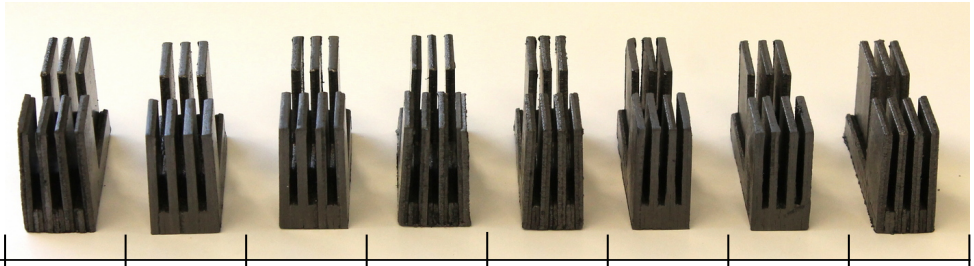

Polymer impregnated	×	×	✓	✓	×	×	✓	✓
NGS density [g cm^{-3}]	0.79				1.25			

Figure 5.13: The small scale heat sinks manufactured for the study on the effect of density, clamping pressure, and polymer impregnation.

The heat sinks were clamped by two M3 bolts tightened using the CDI 151NSM torque screwdriver set to 0.01 Nm, 0.05 Nm, and 0.1 Nm, which translates to the clamping pressures of 0.1 MPa, 0.5 MPa, and 1 MPa, respectively. The clamping force of one bolt was calculated as:

$$F_c = \frac{T}{K d_b}, \tag{5.2}$$

where T is the torque, K is the coefficient of friction set to 0.2, and d_b is the bolt diameter. The clamping pressure was determined as:

$$p_c = \frac{F_c}{A_d}, \tag{5.3}$$

where A_d is the device area of 336 mm^2.

Multiple measurement repetitions were made for each of the configurations, resulting in a total of 64 measurements. The data processing was identical to that described in section 5.1. The value of the junction-to-case thermal resistance R_{thJC} of the device was set to 0.2 KW^{-1} based on the manufacturer's specifications [123], and the validity of the value was confirmed by determining the C point from the diversion of structure functions.

5.2.2.3 Results

The results of the measurements are summarized in Figure 5.14 where the light bars represent the case-to-sink thermal resistance (R_{thCS}), the dark gray bars represent the sink-to-ambient resistance (R_{thSA}), and total height of the bars represents the total case-to-ambient resistance (R_{thCA}). It must be noted here that multiple of the observations described later

in this section are statistically insignificant due to overlapping error bars. Repeating or otherwise improving the results was not possible as the data were collected during a one-week-long stay at an external commercial facility. The observations are discussed despite the statistical insignificance, and recommendations on future measurements are made.

Among all the measured heat sinks, the one manufactured from the high density 1.25 $\mathrm{gcm^{-3}}$ sheet with no polymer impregnation shows the lowest total thermal resistance of 2.03 $\mathrm{KW^{-1}}$, while the one manufactured from the low density 0.79 $\mathrm{gcm^{-3}}$ sheet with polymer impregnation shows the highest total thermal resistnace of 2.74 $\mathrm{KW^{-1}}$. The sink-to-ambient resistance does not vary significantly for all the measured heat sinks and remains at the value of approximately 1.6 $\mathrm{KW^{-1}}$. Its magnitude is independent of the clamping pressure and polymer impregnation. The average sink-to-ambient resistance of the heat sinks made of 1.25 $\mathrm{gcm^{-3}}$ sheet with the in–plane thermal conductivity of 243 $\mathrm{Wm^{-1}K^{-1}}$ is 7 % higher that of heat sinks made of 0.79 $\mathrm{gcm^{-3}}$ sheet with the in–plane thermal conductivity of 145 $\mathrm{Wm^{-1}K^{-1}}$. The sensitivity of the sink-to-ambient resistance to the thermal conductivity is dictated by the shape of the heat sink, its material properties, and the flowfield conditions. The low changes of the sink-to-ambient thermal resistance with the increased thermal conductivity of the high-density sheet must not be interpreted as a general trend, but only as a case-specific results. The primary reason for including the density as a parameter in this study was to investigate its effect on the TCR at the device-sink interface.

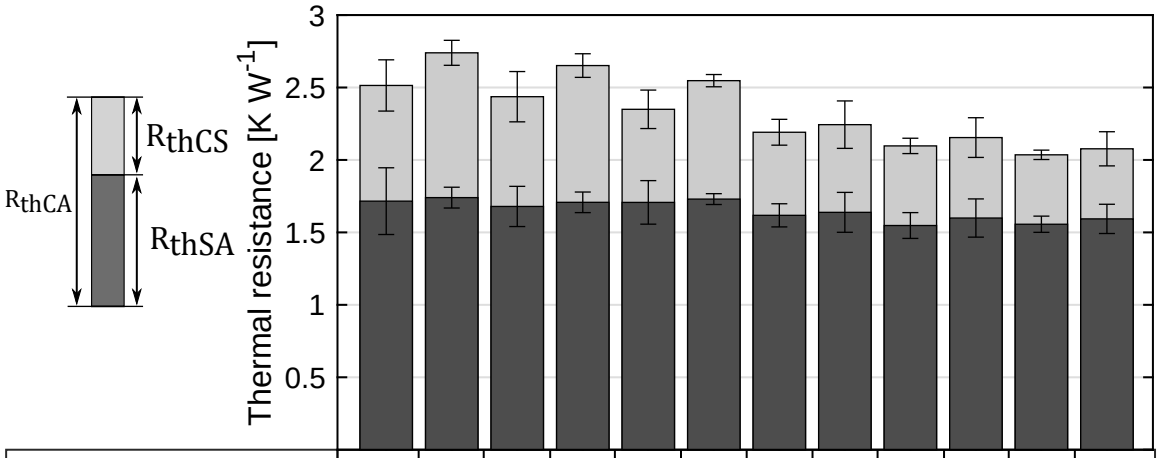

Polymer impregnated		×	✓	×	✓	×	✓	×	✓	×	✓	×	✓
Clamping pressure [MPa]		0.1		0.5		1		0.1		0.5		1	
NGS density [g cm^{-3}]		0.79						1.25					
Thermal conduct. [Wm^{-1}K^{-1}]	In-plane	145						243					
	Throuh-plane (at 100 kPa)	4.5						3.6					

Figure 5.14: Results of the measurement of small-scale NGS heat sinks

Figure 5.14 shows that the variation in the case-to-ambient resistance is primarily due to the variation in the case-to-sink resistance. In Figure 5.15, the case-to-sink resistance was plotted separately, and the overlapps of the error bars, which are relevant to judging the effect of polymer impregnation, were highlighted by the semitransparent gray areas with dashed-line borders. In all cases the error bars are overlapping, which prevents forming statistically significant conclusions. It appears that polymer impregnation causes an increase in the device-to-sink TCR and that the the low-density ($0.79\,\mathrm{gcm^{-3}}$) sheet is more sensitive to the effects of resin impregnation. The latter trend can be explained by the higher porosity of the low-density NGS that allows for a higher polymer uptake, which in turn causes an increases in hardness and TCR. The present data cannot confirm this assumption.

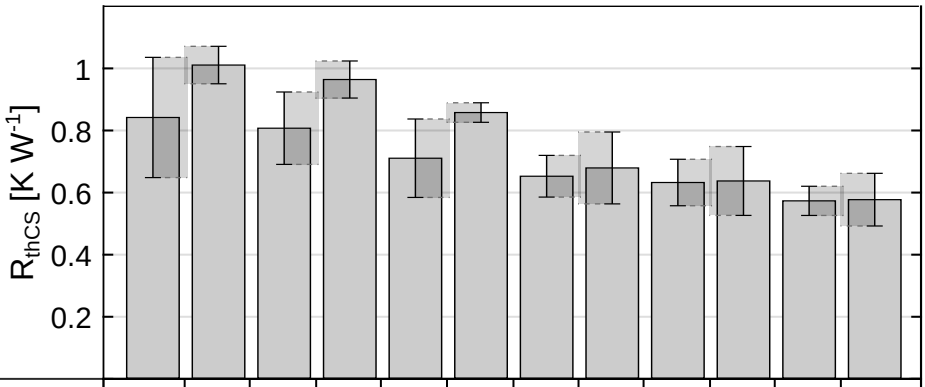

Polymer impregnated	×	✓	×	✓	×	✓	×	✓	×	✓	×	✓
Clamping pressure [MPa]	0.1		0.5		1		0.1		0.5		1	
NGS density [g cm^{-3}]	0.79						1.25					

Figure 5.15: The case-to-sink thermal resistance of small scale heat sinks. The order of the bars is selected to resolve the effect of resin impregnation. The overlapping error bars are highlighted by the semitransparent gray rectangles and dashed-line border

In Figure 5.16 the case-to-sink resistance was plotted in an order that allows for evaluating the effect of sheet density. Similar to Figure 5.14, the overlaps of error bars were highlighted to assist in the evaluation of uncertainty. In cases without polymer impregnation, the case-to-sink resistance appears to decrease with increasing density, however, the differences are within the uncertainty limit. For the polymer impregnated cases, the decrease is statistically significant and the sensitivity of the case-to-sink resistance to the increase in density is higher than that in cases without polymer impregnation. The explanation of the trend is in line with the statement in the previous paragraph. The difference in polymer uptake may affect the mechanical properties of NGS and the high-density can conform to the surface imperfections better than the low-density one.

It must be noted here, that the conclusions in section 5.1 stated that the case-to-sink resistance determined by the transient thermal method is affected by the thermal conduc-

tivity of the heat sink. In particular, increasing the heat sink thermal conductivity will lead to a lower case-to-sink resistance. It is likely that the lower case-to-sink resistance of the $1.25\,\mathrm{g cm^{-3}}$ heat sinks is partially or fully due to the higher in–plane thermal conductivity. To validate if increased NGS density leads to lower case-to-sink resistance, a standalone study of the TCR between stacked NGS and a metal counterpart must be studied using the specialized methods such as the guarded heat flow meter.

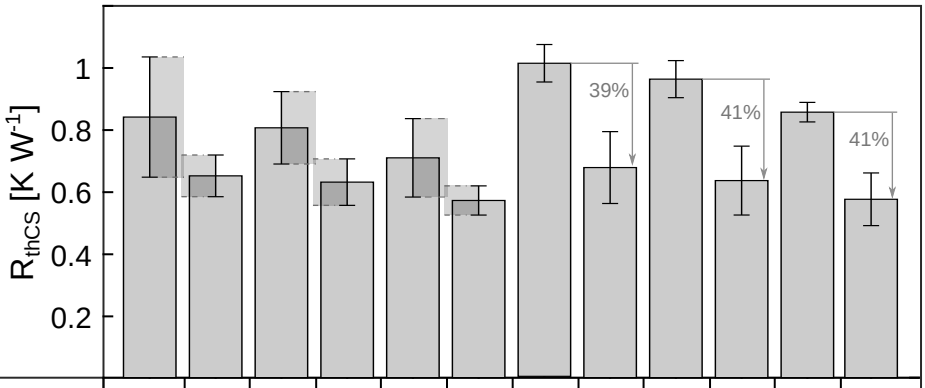

NGS density [g cm^{-3}]	0.79	1.25	0.79	1.25	0.79	1.25	0.79	1.25	0.79	1.25	0.79	1.25
Clamping pressure [MPa]	0.1		0.5		1		0.1		0.5		1	
Polymer impregnated	×						✓					

Figure 5.16: The case-to-sink thermal resistance of small scale heat sinks. The order of the bars is selected to resolve the effect of NGS density. The overlapping error bars are highlighted by the semitransparent gray rectangles and dashed-line border

The pressure dependence of the case-to-sink thermal resistance was plotted in Figure 5.17. All heat sink show a decrease in the case-to-sink resistance with increasing pressure, and the decrease is slightly steeper at high pressures. However, the large uncertainty results in the decrease being statistically significant only for the $0.79\,\mathrm{g cm^{-3}}$ sheet density without polymer impregnation. Calculating the decrease of the case-to-sink resistance over the measured pressure range 100 to 1000 kPa yields similar values in the range 16 to 20 % for all the measurements, which suggests that the pressure dependence is not affected by the polymer impregnation or NGS density. The decrease in the case-to-sink resistance is due to the decreased case-to-sink TCR, which is caused by a better compliance of imperfect surfaces at higher pressures.

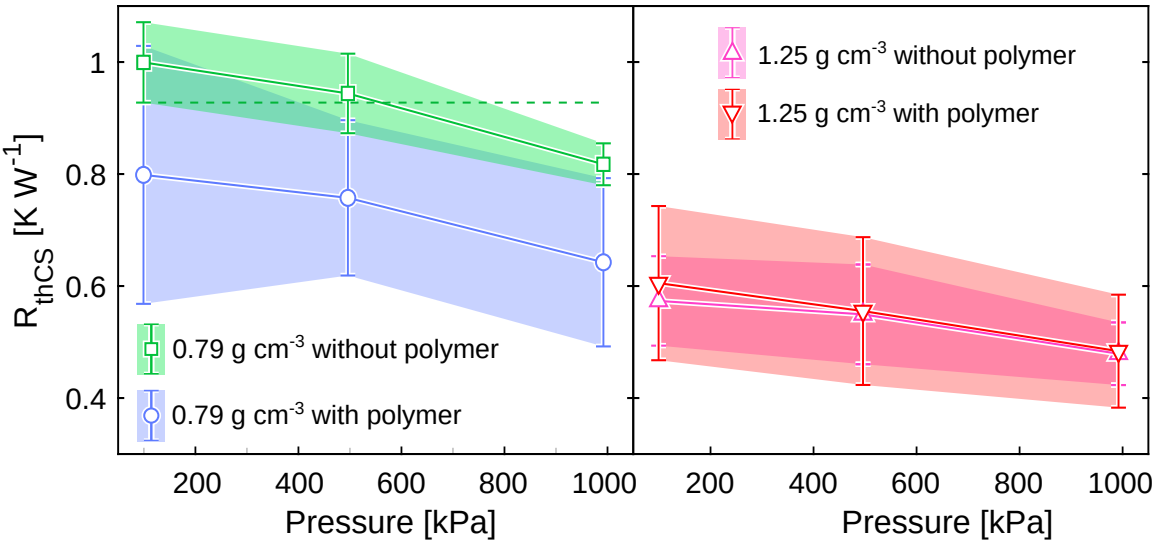

Figure 5.17: The case-to-sink thermal resistance of small-scale NGS heat sinks as a function of clamping pressure. The dashed line visualizes the only case (0.79 gcm^{-3} without polymer) where the decrease of the case-to-sink resistance is significant over the measured pressure range. In all other cases, the decrease is within the uncertainty limit.

5.2.3 Section conclusions

This section first focused on comparing the thermal performance of a NGS heat sink with a geometrically identical aluminum one. In the second part, the small scale NGS heat sinks were studied in detail with an emphasis on the effect of density, clamping pressure, and polymer impregnation.

The measured small scale NGS heat sink showed the total thermal resistance 33 to 36 % lower than the aluminum one without thermal grease and 15 to 16 % higher than the aluminum one with thermal grease. The total thermal resistance is a sum of the sink and interface resistances. Determining which of the two resistances causes the total resistance to increase is not possible due to the overlapping error bars.

The measurements of the effect of density, clamping pressure, and polymer impregnation are burdened with high uncertainty. The sink-to-ambient resistance does not change significantly with any of the studied parameters. The case-to-sink resistance of the polymer impregnated samples decreases by 40 % when the density increases from 0.79 gcm^{-3} to 1.25 gcm^{-3}. However, due to the inherent uncertainty of the transient thermal method, the change cannot be attributed to a decreased TCR at the device-sink interface. Instead, it is likely that the decrease is due to the increased in–plane thermal conductivity of NGS. Over the measured clamping pressure range 100 kPa to 1 MPa, the case-to-sink resistance of the 0.79 gcm^{-3} heat sink without polymer impregnation decreased by 20 %, which is can be attributed to the reduction in the TCR at the device-sink-resistance.

To address the high uncertainty in the future measurements, the following points should be considered. The variation in the collected data may arise from the heat sink manufacturing process. Improved manufacturing precision can lead to a reduced difference between heat sinks manufactured from the same material in the same batch. The repeatability of the TCR at the device-sink interface may be poor due to the different contact after re-mounting. Standalone measurements of the TCR using specialized equipment can help to explain the sensitivity of the TCR to re-mounting. The present data were collected at a facility where the ambient air temperature varied over the course of the day. Since one of the assumptions of the transient thermal method is a constant ambient temperature, the drift of the ambient temperature during the test could have affected the results. The effect of unsteady ambient temperature should be studied, and if proven to be significant, air conditioning at the inlet of the test bed should be considered.

5.3 Large-scale prototye NGS heat sinks with integrated heat pipes

In the study of small-scale heat sinks in the previous section, the width of the heat sink was kept comparable to that of the heat source so that the effect of the low through-plane thermal conductivity is minimized, and the complexity of the measurement is reduced. In this section, the focus is expanded to large heat sinks whose performance is limited by the low through-plane thermal conductivity. A concept of NGS heat sinks with embedded heat pipes is introduced, and the effect of electric insulation at the device-sink interface is studied.

5.3.1 Measurement description

Figure 5.18 shows the three heat sinks used for this study: i) reference CNC machined 6061 aluminum heat sink (AL), ii) NGS heat sink with aligning plastic rods in the base (NGS) and iii) NGS heat sink with two 4 mm diameter U-shape heat pipes (NGS+HP). The used heat pipes were 300 mm long, 4 mm in diameter, the manufacturer was Advanced Thermal Solutions Inc. and the product number ATS-HP-D4L300G20W-002. The shape of the heat sink was dictated by the NGS prototyping limitations and the it was not optimized for the best heat transfer under given conditions. All the heat sinks have 42 fins, and the target dimensions were 50.8 mm width, 34.1 mm height, 117.6 mm length, and 2.8 mm fin thickness. CNC machining delivered a perfect result, but the same level of accuracy was not possible when building the NGS heat sinks. As a result, the fin spacing and thicknes of the NGS and NGS+HP heat sinks varied by fractions of millimeters, which resulted in the total width of the NGS and NGS+HP heat sinks to be 119 mm and 123.7 mm, respectively. The CAD model of the heat sink is available in the accompanying data set [124]. Both NGS heat sinks were prepared from a 140 $\mathrm{mgcm^{-2}}$ NGS that was described in section 3.1. The final sheet density was 1 $\mathrm{gcm^{-3}}$, which corresponds to the in–plane and through–plane thermal conductivities of 190 $\mathrm{Wm^{-1}K^{-1}}$ and 4 $\mathrm{Wm^{-1}K^{-1}}$, respectively. To improve the mechanical strength and machinability, the sheets were polymer-impregnated with Hernon HPS 991 porosity sealant.

The measurement setup was designed to mimic the real-world power converters. A power electronics diode (IXYS DSEI 30-06A) was used as the heat source and each of the heat sinks was tested i) with no electrical insulation, ii) with an adhesive coated polyimide film insulator (Nitto P-221 [125], polyimide thickness 0.0254 mm, adhesive layer thickness 0.04 mm), and iii) with an aluminum oxide (Al_2O_3) insulating pad (Aavid 4169G [126], 19.23 mm x 13.84 mm x 1.57 mm).

The test setup consisted of an acrylic frame with two axial 40 mm diameter fans (JMC 4028-12) in an impinging flow configuration as shown in Figure 5.19. The fans were driven by a 5 V power supply and their alignment with the heat sink was kept by the mounting

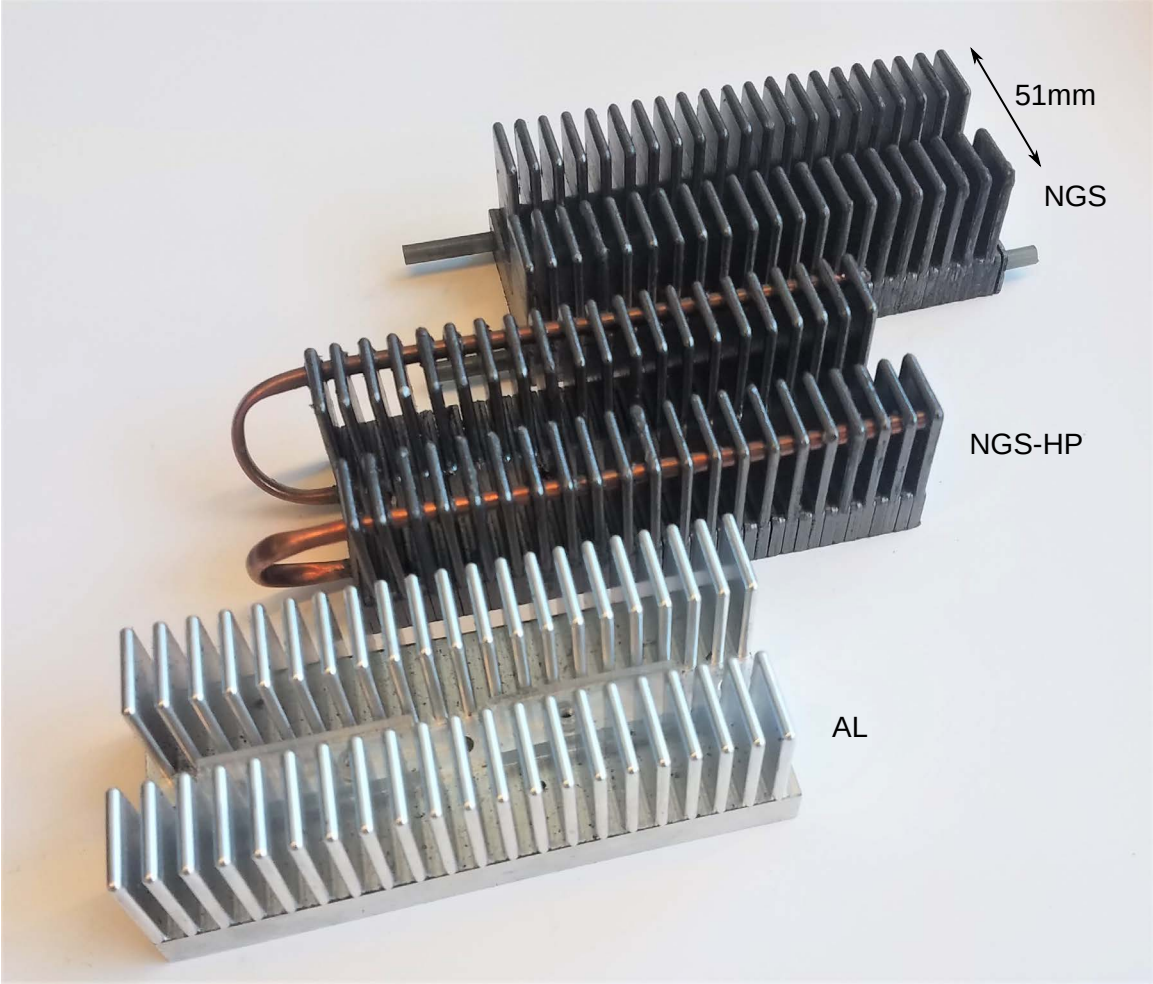

Figure 5.18: Three heat sinks manufactured for this study. AL - Aluminum, NGS - Natural graphite sheet, and NGS+HP - Natural graphite sheet with heat pipes

rods that fit into the holes in the base of the heat sink. The diode was attached to the heat sink with an M3 bolt, but since tapping threads in NGS is not possible, an acrylic part with a M3 nut was installed between the fins on the other side of the base. The bolt was tightened using the CDI 151NSM torque screwdriver set to 0.2 Nm, which translates to the contact pressure of 1 MPa.

Identically to the measurements of the small-scale heat sinks, the device (diode) temperature was measured by the Omega 5SRTC, T-type, 36 AWG thermocouple that was installed as shown in Figure 5.4. Four thermocouples were attached to the heat sinks using an aluminum tape at locations shown in Figure 5.19, and one thermocouple was used to sense the ambient air temperature at the inlet of the fans T_A. A labview interface was used to collect the temperature data at 1 s intervals. The measurement was considered to have reached the steady state when the slope of a line fitted thought the last 60 data points was less than $0.05\,^{\circ}\mathrm{Cmin}^{-1}$. A Chroma 62012P-40-120 programmable DC power supply kept

a constant I=15 A current through the diode, which translated to the dissipated heat of approximately 16 W. A National Instruments NI N9229 module **??** was used to measure the voltage drop V across the diode terminals so that the dissipated heat can be determined as:

$$\dot{Q} = VI. \tag{5.4}$$

The relevant thermal resistances were calculated as:

$$R_{thDS} = \frac{T_D - T_S}{\dot{Q}}, R_{thSA} = \frac{T_S - T_A}{\dot{Q}}, R_{thDA} = \frac{T_D - T_A}{\dot{Q}}, \tag{5.5}$$

where R_{thDS} is the device-to-sink thermal resistance, R_{thSA} is the sink-to-ambient thermal resistance, R_{thDA} is the device-to-ambient thermal resistance, T_D is the device temperature, T_S is the heat sink temperature, and T_A is the ambient air temperature. The values of the temperatures were calculated as averages over last 60 s of the measurements. The raw data, the implementation of the data processing method, CAD model of the heat sink, and additional images are available in [124].

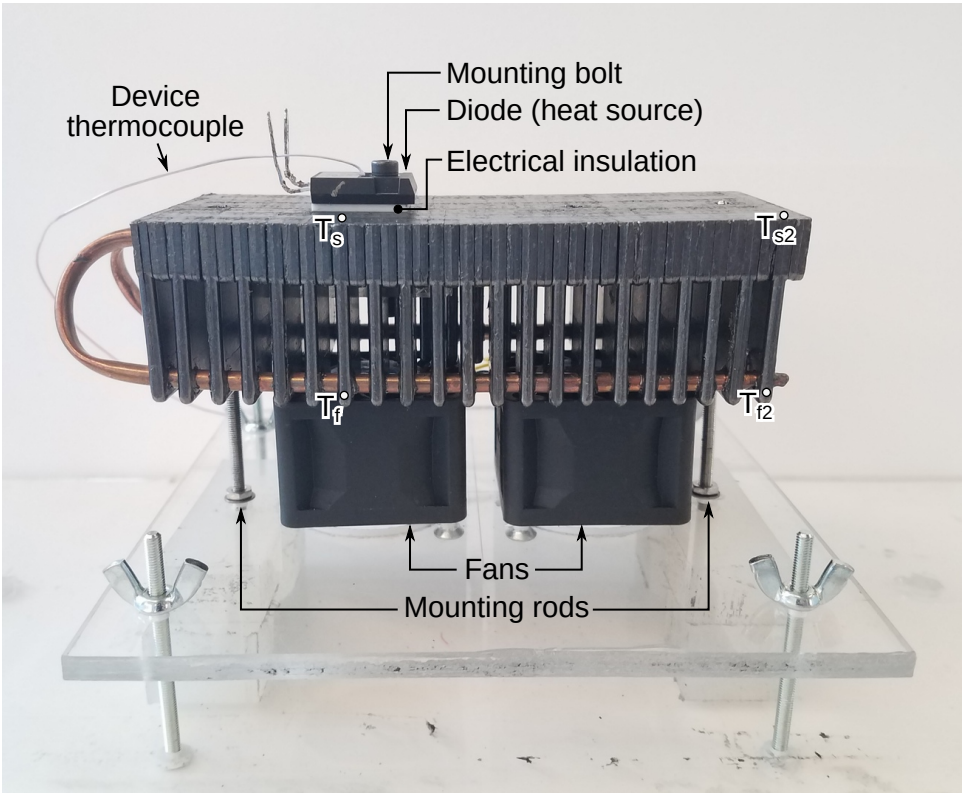

Figure 5.19: A photograph of the measurement setup with marked thermocouple locations.

5.3.2 Results

In Figure 5.20, the results are summarized in the bar chart form identical to the previous sections. The light gray bars represent the device-to-sink thermal resistance (R_{thDS}), the dark gray bars represent the sink-to-ambient resistance (R_{thSA}), and total height of the bars represents the total device-to-ambient resistance (R_{thDA}). The device-to-sink resistance corresponds to the portion of the total resistance due to the device, the insulation material, and the corresponding interfaces. The sink-to-ambient resistance corresponds the conduction within the heat sink and convection from the heat sink to the ambient air.

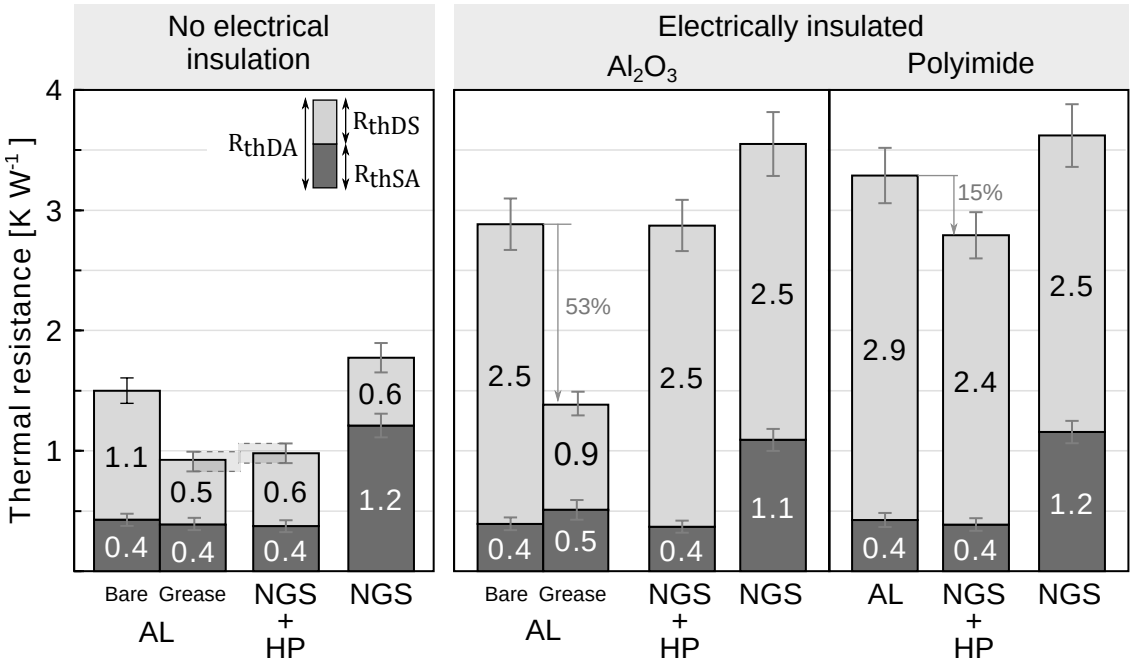

Figure 5.20: Measured thermal resistnace of AL, NGS-HS, and NGS heat sinks with and without electrical insulation.

In all measured cases, the AL and NGS+HP heat sinks show a comparable sink-to-ambient resistance of 0.4 to 0.5 KW^{-1}, while that of the NGS heat sink is approximately three times higher with the value of 1.1 to 1.2 KW^{-1}. In the measurements without electrical insulation, the total device-to-ambient resistance of the NGS+HP heat sink is comparable to that of the AL one with thermal grease, and the difference falls within the range of uncertainty as was highlighted by the semi transparent rectangles in Figure 5.20. It is therefore possible to conclude that for the considered geometry, NGS heat sinks with embedded heat pipes deliver the same thermal resistance as geometrically identical aluminum ones with thermal grease at the device-sink interface. As discussed in the previous section, the device-to-sink thermal resistance of NGS heat sinks is comparable to that of AL heat sinks with thermal grease because the lower hardness of NGS allows for a better conforming to sur-

face imperfections, which in turn results in a lower TCR. The reason for the comparable sink-to-ambient resistance of the NGS+HP and AL heat sinks is discussed below.

The difference between the sink-to-ambient resistance of the NGS and NGS+HP heat sinks is caused by an improvement in the heat transfer in the through–plane direction. In case of the NGS heat sink, the low through–plane thermal conductivity limits the heat spreading in the base of the heat sink. Adding the heat pipes mitigates this limitation and allows the heat to be spread easily into all the fins. The infrared camera images in Figure 5.21 clearly show that the temperature distribution in the NGS+HP heat sink is uniform, and that the entire heat sink dissipates the heat into the ambient air. In case of the NGS heat sink the hot spot below the heat source suggests that the heat cannot reach all the fins and only a small portion of the heat sink transfers the heat to the air.

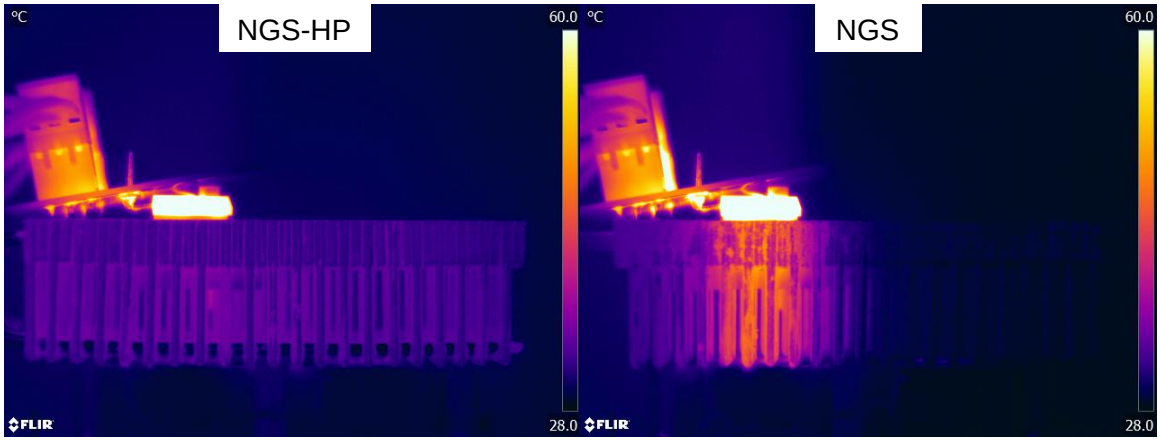

Figure 5.21: Infrared camera images of NGS+HP (left) and NGS(right) heat sinks

The qualitative analysis using the infrared camera was possible because the NGS and NGS+HP heat sinks were made from the same material and the emissivity did not vary. The same technique is significantly more complicated for comparing the NGS and AL heat sinks. The highly reflective aluminum surface reflects thermal radiation from other surfaces, which results in a measurement error. Anodizing can help by decreasing the reflectivity, but the difference in surface emissivity needs to be accounted for when comparing the infrared images. To investigate the difference in the detailed thermal behavior of NGS and AL heat sinks, an alternative analysis of based on thermocouple readings was used instead of thermal imaging.

The thermocouple locations are shown in Figure 5.22. The sink and ambient thermocouples T_S and T_A were used to calculated the sink-to-ambient resistance that describes the overall resistance of the heat sink. Detailed information about the heat conduction within the heat sink can be obtained by analyzing the readings of all the heat sink thermocouples. To do so in an intuitive way, the concept of a thermal performance diagram is introduced

in Figure 5.22. The normalized heat sink temperatures T^* are calculated as:

$$T^* = \frac{(T - T_A)}{\dot{Q}} \tag{5.6}$$

and plotted in a diagram with the location on the horizontal axis and T^* on the vertical axis. The shape created by connecting the T^* points can be used for evaluating the thermal performance of heat sinks. The vertical distance between T_S^* and T_{S2}^* determines the quality of heat spreading in the base. The vertical distance between T_S^* and T_F^* points is proportional to the temperature difference between the base and the tip of the fin located directly below the heat source. The vertical distance between T_{S2}^* and T_{F2}^* points is proportional to the temperature difference between the base and the tip of the right-most fin. Examples of the performance diagrams for three idealized heat sinks are given in Figure 5.23. The ideal isothermal heat sink, which would in practice require a material with very high thermal conductivity, is represented by a horizontal line. A heat sink with poor spreading in the base but perfect conduction in the fin direction (vertical direction in Figure 5.23) is represented by a rectangle whose area is proportional to the spreading resistance. A heat sink with perfect spreading in the base but poor conduction in the fin direction is represented by a line whose slope is proportional to the fin resistance.

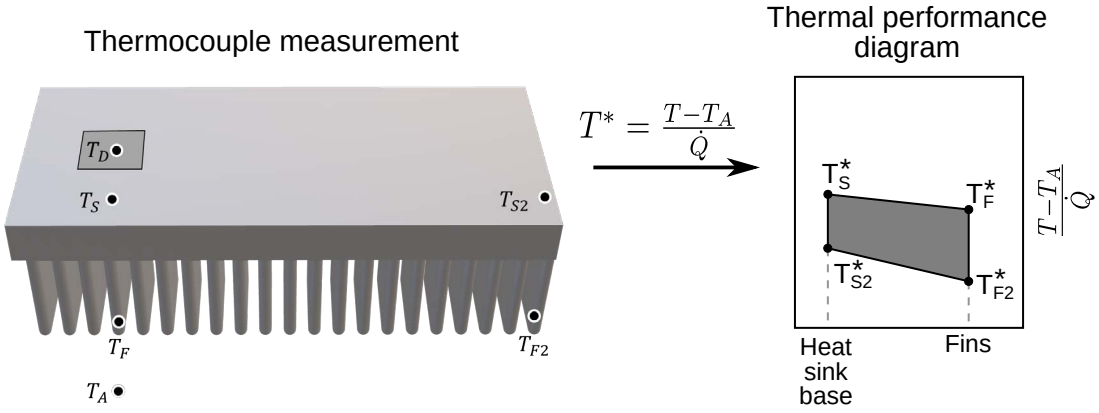

Figure 5.22: The thermocouple locations (left) and an illustration of the thermal performance diagram (right).

The thermal performance diagrams generated for the heat sinks in the present study are shown in Figure 5.23. The large red area of the NGS heat sink shows that spreading in the base limits its performance. Since the diagram is reaching zero in the vertical direction, it can be concluded that the right-most fin does not participate in the heat transfer, which is a conclusion that agrees with the measurements using an infrared camera. The diagram for the NGS+HP heat sink shows a significantly reduced vertical size, which indicates an improved heat spreading in the base. The T_F^* and T_{F2}^* points show a comparable value that is larger than zero, which suggests that the tip temperature of the two measured fins

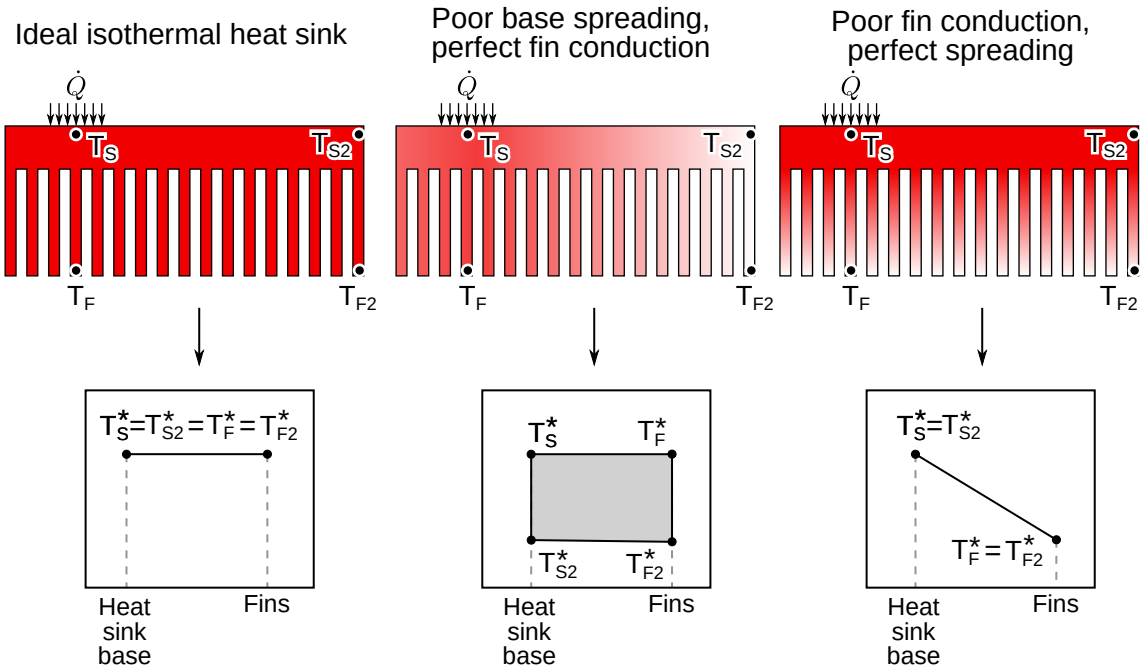

Figure 5.23: Examples of thermal performance diagrams for three idealized heat sinks

is identical, and that all the fins participate in the heat transfer with their entire length. The diagram of the AL heat sink is overlapping with the NGS+HP one which confirms the comparable performance seen in Figure 5.20. Evaluating the detailed difference between the diagrams for AL and NGS+HP heat sinks was omitted because the differences fall within the uncertainty limit.

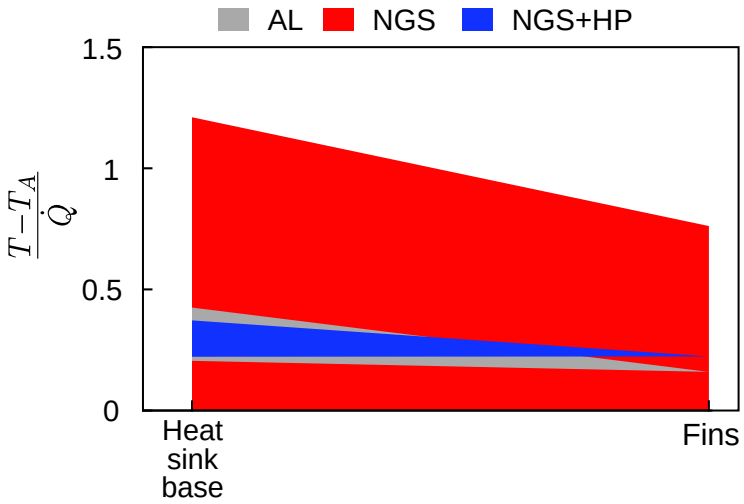

Figure 5.24: Thermal performance diagrams for the three measured heat sinks. The reference data were for the non-insulated case.

To make conclusions about the device-to-sink resistance, the data in Figure 5.20 were reduced and plotted in Figure 5.25. In the case without electrical insulation, the device-to-sink resistance of the the AL heat sink reduces by 50 % from 1.1 KW^{-1} to 0.5 KW^{-1} (note the numbers were rounded) when thermal grease is applied to the device-sink interface. The device-to-sink resistance of the NGS, NGS+HP, ands AL heat sinks is deemed to be identical because of the overlapping error bars. The trends in data agree with the results for the small scale heat sinks presented in Figure 5.12. The only difference is the magnitude of the reduction of the interface resistance after applying the thermal grease. The small scale heat sinks showed a 70 to 73 % decrease, while the large scale heat sinks showed a 50 % decrese.

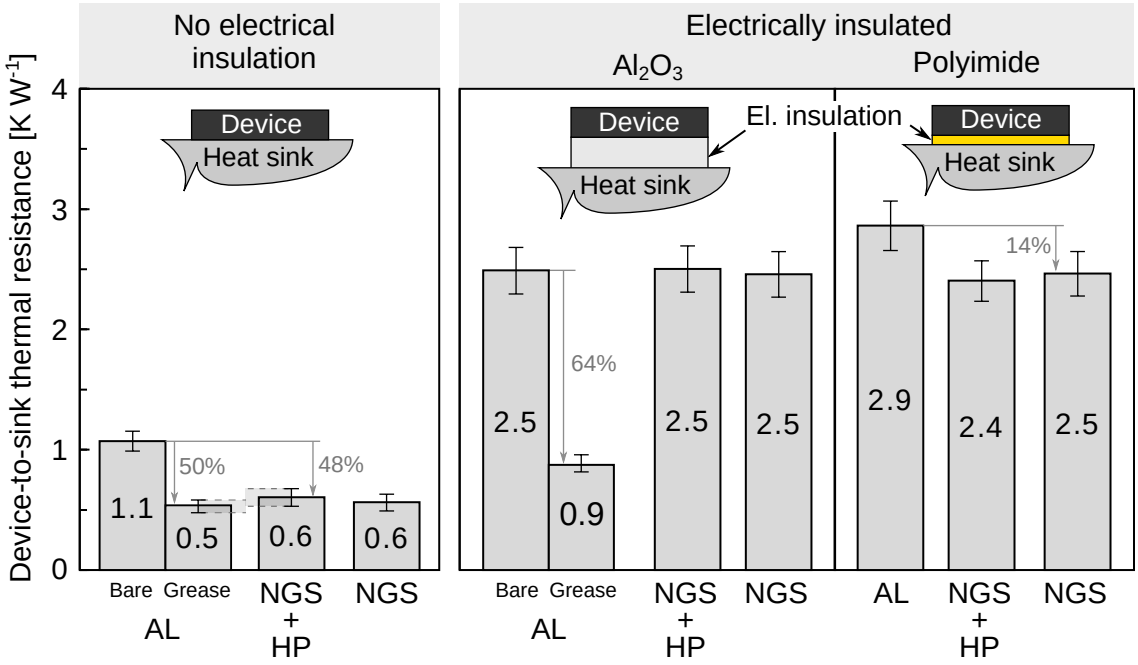

Figure 5.25: The device-to-sink thermal resistance for the measured large scale heat sinks.

Adding an electrical insulation increas the device-to-sink resistance to approximately 2.5 KW^{-1} with the exception of the polyimide film on AL heat sink for which the value reached 2.9 KW^{-1}. When Al_2O_3 insulation is used, no difference in the device-to-sink thermal resistance can be seen between the AL and NGS heat sinks. Since the only difference in the three Al_2O_3 measurements in Figure 5.20 is the TCR between the insulation pad and the heat sink, it can be inferred that the TCR at Al_2O_3-aluminum and Al_2O_3-NGS interfaces are equal, and the possibility to eliminate the need for a thermal grease seen in aluminum-NGS interfaces does not apply to Al_2O_3-NGS ones. While a detailed study of the TCR at Al_2O_3-aluminum and Al_2O_3-NGS interfaces is necessary to explain the present results, the SEM images in Figure 5.26 show that the surface structure of Al_2O_3 is substantially different in comparison with machined aluminum. It is likely that NGS cannot

conform to the fine surface features of Al_2O_3, but other parameters such as the thermal conductivity likely contribute to the TCR value too.

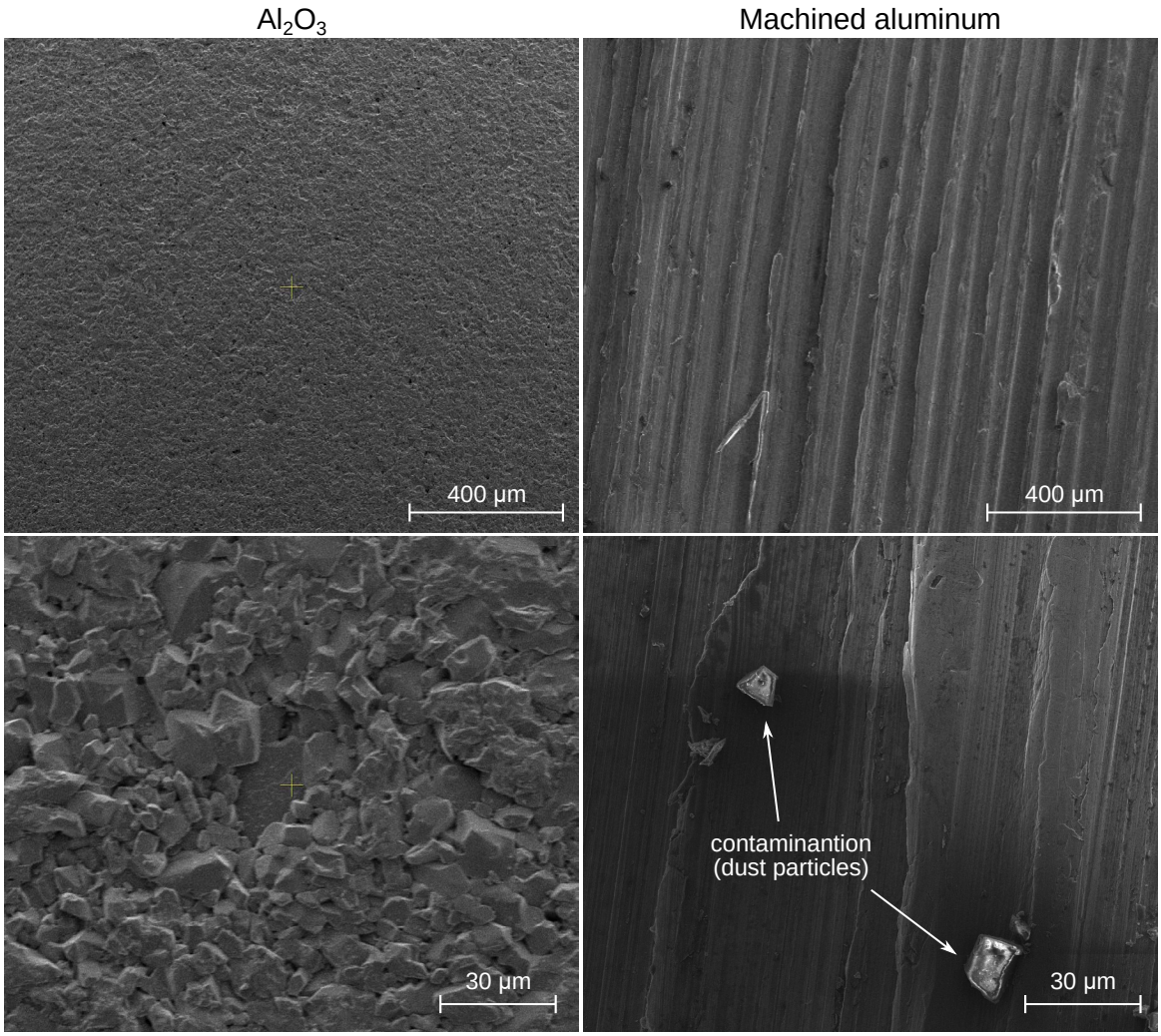

Figure 5.26: SEM images of the surface of an Al_2O_3 insulation pad (left column), and machined 6061 T6 aluminum (right column). The images of Al_2O_3 pad are a courtesy of Mikel Garcia Poulin. The images of machined aluminum are a courtesy of Zhongchen Zhang.

The results presented in Figure 5.20 suggest that when polyimide film is used for insulation, the device-to-sink resistance for the AL heat sink is $0.4\,\mathrm{KW}^{-1}$ higher than that of NGS and NGS+HP ones. The difference can be considered statistically significant because the error bars are not overlapping, however, the close proximity of the error bars makes the conclusion prone to error. Since the polyimide film was attached to the device in the same way in all of the measurements, the variation could only arise from the polyimide-aluminum interface. It can be therefore concluded that the TCR at polyimide-aluminum interfaces is higher than that at polyimide-NGS ones, which is in agreement with the measurements with no insulation.

The device-to-sink resistance is comparable for both the Al_2O_3 and polyimide insulation despite the vast difference in the thickness, which can be explained by considering the thermal conductivity of the insulation material. The thickness of the Al_2O_3 pad is 1.57 mm while that of polyimide film is 0.066 mm. The thermal conductivities are 18 $Wm^{-1}K^{-1}$ and approximately 1 $Wm^{-1}K^{-1}$, respectively [126, 127]. Assuming the device-sink interface area to be 314 mm^2, the bulk thermal resistance can be calculated as:

$$R_{th,b} = \frac{t}{kA} \; [KW^{-1}], \tag{5.7}$$

where k is the thermal conductivity and t is the thickness. The bulk thermal resistance is 0.27 KW^{-1} for the Al_2O_3 pad and 0.21 KW^{-1} for the polyimide film, which is only 11 % and 7 %, respectively, of the measured device-to-sink resistance of the AL heat sink. In the cases with electrical insulation, the device-to-sink resistance is dictated by not only the bulk properties of the insulation material, but also by the TCR at the interfaces. It must be also noted here that due to the location of thermocouples, the measured device-to-sink resistance is likely higher than the sum of bulk and interface resistances by the parasitic resistance that includes a part of the bulk resistance of the heat sink and the device, as was discussed in section 5.1. The magnitude of the parasitic resistance is a function of the thermocouple location, thermal conductivity of heat sink and lead frame, and other parameters that affect the temperature field in the heat sink and the device. To measure the TCR directly, standalone methods such as guarded heat flow meter should be used.

The importance of the interfaces is illustrated by the measurement of the AL heat sink with thermal grease applied at the device-Al_2O_3 and Al_2O_3-sink interfaces, which showed a 64 % reduction in device-to-sink thermal resistance compared to the case without a thermal grease. The reduction is comparable to the value of 75 % reported in [128].

The comparative study in this section was based on imposing the same convective conditions on all heat sinks. However, the effect of radiation was neglected. To verify the validity of neglecting the radiative heat transfer, the following simplified calculation was carried out. A box-shaped envelope with dimensions 50.8 mm by 34.1 mm by 117.6 mm was assumed to be the substitute radiation body and its area was calculated to be $A_R = 0.024m^2$. The temperature of the heat sink T_S was 31 °C based on the measurement data. The emissivity of NGS and aluminum was $\epsilon_{NGS} = 0.47$ and $\epsilon_{AL} = 0.1$, respectively. The radiative heat flux was calculated as:

$$\dot{Q}_R = \epsilon \sigma_{SB} A_R (T_S^4 - T_{A,R}^4), \tag{5.8}$$

where σ_{SB} is the Stefan–Boltzmann constant, and $T_{A,R} = 25$ °C is the temperature of the surrounding environment. The estimated radiative heat flux is 0.43 W for NGS and 0.09 W for aluminum, which is 2.7 % and 0.6 % of the total heat flux, respectively.

5.3.3 Section conclusions

Three geometrically identical heat sinks made of aluminum (AL), NGS without heat pipes (NGS), and NGS with heat pipes (NGS+HP) were manufactured and their thermal performance was measured. The sink-to-ambient thermal resistance of the NGS heat sink is $1.2\,\mathrm{KW}^{-1}$, which is three times higher than $0.4\,\mathrm{KW}^{-1}$ for the AL heat sink. The NGS+HP heat sink showed a comparable thermal resistance as the aluminum one. Adding the heat pipes mitigates the poor heat spreading in the base of the heat sink caused by the low through–plane thermal conductivity of NGS.

When no electrical insulation is used, the trends in the device-to-sink resistance agree with the small scale heat sink measurements in section 5.2. In particular, the interface resistance of NGS heat sinks is comparable to that of the AL heat sink with thermal grease. When an Al_2O_3 insulating pad is used between the device and the heat sink, the interface resistance of the NGS heat sinks is not comparable to the AL one with thermal grease. Using NGS heat sinks with adhesive-coated polyimide insulation offers a possibility to decrease the device-to-sink thermal resistance by 14 % with respect to the aluminum heat sink reference case.

In cases without electrical insulation, the overall device-to-ambient thermal performance of the NGS+HP heat sink is comparable to that of the reference AL one. Among all the electrically insulated configurations tested in this work, the AL heat sink with Al_2O_3 insulation and thermal grease shows the best device-to-ambient thermal resistance of $1.4\,\mathrm{KW}^{-1}$, which is 51 % lower than the best performing NGS case that consisted of the NGS+HP heat sink and polyimide insulation. Detailed studies of TCR at interfaces between NGS and insulating materials are required to determine whether NGS heat sinks can be a viable solution for applications requiring electrical insulation.

5.3.4 Uncertainty analysis

The raw measured quantities are the diode voltage $V'_{D,n}$, diode current $I'_{D,n}$, diode temperature $T'_{D,n}$, heat sink temperatures $T'_{S,n}$ and $T'_{S2,n}$, and fin temperatures $T'_{F,n}$ and $T'_{F2,n}$, where the subscript n represents the n-th repetition of the measured configuration. Each of the raw quantities was recorded in a 1 second interval, and the steady-state values $V_{D,n}$, $I_{D,n}$, $T_{D,n}$, $T_{S,n}$, $T_{S2,n}$, $T_{F,n}$, and $T_{F2,n}$ were calculated as averages of the last 60 samples. The corresponding standard deviations are $\sigma_{V_D,n}$, $\sigma_{I_D,n}$, $\sigma_{T_D,n}$, $\sigma_{T_S,n}$, $\sigma_{T_{S2},n}$, $\sigma_{T_F,n}$, and $\sigma_{T_{F2},n}$ were calculated from the same 60 samples.

The uncertainty of the steady-state temperatures $u_{T_D,n}$, $u_{T_S,n}$, $u_{T_{S2},n}$, $u_{T_F,n}$, and $u_{T_{F2},n}$ was determined as:

$$u_{T_x,n} = \sqrt{u_{T'}^2 + \sigma_{T_x,n}^2}, \tag{5.9}$$

where $u_{T'}$ is the uncertainty of the thermocouple measurement, which is given by the manufacturer as $\pm 0.5\,^{\circ}\mathrm{C}$ (T-type, Omega 5SRTC). The subscript x in eq. 5.9 was used instead of D, S, A, F, $S2$, and $F2$ to generalize the relationship for all the measured temperatures.

The uncertainties of the steady state diode voltage $u_{V_D,n}$ and current $\sigma_{I_D,n}$ were calculated as:

$$u_{V_D,n} = \sqrt{u_{V_D'}^2 + \sigma_{V_D,n}^2} \tag{5.10}$$

and

$$u_{I_D,n} = \sqrt{u_{I_D'}^2 + \sigma_{V_D,n}^2}, \tag{5.11}$$

where $u_{V_D'}$ and $u_{I_D'}$ are the uncertainties of the voltage and current measurements, respectively. Based on the equipment specifications [129, 130], $u_{V_D'}$ and $u_{I_D'}$ are:

$$u_{V_D'} = 0.3\,\% + 0.11\,\%F.S. = 0.003U + 0.0011 \cdot 62.64, \tag{5.12}$$

and

$$u_{I_D'} = 0.1\,\% + 0.1\,\%F.S. = 0.001I + 0.001 \cdot 24, \tag{5.13}$$

where $F.S.$ stands for the full scale.

A general relationship for a steady-state thermal resistance is:

$$R_{th,XY,n} = \frac{T_{X,n} - T_{Y,n}}{\dot{Q}_n} = \frac{\Delta T_{XY,n}}{\dot{Q}_n}, \tag{5.14}$$

where $\Delta T_{XY,n}$ is the temperature difference and $\dot{Q}_n$ is the heat flow. Using the partial derivative method the uncertainty of the thermal resistance $u_{R_{th,XY,n}}$ is:

$$\begin{aligned} u_{R_{th,XY,n}} &= \sqrt{\left(\frac{\partial R_{th,XY,n}}{\partial \Delta T_{XY,n}} u_{\Delta T_{XY,n}}\right)^2 + \left(\frac{\partial R_{th,XY,n}}{\partial \dot{Q}_n} u_{\dot{Q}_n}\right)^2} \\ &= \sqrt{\left(\frac{1}{\dot{Q}_n} u_{\Delta T_{XY,n}}\right)^2 + \left(\frac{-\Delta T_{XY,n}}{\dot{Q}_n{}^2} u_{\dot{Q}_n}\right)^2}, \end{aligned} \tag{5.15}$$

where $u_{\Delta T_{XY,n}}$ and $u_{\dot{Q}_n}$ are the uncertainties of temperature difference and heat flow, respectively. The uncertainty of the temperature difference is:

$$u_{\Delta T_{XY,n}} = \sqrt{u_{T_X,n}^2 + u_{T_Y,n}^2}. \tag{5.16}$$

The heat flow was calculated from the current and voltage measurements as:

$$\dot{Q}_n = V_{D,n} I_{D,n}, \tag{5.17}$$

and the resulting uncertainty is:

$$u_{\dot{Q}_n} = \sqrt{\left(\frac{\partial \dot{Q}_n}{\partial V_D} u_{V_D,n}\right)^2 + \left(\frac{\partial \dot{Q}_n}{\partial I_{D,n}} u_{I_D,n}\right)^2} = \sqrt{(I_{D,n} u_{V_D,n})^2 + (V_{D,n} u_{I_D,n})^2}. \tag{5.18}$$

The steady state thermal resistances $R_{th,DS,n}$, $R_{th,SA,n}$, $R_{th,DA,n}$ and the corresponding uncertainties $u_{R_{th,DS,n}}$, $u_{R_{th,SA,n}}$, $u_{R_{th,DA,n}}$ were calculated for each of the repetitions by substituting the relevant values into equations 5.14 and 5.15. The final reported thermal resistance values were calculated as averages of the repetitions:

$$R_{th,XY} = \frac{1}{N} \sum_{n=1}^{N} R_{th,XY,n}, \tag{5.19}$$

where N is the number of repetitions. The corresponding uncertainties are:

$$u_{R_{th,XY}} = \sqrt{(\frac{1}{N} \sum_{n=1}^{N} u_{R_{th,XY,n}})^2 + \sigma^2_{R_{th,XY}}}, \tag{5.20}$$

where the term $\frac{1}{N} \sum_{n=1}^{N} u_{R_{th,XY,n}}$ is the average uncertainty of the N steady-state values, and $\sigma_{R_{th,XY}}$ is the standard deviation of the N steady-state values.

5.4 Thermal contact resistance at NGS-metal interface

The results of the measurements of small scale and large scale heat sinks in sections 5.2 and 5.3 suggest that in applications where no electrical insulation is needed, NGS heat sinks are a feasible alternative to aluminum because the TCR at the device-sink interface is comparable to aluminum with thermal grease. The discussion in section 5.1 revealed that the interface resistance measured by the thermocouple and transient thermal methods does not capture the device-to-sink TCR accurately. The value of the device-to-sink TCR is required for validating the conclusions of the small scale and large scale results, but also for modeling the performance of NGS heat sinks. This section describes the measurement carried out to obtain the value of the TCR at NGS-metal interfaces.

NGS has been previously used as a thermal interface material (TIM). In such applications, thin NGS is inserted between two hard surfaces to reduce the interface resistance, as is shown in Figure 5.27a. In case of NGS heat sinks, the sheets are stacked and attached to a heat source as shown in Figure 5.27b. In TIM applications, the heat flows through the surfaces whose normal is parallel to the NGS compression direction, and the relevant TCR can be denoted as $TCR_{\parallel}$. In the heat sink applications, the heat flows through the surfaces whose normal is perpendicular to the NGS compression direction, and the relevant TCR can be denoted as $TCR_{\perp}$. Due to the high anisotropy of NGS material properties, it is likely that $TCR_{\parallel}$ and $TCR_{\perp}$ are not equivalent and must be measured separately. Throughout this section, it was assumed that the TCR at NGS-metal interfaces is independent of the type of metal because of the high hardness and thermal conductivity of metals.

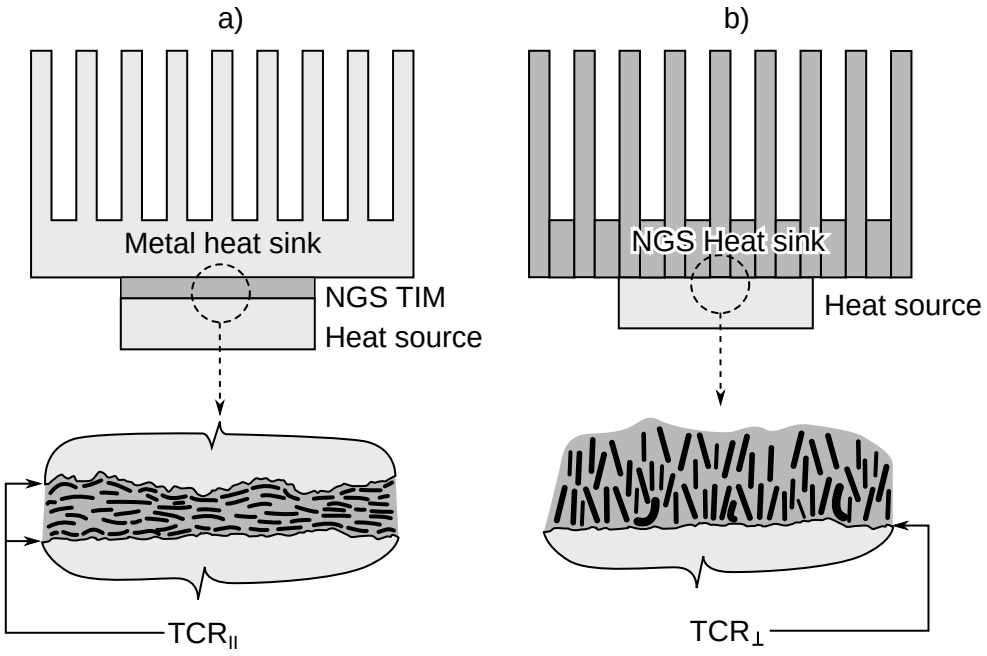

Figure 5.27: Illustration of differences in TCR of NGS in a) thermal interface material applications and b) heat sink applications.

5.4.1 Previous work

Smalc et al. [81] measured the through–plane thermal conductivity of NGS using the guarded heat flow meter method and evaluated $TCR_{\parallel}$ at the interface between the sample and the copper flow meter. $TCR_{\parallel}$ for pure NGS was $132\,\mathrm{mm^2KW^{-1}}$, and that for NGS impregnated with a mineral and synthetic polymer was $59\,\mathrm{mm^2KW^{-1}}$ and $67\,\mathrm{mm^2KW^{-1}}$, respectively. The density of the measured samples was not reported.

Marotta et al. (2005) [29] developed a model for predicting the interface thermal resistance of metal-metal joints with NGS used as a TIM. The model was validated using the experimental data for the range of pressures from 34.4 to 1033.7 kPa. At pressures below 413.5 kPa the joint resistance was deemed to be dominated by the gaps at the NGS-metal interfaces, while above 413.5 kPa, the resistance was deemed to be dominated by the through–plane thermal conductivity of NGS. The density of the NGS sheet was not reported.

To calculate $TCR_{\parallel}$ from the results reported by Marotta et al. (2005) [29], the bulk resistance must be subtracted from the interface resistance. The thermal conductivity was properly reported only at 172.3 kPa, and therefore $TCR_{\parallel}$ can be calculated only at that pressure. It should be noted that the through–plane thermal conductivity reported by Marotta et al. (2005) [29] is significantly higher than that measured in this work. However, the contribution of the bulk resistance to the interface resistance is expected to be low at low

pressures, and the possible error in the thermal conductivity does not affect the calculated $TCR_{\parallel}$ significantly. The calculated value of $TCR_{\parallel}$ at 172.3 kPa is 18 $\mathrm{mm^2KW^{-1}}$.

In another publication by Marotta et al. (2003) [35], the authors built a parallel plate graphite/epoxy heat sink, which was used in a configuration shown in Figure 5.27b. $TCR_{\perp}$ at the interface between the heat source and heat sink can be calculated from the reported temperature drop and heat flow. The values ranged from 34 to 194 $\mathrm{Kmm^2W^{-1}}$. The range is due to the variation in surface flatness, and due to using two thermal interface materials (PAO-100 synthetic oil and PowerStrate60 phase change TIM).

5.4.2 Experimental method

The measurements were performed using the Mentor Graphics DynTIM tester whose development was summarized by Vass-Várnai et al. [131]. The samples were prepared from a 1.23 $\mathrm{gcm^{-3}}$ sheet that was cut and stacked into two approximate cylinders with the diameter of 12.8 mm, and length of 15 mm and 35 mm as shown in Figure 5.28. To explore the effect of polymer impregnation on $TCR_{\parallel}$, two sets of samples were prepared. The first one was made of pure NGS, while the other one was impregnated with Hernon HPS 991 porosity sealant. The compression pressure was 1100 kPa, which is higher than the typical clamping pressure in eletronic cooling assemblies. However, the measuring equipment did not allow using a lower pressure.

Figure 5.28: A photograph of samples for measuring the $TCR_{\perp}$ at NGS-metal interfaces

The output of the DynTIM tester is the thermal resistance and thickness of the measured sample. The two-thickness method, whose principle was described in section 3.8, was used to determine the TCR between the NGS sample and the copper jaws. All collected data points were plotted in Figure 5.29. The values of $TCR_{\perp}$ and the thermal conductivity were calculated from the slope of the linear fits. The calculation steps were identical to those used for calculating electrical conductivity in section 3.8.

5.4.3 Results

As summarized on the right side of Figure 5.29, the measured specific $TCR_{\perp}$ for the pure and polymer-impregnated samples is $46\,\mathrm{mm^2KW^{-1}}$ and $230\,\mathrm{mm^2KW^{-1}}$, respectively. The calculated values of thermal conductivity can be used to validate the measurements by comparing them to the values of the in–plane thermal conductivity obtained in section 3.7. For the pure samples, the value calculated in this section is $200\pm32\mathrm{Wm^{-1}K^{-1}}$ and that in section 3.7 is $240\pm15\mathrm{Wm^{-1}K^{-1}}$, which is a satisfactory agreement, and $TCR_{\perp}$ of the pure sample is therefore considered valid.

The measurement of the polymer-impregnated samples showed the in–plane thermal conductivity of $654\pm225\mathrm{Wm^{-1}K^{-1}}$, which suggests that the result is not valid. Observing the data points in Figure 5.29 reveals that the long 35 mm samples showed a comparable thermal resistance for both pure and polymer-impregnate NGS. The thermal resistance of the short 15 mm samples varies substantially, and the data for the polymer-impregnated samples are significantly higher that those for pure NGS. It is likely that the poor flatness of the small polymer-impregnated sample caused the measurement to be unreliable. The measured value of $TCR_{\perp}$ for the polymer-impregnated samples is not considered valid and the measurement should be repeated.

In Figure 5.30, the measured $TCR_{\perp}$ was compared to the data in the literature. The present value of $47\,\mathrm{mm^2KW^{-1}}$ at 1100 kPa is comparable to the low-range values in the study by Marotta et al. (2003) [35]. Since the pressure was not reported, it is impossible to comment on the reasons for the observed trend. In addition to the NGS, the TCR of several common thermal greases were included in Figure 5.30. $TCR_{\perp}$ at metal-NGS interfaces appears to be comparable to the TCR of metal-metal ones with the thermal grease that performed the best in the study by Narumanchi et al. [132]. It must be noted that the pressure was not the same and the difference should be addressed in the future work.

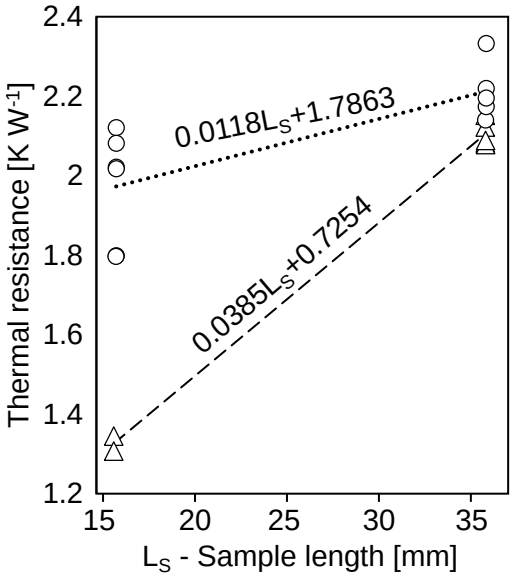

Symbol		△−−	○·····
Sample		NGS	NGS w/ polymer
Line fit	Slope	0.0385	0.0118
	Intercept	0.7254	1.7863
Measured thermal conductivity [W m^{-1} K^{-1}]		200 ± 32	650 ± 225
Expected thermal conductivity [W m^{-1} K^{-1}]		240	-
Specific TCR [mm^2 K W^{-1}]		47 ± 16	230 ± 38

Figure 5.29: Results of the TCR measurements.

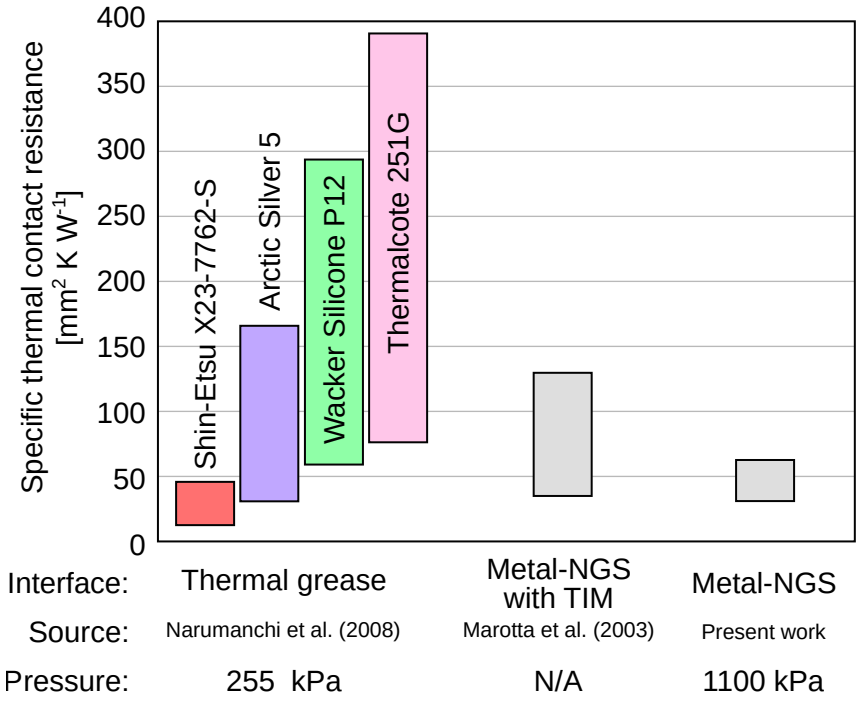

Figure 5.30: Comparison of the results of the TCR measurements with the literature data for commonly used thermal interface materials. The lower and upper limits of the thermal grease data are related to bond line thicknesses of 31 µm and 200 µm. The data by Marotta et al. [35] for NGS were collected with PAO-100 synthetic oil and PowerStrate60 phase change thermal interface materials. Both the present data and data by Marotta et al. [35] correspond to $TCR_{\perp}$ (see definition in section 5.4.1)

.

5.4.4 Section conclusions

A first-approach measurement of the specific TCR between stacked NGS and metal was performed and yielded the value of $47\,\mathrm{mm^2KW^{-1}}$ at 1100 kPa. The quality of the heat transfer through a NGS-metal interface is comparable to that of metal-metal interfaces with commonly used thermal greases. Further measurements to understand the effect of density, surface roughness, and clamping pressure need to be carried out in the future. The DynTIM tester was used in the present study for its ease of use and short measurement time. However, the low pressure spectrum could not be measured and the fixed jaws of the machine did not allow for exploring the effect of the metal surface roughness. The future work should consider using the guarded heat flow meter method that is typically used for TCR measurements. To bypass the complex and time-consuming sample preparation employed in this work, using samples and flux meters with square cross-sections is suggested instead of circular ones. Caution should be exercised during the design of the experiment as the TCR at low pressures is expected to be highly sensitive to sample mounting.

5.5 Chapter conclusions

Experimental characterization of heat sinks is limited by the capabilities of available methods. Using the data from the transient thermal method to calibrate 3D numerical model is predicted to provide a better tool for identifying the heat transfer bottlenecks. However, the necessary equipment is costly, the model calibration requires high computational power, and the methods for evaluating uncertainty yet need to be developed. Thermocouples will likely remain the most popular choice despite the labor intensity because of the simplicity and low cost.

When electrical insulation is not required, both the small scale and large scale NGS heat sinks can deliver a thermal performance comparable to geometrically identical aluminum heat sinks without the need to use thermal grease. In case of small scale NGS heat sinks, the low through–plane thermal conductivity of NGS does not significantly affect the thermal performance. In case of large scale heat sinks, embedding heat pipes into the heat sink base mitigates the poor heat spreading caused by the low through–plane thermal conductivity. The reason for the good performance of NGS is its soft complying nature that results in a low thermal contact resistance that is comparable to metal-to-metal interfaces with commercially available thermal greases.

Chapter 6

Electromagnetic performance of heat NGS sinks

In switch mode power converters, the voltage at the lead frame of power switches follows a trapezoidal waveform with the typical amplitudes of up to 400 V and frequencies of tens to hundreds of kiloHertz. Parts in the proximity of the switches, such as heat sinks, become capacitatively and inductively coupled to the switches, which causes a degradation of the optimal shape of the voltage waveform [133], and allows unwanted currents to flow to other parts of the circuit or the ground. Additionally, the high frequency currents generate unwanted electromagnetic waves, which can disturb the function of components within the same device, or in other devices nearby. The size, shape, and material of a heat sink affects the magnitude of the parasitic capacitances and inductances, as well as the magnitude, harmonic content, and directionality of emitted electromagnetic waves. In the power electronics community, the unwanted currents and electromagnetic waves are referred to as conducted and radiated emissions, respectively, and the sub-discipline is known as electromagnetic interference (EMI) or electromagnetic compliance (EMC). Methods to mitigate or reduce the emissions exist and have been described for example in [134, 135].

This chapter aims to investigate if a reduction in emissions can be achieved by substituting conventional aluminum heat sinks with ones made of NGS. The main motivation for this work was the two-to-four orders of magnitude difference in the electrical conductivity which is shown in Figure 6.1. An audiovisual summary of the chapter is available at `https://www.youtube.com/watch?v=CKv9vtzhAOA&list=PLaX55SIXaD20NQQ2JLP-7abmET7l-6LS4&index=5` [1].

[1] The video files are also available in Appendix F

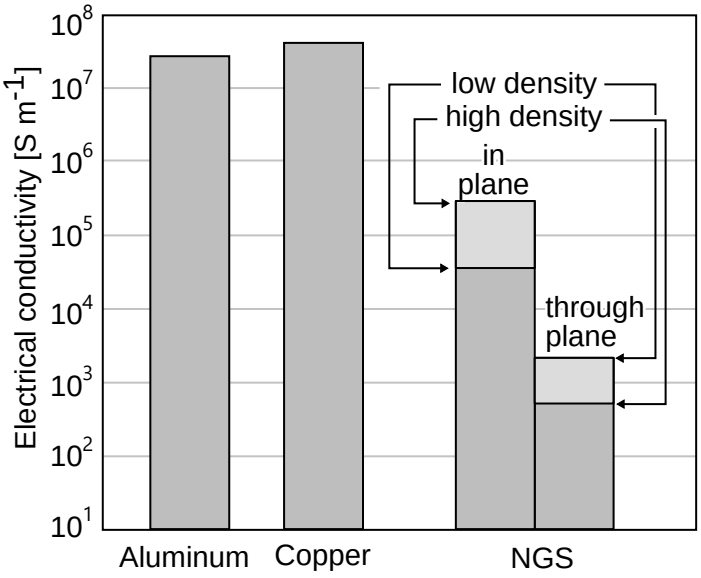

Figure 6.1: Comparison of electrical conductivity of aluminum, copper, and NGS.

6.1 Conducted emissions

In a typical power converter, multiple discrete semiconductor devices (transistors or diodes) are mounted on a heat sink as is illustrated in Figure 6.2. The electric insulation between the device and the heat sink prevents any direct current from flowing through the device-heat sink interface. However, since the interface acts as a parallel plate capactior with the capacitance C_{D-HS}, alternating current can flow through the interface and return to the device either through other devices or the ground. The currents flowing through the heat sink and the ground are referred to as the common mode conducted emissions, while the currents flowing from a device through the heat sink to another device are referred to as the differential mode conducted emissions. In Figure 6.2, the resistances of the heat sink for the differential mode and common mode emissions were labeled $R_{HS,DM}$ and $R_{HS,CM}$, respectively. The heat sink resistance is low and negligible for highly conductive metal heat sinks but can become significant for lossy materials such as NGS. The illustrated example represents the case of an isolated grounded heat sink, but other designs are possible. The heat sink can be floating (ungrounded), or connected to other parts of the circuit such as the 0 V trace.

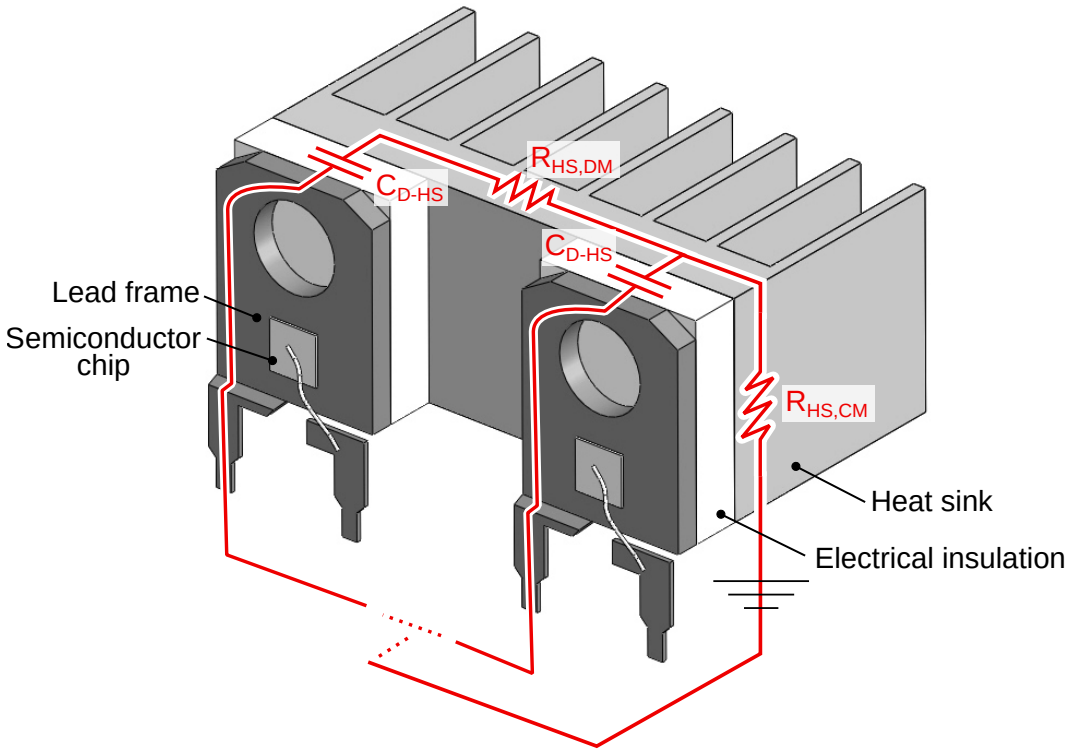

Figure 6.2: Illustration of paths for differential-mode and common-mode conducted emissions.

6.1.1 Previous work

Williams [14] modeled and measured the common mode conducted emissions of three circuit configurations in which a power transistor was i) electrically connected to the heat sink, ii) insulated from the heat sink, which was connected to the 0 V trace, and iii) mounted directly on the chassis with a layer of electric insulation. Both the predicted and experimental data showed that the configuration ii) had the lowest emissions, followed by i) and iii). The author noted the trade-off between the EMI and thermal performance, and pointed out that in many case the configuration iii) has the best thermal performance. If the configuration iii) is necessary, additional filtering using capacitors was suggested to mitigate the high conducted emissions.

Grobler and Gitau [136] investigated the effect of the heat sink material on the thermal and EMI performance of low power converters. In their experiments, a TO-247 transistor was bolted to a natural-convection-cooled heat sink in a form of a block 7 cm by 6 cm by 1 cm. Aluminum was used as the reference material, and the performance of epoxy and urethane resins with and without up to 82 % (per mass) of copper particles were tested. For the aluminum heat sink, a silicone insulating pad was used between the transistor and

the heat sink. For the resin heat sink, the transistor was mounted directly on the heat sink. Measurements of the transistor-to-ground capacitance resulted in the value of 40 pF for the reference aluminum heat sink, and the range of 2.15 to 7.07 pF for the four resin heat sinks where the higher values correspond to the copper filled resins. The lower capacitance of the epoxy heat sinks resulted in approximately 25 % decrease in the common-mode emissions in the range of frequencies from 300 kHz to 20 MHz. At higher frequencies, the emissions of aluminum and resin heat sinks were comparable. No difference in differential-mode emissions was seen. The temperature of the transistor was monitored by an infrared camera and the results showed the value of 36.7 °C for the aluminum heat sink, and 41.2 to 54.7 °C for the resin heat sinks (the lower values of the range corresponded to the copper filled resins). When a nylon bolt was used for clamping instead of a steel one, the transistor-to-ground capacitance reduced by 2.2 pF.

Gong and Ferreira [137] pursued a reduction of conducted emissions in a 2.2 kW inverter for motor drives. The baseline design, which included a single large heat sink, was modified by cutting the heat sinks into six separate heat sinks. Only a minor reduction in common-mode and differential mode emissions was seen, and further modifications including snubbers and ferrite beads were necessary to achieve the given emission target. A similar study was performed in the PhD thesis by Dolente [138]. In the majority of the measured frequency range, no significant difference between the single large heat sink and four small heat sinks was observed. However, the conducted emissions of the separated configuration were up to 10 dB lower at frequencies around 5 MHz.

6.1.2 Theoretical analysis

The following analysis focuses on the common mode emissions, which are typically more difficult to mitigate and their magnitude is affected by the heat sinks more than in the case of differential mode emission [139]. While in a real world converter there are multiple paths for the common mode current, in a well designed converter the path going through the heat sink is dominant [139].

In Figure 6.3a, the assumed equivalent circuit is overlaid on a section-view of the heat sink assembly. For improved clarity, the circuit has been isolated in Figure 6.3b, and all the elements were labeled there. The circuit contains the excitation voltage source V_{EX}, device-to-heat sink capacitor C_{D-HS}, heat sink resistance $R_{HS,CM}$, heat sink inductance $L_{HS,CM}$, and the impedance of the ground coupling Z_G.

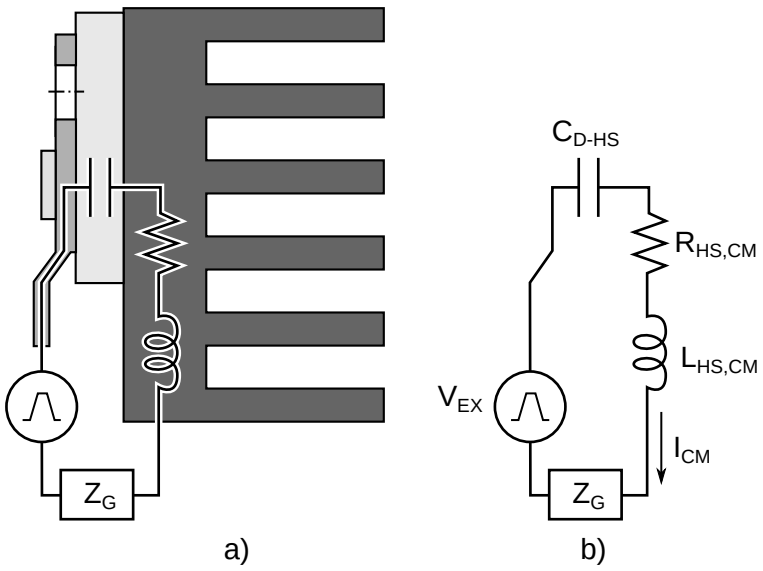

Figure 6.3: The equivalent circuit for the theoretical analysis of common-mode conducted emissions.

The current I through the circuit is given as:

$$I_{CM} = \frac{V_{EX}}{Z_{CM}}, \tag{6.1}$$

where Z_{CM} is the total impedance of the circuit, which is:

$$Z_{CM} = R_{HS,CM} + j\omega L_{HS,CM} - j\frac{1}{\omega C_{D-HS}} + Z_G. \tag{6.2}$$

The impedance of the ground coupling Z_G and the inductance of the heat sink L_{HS} are dependent on the physical circuit layout and the heat sink geometry. The goal of this analysis is to compare aluminum and NGS. Z_G and L_{HS} were considered to be identical in the two cases, which allows eliminating them in the further calculations. As a result, Equation 6.2 reduces to:

$$Z_{CM} = R_{HS} - j\frac{1}{C_{D-HS}\omega}. \tag{6.3}$$

The magnitude of the overall common mode impedance, which is proportional to the amplitude of the common mode current, is:

$$|Z_{CM}| = \sqrt{R_{HS}^2 + (\frac{1}{C_{D-HS}\omega})^2}. \tag{6.4}$$

The term on the right is the contribution of the capacitor to the overall impedance. By evaluating its magnitude, it is possible to estimate what values of the heat sink resistance can significantly affect the common mode current. The capacitance C_{D-HS} is known to be

in the order of tens of pico Farads for TO-247 devices [136]. In this analysis, a conservative value of 10 pF was assumed. The contribution of the C_{D-HS} capacitance to the overall impedance at 1 MHz is:

$$\frac{1}{C_{D-HS}\omega} = \frac{1}{C_{D-HS}2\pi f} \approx 15\,\text{k}\Omega, \tag{6.5}$$

and therefore the heat sink resistance would have to be in the order of kilo Ohms to significantly contribute to the overall impedance. A conservative estimate of the heat sink resistance can be made by ignoring the fins and assuming that the current flows only through the base of the heat sink. Using the through–plane NGS resistivity ρ_{th} of 0.1 Ωcm and the length L, width W, and height H of the base plate of 10 cm, 5 cm, and 0.8 cm, respectively, the estimated NGS heat sink resistance is:

$$R'_{NGS} = \rho_{th}\frac{L}{WH} = 0.25\,\Omega, \tag{6.6}$$

which is five orders of magnitude lower than the capacitive contribution. NGS heat sinks are therefore not expected to affect the conducted emissions significantly.

6.1.3 Impedance measurements

To verify the theoretical analysis in the previous section, the heat sinks described in Chapter 5 were measured using the Keysight E4990A Impedance analyzer with the 42941A probe as shown in Figure 6.4. The labeling of the heat sinks is the same as in section 5.3, namely AL for the reference aluminum heat sink, NGS for the baseline NGS heat sink, and NGS+HP for the NGS heat sink with embedded copper heat pipes. Same as in the thermal measurements, three cases were measured for each of the three heat sinks: i) no electrical insulation, ii) adhesive-coated polyimide film insulation, and iii) Al_2O_3 insulation pad. Four measurement repetitions were performed for each of the cases. The raw data, the implementation of the data processing method, CAD model of the heat sink, and additional images are available in [124]. The measured impedance is shown in Figure 6.5 where the the absolute value (amplitude) $|Z|$ and phase θ were plotted in two separate plots with a matching horizontal axis.

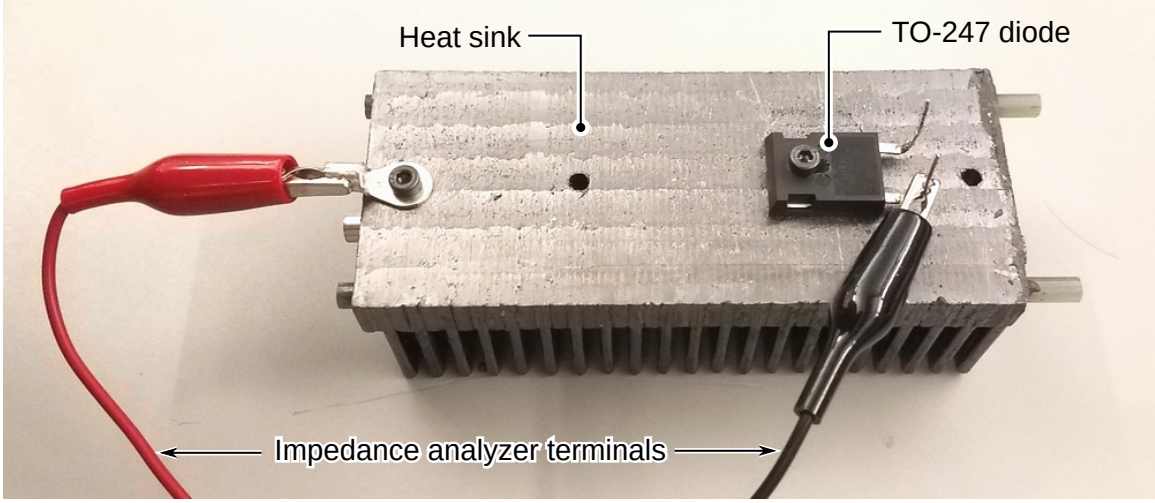

Figure 6.4: A photograph of the test setup during the impedance measurement.

In cases with no electrical insulation (dentoed AL, NGS, and NGS+HP in Figure 6.5), the measured impedance is expected to be mainly due the heat sink. At frequencies lower than 1 kHz all the heat sinks show the phase angle of 0 deg which implies that they behave as pure resistors with the resistance values of 0.026 Ω, 0.15 Ω, and 0.34 Ω for the AL, NGS+HP, and NGS heat sinks, respectively. The resistance of the NGS heat sink (0.35 Ω) is in a good agreement with the estimate of 0.25 Ω that was used in the theoretical analysis. The resistance of the NGS+HP heat sink is lower than that of the NGS one because the current can flow through the highly conductive copper heat pipes. The resistance of the AL heat sink is one order of magnitude lower than the NGS heat sinks, which is contrary to the expectations based on the four orders of magnitude difference in the electrical conductivity of aluminum and NGS (Figure 6.1). The unexpectedly high resistance of the AL heat sink was accounted to the contact resistance at the device-sink interface and in other connections. At frequencies above 1 kHz, the phase angle begins to change from 0 deg to 90 deg, and the impedance amplitude increases. The change in the phase angle suggests that the inductive part of the impedance is becoming to be dominant. All the measured heat sinks show the same impedance amplitude at frequencies higher than 1 MHz.

In the cases with electrical insulation, the impedance at low frequencies is dominated by the capacitive contribution as can be seen from the $-90°$ phase angle. The sharp minimums seen in the impedance amplitude curves correspond to the resonant frequencies in which the capacitive and inductive contributions are equal. The impedance amplitude of the cases with the polyimide film is lower than that of those with the Al_2O_3 pad, which is due the the higher parasitic capacitance at the device-sink interface caused by the lower thickness of the polyimide film. By using an equivalent RLC circuit with the components connected in series, the average capacitance was determined to be 23 pF for Al_2O_3 and 80 pF for the polyimide film.

The most important conclusion can be made by comparing the values of the impedance amplitude with and without electrical insulation. It is clear that the capacitive contribution is up to eight orders of magnitude higher than the resistive one, which confirms the conclusion in the theoretical analysis saying that the four-orders-of-magnitude change in electrical conductivity does not significantly affect the total impedance.

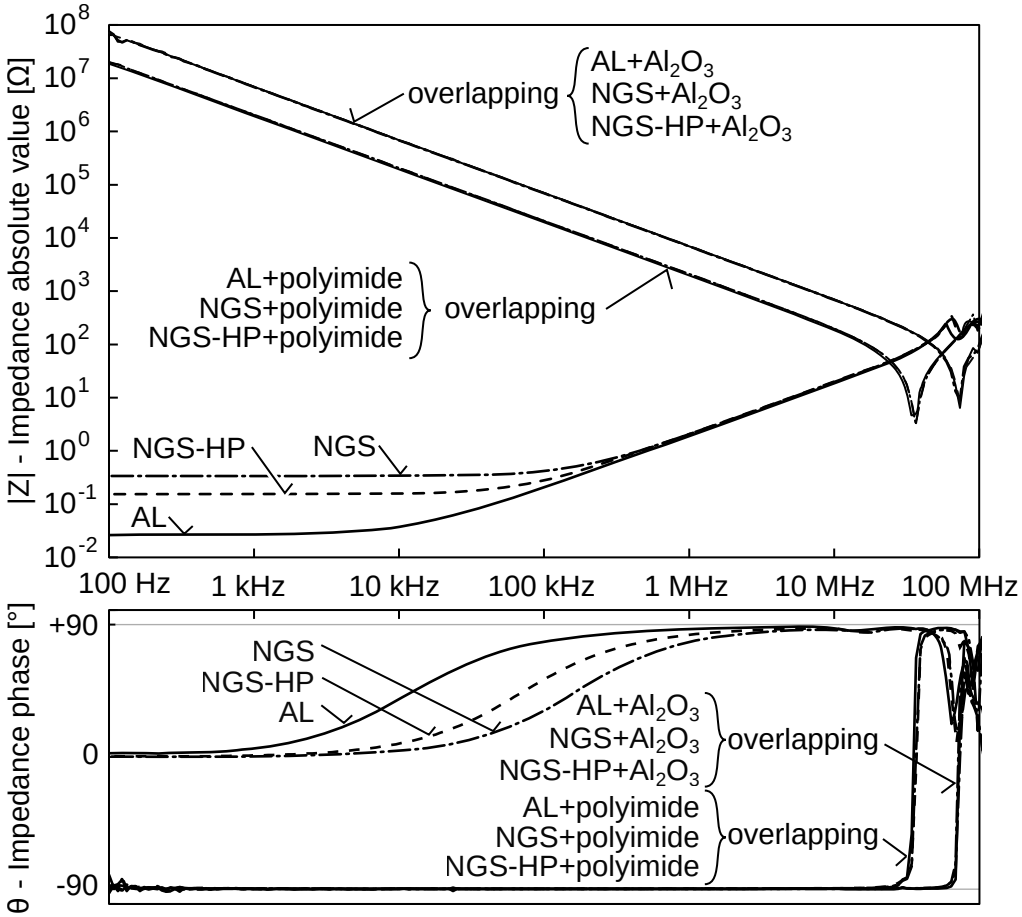

Figure 6.5: Results of the common-mode impedance measurements.

6.1.4 Section conclusions

A theoretical and experimental studies were performed to evaluate the potential reduction of conducted emissions by using heat sinks manufactured from NGS instead of highly conductive aluminum. Despite the four orders of magnitude lower electrical conductivity, NGS heat sinks cannot reduce the conducted EMI emissions because the total impedance of the common-mode current path is dominated by the parasitic capacitance at the device-sink interface. For significant emission reduction, the heat sink resistance would have to be equal to the capacitive reactance. Assuming a capacitance of 80 pF and a frequency of 1 MHz,

the electrical conductivity of the heat sink would have to be in the order of $10\,\mathrm{Scm}^{-1}$, which is two orders of magnitude lower than the through–plane conductivity of NGS.

6.2 Radiated emissions

Heat sinks affect the magnitude and directionality of radiated emissions by interacting with the electromagnetic fields generated by electronic devices. The shape and material properties of the heat sink can be adjusted to achieve the desired EMI performance of electronic products. In this chapter, a first-approach study of the effect of NGS heat sinks on the radiative EMI of power electronics is carried out.

6.2.1 Previous work

Felic and Evans [140] studied the radiated emissions in switch mode power supplies by modeling and measurements using an electric field probe. The authors observed that the emission spectrum in the near field changes for cases with and without a heat sink on a power transistor, but the difference was not detectable in the far field at the distance of 1 m from the transistor. The change in the emission spectrum was not a constant increase or decrease. Instead, the presence of the heat sink apmlified emissions at some frequencies, but also dampened the emisssion at other frequencies.

Bhobe et al. [15] compared the thermal performace and radiated emissions of heat sinks made of aluminum and two plastic composites designed to absorb electromagnetic waves. The details about the composite materials were not disclosed and only labels A and B were defined. Tests in a reverberation chamber showed approximately constant 2 dB decrease in the total radiated power over the whole spectrum range for material B, and very high decrease up to 25 dB at low frequencies for material A. The authors argued that the broadband behavior of material B is due to the low electrical conductivity that causes the common mode emissions to reflect back to the radiation source. The measured thermal resistance of the composite heat sinks was approximately 15 to 25 times more than that of the aluminum one because of the low thermal conductivity of the composites, which was reported to be anisotropic in the range 2 to $20\,\mathrm{Wm}^{-1}\mathrm{K}^{-1}$

A commonly used solutions to reducting the radiated emissions are grounding using a low-impedance line or adding ferrite cores [135]. Ahn et al. [141] proposed grounding using resistors, and in their case a 12 dB decrease in electric field intensity 3 m from the source was achieved by using 10 to $20\,\Omega$ resistors.

If the heat sink is identified as the source of the emissions later in the design process when adding grounding posts to the PCB is not feasible, emission reduction can be achieved by using a strip of engineered lossy material at the gap between the chip and the heat sink [142]. In the work by Cheng et al. [143], the region between the heat sink and the IC substrate was identified to be the source of the radiation, and a hybrid insert consisting of

graphite and a lossy material was used to reduce the radiated emissions while keeping the thermal resistance low.

Chromy et al. [144] measured the thermal performance and radiation characteristic of geometrically identical liquid cooled heat sinks manufactured from aluminum and aluminum nitride (insulating ceramic). A replica of a TO-247 device was attached to the heat sink and connected to a spectrum analyzer. The second terminal of the spectrum analyzer was connected to an antenna. The entire experiment was performed in a semi-anechoic chamber. While the details about the thermal measurements are missing, the authors concluded that the thermal performance of the two heat sinks was comparable. The effect of the heat sink material on the radiated emissions was deemed to be dependent on the system impedance. The authors stated that changing the material from aluminum to ceramic can lead to increased radiated emissions. Ceramic heat sinks are commercially available and their manufacturers often list the EMI performance as the benefit. However, no scientific study aimed at quantifying the reduction is available.

NGS has been reported to perform well in shielding applications [145] where the purpose is to reflect or absorb any incoming electromagnetic waves. This property is not expected to be relevant to the emissions, however, the susceptibility of the electronic devices under the heat sink may be improved.

6.2.2 Summary of work performed

The work on this part of the present research was limited by the lack of expertise and the need to initiate a multi disciplinary collaboration. The following section summarizes the steps that have been performed and suggests the future work.

To explore the potential of reducing radiated emissions by using NGS heat sinks, two relevant approaches were identified: A comparative experimental study similar to that performed for the thermal performance and conducted EMI, or modeling using either low order or full numerical models. Due to the lack of access to an experimental facility, the latter approach was pursued. Any modeling work requires the knowledge of the electromagnetic properties of NGS, namely the electric permittivity and magnetic permeability. For the first-approach calculations, the magnetic contribution to the interaction of NGS with electromagnetic fields is expected to be negligible due to the diamagnetic nature of graphite [71].

6.2.2.1 Permittivity of NGS

The open literature contains a several studies of permittivity of graphitic materials [146, 147, 148, 149]. However, a complex study of permittivity of NGS including the effect of density and compression pressure is missing. Four NGS samples were sent to Micro-Electronics and Advanced Sensors Laboratory at University of British Columbia Okanagan. Permittivity measurements were performed using an Agilent Technologies PNA-X network analyzer

(Figure 6.6) with the conventional probe that is not designed to measure anisotropic materials. The measured values were expected to be satisfactory for a first-approach evaluation of whether NGS heat sinks have the potential to reduce radiated emissions. The measured values of the real and imaginary part of permittivity are shown in Figures 6.7 and 6.8, respectively.

The real part of permittivity ϵ' remains within the 10 to 12 range for the entire measured frequency spectrum except for the initial increase at the low-frequency end of the spectrum. Samples A and B had the same density but their thickness was different. It was expected that the corresponding curves will overlap because the permittivity was assumed to be independent of thickness as was seen in measurements of electrical conductivity. In the present results, the curves for samples A and B do not overlap, which suggests that thickness plays a role, or that the sample thickness was too low. Comparing the curves for samples A, C, and D, for which the corresponding densities are $0.5\,\mathrm{gcm}^{-3}$, $1.0\,\mathrm{gcm}^{-3}$, and $1.5\,\mathrm{gcm}^{-3}$, there is no obvious stacking order showing a monotonic increase or decrease of the real permittivity with density. Assuming that non-monotonic behavior is confirmed by future measurements, a possible explanation is that the measured value is a combination of the in–plane and through–plane permittivity that increase and decrease with density, respectively.

The results for the imaginary part of permittivity ϵ'' show negative values at low frequencies, which suggests an error in the measurements, or an incompatibility of the measurement method with highly anisotropic materials. The conclusions made for the real part (ϵ') also apply to the imaginary part. From the heat sink development perspective, the imaginary part is the most relevant to the potential reduction in radiated emission as it dictates the amount of energy that is dissipated as heat instead of being radiated from the heat sink in the form of electromagnetic waves. Comparing the ϵ'' at 2 GHz with the data for graphite reported by Hotta et al. [148] yields the approximate values of 0.5 and 15, respectively. The difference suggest that the permittivity measurements presented in this work should be revised.

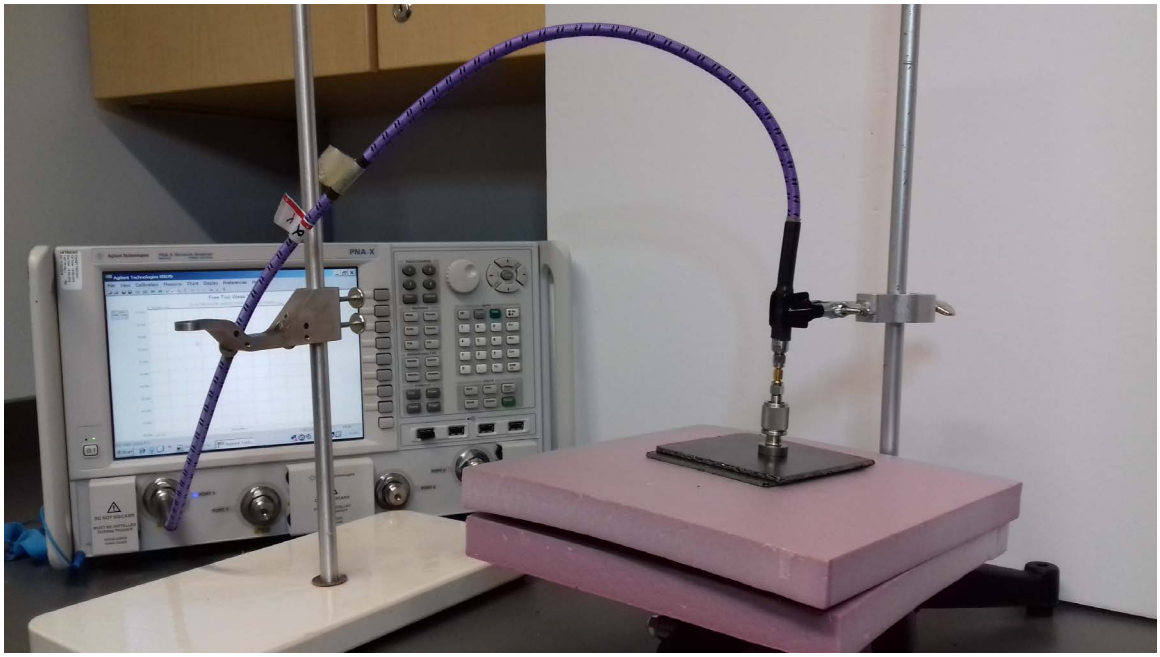

Figure 6.6: Experimental setup used for measuring permittivity

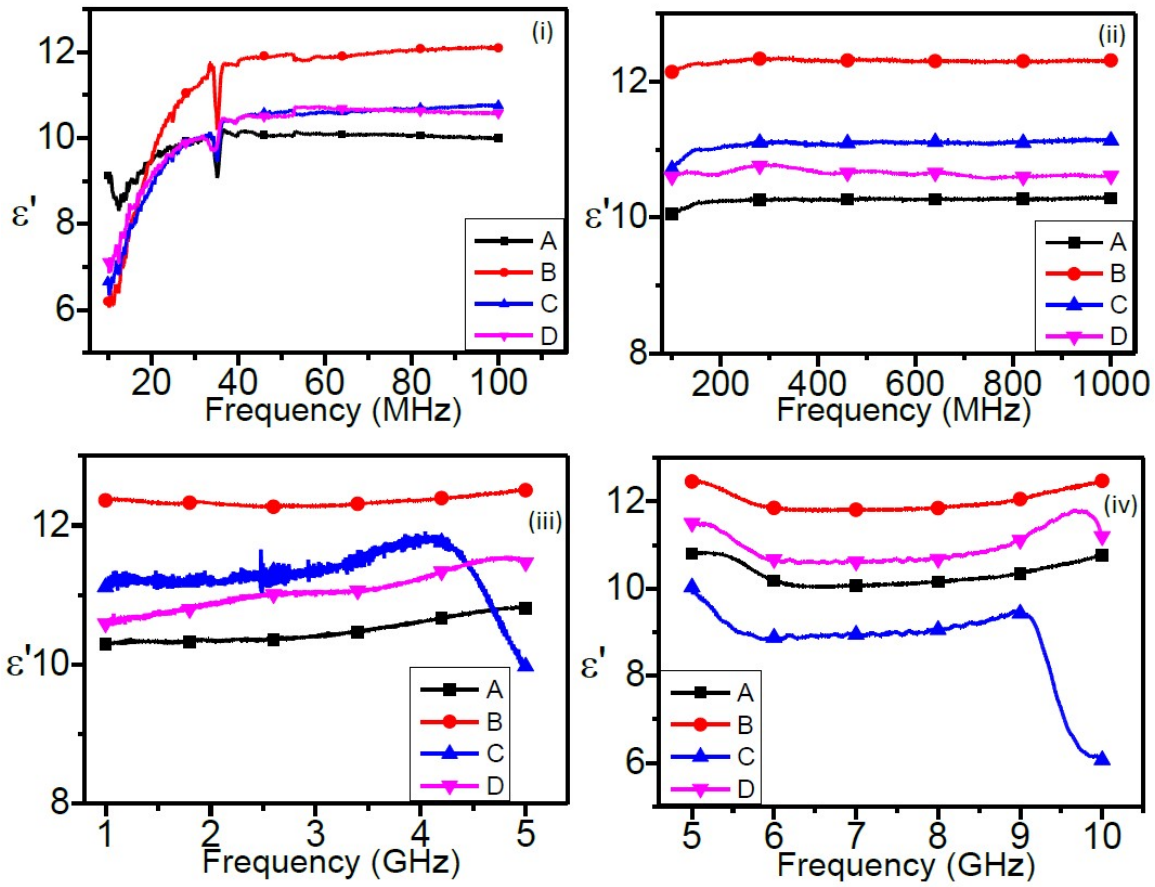

Figure 6.7: The real part of permittivity of NGS. A - density 0.5 gcm^{-3}, thickness 2.8 mm; B - density 0.5 gcm^{-3}, thickness 1.4 mm; C - density 1 gcm^{-3}, thickness 1.4 mm; D - density 1.5 gcm^{-3}, thickness 0.93 mm;

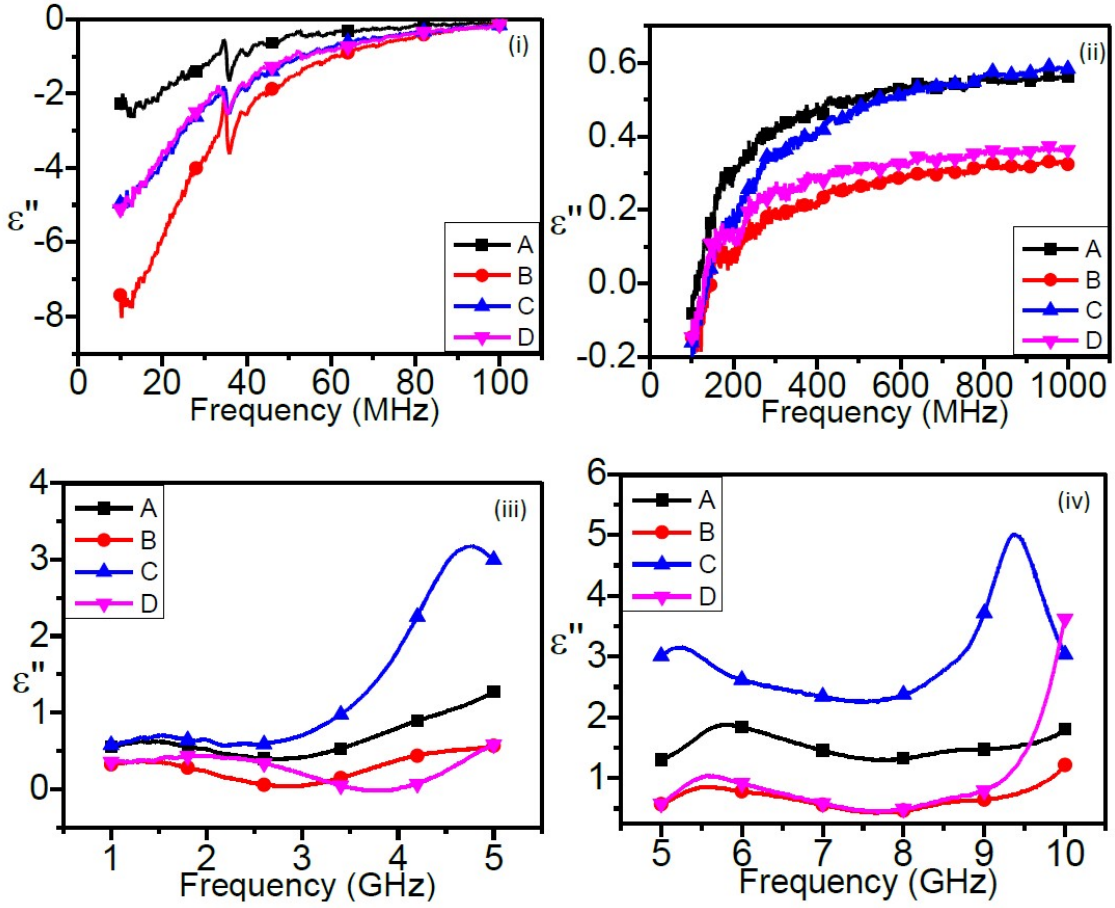

Figure 6.8: The imaginary part of permittivity of NGS. A - density 0.5 gcm^{-3}, thickness 2.8 mm; B - density 0.5 gcm^{-3}, thickness 1.4 mm; C - density 1 gcm^{-3}, thickness 1.4 mm; D - density 1.5 gcm^{-3}, thickness 0.93 mm;

6.2.2.2 Potential emission reduction

The potential of NGS heat sinks to reduce radiated emissions can be based on an analogy with antennas. As shown in Figure 6.9, a non-insulated ungrounded heat sink is conceptually identical to a monopole antenna. In antenna design, the radiation efficiency is a quantity that expresses the ratio of radiated and input energy. While antennas are designed for maximum radiation efficiency, a low value is desired for heat sinks to minimize the radiated emissions. Shahpari and Thiel [150] analyzed the effect of electrical conductivity on the radiation efficiency of antennas in three shapes: dipole, yagi, and meander. The results of their numerical work are shown in Figure 6.10 and the regions of interest for this work are overlaid on top. Assuming that a heat sink excited by a semiconductor device behaves the same as an antenna, the following conclusions can be made. If the electrical conductivity of conventional metal heat sinks is used as a reference, reductions in radiation efficiency of 12 to 45 % for the dipole and 70 to 97 % for the meander antenna are expected. The lower values correspond to the high in–plane electrical conductivity of NGS, while the high values correspond to the low through-plane electrical conductivity of NGS. Besides numerical work, Shahpari and Thiel [150] also manufactured the antennas from graphite (round pencil lead $\sigma = 6.4 \times 10^4\,\mathrm{Sm}^{-1}$) and brass ($\sigma = 2.56 \times 10^7\,\mathrm{Sm}^{-1}$) and experimentally showed that the radiation efficiency of the graphite one is 9 % and 51 % lower for the dipole and meander shapes, respectively. In another study, Chen and Fumeaux [151] manufactured two flexible microstrip antennas from pyrolytic graphite ($\sigma = 2 \times 10^6\,\mathrm{Sm}^{-1}$) and reported their radiation efficiency to be 8 % and 20 % lower than reference copper ones. Based on all the results, NGS is expected to reduce the radiation efficiency of heat sinks by up to 97 %. However, it is not possible to guarantee that an equal reduction in radiation emissions will be achieved.

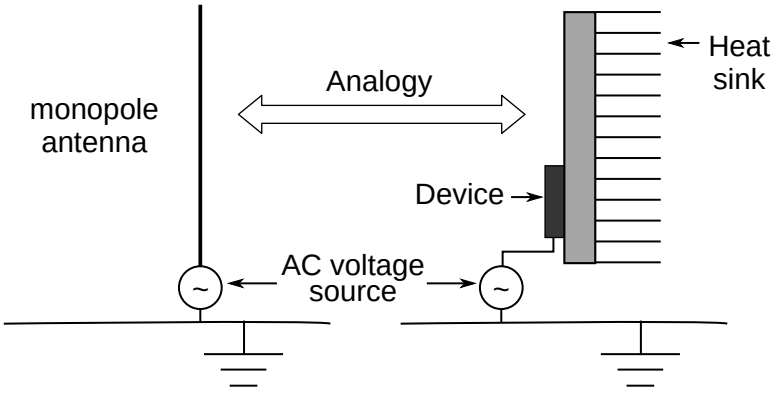

Figure 6.9: An illustration of the analogy between an antenna (monopole) and ungrounded heat sinks.

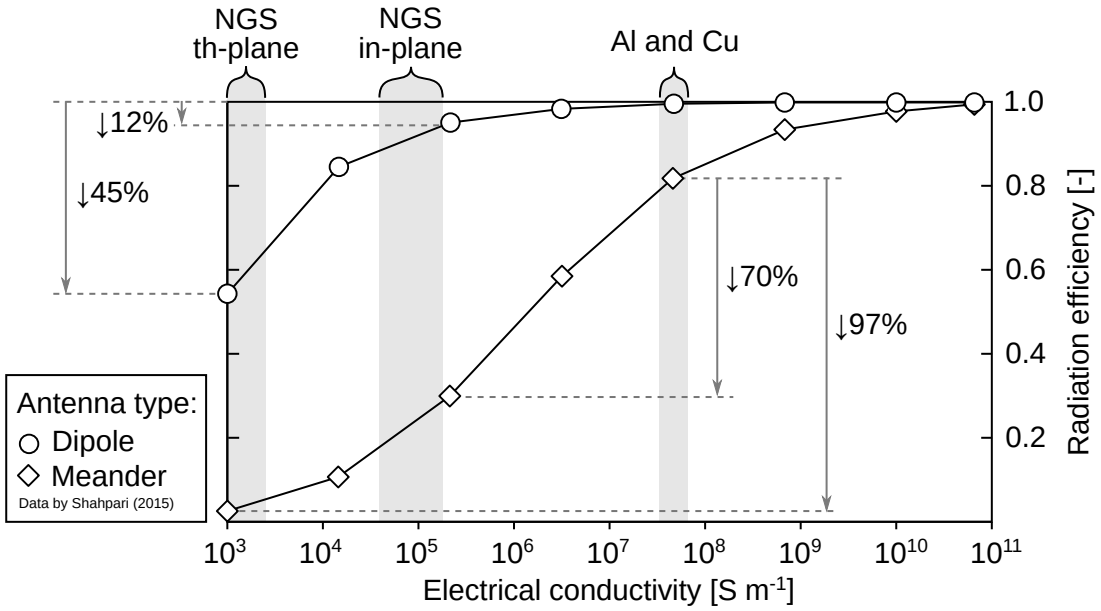

Figure 6.10: The radiation efficiency as a function of electrical conductivity for two types of antennas (data by [150]). The gray regions highlight the electrical conductivity of NGS and metals. The potential reductions in radiation efficiency are shown by arrows.

6.2.3 Future work

From a practical standpoint, the most time-efficient and persuasive way to prove the expected reduction in radiated emissions is to perform a comparative study with geometrically identical NGS and aluminum heat sinks in the same way as was described in section 5.3 for the thermal performance, and 6.1 for conducted emissions. While an anechoic chamber is a relevant method, a reverberation chamber described in [142] may be more useful as no directional averaging is necessary. Alternatively, an in-situ measurement using a commercial product can be considered. The existing heat sink can be replaced with an NGS one, and the electric field can be measured using an electric field probe.

6.2.4 Section conclusions

Compared to metals, graphite is a lossy material. The additional resistance is expected to cause a decreased radiation efficiency of the heat sink, and, in turn, reduced radiated emission. Quantifying the reduction requires measuring the material properties and developing a mathematical model, or building geometrically identical heat sinks and comparing their radiation behavior by measurements using specialized equipment. A theoretical analysis based on studies of graphite antennas suggests that NGS heat sinks can reduce the radiation efficiency by 12 to 97 %.

Chapter 7

Cost of NGS heat sinks

A cost analysis of the large-scale NGS heat sinks produced within this thesis is performed to support the holistic evaluation of the feasibility of NGS heat sinks. The low material cost, which was stated as one of the research motivations, is reviewed and compared to the other costs. The cost of NGS heat sinks is compared to the conventional, commercially available aluminum ones, and the indirect cost benefits arising from using NGS heat sinks are reviewed. Predictions on the financially feasible applicatoins, future development of the cost, and the necessary future work are made.

7.1 Material cost

Determining the material cost of NGS heat sinks can be ambiguous as the boundary between material supply and manufacturing is not clearly defined. The heat sinks in this work were manufactured from a low-density NGS, which was produced from raw graphite flakes by an external supplier. In future, the technology commercialization is expected to lead to process integration, which will result in graphite flakes becoming the raw material entering the heat sink manufacturing facility. Therefore, an effort is made here to split the cost of raw flakes and NGS production.

The cost of graphite flakes is lower than that of aluminum or copper as can be seen in Figure 7.1. United States Geological Survey [32] reports the average flake graphite cost of 1.5 $\mathrm{USDkg^{-1}}$, which is 42 % lower than that of aluminum, and 78 % lower than that of copper. The average value in [32] considers all the flake sizes and carbon contents that are available on the market. Two additional sources [152, 153] were included to estimate the price of flake graphite with the flake size larger than 180 µm (+80 mesh size) and the carbon content of 94 to 97 %. For the purposes of NGS heat sinks, the +80 flake size was considered the most relevant and the flake cost of 0.91 $\mathrm{USDkg^{-1}}$ was used for further calculations. It must be noted here that a clear relationship between the flake size and the final NGS properties are missing in the open literature. None of the previous studies reported the distribution of the flake size. In the material characterization part of this thesis (chapter 3),

the exact size distribution was not provided by the NGS supplier. When this knowledge gap has been filled, the relevant flake cost for NGS heat sink applications should be revisited and adjusted.

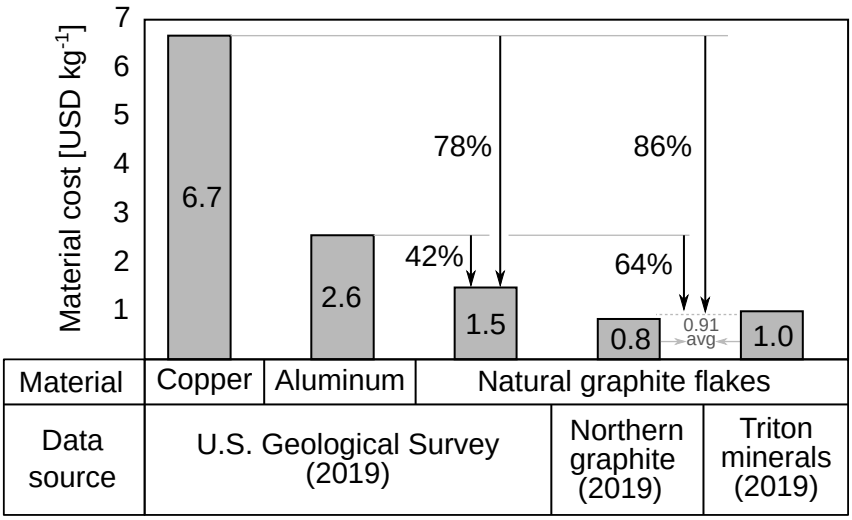

Figure 7.1: A comparison of per-mass cost of graphite flakes. The data by U.S. Geological survey [32] are averages in United States, while the data by Northern Graphite [152] and Triton Minerals [153] are the values for specific class of flakes, namely +80 mesh size at 95 to 97 % carbon content for [152], and +80 mesh size at carbon content larger than 97 % for [153].

For comparing heat sink materials, it is more relevant to present the cost per-volume, as is shown in Figure 7.2 where the dark gray bars correspond to the values reported in Figure 7.1 multiplied by the density of each of the materials, namely $8.9\,\mathrm{gcm}^{-3}$ for copper, $2.7\,\mathrm{gcm}^{-3}$ for aluminum, $0.5\,\mathrm{gcm}^{-3}$ for low-density NGS, and $1.9\,\mathrm{gcm}^{-3}$ for high-density NGS. Since the density of copper and aluminum is higher than that of NGS, the relative cost difference seen in the per-mass comparison in Figure 7.1 is further amplified to 97 to 99 % for copper and 75 to 93 % for aluminum. However, including the cost of NGS production (light gray bars) drastically changes the comparison. The cost of NGS production was estimated by subtracting the average cost of graphite flakes from the cost of the NGS order that was placed as a part of this research. The total cost of NGS (including graphite flakes) is dominated by the 95 % contribution of NGS production, which consists of purification, exfoliation, and compression. In comparison with the conventional metals, the total cost of NGS is 29 to 391 % higher than aluminum, and 43 to 85 % lower than copper.

It should be noted here that the NGS supply chain is not as developed as those for aluminum and copper, which complicates the cost estimates. When sourcing the material for this research, the majority of suppliers refused to sell small amounts of NGS. The smallest possible order size was 100 square sheets 1 m wide. The NGS in this work was sourced from a Chinese supplier and the material cost determined in the previous paragraph is

likely incorrect when considering suppliers in other parts of the world. The value should be considered a first-approach estimate. For the future work, it is crucial to factor in the varying purity and chemical content, and also consider other factors such as the predicted market growth, the effect of environmental regulations on graphite prices, and the cost of existing and emerging exfoliation methods.

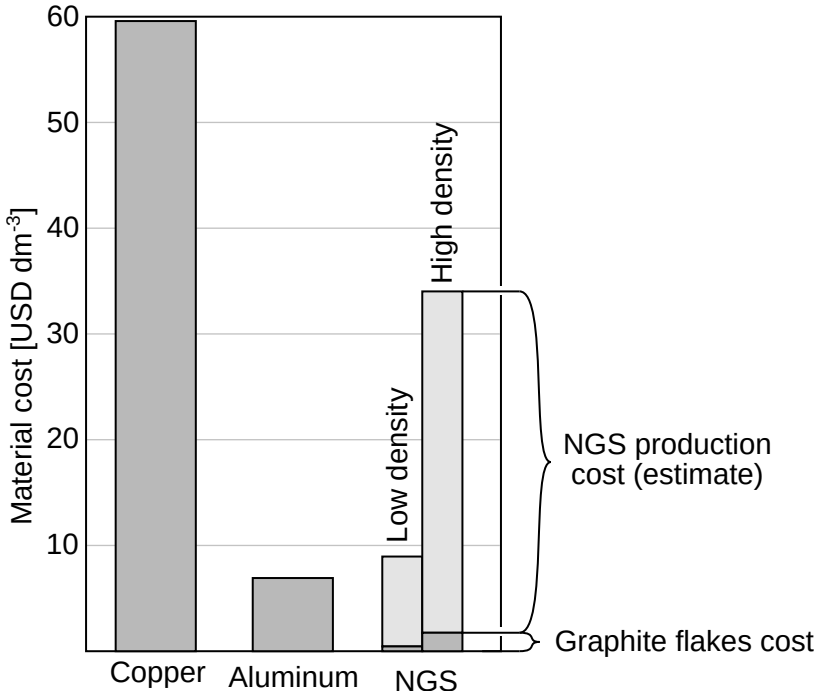

Figure 7.2: Comparison of the material cost of copper, aluminum, and NGS.

7.2 Heat sink cost

7.2.1 Prediction of NGS heat sink cost

The cost of the NGS heat sinks manufactured in section 5.3 (Figure 5.18) was estimated in collaboration with Terrella Energy Systems - an industrial partner that has an extensive experience in manufacturing NGS parts for the fuel cell industry. The estimate assumed forming the sheets (Figure 4.4a) using the calendering technology, for which the upfront cost is high and it is therfore suitable for high-volume production of heat sinks. Most of the parameters in the cost analysis were given by the industrial partner. Only the sheet geometry, sheet density, NGS cost, and heat pipe cost were based on the work in this thesis. The NGS cost was assumed to be 17.8 USDkg^{-1}. The cost of the U-shape heat pipes shown in Figure 5.18 was estimated based on a communication with a heat pipe supplier [154]. At 500 heat sinks production volume, the heat pipe cost was assumed to be 5 USD, and at 10,000 volume it was 1 USD. The two data points were linearly interpolated to determine the cost at other production volumes.

The results of the cost analysis are visualized in Figure 7.3 where the total heat sink cost was split into the cost of low-density NGS, cost of additional materials such as a glue for bonding and polymer for the impregnation process, cost of manufacturing labor, the cost of the tool for forming the sheets, and the cost of heat pipes. For all the following observations, the relative percentage values were evaluated with respect to the cost of the heat sink without heat pipes. The cost of embedding heat pipes is discussed separately.

The results confirm the expectation of a high cost at low production volumes. At the lowest considered production volume of 500 heat sinks, the total heat sink cost is high (55.1 USD) and the tooling cost makes up 78 % of the total cost. Values for less than 500 heat sinks were not shown because they are not financially feasible. For low production volumes, simple uniaxial compression forming should be considered, and a separate cost analysis should be performed. It is likely that the tooling cost of uniaxial compression will be lower than that of calendering, however, the labor cost will likely increase.

With increasing production volume, the heat sink cost decreases due to the return of investment into the manufacturing tool, and due to the reduced heat pipe cost. At the highest considered production volume of 10,000 heat sinks, which was assumed to be the most relevant to high-volume production estimates, the total heat sink cost is 14.5 USD, the contribution of the tooling cost drops to 15 %, and the manufacturing labor becomes the dominating cost with the relative contribution of 62 %. The material cost is 23 % of the total cost with 11 % for glue and impregnation polymer, and 12 % for the raw low-density NGS. Both the material and labor cost were assumed not to vary with the number of produced heat sinks. It is possible that this assumption is not realistic and it should be reconsidered in future detailed cost analyses.

NGS heat sinks with embedded heat pipes are 14 to 28 % more expensive than those without heat pipes. At the highest considered production volume of 10,000 heat sinks, which is the most relevant for the selected calendering technology, the cost of the heat sink with embedded heat pipes is 16.5 USD, which is 14 % (2 USD) more than that without heat pipes. Installing the heat pipes will likely result in an increased labor cost, however, the increase is expected to be minor and it has been neglected in this study.

A detailed break down of the cost of the considered NGS heat sinks without heat pipes is shown if Figure 7.4. The total relative labor cost of 61.5 % consists 26.6 % for assembling and 34.8 % for sheet forming and polymer impregnation. The 11.3 % additional material cost is a combination of 6 % for glue and 5.3 % for the polymer in the impregnation process. The cost of the low-density NGS is a combination of the cost of raw flakes and the cost of NGS production. As was discussed in section 7.1, the NGS cost is dominated by the production process, and Figure 7.4 shows the same trend with only 0.6 % of the heat sink cost being due to the raw graphite flakes. The production of NGS contributes 11.9 % to the total heat sink cost.

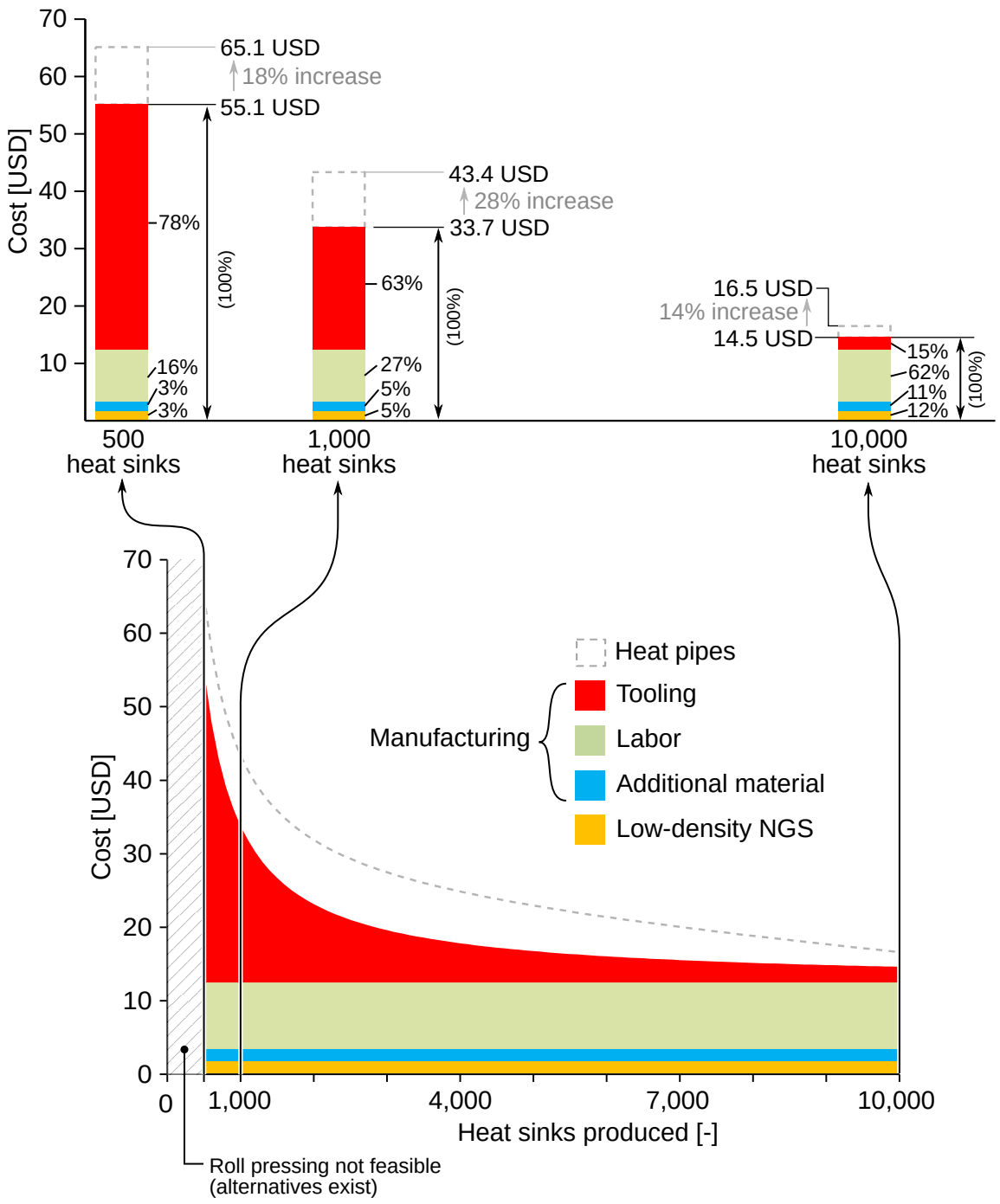

Figure 7.3: The results of the cost analysis. The bars at the top are details of the cost breakdown for production run of 500, 1000, and 10 000 heat sinks.

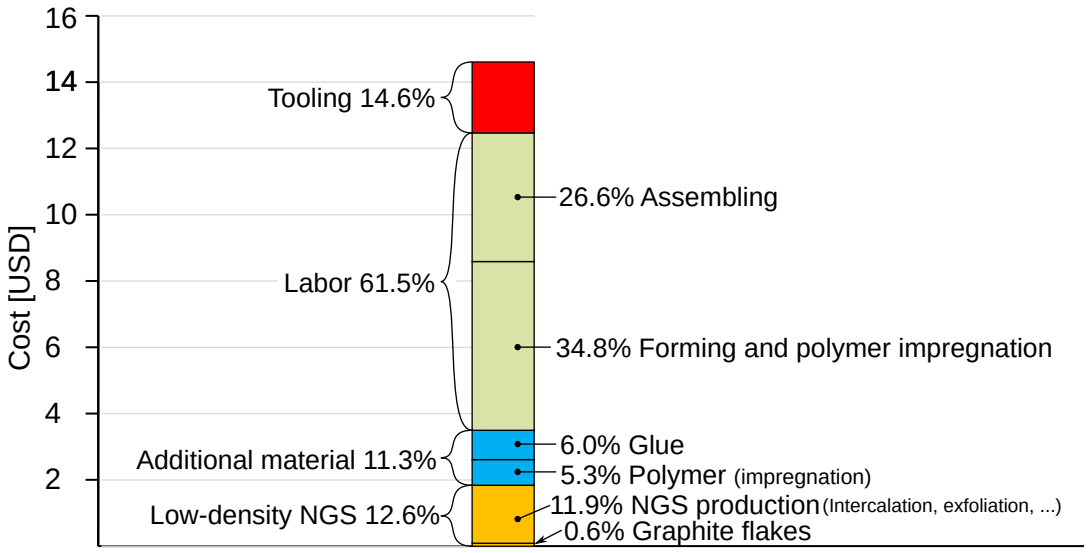

Figure 7.4: A detailed cost breakdown for the case of producing 10 000 heat sinks.

7.2.2 Comparison of conventional and NGS heat sinks

Comparing the cost of NGS heat sinks to that of existing conventional metal heat sinks is important for evaluating the feasibility. In Figure 7.5, the previously calculated cost of NGS heat sink is compared to that of a commercially available Alpha Novatech UB12060-30B aluminum heat sink whose cost was provided by the manufacturer [155]. The outer dimensions of the compared heat sinks are similar, but the fin topology is significantly different as can be seen at the bototm of Figure 7.5. The goal of the comparison is to offer a rough first-approach estimate of the cost of NGS heat sinks relative to the existing ones. The difference in fin topology was therefore considered acceptable.

The retail cost of the Alpha Novatech UB12060-30B heat sink decreases with the purchased amount, and the difference was reflected by the light gray portion of the bar chart in Figure 7.5. Similarly, the estimated cost of NGS heat sinks varies with the number of heat sinks produced, and the light gray portion of the bar charts represents the variation. Comparing the two heat sink is complicated by the high variation of the prices. The lowest cost of the aluminum heat sink was considered to be the most suitable for the comparison because the overhead retail charge is expected to be the lowest, and the cost is therefore the closest to the production cost. Similarly, the cost of NGS the heat sink at the highest production volume was considered the most relevant for the comparison because the compared aluminum heat sink was also most likely produced in a large production volume.

Based on the above comparison criteria, the cost of the NGS heat sink is 64 % higher than that of the aluminum one. When heat pipes are embedded in the NGS heat sink, the cost difference increases to 87 %. Using the exact percentage of the cost difference is prone to errors due to the high variation in the reference values. For the purposes of this thesis, the cost of NGS heat sinks is considered to be approximately double that of conventional mass produced aluminum heat sinks. By using this expression, the uncertainty in the cost comparison is reflected in the conclusions.

Besides the most relevant cost comparison based on the lowest values, Figure 7.5 also contains the worst-case scenario comparison in which the cost of NGS heat sinks with and without heat pipes is 637 % and 524 % that of the aluminum heat sink, respectively. The comparison is, however, not well posed because the reference aluminum heat sink was likely not manufactured in a small 500-pieces production volume.

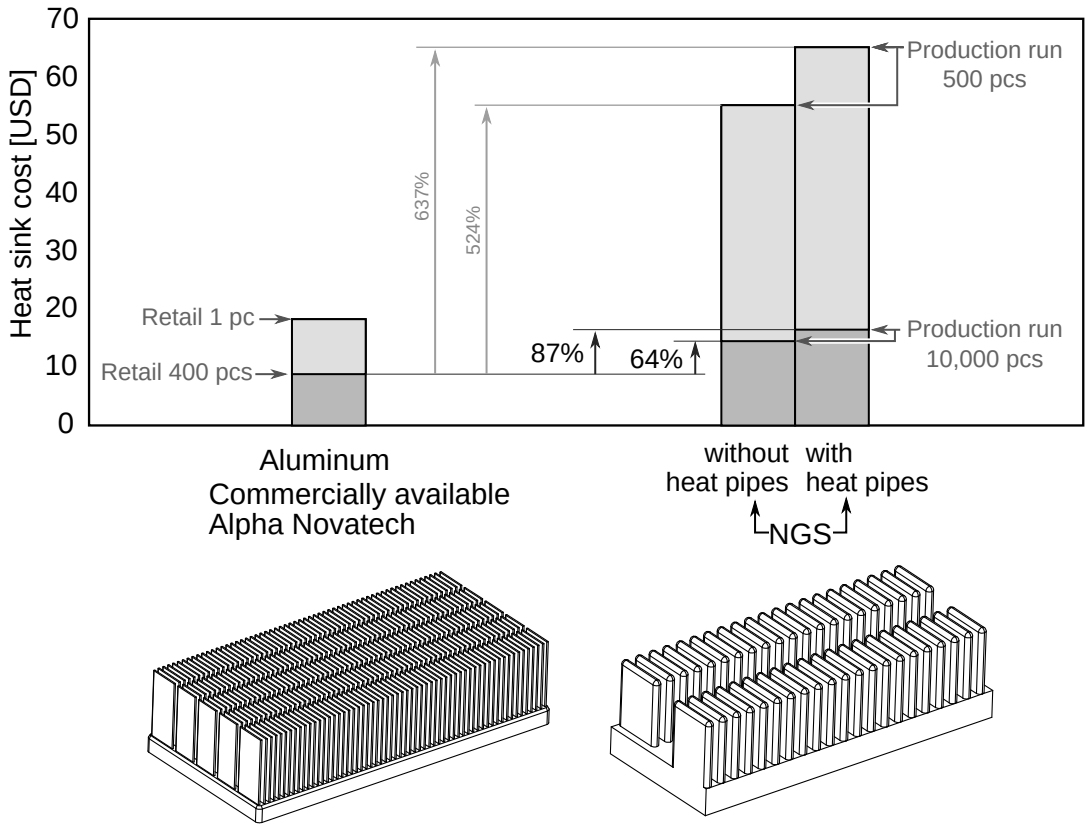

Figure 7.5: A comparison of the cost of NGS heat sinks with an existing, comparable, commercially available aluminum one

The conclusion that the cost of NGS heat sinks is approximately double that of conventional aluminum ones is not valid generally. The validity region was highlighted in Figure 7.6 together with a rough cost estimation of multiple heat sink manufacturing methods. The cost predicted in this thesis is valid for large production runs of approximately 10,000 heat sinks using the calendering technology. The comparison of NGS and aluminum heat sinks assumes that the compared aluminum heat sink is manufactured using a high-volume production method such as extrusion or forging. At small production runs, extrusion, forging, and NGS calendering become costly and infeasible. No relevant quantitative work was performed within this thesis for the small production volume region, however, a qualitative estimate of the cost of available methods was included in Figure 7.6. It is expected that unidirectional compression will be a feasible technology with the cost decreasing due to the pay-off of the pressing tool. For large production runs the cost of unidirectional compression does not decrease significantly because of its labor intensity. 3D printing was included as an example of a method for producing metal heat sinks at small quantities. It is expected that 3D printing and NGS forming will be competitive for small production batches of highly customized heat sinks because both methods allow designing geometrically complex shapes. The details of this prediction are addressed in chapter 10.

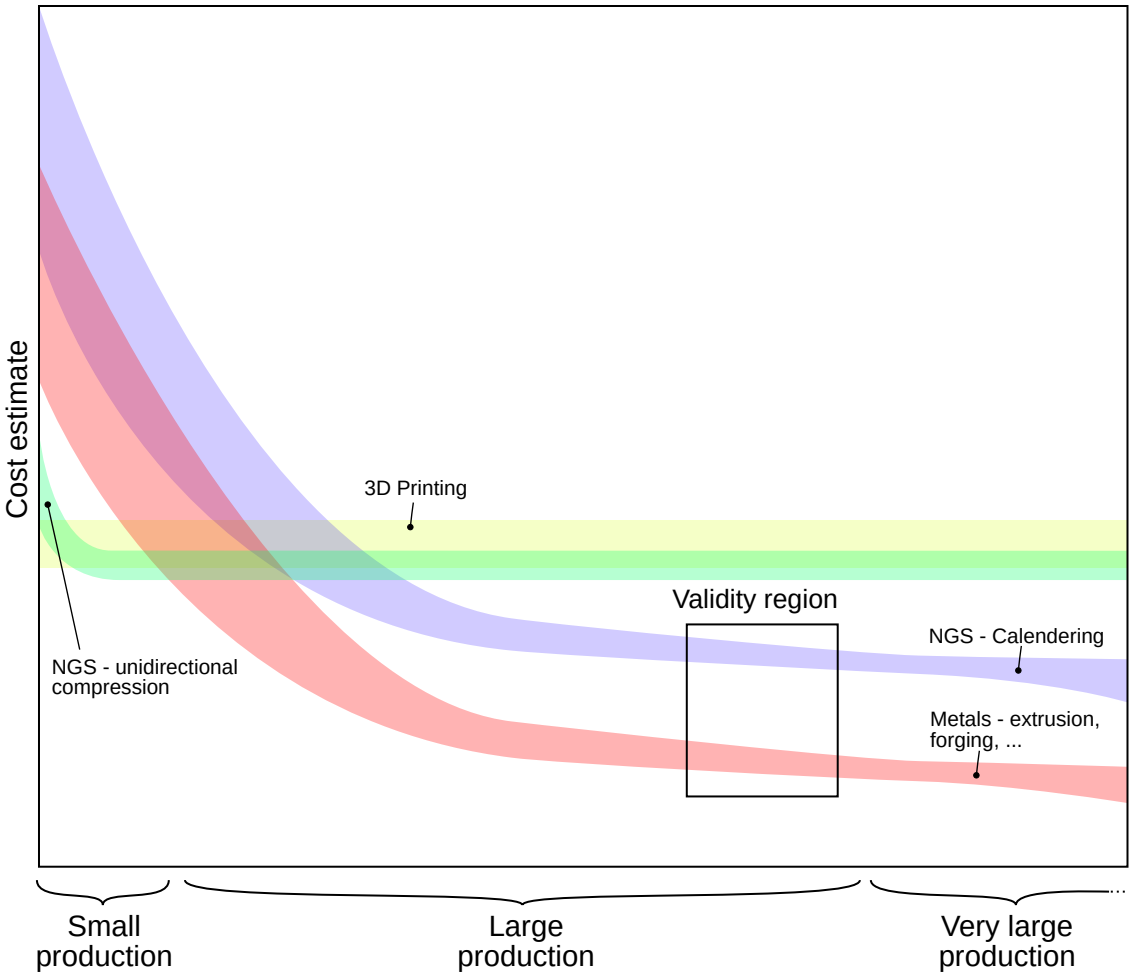

Figure 7.6: An illustration of the validity region of the present heat sink cost estimate. The expected trends at low production volumes are outlined on the left side of the figure.

7.3 Implications on power electronics cost

Switching from metal to NGS heat sinks has implications on the cost of the entire product (e.g. a power converter). In products where thermal grease is used, switching to NGS heat sinks–which do not require thermal grease–eliminates the cost of the thermal grease and its application in the assembly process. The selection of the mounting mechanism also affects the cost of the final product directly by the cost of the parts and indirectly by the labor cost during the assembly. To correctly evaluate the financial feasibility of using NGS heat sinks, the cost analysis must go beyond just comparing the cost of candidate heat sinks. The system changes due to a different heat sink must be evaluated and reflected in the total cost estimate.

7.4 Section conclusions

Based on a case-specific first-approach cost analysis, the cost of NGS heat sinks produced in high volumes appears to be approximately double that of comparable mass-produced aluminum ones. Using embedded heat pipes increases the cost by 14 to 28 %. The high-volume cost is dominated by the labor cost, and the potential commercialization of the technology is expected to lead to decreasing the cost. The raw low-density NGS from an external supplier accounts for only 12.6 % of the total heat sink cost, but the NGS cost was based on a single order and its value must be validated. The cost of the raw graphite flakes is only 0.6 % of the total heat sink cost. If the future development of the NGS technology results in a reduced labor cost and the material becomes a significant expense, it is recommended to focus on determining the optimal purity, size, and exfoliation method of the graphite flakes. The current market appears to be driven by applications such as batteries and fuel cells which require highly processed high-grade flakes. Heat sink applications are likely less demanding and a significant cost reduction can be achieved when using an appropriate grade.

NGS heat sinks are expected to be a cost-effective option in applications where the optimal heat sink shape is easy to manufacture using the NGS forming methods and difficult to manufacture using the conventional metal forming techniques. The cost of the low-volume production has not been studied in detail and it should be addressed in the future. NGS heat sinks with complex shapes that are required in small, highly specialized market segments are expected to be cost competitive with those manufactured using the conventional metal-forming prototyping methods such as CNC machining or 3D printing.

Chapter 8

Environmental impact of heat sink materials

The environmental impact of electronic products is a result of not only their energy efficiency but also of the production and disposal of all the parts. To evaluate the overall environmental impact, the life cycle assessment method (LCA) is typically used to quantify the impact in several categories such as greenhouse gas emissions, water depletion, or acidification potential. While aluminum and copper are common materials and many LCA studies are available, the coverage of natural graphite is relatvely low, with the exception of the recent development of Li-ion batteries that use natural graphite for their anodes. In this chapter, the available data for NGS are reviewed and compared to those of aluminum and copper, and the work is expected to serve as the basis for future LCA studies. An audiovisual summary of the chapter is available at `https://www.youtube.com/watch?v=2Yvb4wIY9uY&list=PLaX55SIXaD20NQQ2JLP-7abmET7l-6LS4&index=6` [1].

The life cycle of a product can be split into four logical parts: material production, manufacturing, usage, and end-of-life disposal as shown in Figure 8.1. The details of each of the steps are covered in the following sections.

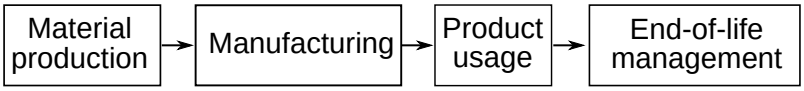

Figure 8.1: The life cycle of a NGS product

8.1 Material production

The material production processes for aluminum, copper, and graphite flakes are summarized in Figure 8.2. In all cases, the ore is mined and upgraded to a raw material at the desired purity. The energy input needed to produce a mass unit of the raw material is one

[1] The video files are also available in Appendix F

of the most studied metrics in evaluating the environmental impact of material production. In Figure 8.3, multiple resources were compiled to compare the energy requirement of aluminum, copper, and graphite flakes. The large variation of the data can be caused by many factors such as the selected boundary of the system, inclusion of electricity generation (grid mix), or variation in the production method. In addition, the reported energy requirement metric is not unified as can be seen in the middle column in Figure 8.3. This further increases the uncertainty.

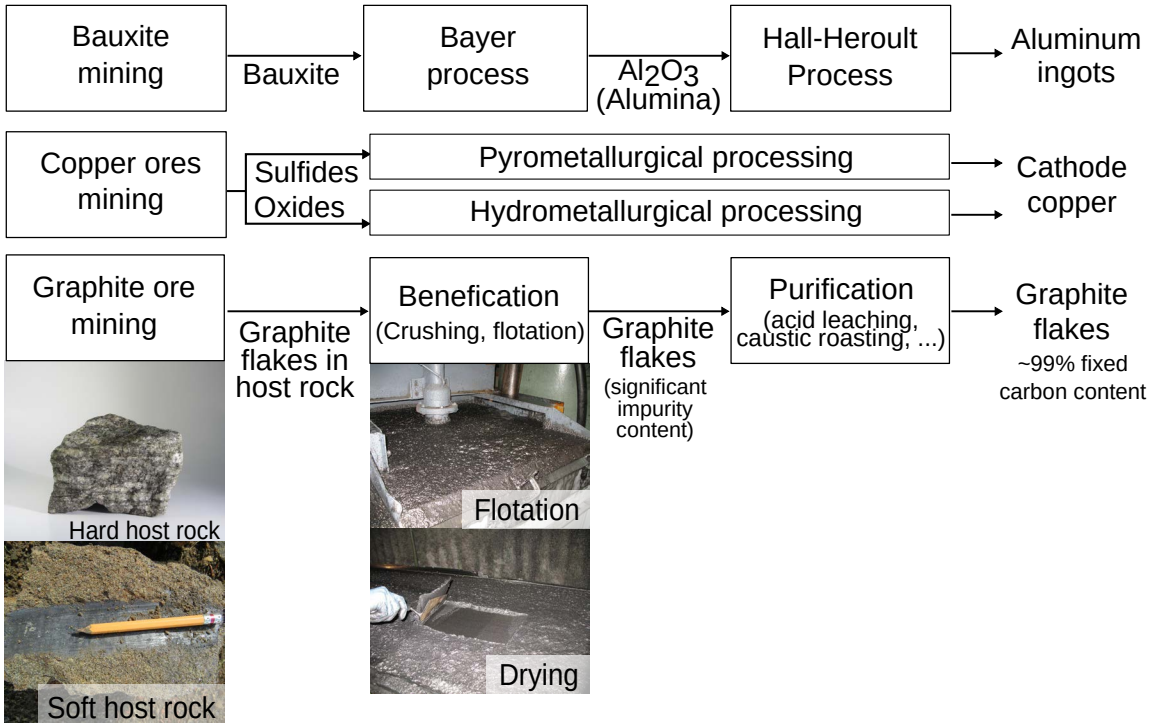

Figure 8.2: Material production steps of aluminum, copper, and graphite flakes. Pictures of the soft host rock, flotation, and drying were reprinted with the permission of Jamie Deith of Eagle Graphite.

For graphite flakes, the reported data vary from $0.23\,\mathrm{MJkg^{-1}}$ [156] to $65.4\,\mathrm{MJkg^{-1}}$ [157]. Out of the three reviewed studies [156, 157, 158], only the one by Gao et al. [157] was published in the scientific literature. The authors of [157] focused on graphite flakes for lithium-ion batteries, which require additional processing step. To compensate for this difference, the 41.7 % contribution of the processing step to the overall energy requirement was subtracted from the reported value of $112.48\,\mathrm{MJkg^{-1}}$ to yield the value of $65.4\,\mathrm{MJkg^{-1}}$, which was used in this work. From the description of the method in [157], it is not clear how the electricity generation was treated. The authors were contacted for clarification, but the language barrier did not allow for a reliable understanding of the reported values. The scatter of the available data and the lack of scientific studies has to be addressed in the future by a comprehensive LCA study performed in collaboration with the industry.

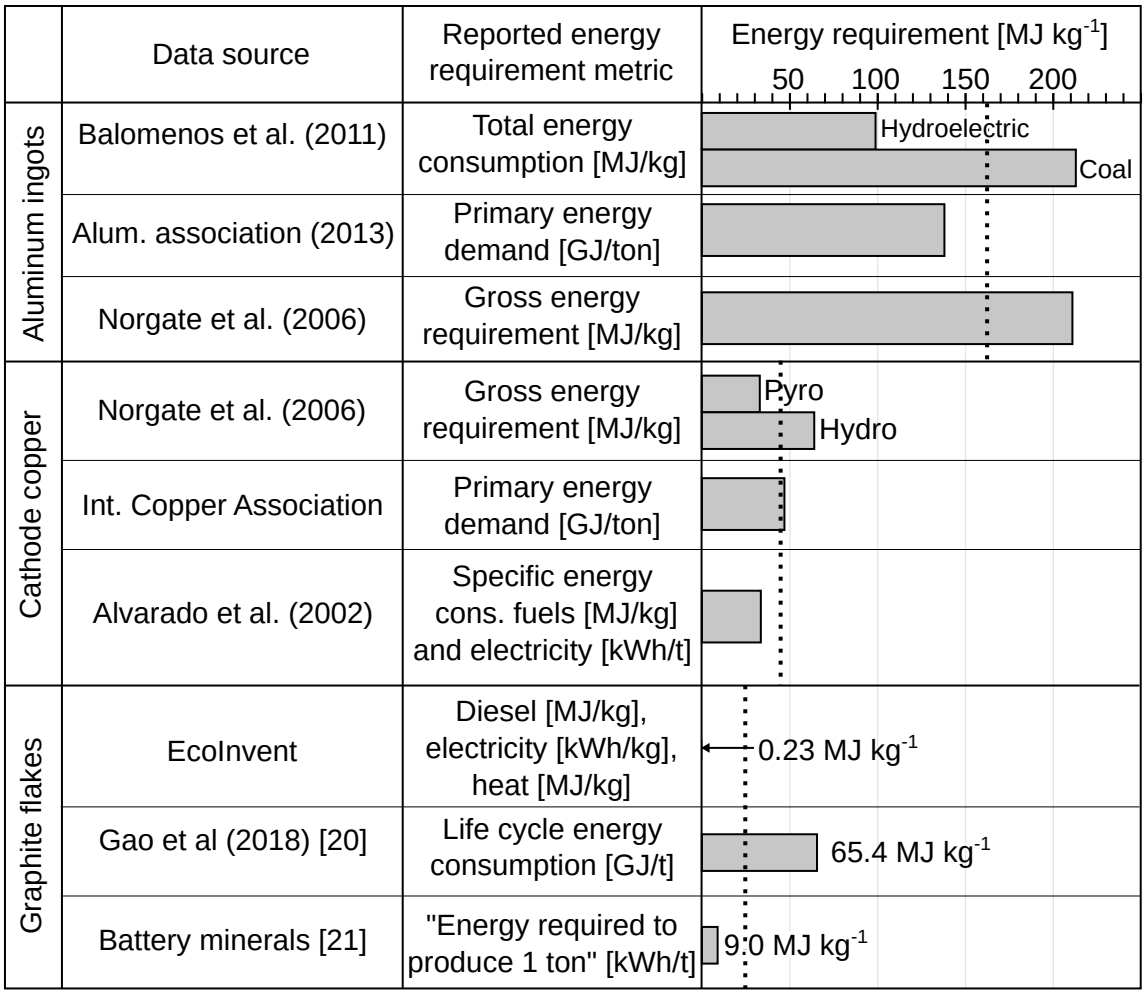

Figure 8.3: A compilation of gross energy requirement of material production of aluminum, copper, and graphite flakes. The dotted vertical lines represent the average values used for calculations in this work.

In the context of heat sinks, the volumetric energy requirement of material production is more relevant for comparing the candidate heat sink materials because the thermal design process outputs the shape. The mass is dictated by the density of the used material. The average values of the energy requirement presented in Figure 8.3 were used to create the comparison of the volumetric energy requirement in Figure 8.4. The high density of copper causes the difference between the volumetric energy requirement of aluminum and copper to decrease in comparison with the per-mass one. The volumetric energy requrement of NGS varies based on the selected sheet density, but it is always significantly lower than that of aluminum or copper. At the highest density of $1.9\,\mathrm{gcm}^{-3}$, the volumetric energy requirement of graphite flakes is 12 % that of copper and 10 % that aluminum. At the lowest density of $0.5\,\mathrm{gcm}^{-3}$, it is 3 % that of copper and 2.7 % that of aluminum.

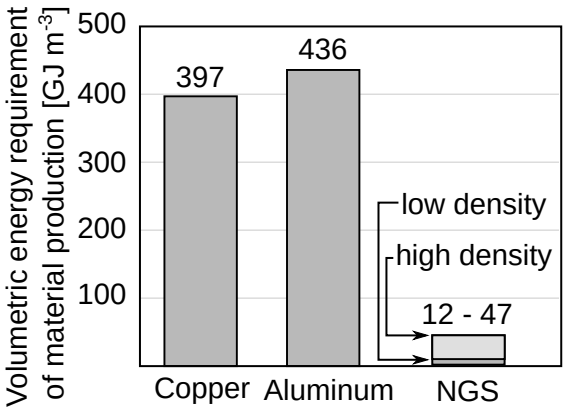

Figure 8.4: Volumetric energy requirement of material productioin of aluminum, copper, and graphite flakes

Based on the data presented in Figures 8.3 and 8.4, the energy requirement of NGS production is approximately 89 % and 93 % lower than that of aluminum and copper, respectively, which suggests a lower environmental fooprint of NGS. However, the conventional purification and exfoliation processes use large amounts of high concentration acids [47, 159], which may result in NGS having a higher overall environmental footprint. Methods for purification and exfoliation are an active area of research both in academia [50, 47, 160, 161] and in industry [162]. Any future LCA study of NGS should consider the current methods but also the future projections.

The parameters of the purification process, such as type of acid, its concentration, and exposure time, are selected based on the requirements on the purity of graphite flakes and properties of NGS. While most of the studies assume applications in lithium-ion batteries where high purity with 99.95 % of fixed carbon is required [162], heat sink applications do not requre such high purity. However, since the relationships between the purity and NGS material properties are not known, it is not possible to determine the optimal purity. If properties such as thermal conductivity are not sensitive to the impurity content, flakes with lower purity can be used and the environmental footprint can be reduced.

Besides mining, flake graphite can be also recovered from the steelmaking waste called kish [52, 163, 61]. Liu and Loper [163] stated that even though a large amount of kish is being generated by the steelmaking industry, the recovery of flake graphite is limited by the lack of processing methods. While recovering flake graphite from kish is in principle similar to processing of natural flake graphite, the chemical composition of impurities is different, and a direct transfer of the recovery methods is not possible. Evaluating whether using kish graphite can have positive implications on the environmental impact of production of the flake graphite requires the methods for purification of kish graphite to be developed, analyzed using the LCA approach, and compared to those of natural graphite. In parallel, the economy of the recovery process must be studied. Currently, kish graphite is commer-

cially available for research purposes. However, it is produced at small scale in a laboratory environment, which causes its price to be very high. R. Frost [61] performed a cost analysis of a facility for recovering kish graphite as a part of their master's thesis. The recovery was concluded to be economically feasible.

Another alternative to mining is using non-biodegradable plasitc waste as a source of carbon for production of flake graphite in liquid iron as proposed by Sri Devi Kumari et al. [164].

8.2 Manufacturing

The manufacturing process of NGS products consists of exfoliation, rolling, pressing, optional polymer impregnation, and assembling, as is shown in Figure 8.5. Similarly to the purification step in the production of graphite flakes, the conventional exfoliation method requires a use of acids. However, novel methods with lower environmental impact are being developed [165, 166, 167, 168]. Any future LCA study must account for the new methods and the probability of their use by the emerging NGS industry. The method of exfoliation affects the properties of ENG particles, such as SEV, which in turn affect the NGS properties (see section 3.7). Many exfoliation methods are aimed at producing graphite nanoplatelets [159, 169, 166] that require high SEV and using them for production of ENG for NGS can be unnecessary, or even adverse to the desirable material properties. Studies on the relationship between the exfoliation method and material properties of NGS are currently not available. However, once they have been performed, the appropriate exfoliationg methods for NGS heat sink purposes can be chosen and their environmental footprint can be evaluated and optimized. Upon commercialization of NGS products, the market pressure is expected to stimulate the above mentioned future studies because optimizing the use of chemicals is typically linked with a cost reduction.

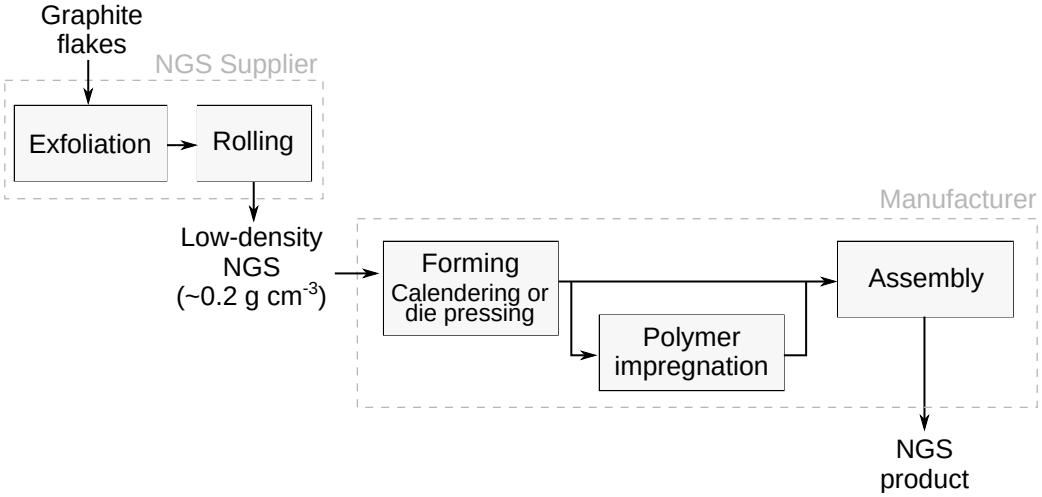

Figure 8.5: Manufacturing steps in production of NGS parts

The energy requirement of the exfoliation step can be inferred from the work of Pizza et al. [159] who assumed the microwave exfoliation method, and estimated the energy input to be $0.9\,\mathrm{MJkg}^{-3}$. The rolling step in which the ENG particles are compressed into low-density NGS is a simple mechanical low-pressure compression task which is not expected to have a significant environmental impact. Nevertheless, the electricity consumption of electric motors and the weight of the machinery can be quantified and used for life cycle inventories (LCI) such as EcoInvent [156].

The pressing step, in which the semi-finished NGS is formed into the final sheets, requires presses with the capacity of no more than 20 t. As a reference, the sheets for the heat sinks prepared in this work were pressed using a small manual hydraulic press with the maximum force of 5 t. The pressing step can be included in LCI in the same way as the rolling step.

While the details of the polymer impregnation step depend on the selected polymer, it typically consists of vacuum impregnation and curing at polymerization temperature. The LCA of polymer-graphite composites performed by Pizza et al. [159] can be modified to evaluate the impact of polymer-impregnated NGS by changing the assumed fraction of ENG particles from 5.8 wt% to 24 wt% and for low-density NGS ($0.5\,\mathrm{gcm}^{-3}$) and 86 % for high-density NGS ($1.9\,\mathrm{gcm}^{-3}$). The polymer was assumed to fill all the pores, and its density was assumed to be $2\,\mathrm{gcm}^{-3}$. Pizza et al. [159] concluded that only 2.6 % of the total energy requirement comes from the preparation step and the resulting 97.4 % arise from the energy usage during the primary production of the materials. The energy requirement of vacuuming and curing was estimated to be 0.16 MJ per kg of polymer, which translates to the volumetric energy consumption of the polymer impregnation process of 0.05 to $0.25\,\mathrm{GJm}^{-3}$ (with respect to NGS volume). The energy consumption of the polymer impregnation is 0.4 to 0.5 % of that of primary material production.

For comparing the energy consumption of manufacturing of NGS heat sinks with conventional heat sinks, extruded aluminum heat sinks were selected as the reference case due to their widespread use and data availability. The energy consumption of aluminum extrusion, which is a combination of pre-heating of aluminum ingot to 450 to 550 °C and pressing it through the die, is $12.6\,\mathrm{GJm}^{-3}$, out of which 87 % is the energy for heating [170] (assuming density $2.7\,\mathrm{gcm}^{-3}$). The typical capacity of the press in aluminum extrusion machines was considered to be 2500 t, which is 125-times more than that in NGS pressing step. The energy consumption of the NGS pressing step was conservatively estimated to be $1.6\,\mathrm{GJm}^{-3}$ by eliminating the heating portion from the extrusion consumption. Copper is typically formed by cold forging whose energy requirement was assumed to be identical to that of NGS pressing.

It should be noted that aluminum heat sinks are typically anodized to increase the radiative heat trasfer. Anodization is an electrochemical process involves submerging the parts in acid (most often sulfuric acid at 10 to 15 % concentration [171]) and its environmental footprint should not be overlooked in the future studies.

8.3 End-of-life management

Conventional aluminum and copper heat sinks are easy to recycle with only minor complications arising from accumulation of manganese and lead [172]. The end-of-life management of graphite is much more complex and has not been developed thoroughly due to its relatively low usage. Efforts have been made to recycle the synthetic graphite used in nuclear reactors [173], and the recent development in lithium-ion batteries stimulated a research interest in recycling flake graphite in their anodes [174, 175]. In the LCA study of graphite-polymer composites by Pizza et al. [159], the authors used landfill and incineration as the disposal method, and highlighted the difficulty of separating the individual parts of the composite. It was also noted that after incineration, around 50 % of the composite remains as ash. Recycling of NGS has not been studied before. In the following section the problem is analyzed and recommendations are made.

All the recycling or re-purposing options stated in this text assume that at the end of the life time, the electronic products are recollected and transported to a recycling facility, in which the NGS parts are recovered either directly by disassembling it from the product, or indirectly by shredding and subsequent separation. In Figure 8.6, the process of recycling of NGS parts is outlined and the direct recovery is assumed. To input the recovered material back to the manufacturing process, it must be in the form of ENG particles. Whether NGS can be re-exfoliated using the same techniques as in the primary material production has not been studied and future studies are required to prove the feasibility of this step. In case of polymer-impregnated NGS, additional thermal or chemical separation step is necessary to remove the polymer. The wet exfoliation process contains the intercalation step in which graphite flakes are soaked in acid. An integration of the the polymer removal and intercalation steps might be possible.

If re-exfoliation is shown not to be feasible, NGS can be used for other purposes such as a precursor in manufacturing of synthetic graphite, recarburizer in production of steel, or if polyimide impregnation is used, the graphite-polyimide mix may be a suitable precursor for producing thin pyrolytic graphite sheets [45].

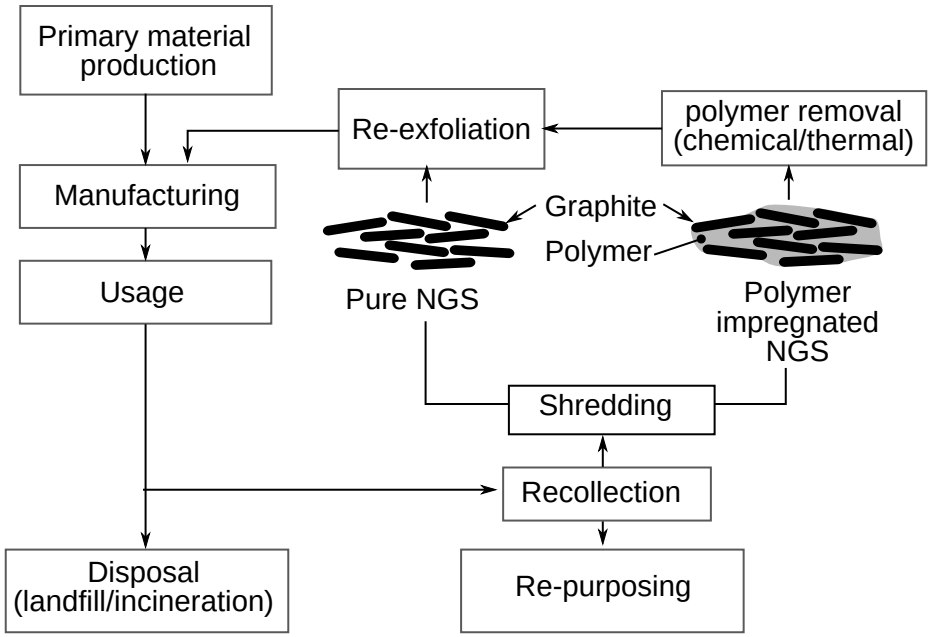

Figure 8.6: A schematic of possible end-of-life disposal of NGS products.

8.4 Conclusions

The environmental impact of NGS was compared to that of conventional heat sink materials by investigating the energy requirement, and reviewing other relevant aspects of production, manufacturing, and end-of-life management. The energy requirement of NGS production and manufacturing was found to be lowerthan that of aluminum and copper primarily due to the low energy intensity of production of graphite flakes. However, the energy requirement data in the literature show high scatter and low reliability, which increases the uncertainty of the present conclusions. A comprehensive LCA of production of graphite flakes with a strong focus on predicting the future trends in the industry is suggested to mitigate the encountered shortcomings. The volumetric energy requirement of aluminum and copper production is comparable with aluminum showing only 10 % higher value. The end-of-life management of NGS is poorly studied and significantly more complex than that of easy-to-recycle metals. Recyclability of NGS is expected to be inferior to that of metals, which will likely result in an increased overall environmental impact of NGS.

This study showed that introducing NGS heat sinks in power electronics will likely not increase the environmental impact arising from the energy consumption. However, a detailed LCA is required to make the similar conclusions about other aspects of environmental impact such as ecotoxicity, acidification potential, or greenhouse gas emissions.

Kish graphite was identified as an attractive alternative to natural graphite sheet, however, its processing and resulting material properties have not been well studied. The future research should focus on: i) developing recovery methods and comparing their environmen-

tal footprint to that of methods used in natural graphite processing, and ii) measuring the properties of graphite sheets prepared from exfoliated kish graphite. Combining the results of the two proposed research topics will determine the feasibility of using kish graphite as an alternative to natural flake graphite.

Chapter 9

Holistic evaluation of feasibility of NGS heat sinks

Evaluating the feasibility of NGS heat sinks requires considering all the benefits and challenges. This chapter offers a concise summary of all relevant feasibility aspects, and aims to provide the basis for determining whether using NGS heat sinks can lead to improvements in *overall* performance of power electronic products. An audiovisual summary of the chapter is available at `https://www.youtube.com/watch?v=u8dR0fdAdXo&list=PLaX55SIXaD20NQQ2JLP-7abmET7l-6LS4& index=7` [1].

9.1 Thermal performance

In chapter 5, it was shown that the thermal performance of NGS heat sinks can be comparable to that of geometrically identical aluminum ones. However, the assumption of identical geometry is relevant only to the fundamental research work. In practical applications, a direct replacement of an existing aluminum heat sink with a geometrically identical NGS one will significantly limit the potential to improve the thermal performance. The optimum geometry for given conditions is different for aluminum and NGS because of the different material properties and manufacturing constraints. The feasibility of using NGS heat sinks is case-specific and depends on design restrictions such as available volume or air flow rate. Nevertheless, the points that can be generalized are discussed below.

The total thermal resistance of a heat sink is dictated by i) the device-sink interface, ii) conduction within the heat sink, and iii) convection at the sink-air interface. Out of the three, only i) is independent of the heat sink geometry and its contribution to the NGS feasibility can be discussed generally.

Based on Figure 9.1, which shows a comparison of the specific TCR at metal-metal and NGS-metal interfaces, it can be concluded that the thermal resistance at the sink-device

[1] The video files are also available in Appendix F

interface of NGS heat sinks is comparable to the best-performing thermal greases in the reference study. The results of the heat sinks measurements presented in chapter 5 confirm this conclusion.

Both the conduction and convection resistances of the heat sink are a function of the geometry and material properties. NGS heat sinks are expected to have lower convection resistance because the manufacturing method allows making complex shapes at low cost. A detailed explanation of expected advantages is given in Chapter 10.

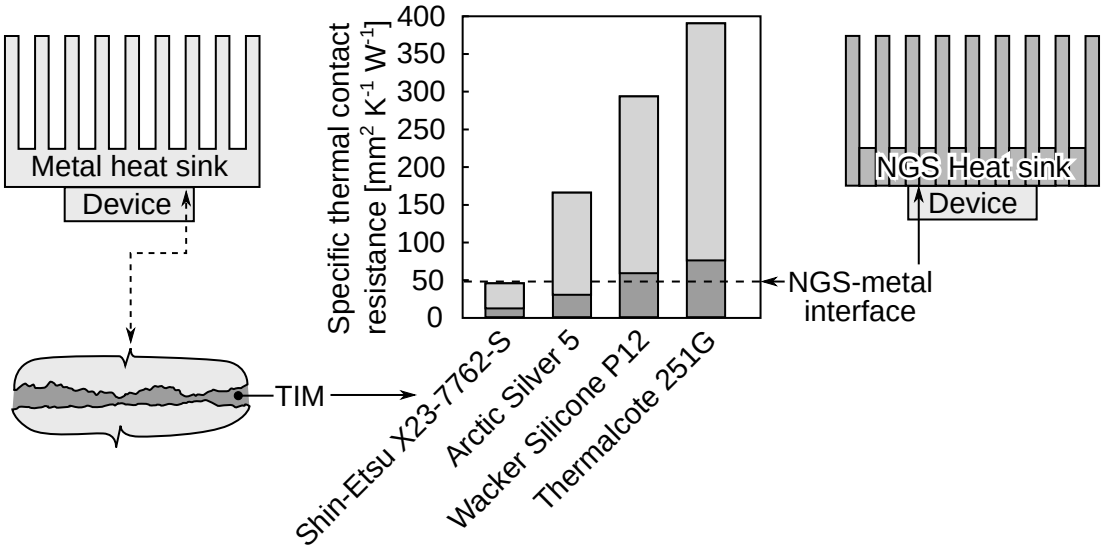

Figure 9.1: Comparison of the specific TCR of metal-metal interfaces with common thermal greases (left) and NGS-metal interfaces (right). The TIM data are from Narumanchi et al. [132] and the high and low values visualized by the light-gray portion correspond to the data for 200 µm and 31 µm bond line thickness, respectively. The value of NGS-metal TCR was measured in this work and described in section 5.4. The NGS-metal data were collected at 1100 kPa, while the TIM data by Narumanchi et al. [132] were available only at 255 kPa.

9.2 Electromagnetic performance

The main difference between NGS and conventional heat sink materials from the EMI/EMC[2] perspective is the electrical conductivity. NGS has two to four orders of magnitude lower electrical conductivity, which puts it into the lossy conductors category. In chapter 6, it was shown that the conducted common mode emissions are not affected by changing the heat sink material from metal to NGS because the impedance of the emission path is dominated by the parasitic capacitance between the device and the heat sink. The effect of heat sink material on radiated emission was not quantified directly, but based on an analogy with

[2]Electromagnetic interference, Electromagnetic compliance

antennas, the radiated emissions of NGS heat sinks were estimated to be 12 to 97 % lower than that of metal ones.

9.3 Weight

Contrary to the conventional heat sink materials such as aluminum and copper whose density varies insignificantly between different alloys, the density of NGS can be selected by the heat sink designer within the range starting from the lowest practical value of $0.5\,\mathrm{gcm}^{-3}$ and reaching up to $1.9\,\mathrm{gcm}^{-3}$. A comparison of the density of NGS, aluminum, and copper is given in Figure 9.2. By replacing an existing heat sink with a geometrically identical NGS one, the weight reduction of 30 to 81 % can be achieved in case of aluminum, and 79 to 94 % in case of copper. If polymer-impregnated NGS is used, the weight reduction potential reduces slightly. A detailed graphical illustration of the possible weight reduction is given in section 9.9.

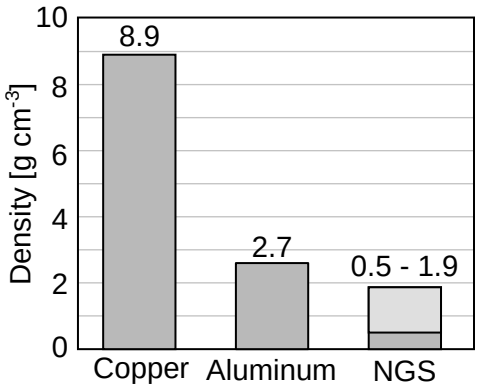

Figure 9.2: A comparison of the density of copper, aluminum, and NGS.

9.4 Cost

The results of a case-specific first-approach cost analysis of NGS heat sinks are shown in Figure 9.3. At high production volumes, the large scale NGS heat sinks produced within this thesis are expected to be 64 % more expensive than a comparable mass-produced aluminum heat sinks. For NGS heat sinks with embedded heat pipes the difference increases to 87 %. Due to the high uncertainty in the cost analysis (see chapter 7) using the numerical results is not suggested and instead, the cost of NGS heat sinks is considered to be approximately double that of conventional aluminum ones. The cost at small production volumes has not been quantified, but a qualitative estimate suggests that NGS heat sinks can be cost competitive in highly-specialized demanding applications, which require the heat sinks to be 3D printed or CNC machined.

It is recommended that the financial feasibility of NGS heat sinks is judged carefully by considering not only the heat sink cost but also the indirect factors such as the the possibility to eliminate the need for a thermal grease, the weight benefit, the potential to reduce the radiated emissions of power electronics, or even the long term cost benefit arising from improved reliability and longer lifetime. The financial feasibility of NGS heat sinks is–same as most of the other heat sink selection criteria–case specific and a suggestion on an integrated approach to judging the feasibility is given in chapter 10.

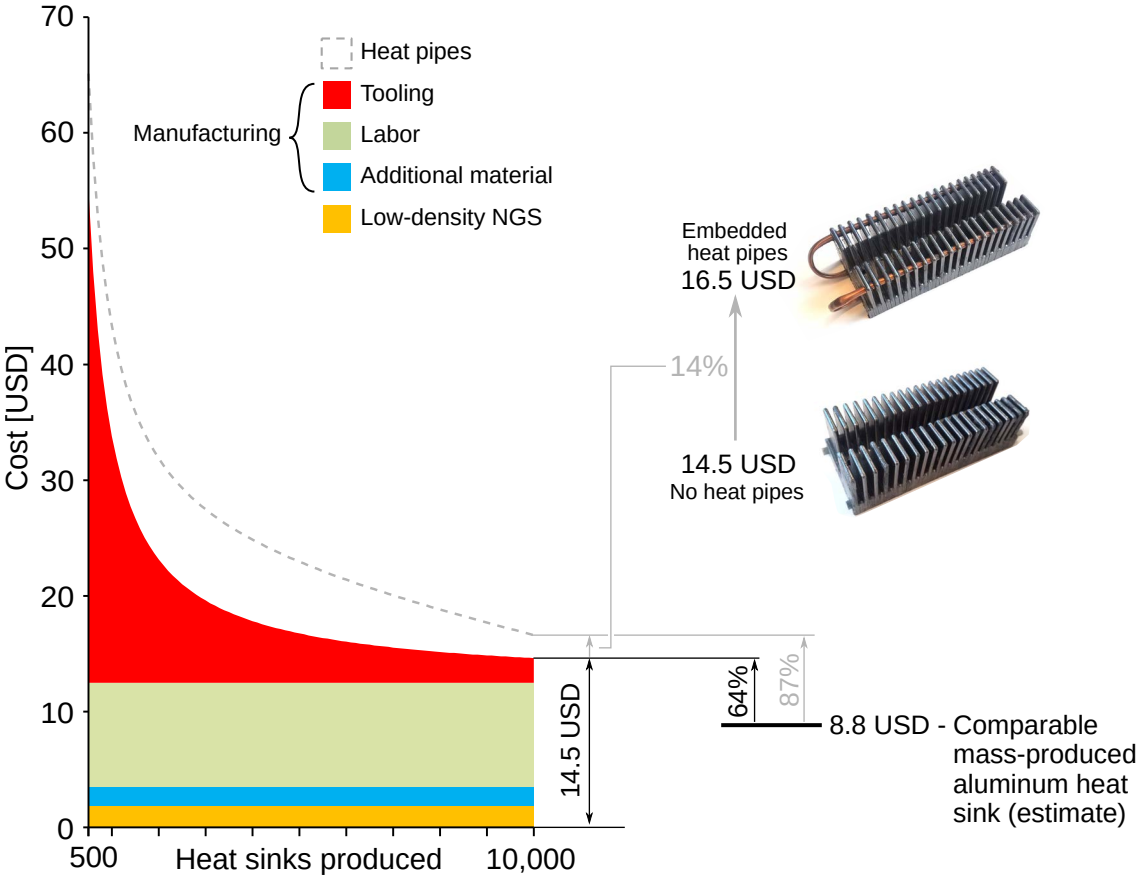

Figure 9.3: A compilation of the results of cost analysis of NGS heat sinks.

9.5 Reliability

Replacing a metal heat sink with an NGS one can affect the reliability of electronic devices directly and indirectly. The direct implications arise from the failure or degradation of the heat sink itself, while the indirect ones are the result of the changed operating conditions of the device. The direct reliability concerns are related to the exposure to vibrations and humidity. Due to the low mechanical strength of NGS, the fins can break in highly vibrating environment. However, the low strength can be balanced by the lower density of NGS that reduces the magnitude of inertial forces. Operation in a vibrating environment can also lead

to detachment of conductive particles from the NGS structure, thus creating a risk of short circuiting exposed terminals within the device. Penetration of humidity or liquid water into NGS and subsequent freezing temperatures can disturb the internal structure and cause a degradation of the material properties. Polymer impregnation is expected to mitigate both the vibration and humidity issues by improving the mechanical strength and by preventing the moisture uptake. The measurements to confirm the expectations must be carried out in the future work.

The indirect reliability concerns are caused by the different thermal and mechanical boundary conditions that the cooling system imposes on the device. Replacing an existing metal heat sink with an NGS one will change the thermal and mechanical conditions because the thermophysical properties such as the heat capacity, CTE, compression modulus, or flexural strength of NGS are significantly different in comparison with metals.

The lower heat capacity of NGS (15 to 58 % that of aluminum, 11 to 40 % that of copper) affects the transient thermal behavior under unsteady loads. The resulting temperature changes are larger and more rapid, which can increase the thermomechanical stresses within the device and decrease the time-to-failure as was discussed in [176]. Polymer impregnation increases the volumetric heat capacity of NGS such that it becomes comparable to aluminum at low densities, and up to 76 % that of aluminum at high densities. The heat capacity of polymer-impregnated NGS is 53 to 74 % that of copper.

The stiffness of heat sinks is one the factors that affects the deformation of devices during temperature cycling. The deformation is caused by the different CTE of materials used in the device packaging. Using NGS heat sinks whose mechanical properties are substantially different than those of conventional metal ones will lead to different thermomechanical stresses in the entire assembly. As a result, the expected lifetime can be reduced or increased. Further research and a dialogue with the manufacturers of semiconductor devices is necessary to identify if the reduced mechanical stiffness of NGS heat sinks can lead to an improved reliability of discrete semiconductors or power modules.

Reliability of interfaces with thermal grease suffers from long term degradation due to the displacement of the grease (pump-out) and its chemical decay (dry out). The latter is further amplified in modern high-temperature semiconductor materials such as silicon carbide. Soft and conforming NGS heat sinks do not require thermal grease, and their temperature stability has been reported to be acceptable up to approximately 400 °C. It is likely that the reliability of NGS-metal interfaces is better than that of metal-metal ones with thermal grease. However, the long term evolution of the interface thermal resistance under fluctuating loads and in vibrating environment should be studied to prove the above claim. The operating temperature must be reflected in the selection of the polymer for impregnation.

9.6 Resiliency

Low mechanical strength makes the NGS heat sinks prone to breaking when impacted by other objects in applications where a risk of a collision exists. While polymer impregnation of NGS improves the mechanical properties, using NGS heat sinks in applications without a protecting case is not recommended.

High chemical stability of graphite suggests its feasibility for applications in harsh environments. Ability of synthetic graphite to withstand acidic environment has been shown in [177]. Whether the results can be extrapolated to NGS is not guaranteed, but the fact that acids are used in the manufacturing of NGS supports this assumption. Oxidation of natural graphite in air occurs only at high temperatures (600 °C) and its rate is dependent on multiple parameters such as the flake size or the amount of impurities [178]. Assessing the corrosion behavior in humid or even marine conditions requires a complex electrochemical analysis and/or experimental studies. Since graphite is more noble than copper or tin, which are typically used for the surfaces of electronic devices that are adjacent to a heat sink, a risk of galvanic corrosion exists [179], but the relevant measurements have not been reported in the literature. The risk of NGS causing corrosion of the mating parts is exacerbated by the possibility of residual sulfur content. The specifications of commercially available NGS state the upper limit of the sulfur content to be in the range from 120 to 1400 ppm.

9.7 Integration

In many of the current power electronics products, the heat sink is attached to the device using a bolt and a threaded hole in the heat sink. The low mechanical strength of NGS does not allow forming threads, and incorporating threaded metal inserts at the base of NGS heat sinks was reported not to be reliable [35]. Alternative clamping methods exist and should be used for NGS heat sinks. In applications where electrical insulation is necessary, pressure-activated adhesive films are a common choice and can be used for NGS heat sinks. To suggest a possible mounting options for non-insulated cases, a plastic bracket has been manufactured and is shown in Figure 9.4. The bracket can contain threaded metal inserts, but other attachment options such as a clip-on mechanism are possible, and their feasibility should be judged based on the required clamping pressure. It is expected that the most suitable mounting methods will be developed during the commercialization stage because a dialog between heat sink manufacturers and system integrators is necessary.

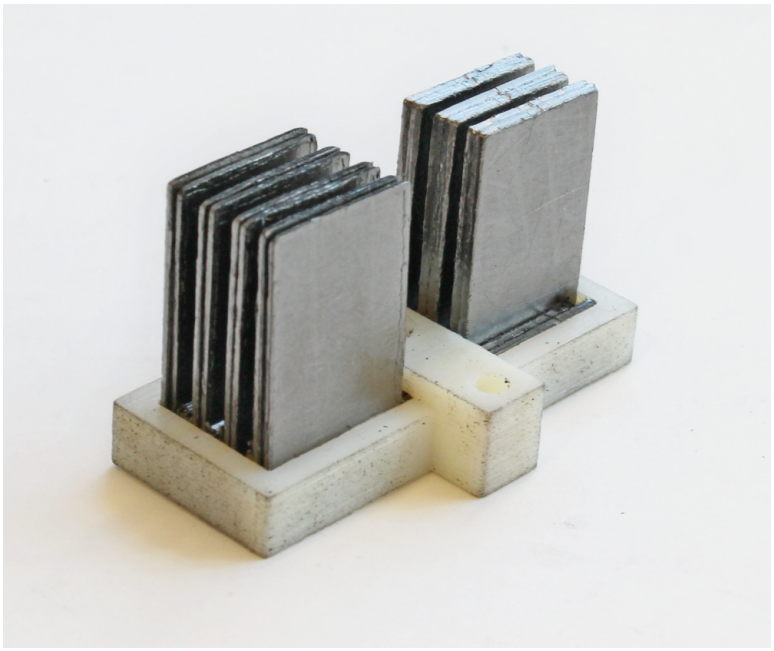

Figure 9.4: A demonstration plastic bracket for mounting NGS heat sinks.

9.8 Energy efficiency and environmental impact

The manufacturing technology of NGS heat sinks allows advanced heat sink shapes that can be optimized for low thermal resistance and low pressure drop. As a result, the energy consumption of the fans can be reduced, and the overall efficiency of the product can be improved.

Judging the environmental impact of various heat sink materials is complex. The energy requirement of NGS appears to be 89 % lower than that of copper, and 88 % lower than that of aluminum. However, the data sources for NGS are sparse and their uncertainty is high. Recyclability of NGS has not been well studied and it is predicted to be problematic especially when NGS is impregnated with a polymer. Extensive future work is necessary to make reliable conclusions.

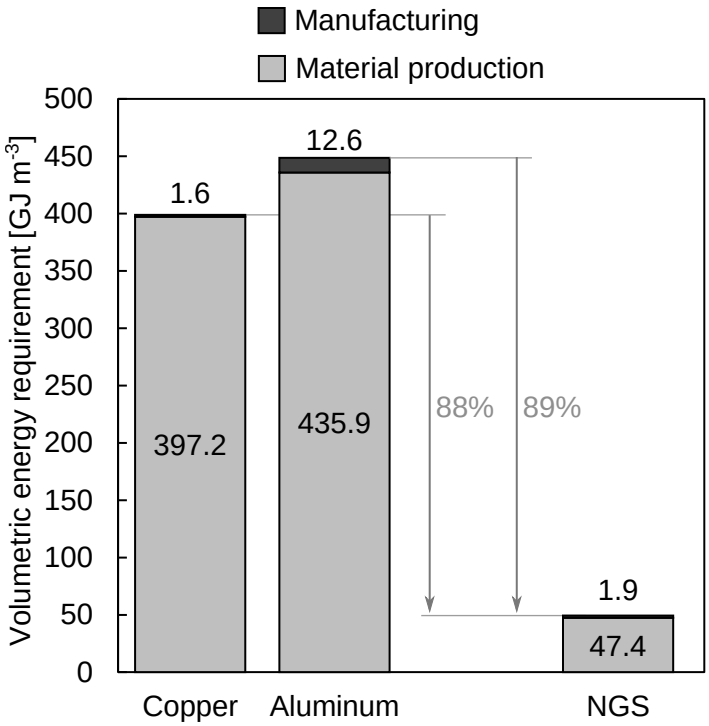

Figure 9.5: Comparison of the volumetric energy requirement of production and manufacturing of copper, aluminum, and NGS. The NGS production data is conservative assuming the highest density of $1.9\,\mathrm{gcm}^{-3}$. The energy requirement of manufacturing assumed cold forging for copper, extrusion for aluminum, and pressing and polymer-impregnation for NGS.

9.9 Trade-off illustration

Selection of a heat sink is a multi-objective optimization task that should consider all the factors listed above in this chapter. The following trade-off illustration is relevant to a situation in which a design team has the time and resources to develop a custom heat sink, as opposed to only purchasing an off-the-shelf mass-produced one. To address all the degrees of freedom, an advanced optimization technique must be employed and the process is outlined in chapter 10. Here, a simplified approach is adopted to highlight the possibility to tailor the NGS density to achieve the required performance. The effect of varying density is shown on the thermal resistance and weight, but the same concept applies to all performance metrics.

To be able to isolate the effect of material and compare NGS, aluminum, and copper, the heat sink geometry is considered to be identical and the heat source is assumed to cover the entire base of the heat sink. Neither of the assumptions is acceptable for most of the practical applications, however, the goal of this section is to demonstrate the trends, not to provide definite conclusions.

In Figure 9.6, the aluminum heat sink was used as the reference for calculating the relative performance of the NGS and copper one. The calculation of the thermal resistance

is described in Appendix D. The thermal resistance of the NGS heat sink is a function of the NGS density because the in–plane thermal conductivity increases with density as was discussed in section 3.7. At the density of $1.05\,\mathrm{gcm}^{-3}$, the in–plane thermal conductivity of NGS is equal to that of aluminum ($200\,\mathrm{Wm}^{-1}\mathrm{K}^{-1}$), and the thermal resistances of the NGS and aluminum heat sinks are therefore identical. At densities lower than $1.05\,\mathrm{gcm}^{-3}$, the thermal resistance of the NGS heat sink is higher than that of the aluminum ones, and vice versa. The thermal resistance of the copper heat sink is lower than that of the aluminum and NGS ones because of the high thermal conductivity of copper ($385\,\mathrm{Wm}^{-1}\mathrm{K}^{-1}$). The relative difference between the aluminum, copper, and NGS heat sinks is also a function of the geometry as is illustrated by the two geometrical configurations (Geometry 1 and Geometry 2 in Figure 9.6). Geometry 1 (blue) consists of short and thick fins, while Geometry 2 (green) consists of long and thin fins. Geometry 2 makes the thermal resistance more sensitive to thermal conductivity and the differences between aluminum, copper, and NGS are therefore more pronounced.

The ratio of the heat sink weight, which is shown at the bottom of Figure 9.6, shows that the NGS heat sink is lighter than the aluminum one even with polymer impregnation. A polymer with the density of $2\,\mathrm{gcm}^{-3}$ was considered to fill the entire porosity of NGS. The high density of copper makes the copper heat sink 3.3 times heavier than the aluminum one.

In weight sensitive applications, NGS heat sinks can be tailored to suite the design priority. If a low weight is the primary requirement, the thermal resistance can be sacrificed and heat sinks with the weight 19 to 76 % of aluminum can be build by using a low density NGS. If a good thermal performance is the highest priority, using high-density NGS can deliver the thermal resistance comparable to that of copper at the weight 65 to 76 % that of aluminum.

It must be noted here that the quantitative comparison presented here is limited the by the idealized assumptions. The relative weight and thermal performance of aluminum, copper, and NGS heat sinks is case-specific and the recommended methodology for evaluating the feasibility is outlined in chapter 10.

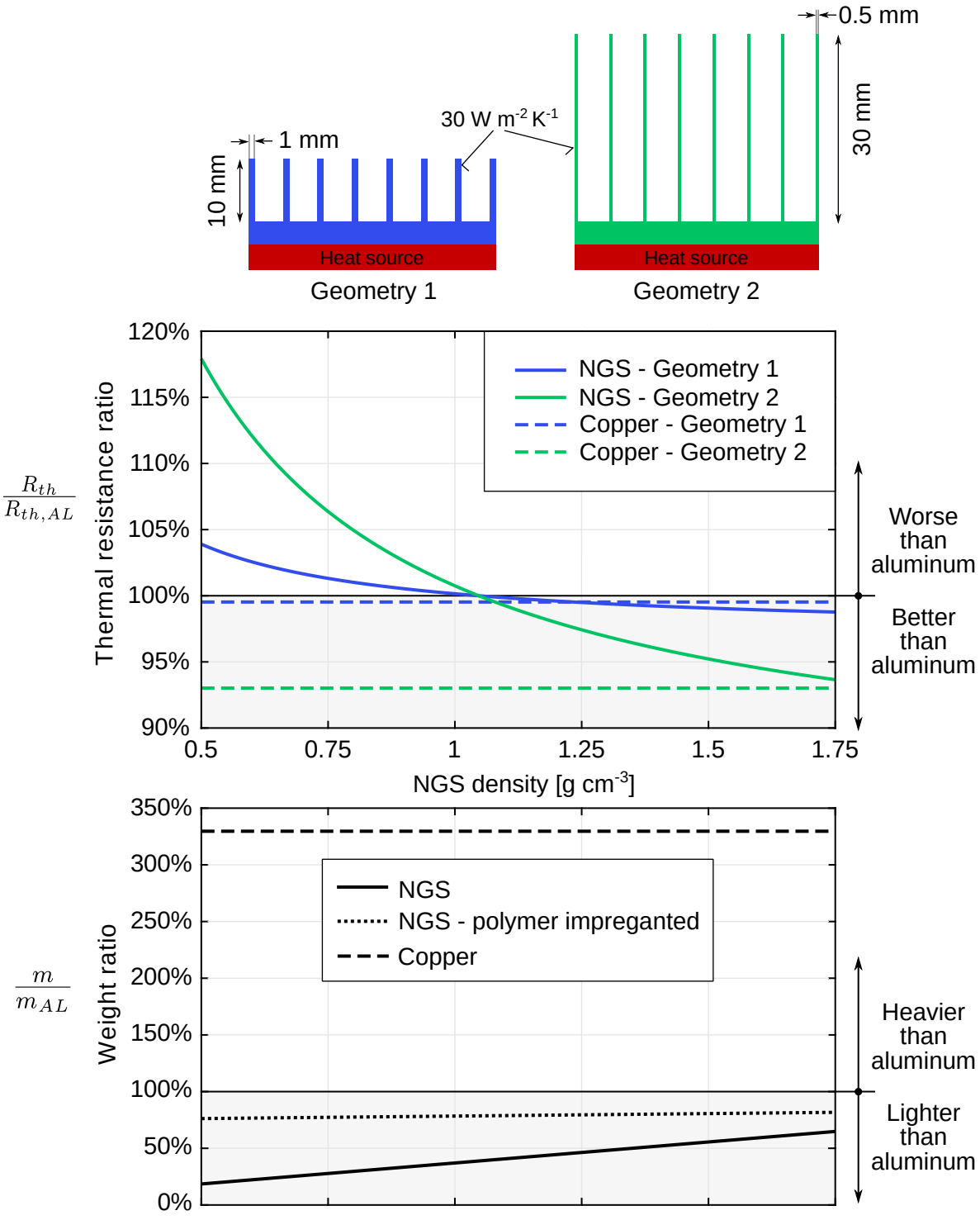

Figure 9.6: A comparison of the thermal resistance and weight of geometrically identical aluminum, copper, and NS heat sinks.

Chapter 10

NGS heat sinks: the path forward

One of the main conclusions of this thesis is that the feasibility of NGS heat sinks cannot be generalized and it has to be evaluated on a per-case or per-application basis. Attempts to investigate the feasibility in Chapter 9 are burdened with unrealistic assumptions such as the identical geometry of conventional and NGS heat sinks. This chapter outlines the future steps that are considered necessary for concluding if NGS heat sinks are a feasible solution for a given application.

The material properties of NGS and conventional heat sink materials are significantly different. When considering replacing an existing heat sink with an NGS one, the difference in material properties must be taken into account to fully exploit the potential of NGS. In Figure 10.1a a typical case with a conventional parallel-plate heat sink on a relatively small heat source is shown. The arrows at the top of the figure symbolize the material properties. The results in section 5.3 can be extrapolated to state that if the heat sink in Figure 10.1a is replaced with a geometrically identical NGS one with embedded heat pipes, the resulting thermal performance will be comparable, and a reduction in weight can be achieved. However, the same outcome can be achieved without heat pipes when a non-identical heat sink geometry is assumed. In Figure 10.1b, one of many possible designs that respect the material properties of NGS at $1.7\,\mathrm{gcm^{-3}}$ is shown. The in–plane thermal conductivity of NGS at $1.7\,\mathrm{gcm^{-3}}$ is $350\,\mathrm{Wm^{-1}K^{-1}}$, which is 75 % higher than the typical aluminum alloy thermal conductivity of $200\,\mathrm{Wm^{-1}K^{-1}}$. In the through–plane direction, the thermal conductivity of NGS si $2.1\,\mathrm{Wm^{-1}K^{-1}}$, which is 99 % lower than that of aluminum. The extended length and width of the heat sink in Figure 10.1b allows for utilizing the higher in–plane thermal conductivity of NGS. The additional fin surface area allows reducing the number of fins, which in turn reduces the impact of the poor through–plane heat transfer in the base.

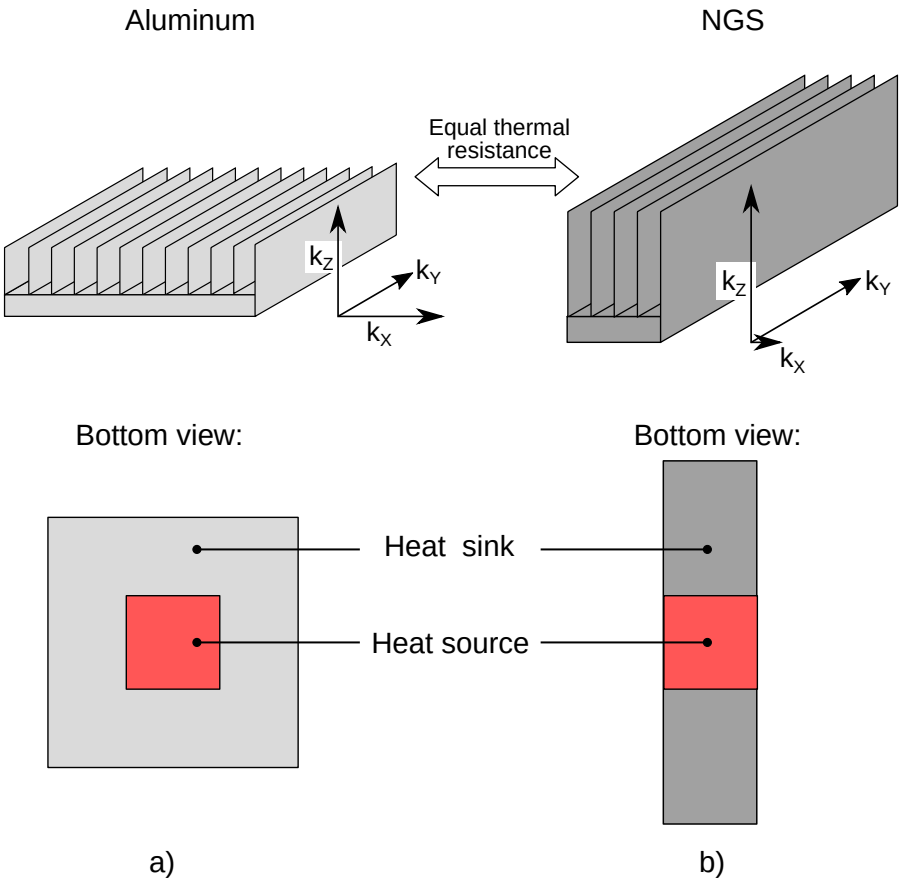

Figure 10.1: a) A conventional metal heat sink and b) an NGS heat sink whose dimensions were adjusted according to the different material properties to achieve the same thermal performance.

While the example in Figure 10.1 provides only a qualitative insight into the issue, quantitative results can be given by reducing the problem into two dimensions as shown in Figure 10.2. The reference aluminum heat sink in Figure 10.2a has twelve fins 10 mm high and 1 mm thick, and its width is larger than the heat source size. The same thermal resistance can be achieved by an NGS heat sink with five fins 25.6 mm high and 1 mm thick, and the overall width that is the same as that of the heat source. The underlying assumptions and calculations are detailed in Appendix E.

To evaluate the feasibility of using an NGS heat sink in an arbitrary case, the demonstrational design process outlined in Figures 10.1 and 10.2 must be automated using a computational tool. The goal is to determine the optimal NGS heat sink geometry for given conditions and compare its performance to that of the heat sink that should be replaced, or that of another candidate heat sink. Such tool will allow the designers to quickly assess whether using NGS can lead to a better performance, lower weight, or lower cost.

The published literature contains multiple studies focused on optimization of heat sink shapes. The most relevant ones introduce versatile algorithms and allow unconventional heat

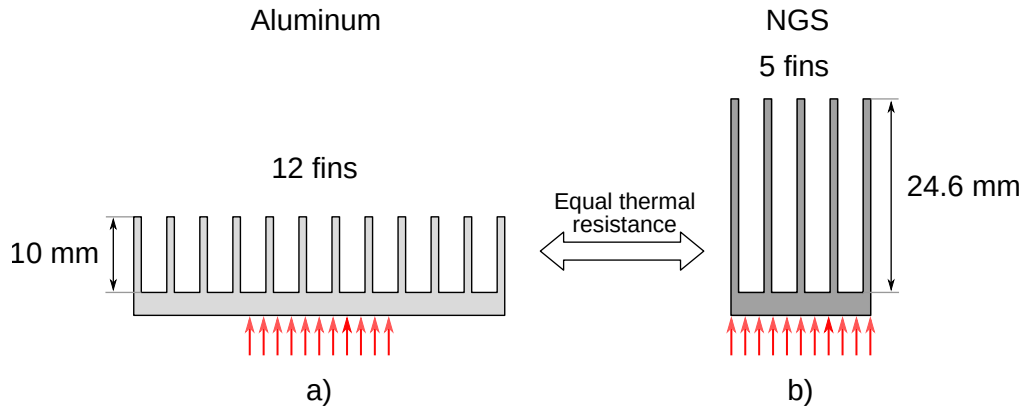

Figure 10.2: A graphical visualization of the results of the simplified two-dimensional calculation of thermal resistance. The reference wide aluminum heat sink with 12 fins shown in a) can be replaced by a narrow and tall NGS one with 5 fins shown in b). The scale of the figure is 1:1.

sink shapes. Wang et al. [180] and Dede et al. [181] utilized the geometrical flexibility offered by the additive manufacturing technology (3D printing) to design and produce novel heat sinks whose shape was optimized for the selected application. In both cases, the methodology involved developing a heat transfer model and coupling it with an optimization algorithm. The same approach is expected to be viable for determining the optimal NGS heat sink geometry.

An outline of the proposed optimization process is shown in Figure 10.3. The design constraints must be first formulated with respect to the considered case. The size of the heat sink is typically limited by the volume within the product that can be dedicated to cooling. The aspect ratio of the available volume is critical for NGS heat sinks because tall and long heat sinks can better benefit from the high in–plane thermal conductivity. The heat source size and air flow limits are dictated by the considered semiconductor devices and air movers. The manufacturing limits must be also taken into account to prevent designs that are practically not achievable. The maximum thermal resistance of the heat sink can be prescribed as a constraint in situation where it is desirable.

Once the constrains are defined, a parametric model considering all the relevant variables can be build. In case of NGS heat sinks, the material properties are not constant and their magnitude varies with the sheet density. The sheet density can be defined as the only variable and the material properties can be then calculated using the best fit relationships of NGS material properties that were developed for this purpose, and are presented in Appendix B. The compression pressure p is included in the best fit equations, but since the heat sinks operate in an uncompressed state, it is irrelevant, and values at the lowest pressure of 100 kPa should be used. It should be noted here that measurements of the through–plane thermal and electrical conductivities at no compression could not be performed within this thesis due to the limitations of the available measurement methods. The future work should

focus on measuring the two properties at no compression to avoid the possibility of under predicting the thermal resistance by using the values at 100 kPa. If designs with embedded heat pipes should be considered in the optimization, their geometrical and performance parameters must be included as variables.

The constraints and variables are inputs to the optimization algorithm. The objective of the optimization must be chosen with respect to the heat sink requirements. Minimizing the thermal resistance of the heat sinks can be satisfactory in some cases, but in weight-sensitive applications a multi-objective minimization of thermal resistance and weight is necessary. If prediction models of cost, electromagnetic performance metrics, or other design objectives are available, they can be incorporated in the optimization algorithm and the optimal heat sink geometry with respect to all the objectives can be determined. Using a cost model can force the optimization algorithm to avoid designs with heat pipes in cases where they are not necessary.

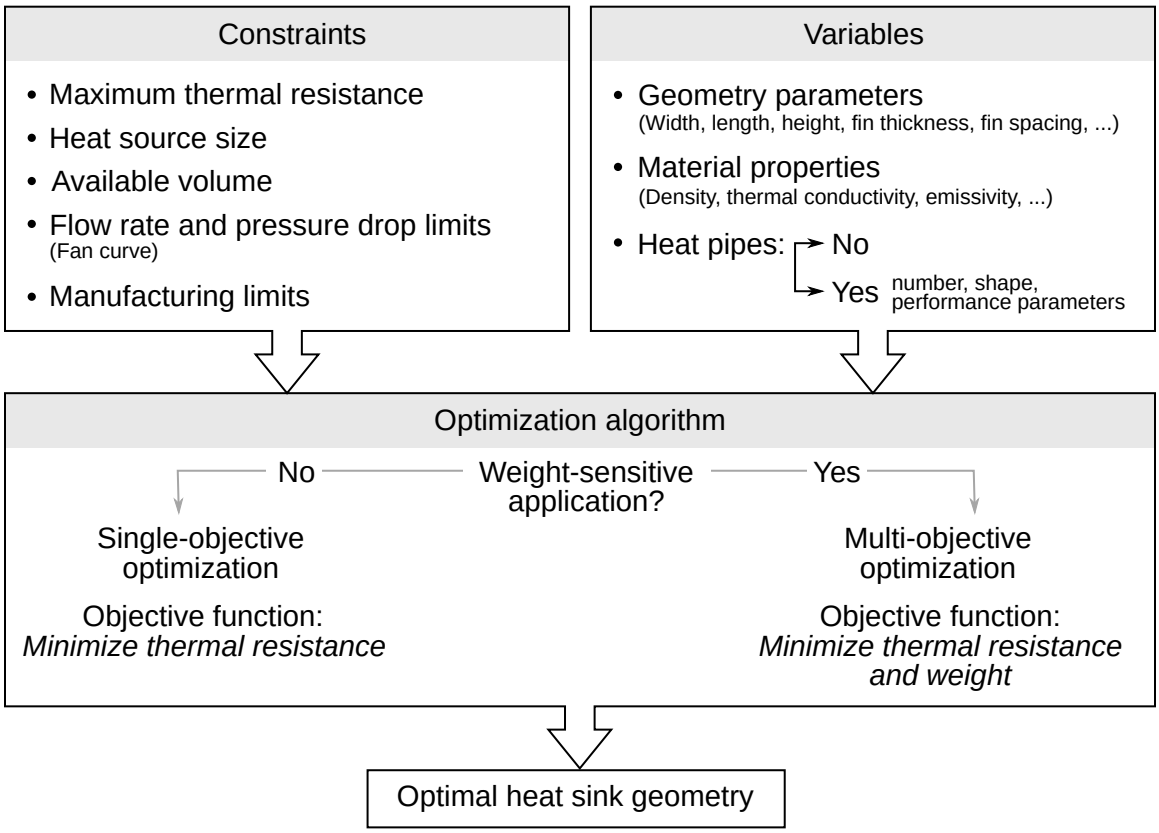

Figure 10.3: A schematic of the proposed optimization computational tool.

When the optimization computational tool has been developed, it can be used to evaluate the feasibility of NGS heat sinks as follows. In a scenario when a power electronics designer considers replacing an existing heat sink with an NGS one, the computational tool can determined whether thermal, weight, or cost benefits can be achieved. When a design team

decides what heat sink material would be the best for their product, the computational tool can be used for determining the optimal geometry for each of the considered materials, comparing their benefits, and making an informed decision.

The proposed optimization approach has known drawbacks. Detailed thermal modeling using finite volume CFD solvers is known to be computationally demanding, which can make the optimization efforts not feasible. On the opposite side of the spectrum, reduced-order models such as resistance-capacitance networks can deliver the solution fast, but their accuracy and versatility is compromised. It is likely that a complementary solution using both methods can be the most suitable approach for practical applications. The reduced-order models can be used for a rough identification of the optimum point, and a numerical model can be used to reach the fine optimum.

It is suggested that the thermal models include the semiconductor packaging because the low through–plane thermal conductivity of NGS makes the thermal resistance sensitive to the heat spreading in the base of the heat sink. Preliminary simulations showed that in some cases the heat flux through the device-sink interface is highly non uniform, and that the heat enters the heat sink in a small area. Detailed phenomena such as this one might be negligible in the most of the applications, but can become significant unexpectedly, and cause a large difference between the predicted and measured thermal performance.

In all the examples above, the optimal NGS heat sink geometry was derived from the conventional heat sink topologies by adjusting their parameters such as height, width, or length. The topology of the conventional heat sinks is dictated by the manufacturing methods. The NGS manufacturing technology is substantially different and it offers the possibility to build heat sink shapes that were previously cost prohibitive or even impossible. An illustration of the possible NGS heat sink shape is shown in Figure 10.4. Multiple features are introduced to minimize the thermal resistance and weight. The fins can be in a staggered configuration, their shape can be arbitrary, and perforations or surface features can be used to enhance the convective heat transfer coefficient. The base does not need to cover the entire heat sink to achieve further weight reduction without sacrificing the thermal resistance. A major advantage of advanced NGS heat sink shapes is the cost, which is not expected to be significantly higher in comparison with the conventional shapes, as is shown in Figure 10.4c. While manufacturing advanced heat sink shapes using the conventional metal-forming methods is likely to result in a high cost, the NGS manufacturing method, which is based on stacking sheets, does not need major modification to achieve advanced shapes, and the cost is therefore expected to increase only marginally.

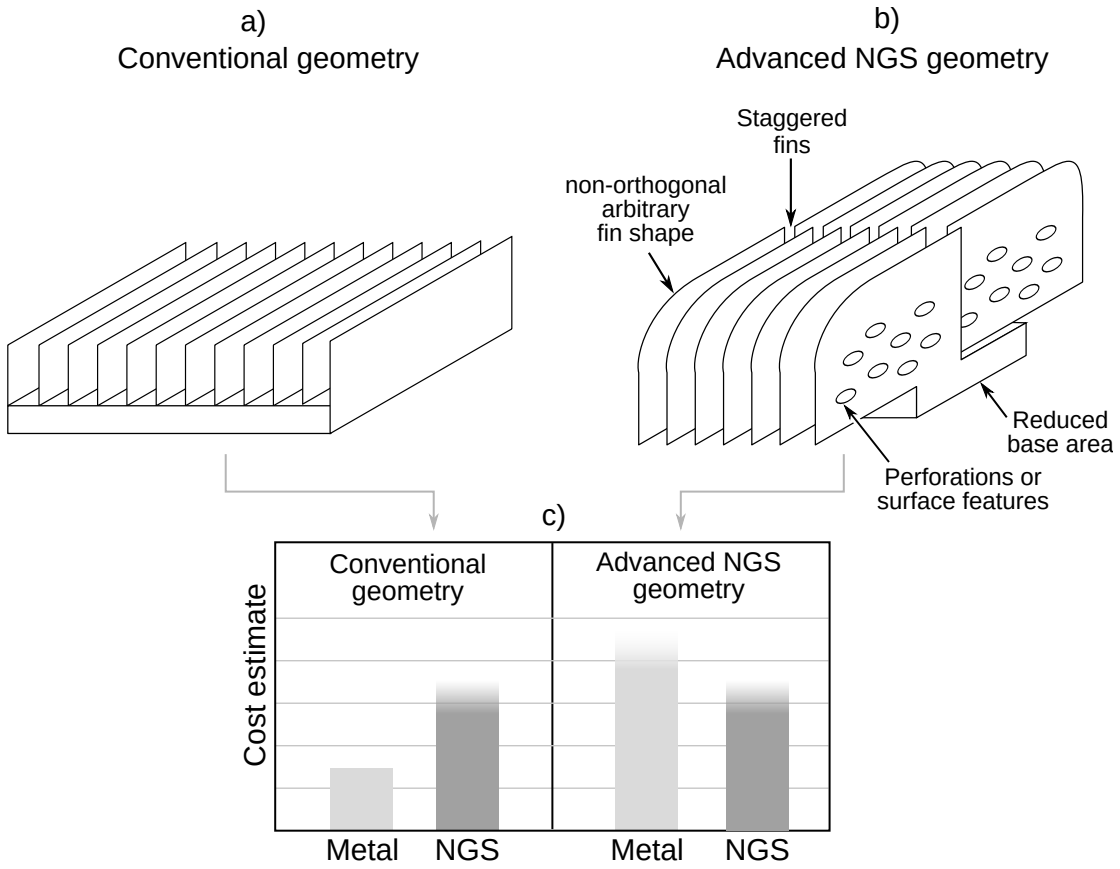

Figure 10.4: An illustration of a) the conventional heat sink geometry and b) the advanced NGS heat sink geometry. An estimate of the cost is shown in c). The blurry edges of the bar charts symbolize the uncertainty of the cost estimate.

The potential of the NGS heat sink is comparable to that of 3D printed ones. Both technologies allow manufacturing novel shapes of heat sinks and tailoring the parameters to individual applications. Future studies can compare the feasibility of the two methods and determine which one is more suitable for next-generation heat sinks. Based on the conclusions in this thesis, it is possible to expect that the feasibility will be, again, case-dependent.

Chapter 11

Conclusions

In the present research, a multitude of steps has been carried out to investigate whether using NGS heat sinks in power electronics can yield an improvement in performance at a competitive cost and low environmental impact. It is shown that heat sink design is a complex task with many case-specific constraints. While an attempt to generalize the findings has been made, the true value of the work lies in providing the fundamental data and suggestions to allow the power electronic designers to perform feasibility studies on a per-case basis. NGS heat sinks are a promising alternative in applications that are weight-sensitive, allow freedom in heat sink size and shape, include a case to protect the heat sink from impacts by other objects, and operate at high temperatures or in harsh conditions. In such applications, factoring in the benefits is expected to justify the higher cost in comparison with conventional metal heat sink. The technology is considered to be ready for a transfer the industries where financial resources for remaining research and development tasks are available. A brief audiovisual summary of the general conclusions is available at `https://www.youtube.com/watch?v=LtvsAcVieaI&list=PLaX55SIXaD20NQQ2JLP-7abmET7l-6LS4&index=8` [1].

In scientific terms, the following hypothesis was tested: *using natural graphite sheet heat sinks leads to improved power electronics products.* The results of the holistic feasibility study in chapter 9 suggest that the possible improvements of power electronics products with NGS heat sinks are case-specific and often require making complex trade-offs. As a result, the proposed hypothesis is rejected due to its generality. The benefits and challenges of using NGS heat sinks in power electronics products must be judged on a per-case basis.

A review of the major findings in each of the considered topics is given in the following paragraphs. Understanding and predicting the thermal performance of NGS heat sinks was found to be hindered by the limited knowledge of material properties of NGS, and by the lack of available experimental heat sink characterization methods capable of identifying the heat transfer bottlenecks. An extensive material characterization study was performed to provide the missing data, and the emerging transient thermal method was investigated and

[1] The video files are also available in Appendix F

compared to the conventional thermocouple-based heat sink characterization method. By completing the two tasks, it is now possible to develop and validate a model for predicting the thermal performance of NGS heat sinks and use it for determining the optimal shape for given conditions and constraints.

The material properties of NGS are known to be anisotropic and density dependent, however, the data variation across sources is often high, some regions of densities have not been covered, the effect of compression has not been reported, and some properties such as coefficient of thermal expansion or emissivity have not been studied at all. The value of the performed comprehensive material characterization lies not only in its span which covers the most of thermophysical properties that are relevant to heat sinks, but also in using the same material for all the measurements, which allows studying the relationship between the material properties without a risk of them being affected by the flake size, impurity content, or other parameters. The present work includes an easy-to-use graphical summary (Appendix B) that allows the researchers to quickly reuse the results. Previously, such a resource was not available, and researchers interested in using NGS in their applications were left to reading multiple publications, neither of which is freely available to the public.

From the thermal perspective, NGS heat sinks are the most suitable for applications with large heat sources and no requirements for electrical insulation. The low through-plane thermal conductivity limits the thermal performance of NGS heat sinks, but heat pipes embedded in the base can be used to mitigate the issue. The thermal contact resistance (TCR) at NGS-metal interfaces was found to be comparable to that at metal-metal ones with thermal grease, which offers a possibility to eliminate the need to use a thermal grease.

NGS is a lossy conductor with the electrical conductivity two-to-four orders of magnitude lower than aluminum or copper. While the conducted common-mode emissions were shown not to be affected by the difference in conductivity, a potential to reduce the radiated emissions by 12 to 97 % was demonstrated. The future measurements were suggested, and if the reduction is proven, NGS heat sinks will become an attractive option for communication electronics where radiation noise is a common problem due to high operating frequencies.

The cost of mass-produced heat sinks was estimated to be approximately double that of commercially available aluminum ones. When using designs with embedded heat pipes, the cost increases by approximately 25 %. At low-volume productions of custom heat sinks, the NGS technology is expected to be cost competitive with machining or 3D printing. Indirect costs arising from the mounting method or the need to use thermal grease must be considered to capture the net effect of replacing an existing heat sink with an NGS one.

Replacing existing heat sinks with NGS ones can affect the product reliability directly, by means of degradation or failure of the heat sink, or indirectly, by changing the operating condition of the devices attached to the heat sink. The possible modes of degradation arising from the heat capacity and mechanical properties of NGS were identified in chapter 9, and they should be reflected in the design of future reliability-related experiments. The potential

to eliminate the need for thermal grease is expected to improve the reliability because the pump-out and dry-out phenomena can be avoided.

Using NGS heat sinks can lead to a theoretical weight reduction of 30 to 81 % in case of an aluminum reference heat sink, and 79 to 94 % in case of a copper one. The range arises from the variable density of NGS that can be tailored to meet the requirements of given applications. The achievable weight reduction must be evaluated on a per-case basis, and factors such as polymer impregnation or mounting method must be taken into account.

The energy efficiency of electronic products can be improved by using energy-efficient cooling systems that were optimized for low thermal resistance and low energy consumption of fans. The advanced heat sink shapes that are possible using the NGS technology are expected to result in better thermal and aerodynamic performance, and – in turn – in better energy efficiency. The energy losses during the operation of an electronic product are only a fraction of the total environmental impact which arises from the production and end-of-life management of all the parts. Production of NGS appears to be less energy intensive than aluminum or copper, but the recyclability of NGS is questionable and has not been studied. A comprehensive life cycle assessment (LCA) analysis is necessary to evaluate not only the net energy requirement, but also the production of toxic waste, water use, or greenhouse gas emission. Only then, the environmental impact of using NGS, metal, or other heat sinks can be compared.

A clear need for a computational tool for determining the optimal heat sink shape was outlined in chapter 10. When available, it will allow evaluating the feasibility of using NGS heat sinks on a per-case basis, which – in turn – is expected to support the penetration of NGS technology into practical applications. This thesis is structured to serve as a comprehensive reference for supporting the early stages of the commercialization process. Besides that, many opportunities for a relevant fundamental research have been identified.

Acknowledgments

Many people helped me throughout the PhD program, both in professional and personal life. Thank you!

The following people directly participated in the research and their help is greatly appreciated. John Kenna and Shoji Kanamori shared the know-how in forming NGS. Xin Zhang of SFU 4D Labs provided the training and help with the SEM microscope. Microscope images of the ENG particles were taken at Thermo Fisher Scientific, Brno, Czech Republic, with a great help of Lubomir Tuma, Lukas Tomasak, and Roman Zouhar. Dr. Kevin Oldknow offered time for a discussion of the compression behavior of NGS. During her co-op term in LAEC, Masha Zalyvadna helped with collecting data for the tests of NGS compression behavior. Michael Thomas and Alysha Seely of Thermtest Inc. provided a valuable technical support for the TPS measurements. The measurements of NGS material properties were performed in collaboration with Nicolaz Perez of The Institut National des Sciences Appliquées de Lyon during his research internship at LAEC. The emissivity measurements were carried out in collaboration with Michael Collins at Solar Thermal Research Laboratory (STRL) at University of Waterloo. The author would like to thank Dr. Sepehr Foroushani for initiating the collaboration between the author of the thesis and STRL. Mr. Gholamreza Abadi kindly translated literature sources written in Korean. The thermal and impedance measurements of large scale heat sinks were performed by Xavier Faure of The Institut National des Sciences Appliquées de Lyon as a part of his research internship at LAEC. Collaboration with Ali Saket of University of British Columbia on the electromagnetic performance of NGS heat sinks is much appreciated and considered a great example of fruitful multi-disciplinary collaborative work. Tom Curran helped with water jet cutting of the NGS sheets that were used for building the small scale heat sinks in section 5.2. Jimmy He of Mentor Graphics provided the training, expertise, and troubleshooting help on the transient thermal tester during the author's stay in Mentor Graphics. Dr. Mohammad Zarifi offered and performed the measurements of NGS permittivity. Dr. Rodney Vaughan was very helpful during the initial stages of research on the electromagnetic performance of NGS heat sinks. A discussion of graphite material properties with Dr. David Broun helped to set the research direction. Wendell Huttema, Claire McCague, and Jeff Taylor patiently proofread a large amount of text. Dr. Majid Bahrami provided a steady funding over the course of the research.

Bibliography

[1] International Renewable Energy Agency, "Global energy transformation: A roadmap to 2050." `https://www.irena.org/-/media/Files/IRENA/Agency/Publication/2019/Apr/IRENA_Global_Energy_Transformation_2019.pdf`, 2018. Abu Dhabi.

[2] J. Lutz, H. Schlangenotto, U. Scheuermann, and R. De Doncker, *Semiconductor power devices: Physics, characteristics, reliability*. Berlin, Heidelberg: Springer Berlin Heidelberg, 2011.

[3] A. D. Kraus and A. Bar-Cohen, *Design and analysis of heat sinks*. Wiley, 1995.

[4] "Joint Electron Device Engineering Council website." `https://www.jedec.org/`.

[5] Xijin Tian, "Cooling fan reliability: failure criteria, accelerated life testing, modeling and qualification," in *RAMS '06. Annual Reliability and Maintainability Symposium, 2006.*, pp. 380–384, Jan 2006.

[6] Xiaohang Jin, E. W. M. Ma, T. W. S. Chow, and M. Pecht, "An investigation into fan reliability," in *Proceedings of the IEEE 2012 Prognostics and System Health Management Conference (PHM-2012 Beijing)*, pp. 1–7, May 2012.

[7] H. Wang, M. Liserre, and F. Blaabjerg, "Toward reliable power electronics: Challenges, design tools, and opportunities," *IEEE Industrial Electronics Magazine*, vol. 7, pp. 17–26, June 2013.

[8] C. Busca, R. Teodorescu, F. Blaabjerg, S. Munk-Nielsen, L. Helle, T. Abeyasekera, and P. Rodriguez, "An overview of the reliability prediction related aspects of high power igbts in wind power applications," *Microelectronics Reliability*, vol. 51, no. 9, pp. 1903 – 1907, 2011. Proceedings of the 22th European Symposium on the RELIABILITY OF ELECTRON DEVICES, FAILURE PHYSICS AND ANALYSIS.

[9] H. Lu, C. Bailey, and C. Yin, "Design for reliability of power electronics modules," *Microelectronics Reliability*, vol. 49, no. 9, pp. 1250 – 1255, 2009. 20th European Symposium on the Reliability of Electron Devices, Failure Physics and Analysis.

[10] Jue Li, P. Myllykoski, and M. Paulasto-Kröckel, "Study on thermomechanical reliability of power modules and thermal grease pump-out mechanism," in *2015 16th International Conference on Thermal, Mechanical and Multi-Physics Simulation and Experiments in Microelectronics and Microsystems*, pp. 1–6, April 2015.

[11] G. K. Morris, M. Polakowski, L. Wei, M. D. Ball, M. G. Phillips, C. Mosey, and R. A. Lukaszewski, "Thermal interface material evaluation for igbt modules under realistic

power cycling conditions," in *2015 IEEE International Workshop on Integrated Power Packaging (IWIPP)*, pp. 111–114, May 2015.

[12] D. DeVoto, J. Major, P. Paret, G. S. Blackman, A. Wong, and J. S. Meth, "Degradation characterization of thermal interface greases," in *2017 16th IEEE Intersociety Conference on Thermal and Thermomechanical Phenomena in Electronic Systems (ITherm)*, pp. 394–399, May 2017.

[13] R. Skuriat, J. Li, P. Agyakwa, N. Mattey, P. Evans, and C. Johnson, "Degradation of thermal interface materials for high-temperature power electronics applications," *Microelectronics Reliability*, vol. 53, no. 12, pp. 1933 – 1942, 2013.

[14] T. Williams, "Characterisation of emissions due to power electronics heatsinks," in *2013 International Symposium on Electromagnetic Compatibility*, pp. 616–621, Sep. 2013.

[15] A. Bhobe, H. Chu, L. Comiskey, X. Jiao, and X. Li, "Thermal and emi performance of composite plastic molded heat sinks and hybrid tim materials," *International Symposium on Microelectronics*, vol. 2014, no. 1, pp. 000222–000228, 2014.

[16] P. Sochoux, J. Yu, A. Bhobe, and F. Centola, "Heat Sink Design Flow for EMC," in *DesignCon 2008*, pp. 1–17, 2008.

[17] D. Christen, M. Stojadinovic, and J. Biela, "Energy efficient heat sink design: Natural versus forced convection cooling," *IEEE Transactions on Power Electronics*, vol. 32, pp. 8693–8704, Nov 2017.

[18] J. Eskew, M. Ratledge, M. Wallace, S. H. Gheewala, and P. Rakkwamsuk, "An environmental life cycle assessment of rooftop solar in bangkok, thailand," *Renewable Energy*, vol. 123, pp. 781 – 792, 2018.

[19] T. R. Hawkins, B. Singh, G. Majeau-Bettez, and A. H. Strømman, "Comparative environmental life cycle assessment of conventional and electric vehicles," *Journal of Industrial Ecology*, vol. 17, no. 1, pp. 53–64, 2013.

[20] I. Humar, X. Ge, L. Xiang, M. Jo, M. Chen, and J. Zhang, "Rethinking energy efficiency models of cellular networks with embodied energy," *IEEE Network*, vol. 25, pp. 40–49, March 2011.

[21] S. Flucker, R. Tozer, and B. Whitehead, "Data centre sustainability–beyond energy efficiency," *Building Services Engineering Research and Technology*, vol. 39, no. 2, pp. 173–182, 2018.

[22] D. A. Nelson, "In search of a quiet fan," in *2018 34th Thermal Measurement, Modeling Management Symposium (SEMI-THERM)*, pp. 200–204, March 2018.

[23] M. Vogel, J. Galloway, and D. Nelson, "Improved router server opex, acoustics and leakage power through advancements in asic / cpu design," in *2016 32nd Thermal Measurement, Modeling Management Symposium (SEMI-THERM)*, pp. 27–32, March 2016.

[24] C. Darvennes, M. Young, and S. Idem, "Acoustic system effects of propeller fans due to inlet installations.," *ASHRAE Transactions*, vol. 115, no. 2, 2009.

[25] M. A. MacDonald, J. Gullbrand, Y. Nishi, and E. Baugh, "Notebook blower inlet flow and acoustics: Experiments and simulations," *Noise Control Engineering Journal*, vol. 57, no. 4, pp. 348–359, 2009.

[26] K. Y. Kim, M. G. Choi, D. J. Lee, and W.-H. Jeon, "Experimental study of noise reduction and improved cooling fan performance in a pdp tv.," *Noise control engineering journal*, vol. 54, no. 1, 2006.

[27] J. Hyrynen, K. Saarinen, and K. Heinonen, "Fan concept study for low noise cooling of mobile machinery," *Noise Control Engineering Journal*, vol. 57, no. 4, pp. 304–309, 2009.

[28] X. H. Wei, L. Liu, J. X. Zhang, J. L. Shi, and Q. G. Guo, "Mechanical, electrical, thermal performances and structure characteristics of flexible graphite sheets," *Journal of Materials Science*, vol. 45, pp. 2449–2455, May 2010.

[29] E. E. Marotta, S. J. Mazzuca, and J. Norley, "Thermal joint conductance for flexible graphite materials: analytical and experimental study," *IEEE Transactions on Components and Packaging Technologies*, vol. 28, pp. 102–110, March 2005.

[30] P. Subramanian and Augostidis, "New class of graphite TIMs provide performance and reliability," in *PCIM Europe 2016, 10 – 12 May 2016, Nuremberg, Germany*, no. May, pp. 10–12, 2016.

[31] T. Semenic, A. Bhunia, N. Gollhardt, G. Morris, and R. Lukaszewski, "Low Thermal Resistance Thermal Pad for Power Converter Modules," in *IEEE PEDS 2017, Honolulu, USA, 12-15 December 2017*, no. December, pp. 453–455, 2017.

[32] U.S. Geological Survey, "Mineral commodity summaries 2019: U.S. Geological Survey," 2019.

[33] J. Norley, J. J. . Tzeng, G. Getz, J. Klug, and B. Fedor, "The development of a natural graphite heat-spreader," in *Seventeenth Annual IEEE Semiconductor Thermal Measurement and Management Symposium (Cat. No.01CH37189)*, pp. 107–110, March 2001.

[34] G. Chen, J. Capp, G. Getz, D. Flaherty, and J. Norley, "Optimum Design of Heat Sinks Using Non-Isotropic Graphite Composites," in *ASME 2003 Heat Transfer Summer Conference Heat Transfer: Volume 3*, pp. 489–494, ASME, 2003.

[35] E. E. Marotta, M. J. Ellsworth, J. Norley, and G. Getz, "The Development of a Bonded Fin Graphite/Epoxy Heat Sink for High Performance Servers," *2003 International Electronic Packaging Technical Conference and Exhibition, Volume 2*, pp. 139–146, 2003.

[36] G. Shives, J. Norley, M. Smalc, G. Chen, and J. Capp, "Comparative thermal performance evaluation of graphite/epoxy fin heat sinks," in *The Ninth Intersociety Conference on Thermal and Thermomechanical Phenomena In Electronic Systems (IEEE Cat. No.04CH37543)*, vol. 1, pp. 410–417 Vol.1, June 2004.

[37] T. Icoz and M. Arik, "Light weight high performance thermal management with advanced heat sinks and extended surfaces," *IEEE Transactions on Components and Packaging Technologies*, vol. 33, pp. 161–166, March 2010.

[38] Q. Wang, X. Han, A. Sommers, Y. Park, C. T. Joen, and A. Jacobi, "A review on application of carbonaceous materials and carbon matrix composites for heat exchangers and heat sinks," *International Journal of Refrigeration*, vol. 35, no. 1, pp. 7 – 26, 2012.

[39] A. Bouknadel, I. Rah, H. El Omari, and H. El Omari, "Comparative study of fin geometries for heat sinks in natural convection," in *2014 International Renewable and Sustainable Energy Conference (IRSEC)*, pp. 723–728, Oct 2014.

[40] D. Sabatino and K. Yoder, "Pyrolytic graphite heat sinks: A study of circuit board applications," *IEEE Transactions on Components, Packaging and Manufacturing Technology*, vol. 4, pp. 999–1009, June 2014.

[41] M. Inagaki, Y. Kaburagi, and Y. Hishiyama, "Thermal management material: Graphite," *Advanced Engineering Materials*, vol. 16, no. 5, pp. 494–506, 2014.

[42] M. Inagaki and F. Kang, "Chapter 2 - fundamental science of carbon materials," in *Materials Science and Engineering of Carbon: Fundamentals (Second Edition)* (M. Inagaki and F. Kang, eds.), pp. 17 – 217, Oxford: Butterworth-Heinemann, second edition ed., 2014.

[43] H. O. Pierson, "3 - graphite structure and properties," in *Handbook of Carbon, Graphite, Diamonds and Fullerenes* (H. O. Pierson, ed.), pp. 43 – 69, Oxford: William Andrew Publishing, 1993.

[44] Panasonic Corporation, "PGS Graphite Sheets - Product brochure." `https://industrial.panasonic.com/cdbs/www-data/pdf/AYA0000/AYA0000C27.pdf`, 2015. Online; accessed 13 June 2020.

[45] Y. Kaburagi, H. Aoki, and A. Yoshida, "Thermal and electrical conductivity and magnetoresistance of graphite films prepared from aromatic polyimide films," *Tanso*, no. 253, pp. 5–9, 2012.

[46] "Amorphous | Definition of Amorphous by Merriam-Webster." `https://www.merriam-webster.com/dictionary/amorphous`. Online; accessed 13 June 2020.

[47] S. C. Chelgani, M. Rudolph, R. Kratzsch, D.Sandmann, and J.Gutzmer, "A Review of Graphite Beneficiation Techniques," *Mineral Processing and Extractive Metallurgy Review*, vol. 37, no. April, pp. 58–68, 2016.

[48] G. J. Simandl, S. Paradis, and C. Akam, "Graphite deposit types , their origin , and economic significance," in *Symposium on Strategic and Critical Materials Proceedings*, vol. 3, pp. 163–171, 2015.

[49] C. J. Mitchell, "Flake Graphite - Industrial Minerals Laboratory Manual." `http://www.bgs.ac.uk/research/international/dfid-kar/wg92030_col.pdf`. Online; accessed 13 June 2020.

[50] A. D. Jara, A. Betemariam, G. Woldetinsae, and J. Y. Kim, "Purification, application and current market trend of natural graphite: A review," *International Journal of Mining Science and Technology*, vol. 29, no. 5, pp. 671 – 689, 2019.

[51] D. D. L. Chung, "A review of exfoliated graphite," *Journal of Materials Science*, vol. 51, pp. 554–568, Jan 2016.

[52] L. J. Nicks, F. H. Nehl, and M. F. Chambers, "Recovering flake graphite from steelmaking kish," *JOM*, vol. 47, pp. 48–51, Jun 1995.

[53] W. Wang, K. M. Thomas, R. M. Poultney, and R. R. Willmers, "Iron catalysed graphitisation in the blast furnace," *Carbon*, vol. 33, no. 11, pp. 1525–1535, 1995.

[54] S. S. Gornostayev and J. J. Härkki, "Graphite crystals in blast furnace coke," *Carbon*, vol. 45, no. 6, pp. 1145–1151, 2007.

[55] S. Liu and C. R. Loper, "The formation of kish graphite," *Carbon*, vol. 29, no. 4-5, pp. 547–555, 1991.

[56] S. Dimovski, A. Nikitin, H. Ye, and Y. Gogotsi, "Synthesis of graphite by chlorination of iron carbide at moderate temperatures," *Journal of Materials Chemistry*, vol. 14, no. 2, p. 238, 2004.

[57] T. Noda, Y. Sumiyoshi, and N. Ito, "Growth of single crystals of graphite from a carbon-iron melt," *Carbon*, vol. 6, no. 6, pp. 813–816, 1968.

[58] S. Liu and C. R. Loper, "Kish, a source of crystalline graphite," *Carbon*, vol. 29, no. 8, pp. 1119 – 1124, 1991.

[59] J. L. Gu, Y. Leng, E. Kang, and W. C. Shen, "Microstructure effect on mechanical properties of flexible graphite sheet," *Engineering Fracture Mechanics*, 1985.

[60] J. Klett, P. Pappano, and P. Boudreaux, "Kish-derived graphitic heat spreaders and foils," May 17 2007. US Patent App. 11/274,389.

[61] R. Frost, "The Recovery of Kish Graphite from Secondary Sources," Master's thesis, University of Birmingham, December 2014.

[62] M. Cermak, N. Perez, M. Collins, and M. Bahrami, "Material properties and structure of natural graphite sheet - dataset." https://doi.org/10.20383/101.0216, 2020.

[63] A. Celzard, S. Schneider, and J. Marêché, "Densification of expanded graphite," *Carbon*, vol. 40, no. 12, pp. 2185 – 2191, 2002.

[64] M. Dowell and R. Howard, "Tensile and compressive properties of flexible graphite foils," *Carbon*, vol. 24, no. 3, pp. 311 – 323, 1986.

[65] A. Celzard, J. Marêché, and G. Furdin, "Surface area of compressed expanded graphite," *Carbon*, vol. 40, no. 14, pp. 2713 – 2718, 2002.

[66] M. Null, W. Lozier, and A. Moore, "Thermal diffusivity and thermal conductivity of pyrolytic graphite from 300 to 2700 k," *Carbon*, vol. 11, no. 2, pp. 81 – 87, 1973.

[67] J. L. Gu, W. Q. Cao, N. Z. Cao, and W. C. Shen, "Effect of mictrostructure on compressive properties of flexible graphite sheet," in *The European Carbon Conference "Carbon 96"*, pp. 346–347, 1996.

[68] I. M. Afanasov, D. V. Savchenko, S. G. Ionov, D. A. Rusakov, A. N. Seleznev, and V. V. Avdeev, "Thermal conductivity and mechanical properties of expanded graphite," *Inorganic Materials*, vol. 45, pp. 486–490, May 2009.

[69] H. Toda, K. Tsubone, K. Shimizu, K. Uesugi, A. Takeuchi, Y. Suzuki, M. Nakazawa, Y. Aoki, and M. Kobayashi, "Compression and recovery micro-mechanisms in flexible graphite," *Carbon*, vol. 59, pp. 184 – 191, 2013.

[70] M. Bonnissel, L. Luo, and D. Tondeur, "Compacted exfoliated natural graphite as heat conduction medium," *Carbon*, vol. 39, no. 14, pp. 2151 – 2161, 2001.

[71] B. T. B. T. Kelly, *Physics of graphite / B.T. Kelly.* London ; Englewood, N.J.: Applied Science, 1981.

[72] M. Kobayashi, H. Toda, A. Takeuchi, K. Uesugi, and Y. Suzuki, "Three-dimensional evaluation of the compression and recovery behavior in a flexible graphite sheet by synchrotron radiation microtomography," *Materials Characterization*, vol. 69, pp. 52 – 62, 2012.

[73] X. Luo and D. Chung, "Flexible graphite under repeated compression studied by electrical resistance measurements," *Carbon*, vol. 39, no. 7, pp. 985 – 990, 2001.

[74] P.-H. Chen and D. Chung, "Viscoelastic behavior of the cell wall of exfoliated graphite," *Carbon*, vol. 61, pp. 305 – 312, 2013.

[75] L. Wang, S. Metcalf, R. Critoph, R. Thorpe, and Z. Tamainot-Telto, "Thermal conductivity and permeability of consolidated expanded natural graphite treated with sulphuric acid," *Carbon*, vol. 49, no. 14, pp. 4812 – 4819, 2011.

[76] X. Wei and K. Chau, "Finite and transversely isotropic elastic cylinders under compression with end constraint induced by friction," *International Journal of Solids and Structures*, vol. 46, no. 9, pp. 1953 – 1965, 2009.

[77] L. Wang, Z. Tamainot-Telto, S. Metcalf, R. Critoph, and R. Wang, "Anisotropic thermal conductivity and permeability of compacted expanded natural graphite," *Applied Thermal Engineering*, vol. 30, no. 13, pp. 1805 – 1811, 2010.

[78] H. Spencer, "Empirical heat capacity equations of gases and graphite," *Ind. and Eng. Chem.*, vol. Vol: 40, 11 1948.

[79] R. Liu, J. Chen, M. Tan, S. Song, Y. Chen, and D. Fu, "Anisotropic high thermal conductivity of flexible graphite sheets used for advanced thermal management materials," in *2013 International Conference on Materials for Renewable Energy and Environment*, vol. 1, pp. 107–111, Aug 2013.

[80] P.-H. Chen and D. Chung, "Thermal and electrical conduction in the compaction direction of exfoliated graphite and their relation to the structure," *Carbon*, vol. 77, pp. 538 – 550, 2014.

[81] M. Smalc, J. Norley, R. A. Reynolds, R. Pachuta, and D. W. Krassowski, "Advanced Thermal Interface Materials Using Natural Graphite," in *2003 International Electronic Packaging Technical Conference and Exhibition, Volume 2*, pp. 253–261, 2003.

[82] M. Gustavsson, E. Karawacki, and S. E. Gustafsson, "Thermal conductivity, thermal diffusivity, and specific heat of thin samples from transient measurements with hot disk sensors," *Review of Scientific Instruments*, vol. 65, no. 12, pp. 3856–3859, 1994.

[83] Y. He, "Rapid thermal conductivity measurement with a hot disk sensor: Part 1. theoretical considerations," *Thermochimica Acta*, vol. 436, no. 1, pp. 122 – 129, 2005.

[84] "Hot disk thermal constants analyser - instruction manual - revision date 2016-11-08," 2016.

[85] Hot Disk AB, "TPS 2500 S Hot Disk Thermal Constants Analyser." `https://www.hotdiskinstruments.com/content/uploads/2017/03/2500S.pdf`. Online; accessed 13 June 2020.

[86] Anter corporation, "QUICKLINE-10 Theraml conductivity meter." `http://www.smmmf.pub.ro/wp-content/uploads/2016/03/QuickLine_10C.pdf`. Online; accessed 13 June 2020.

[87] N. W. Pech-May, A. Mendioroz, and A. Salazar, "Simultaneous measurement of the in-plane and in-depth thermal diffusivity of solids using pulsed infrared thermography with focused illumination," *NDT & E International*, vol. 77, pp. 28 – 34, 2016.

[88] R. Taylor, "The thermal conductivity of pyrolytic graphite," *The Philosophical Magazine: A Journal of Theoretical Experimental and Applied Physics*, vol. 13, no. 121, pp. 157–166, 1966.

[89] Y. SINGH, "Electrical resistivity measurements: A review," *International Journal of Modern Physics: Conference Series*, vol. 22, pp. 745–756, 2013.

[90] A. Celzard, J. F. Marêché, G. Furdin, and S. Puricelli, "Electrical conductivity of anisotropic expanded graphite-based monoliths," *Journal of Physics D: Applied Physics*, vol. 33, pp. 3094–3101, nov 2000.

[91] X. Luo and D. Chung, "Electromagnetic interference shielding reaching 130 db using flexible graphite," *MRS Proceedings*, vol. 445, p. 235, 1996.

[92] P. Qian, H. Zhang, J. Chen, Y. Wen, Q. Luo, Z. Liu, D. You, and B. Yi, "A novel electrode-bipolar plate assembly for vanadium redox flow battery applications," *Journal of Power Sources*, vol. 175, no. 1, pp. 613 – 620, 2008.

[93] O. Rezvanian, C. Brown, M. A. Zikry, A. I. Kingon, J. Krim, D. L. Irving, and D. W. Brenner, "The role of creep in the time-dependent resistance of ohmic gold contacts in radio frequency microelectromechanical system devices," *Journal of Applied Physics*, vol. 104, no. 2, p. 024513, 2008.

[94] C. Zhai, D. Hanaor, G. Proust, and Y. Gan, "Stress-dependent electrical contact resistance at fractal rough surfaces," *Journal of Engineering Mechanics*, vol. 143, no. 3, p. B4015001, 2017.

[95] C. Poulain, L. Boyer, P. Sainso, M. H. Maitournam, F. Houze, M. Leclercq, J. P. Guery, and J. P. Charpentier, "Experimental and theoretical study of creep effects in electrical contacts," in *Electrical Contacts - 1995. Proceedings of the Forty-First IEEE Holm Conference on Electrical Contacts*, pp. 147–153, Oct 1995.

[96] C. A. M. dos Santos, A. de Campos, M. S. da Luz, B. D. White, J. J. Neumeier, B. S. de Lima, and C. Y. Shigue, "Procedure for measuring electrical resistivity of anisotropic materials: A revision of the montgomery method," *Journal of Applied Physics*, vol. 110, no. 8, p. 083703, 2011.

[97] L. B. Lugansky and V. I. Tsebro, "Four-probe methods for measuring the resistivity of samples in the form of rectangular parallelepipeds," *Instruments and Experimental Techniques*, vol. 58, pp. 118–129, Jan 2015.

[98] D. Tsang, B. Marsden, S. Fok, and G. Hall, "Graphite thermal expansion relationship for different temperature ranges," *Carbon*, vol. 43, no. 14, pp. 2902 – 2906, 2005.

[99] A. E. Mag-isa, J.-H. Kim, and C.-S. Oh, "Measurements of the in-plane coefficient of thermal expansion of freestanding single-crystal natural graphite," *Materials Letters*, vol. 171, pp. 312 – 314, 2016.

[100] M. Yazici, D. Krassowski, and J. Prakash, "Flexible graphite as battery anode and current collector," *Journal of Power Sources*, vol. 141, no. 1, pp. 171 – 176, 2005.

[101] D. Chung and Y. Takizawa, "Performance of isotropic and anisotropic heat spreaders," *Journal of Electronic Materials*, vol. 41, pp. 2580–2587, Sep 2012.

[102] Mersen, "Papyex flexible graphite - technical guide," tech. rep., 2012.

[103] S. G. T. C. Company, "Sigraflex - flexible graphite foils and sheets for heat treatment applications," tech. rep., 2016.

[104] G. Autio and E. Scala, "The normal spectral emissivity of isotropic and anisotropic materials," *Carbon*, vol. 4, no. 1, pp. 13 – 28, 1966.

[105] R. E. Hummel, *Electronic properties of materials / Rolf E. Hummel*, vol. 53. 2012.

[106] F. Wang, L. Cheng, H. Mei, Q. Zhang, and L. Zhang, "Effect of surface microstructures on the infrared emissivity of graphite," *International Journal of Thermophysics*, vol. 35, pp. 62–75, Jan 2014.

[107] J.-S. Roh, J.-S. Ahn, B.-J. Kim, H.-Y. Jeon, S.-K. Seo, S. H. Kim, and S.-W. Lee, "Thermal emissivity changes as a function of degree of flakes alignment on the graphite surface," *Journal of the Korean Institute of Surface Engineering*, 2009.

[108] D. A. Jaworske and T. J. Skowronski, "Portable infrared reflectometer for evaluating emittance," *AIP Conference Proceedings*, vol. 504, no. 1, pp. 791–796, 2000.

[109] ASTM, "Standard Test Methods for Total Normal Emittance of Surfaces Using Inspection-Meter, E408 - 13," *ASTM International*, 2013.

[110] Ohaus Corporation, "Adventurer Analytical and Precision Balances - 80774742 I 20181105." https://dmx.ohaus.com/WorkArea/showcontent.aspx?id=4294968488. Online; accessed 13 June 2020.

[111] Mark-10 Corporation, "Advanced Digital Force Gauges Series 5 - Data sheet 32-1111 REV 0119." http://www.mark-10.com/pdf/DataSheetSeries5.pdf. Online; accessed 13 June 2020.

[112] TA Instruments, "TMA Q400EM/Q400 Brochure L90033.001." https://www.tainstruments.com/wp-content/uploads/TMA.pdf. Online; accessed 13 June 2020.

[113] Y. Shuman. email communication. Applications Support Engineer at TA Instruments.

[114] Y. Avenas, L. Dupont, and Z. Khatir, "Temperature measurement of power semiconductor devices by thermo-sensitive electrical parameters—a review," *IEEE Transactions on Power Electronics*, vol. 27, pp. 3081–3092, June 2012.

[115] Q. He, S. Smith, and G. Xiong, "Thermocouple attachment using epoxy in electronic system thermal measurements — a numerical experiment," in *2011 27th Annual IEEE Semiconductor Thermal Measurement and Management Symposium*, pp. 280–291, March 2011.

[116] D. Schweitzer, H. Pape, and L. Chen, "Transient measurement of the junction-to-case thermal resistance using structure functions: Chances and limits," in *2008 Twenty-fourth Annual IEEE Semiconductor Thermal Measurement and Management Symposium*, pp. 191–197, March 2008.

[117] M. Cermak, "Natural graphite sheet heat sinks for power electronics - supplementary data." https://dx.doi.org/10.20383/101.0254, 2020.

[118] H. Pape, D. Schweitzer, L. Chen, R. Kutscherauer, and M. Walder, "Development of a standard for transient measurement of junction-to-case thermal resistance," in *2011 12th Intl. Conf. on Thermal, Mechanical Multi-Physics Simulation and Experiments in Microelectronics and Microsystems*, pp. 1/8–8/8, April 2011.

[119] Jedec Solid State Technology Association, "JESD51-14 Transient Dual Interface Test Method for the Measurement of the Thermal Resistance Junction-To-Case of Semiconductor Devices With Heat Flow Through a Single Path," tech. rep., 2010. Online; accessed 13 June 2020.

[120] A. Poppe, G. Hantos, and J. Hegedus, "Application of the transient dual interface method in test based modeling of heat-sinks aimed at socketable led modules," in *2015 31st Thermal Measurement, Modeling Management Symposium (SEMI-THERM)*, pp. 261–266, March 2015.

[121] Shin Etsu MicroSi, "Technical data sheet for G751." https://www.microsi.com/wp-content/uploads/2016/09/G751TDS-9202016.pdf, 2016. Online; accessed 13 June 2020.

[122] Z. Qiu, J. Zhang, P. Ning, and X. Wen, "Transient thermal fe-model calibration based on thermal structure functions for power modules," in *2017 IEEE Transportation Electrification Conference and Expo, Asia-Pacific (ITEC Asia-Pacific)*, pp. 1–5, Aug 2017.

[123] Infineon Technologies AG, "AUIRGPS4067D1 Product Datasheet." https://www.infineon.com/dgdl/Infineon-AUIRGPS4067D1-DS-v01_02-EN.pdf?fileId=5546d462533600a4015355ba8107152d, July 2018. Online; accessed 13 June 2020.

[124] M. Cermak, X. Faure, A. Saket, M. Ordonez, and M. Bahrami, "Natural graphite sheet heat sinks with embedded heat pipes - dataset." https://dx.doi.org/10.20383/101.0213, 2020.

[125] Nitto Inc., "P-221 AMB 1-MIL KAPTON POLYIMIDE FILM - Product Data Sheet PDS-P-221 AMB-11-16 ." https://www.nitto.com/us/en/others/products/group/file/datasheet/NA_P-221_V2_EN.pdf. Online; accessed 13 June 2020.

[126] Aavid Thermalloy, "Standard products catalog." https://media.digikey.com/pdf/Data%20Sheets/Aavid%20Thermal%20Technologies%20PDFs/Board-Level-Heatsinks_Cat.pdf#page=104. Online; accessed 13 June 2020.

[127] D. Benford, T. Powers, and S. Moseley, "Thermal conductivity of kapton tape," *Cryogenics*, vol. 39, no. 1, pp. 93 – 95, 1999.

[128] M. Garcia-Poulin, M. Ahmadi, M. Bahrami, E. Lau, and C. Botting, "Thermal resistance of electrical insulation for bolted and clamped discrete power devices," in *2018 34th Thermal Measurement, Modeling Management Symposium (SEMI-THERM)*, pp. 176–180, March 2018.

[129] Chroma Systems Solutions, Inc., "Programmable DC Power Supply model 62000P series - 62000P Series-E-201705-2000." http://www.chromausa.com/pdf/Br-62000P-dcsupply-052017.pdf. Online; accessed 13 June 2020.

[130] National Instruments, "DATASHEET NI 9229 - 374184C-02 Apr16." http://www.ni.com/pdf/manuals/374184c_02.pdf. Online; accessed 13 June 2020.

[131] A. Vass-Várnai, Z. Sárkány, and M. Rencz, "Characterization method for thermal interface materials imitating an in-situ environment," *Microelectronics Journal*, vol. 43, no. 9, pp. 661 – 668, 2012. THERMINIC 2010.

[132] S. Narumanchi, M. Mihalic, K. Kelly, and G. Eesley, "Thermal interface materials for power electronics applications," in *2008 11th Intersociety Conference on Thermal and Thermomechanical Phenomena in Electronic Systems*, pp. 395–404, May 2008.

[133] L. Middelstaedt, A. Lindemann, M. Al-Hamid, and R. Vick, "Influence of parasitic elements on radiated emissions of a boost converter," in *2015 IEEE International Symposium on Electromagnetic Compatibility (EMC)*, pp. 755–760, Aug 2015.

[134] M. R. Yazdani, H. Farzanehfard, and J. Faiz, "Classification and comparison of emi mitigation techniques in switching power converters - A review," *Journal of Power Electronics*, vol. 11, no. 5, pp. 767–777, 2011.

[135] J. Kulanayagam, J. H. Hagmann, S. Schenke, K. F. Hoffmann, and S. Dickmann, "Numerical modeling for heatsink emissions in power electronics," *Advances in Radio Science*, vol. 10, pp. 239–243, 2012.

[136] I. Grobler and M. N. Gitau, "Analysis, modelling and measurement of the effects of aluminium and polymer heatsinks on conducted electromagnetic compatibility in dc–dc converters," *IET Science, Measurement Technology*, vol. 11, no. 4, pp. 414–422, 2017.

[137] X. Gong and J. A. Ferreira, "Investigation of conducted emi in sic jfet inverters using separated heat sinks," *IEEE Transactions on Industrial Electronics*, vol. 61, pp. 115–125, Jan 2014.

[138] A. Dolente, *Analysis of the Heatsink Influence on Conducted and Radiated Electromagnetic Interference in Power Electronic Converters*. PhD thesis, University of Bologna, 2007.

[139] P. Ksiazek. personal communication. Power Electronics Engineer at Alpha Technologies Ltd.

[140] G. Felic and R. Evans, "Study of heat sink emi effects in smps circuits," in *2001 IEEE EMC International Symposium. Symposium Record. International Symposium on Electromagnetic Compatibility (Cat. No.01CH37161)*, vol. 1, pp. 254–259 vol.1, Aug 2001.

[141] C.-H. Ahn and J. Oh, "Resistive grounding technique of heat sink for reducing radiation noise," *Journal of Electrical Engineering and Technology*, vol. 5, Sep 2014.

[142] E. Chikando, S. Connor, and B. Archambeault, "Reduction of heatsink emissions by application of lossy materials," in *2010 IEEE International Symposium on Electromagnetic Compatibility*, pp. 239–243, July 2010.

[143] P. Cheng, E. Li, L. Zhang, Y. Li, Q. Min, X. Yang, and H. Jin, "Electromagnetic and thermal characteristics of graphite for radiation suppression in wire-bonded package heat sink," *IEEE Transactions on Electromagnetic Compatibility*, vol. 60, pp. 1445–1453, Oct 2018.

[144] S. Chromy, K. Rathjen, S. Fahlbusch, K. Hoffmann, and S. Dickmann, "Influence of an electrically non-conducting heat sink for power semiconductors on radiated interferences," *Advances in Radio Science*, vol. 16, pp. 117–122, 09 2018.

[145] X. Luo, R. Chugh, B. C. Biller, Y. M. Hoi, and D. D. L. Chung, "Electronic applications of flexible graphite," *Journal of Electronic Materials*, vol. 31, pp. 535–544, May 2002.

[146] A. Wang and D. D. L. Chung, "Dielectric and electrical conduction behavior of carbon paste electrochemical electrodes, with decoupling of carbon, electrolyte and interface contributions," *Carbon*, vol. 72, no. 716, pp. 135–151, 2014.

[147] I. Kranauskaite, J. Macutkevic, P. Kuzhir, N. Volynets, A. Paddubskaya, D. Bychanok, S. Maksimenko, J. Banys, R. Juskenas, S. Bistarelli, A. Cataldo, F. Micciulla, S. Bellucci, V. Fierro, and A. Celzard, "Dielectric properties of graphite-based epoxy composites," *Physica Status Solidi (A) Applications and Materials Science*, vol. 211, no. 7, pp. 1623–1633, 2014.

[148] M. Hotta, M. Hayashi, M. T. Lanagan, D. K. Agrawal, and K. Nagata, "Complex Permittivity of Graphite, Carbon Black and Coal Powders in the Ranges of X-band Frequencies (8.2 to 12.4 GHz) and between 1 and 10 GHz," *ISIJ International*, vol. 51, no. 11, pp. 1766–1772, 2011.

[149] X. Hong, W. Yu, and D. D. L. Chung, "Electric permittivity of reduced graphite oxide," *Carbon*, vol. 111, pp. 182–190, 2017.

[150] M. Shahpari and D. V. Thiel, "The impact of reduced conductivity on the performance of wire antennas," *IEEE Transactions on Antennas and Propagation*, vol. 63, pp. 4686–4692, Nov 2015.

[151] S. J. Chen and C. Fumeaux, "Highly efficient graphite antennas for conformal applications," in *2018 Australian Microwave Symposium (AMS)*, pp. 61–62, Feb 2018.

[152] Northern Graphite, "Graphite Pricing." `http://www.northerngraphite.com/about-graphite/graphite-pricing/`. Online; accessed: 9 October 2019.

[153] Triton Minerals, "Graphite Price." `https://www.tritonminerals.com/graphite-market/about-graphite/graphite-price/`. Online; accessed: 9 October 2019.

[154] G. A. Meyer. personal communication. CEO at Celsia Inc.

[155] Alpha Novatech, Inc., "UB12060 specification and thermal data." `https://www.alphanovatech.com/en/c_ub12060e.html`. Online; accessed 13 June 2020.

[156] Ecoinvent Association, "Ecoinvent database." `https://v30.ecoquery.ecoinvent.org/Home/`. Online; accessed 12 September 2017.

[157] S. Gao, X. Gong, Y. Liu, and Q. Zhang, "Energy consumption and carbon emission analysis of natural graphite anode material for lithium batteries," *Materials Science Forum*, vol. 913, pp. 985–990, feb 2018.

[158] J. Shillito, "Battery minerals: A question of purity?," *Battery Minerals*, pp. 41–45, aug 2015.

[159] A. Pizza, R. Metz, M. Hassanzadeh, and J.-L. Bantignies, "Life cycle assessment of nanocomposites made of thermally conductive graphite nanoplatelets," *The International Journal of Life Cycle Assessment*, vol. 19, pp. 1226–1237, Jun 2014.

[160] K. Zaghib, X. Song, A. Guerfi, R. Rioux, and K. Kinoshita, "Purification process of natural graphite as anode for Li-ion batteries: Chemical versus thermal," *Journal of Power Sources*, vol. 119-121, pp. 8–15, 2003.

[161] Y.-f. Li, S.-f. Zhu, and L. Wang, "Purification of natural graphite by microwave assisted acid leaching," *Carbon*, vol. 55, pp. 377–378, 2013.

[162] G. Bowes, "Northern Graphite Files Final Patent Application for Purification Technology." `http://www.northerngraphite.com/_resources/news/Patent%20Filing.pdf`, 2019. Online; accessed 13 June 2020.

[163] S. Liu and C. R. Loper, "Kish, a source of crystalline graphite," *Carbon*, vol. 29, no. 8, pp. 1119 – 1124, 1991.

[164] T. S. D. Kumari, A. J. Jebaraj, T. A. Raj, D. Jeyakumar, and T. P. Kumar, "A kish graphitic lithium-insertion anode material obtained from non-biodegradable plastic waste," *Energy*, vol. 95, pp. 483 – 493, 2016.

[165] H. M. A. Asghar, S. N. Hussain, H. Sattar, N. W. Brown, and E. P. L. Roberts, "Environmentally friendly preparation of exfoliated graphite," *Journal of Industrial and Engineering Chemistry*, vol. 20, no. 4, pp. 1936–1941, 2014.

[166] M. Cai, D. Thorpe, D. H. Adamson, and H. C. Schniepp, "Methods of graphite exfoliation," *Journal of Materials Chemistry*, pp. 24992–25002, 2012.

[167] P. Press, "Exfoliated Graphite From Various Intercalation Compounds," vol. 2, no. 8, pp. 1227–1231, 1991.

[168] M. Liu, X. Zhang, W. Wu, T. Liu, Y. Liu, B. Guo, and R. Zhang, "One-step chemical exfoliation of graphite to 100and large size at ambient temperature," *Chemical Engineering Journal*, vol. 355, pp. 181 – 185, 2019.

[169] X. Van Heerden and H. Badenhorst, "The influence of three different intercalation techniques on the microstructure of exfoliated graphite," *Carbon*, vol. 88, pp. 173–184, 2015.

[170] U.S. Department of Energy, "U.s. energy requirements for aluminum production: Historical perspective, theoretical limits and current practices," February 2007.

[171] R. Wiltshire, *Anodic Oxidation of Aluminium and its Alloys*. The Pergamon Materials Engineering Practice Series, 1982.

[172] B. K. Reck and T. E. Graedel, "Challenges in metal recycling," *Science*, vol. 337, no. 6095, pp. 690–695, 2012.

[173] T. D. Burchell and P. J. Pappano, "Recycling irradiated nuclear graphite - A greener path forward," *Nuclear Engineering and Design*, vol. 251, pp. 69–77, 2012.

[174] S. Rothermel, M. Evertz, J. Kasnatscheew, X. Qi, M. Grützke, M. Winter, and S. Nowak, "Graphite recycling from spent lithium-ion batteries," *ChemSusChem*, vol. 9, no. 24, pp. 3473–3484, 2016.

[175] B. Moradi and G. G. Botte, "Recycling of graphite anodes for the next generation of lithium ion batteries," *Journal of Applied Electrochemistry*, vol. 46, pp. 123–148, Feb 2016.

[176] L. Meysenc, M. Jylhakallio, and P. Barbosa, "Power electronics cooling effectiveness versus thermal inertia," *IEEE Transactions on Power Electronics*, vol. 20, pp. 687–693, May 2005.

[177] E. Levy, H. Bilirgen, K. Jeong, M. Kessen, C. Samuelson, and C. Whitcombe, "Recovery of water from boiler flue gas." `https://www.osti.gov/servlets/purl/952467`, 2008. Online; accessed 13 June 2020.

[178] W. Jiang, G. Nadeau, K. Zaghib, and K. Kinoshita, "Thermal analysis of the oxidation of natural graphite — effect of particle size," *Thermochimica Acta*, vol. 351, no. 1, pp. 85 – 93, 2000.

[179] W. C. Tucker, "Degradation of Graphite/Polymer Composites in Seawater," *Journal of Energy Resources Technology*, vol. 113, pp. 264–267, 12 1991.

[180] Z. Wang, M. Chinthavali, S. L. Campbell, T. Wu, and B. Ozpineci, "A 50-kw air-cooled sic inverter with 3-d printing enabled power module packaging structure and genetic algorithm optimized heatsinks," *IEEE Transactions on Industry Applications*, vol. 55, pp. 6256–6265, Nov 2019.

[181] E. M. Dede, S. N. Joshi, and F. Zhou, "Topology Optimization, Additive Layer Manufacturing, and Experimental Testing of an Air-Cooled Heat Sink," *Journal of Mechanical Design*, vol. 137, 10 2015. 111403.

[182] F. P. Incropera, A. S. Lavine, T. L. Bergman, and D. P. DeWitt, *Fundamentals of heat and mass transfer*. Wiley, 2007.

Appendix A - Summary of the NGS forming process

Description:
An enlarged version of the summary of NGS forming, which was presented in Chapter 3 in Figure 3.1.

Filename:
AppendixA_NGSForming.pdf

Appendix B - Graphical summary of NGS material properties

Description:
An enlarged version of the summary of NGS material properties, which was presented in Chapter 3 in Figures 3.2 and 3.3.

Filename:
AppendixB_NGSMaterialProperties.pdf

Appendix C - Calculation of expansion of air in the pores

For the lowest and highest measured densities the porosity is:

$$P_{0.5} = 78\,\% \tag{A1}$$

$$P_{1.7} = 25\,\%; \tag{A2}$$

however, only closed pores can cause the sheet to expand. The literature sources vary in prediction of whether the pores in NGS are closed or open. Dowell and Howard [64] concluded that all the pores are open while Toda et al. [69] claimed that 8 % of the pores are closed. In this calculation the 8 % was used; however, it should be noted that it might be inaccurate and the amount of closed of pores can also be a function of the density. The volume of air in closed pores can be calculated as:

$$V_{air} = V_{sheet}\ 0.08P. \tag{A3}$$

The surface volume (or volume per unit area) of a sheet is:

$$\overline{V}_{sheet} = 1 \cdot 1 \cdot t\ [\mathrm{cm^3 cm^{-2}}] = t\ [\mathrm{cm}] \tag{A4}$$

The volume of air per unit area is:

$$\overline{V}_{air} = t\ 0.08P. \tag{A5}$$

The change of volume with temperature under constant pressure is given as:

$$\Delta\overline{V}_{air} = \Delta T \beta_{air} \overline{V}_{air}, \tag{A6}$$

where β_{air} is the volumetric expansion coefficient of air that was assumed to be $\beta_{air} = 0.003\,69\,\mathrm{K^{-1}}$.

Figure (A4) shows that the change in thickness is proportional to the change in volume (assuming that the sheet expands only in the through-plane direction). Therefore, CTE can be calculated as:

$$CTE = \frac{\Delta t}{t\Delta T} = \frac{\Delta\overline{V}}{t\Delta T}. \tag{A7}$$

Substituting Equations A5 and A6 into A7 yields:

$$CTE = \frac{\Delta T \beta_{air} t\ 0.08P}{t\Delta T} = \beta_{air}\ 0.08P, \tag{A8}$$

which for the $0.55\,\mathrm{gcm^{-3}}$ and $1.7\,\mathrm{gcm^{-3}}$ sheets evaluates to:

$$CTE_{0.5,air} = 0.00369 \cdot 0.08 \cdot 0.78 = 230 \times 10^{-6}\,\mathrm{K^{-1}} \tag{A9}$$

$$CTE_{1.7,air} = 0.00369 \cdot 0.08 \cdot 0.25 = 74 \times 10^{-6}\,\mathrm{K^{-1}} \tag{A10}$$

Appendix D - Calculation of relative heat sink thermal resistance

The heat sinks manufactured in this work consist of L-shape sheets stacked in an alternating orientation, which results in the staggered-fin topology as shown in Figure A1. By assuming the heat source to cover the entire heat sink base, and the convective heat transfer coefficient to be comparable for all the fins, the total heat transferred by the heat sink can be assumed to be equal to the heat transferred by a single fin multiplied by the number of fins, and the thermal resistance analysis can be reduced to a single fin.

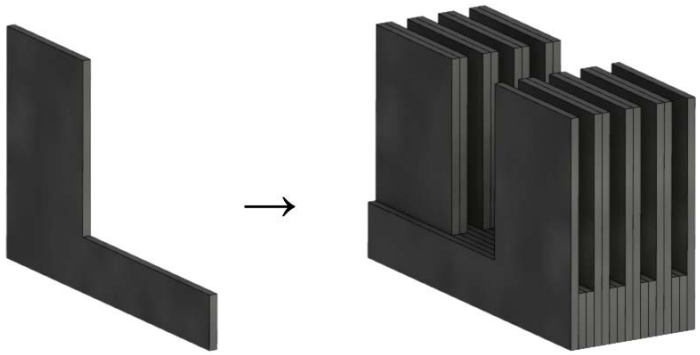

Figure A1: Illustration of the heat sink topology used in the present work. L-shape sheets are stacked in an alternating orientation to form a staggered plate-fin heat sink.

A schematic of the heat transfer in a single fin is shown in Figure A2a. The heat enters at the bottom edge, spreads in the base, travels through the fin and dissipates into the flowing air. By neglecting the spreading in the base, the three-dimensional problem can be reduced to two dimensions as illustrated in in Figure A2b.

The heat flow through a fin with the height H_f, thickness t_f, thermal conductivity k_f, and convective heat transfer coefficient h is given as [182]:

$$\dot{Q}_{fin} = \eta_{fin} h A_{fin} \Delta T, \tag{A11}$$

where η_{fin} is the fin efficiency, A_{fin} is the heat transfer area, and ΔT is the temperature difference between the fin base and the ambient air. The fin efficiency is defined as:

$$\eta_{fin} = \frac{\tanh mH}{mH}, \tag{A12}$$

where m is:

$$m = \sqrt{\frac{2h}{kt}}. \tag{A13}$$

The fin thermal resistance is:

$$R_{th} = \frac{\Delta T}{\dot{Q}_{fin}} = \frac{\Delta T}{\eta_{fin} h A_{fin} \Delta T} = \frac{1}{\eta_{fin} h A_{fin}}. \tag{A14}$$

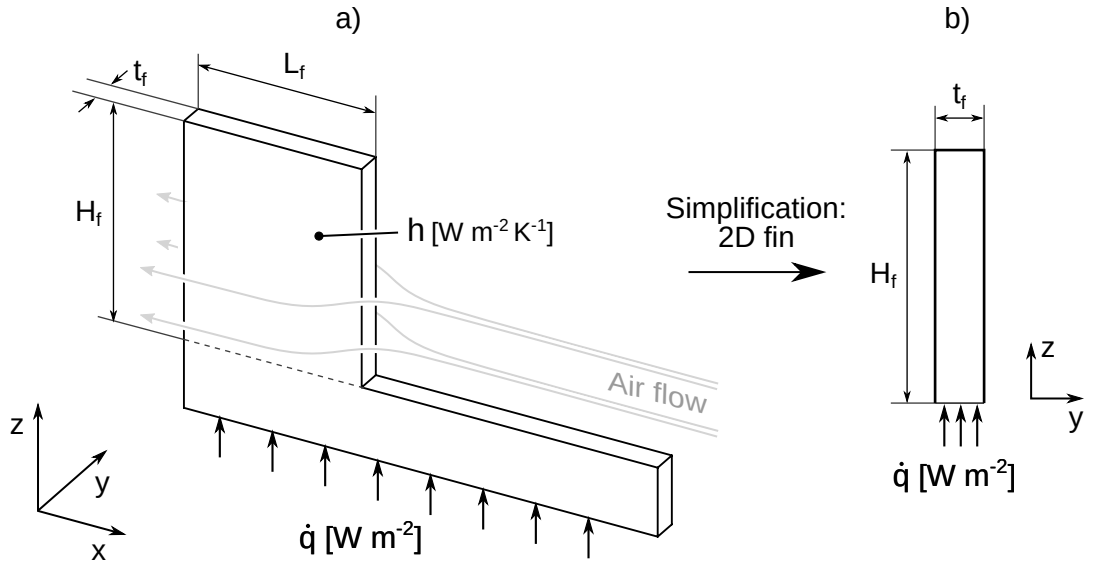

Figure A2: A schematic of the geometry and heat transfer conditions of a) single fin, and b) a simplified two-dimensional case.

For comparing the heat sink materials, aluminum was chosen to be the reference. The relative thermal performance is then:

$$\frac{R_{th}}{R_{th,AL}} = \frac{\frac{1}{\eta_{fin} h A_{fin}}}{\frac{1}{\eta_{fin,AL} h A_{fin}}} = \frac{\eta_{fin,AL}}{\eta_{fin}}. \tag{A15}$$

The thermal conductivity of aluminum and copper was assumed to be $385\,\mathrm{Wm^{-1}K^{-1}}$ and $200\,\mathrm{Wm^{-1}K^{-1}}$. The TCR at the interface between heat source and heat sink was not considered in the calculation. However, the measurements of TCR at NGS-metal interfaces showed comparable results to metal-to-metal interfaces with thermal grease, thus the relative comparison presented here is assumed to be valid for cases where thermal grease is used.

Appendix E - Calculation of equivalent fin height

The following calculation determines the fin height H_{NGS} of an NGS heat sink with the number of fins $n_{f,NGS}$ that has the same thermal resistance as a reference aluminum heat sink with the number of fins $n_{f,AL}$ and fin height H_{AL}. The calculation has mainly an illustration purpose and the following assumptions were made to simplify the problem:

- constant convective heat transfer coefficient on the fin surface $h = 30\,\mathrm{Wm^{-2}K^{-1}}$
- neglecting the spreading and conduction in the base of the heat sink
- neglecting the radiation heat transfer
- the thermal contact resistance between the heat source and the heat sink was considered identical. This assumption can be validated by the measured trends in section 5.4 that show that metal-metal interfaces with thermal grease perform comparable to the NGS-metal ones.

The calculation can be based on the equality:

$$n_{f,NGS}\dot{Q}_{fin,NGS} = n_{f,AL}\dot{Q}_{fin,AL}, \tag{A16}$$

where $\dot{Q}_{fin,AL}$ is the heat dissipated by one fin of the aluminum heat sink, $\dot{Q}_{fin,NGS}$ is the heat dissipated by one fin of the NGS heat sink. The heat dissipation of a fin $\dot{Q}_{fin}$ was defined in Equations A11 and A12 in Appendix D, and substituting the equations into Equation A16 yields:

$$n_{f,NGS}\frac{\tanh(m_{NGS}H_{NGS})}{m_{NGS}H_{NGS}}2H_{NGS} = n_{f,AL}\frac{\tanh(m_{AL}H_{AL})}{m_{AL}H_{AL}}2H_{AL}, \tag{A17}$$

which can be rearranged to:

$$H_{NGS} = \frac{\tanh^{-1}(\frac{n_{f,AL}}{n_{f,NGS}}\tanh(m_{AL}H_{AL})\frac{m_{NGS}}{m_{AL}})}{m_{NGS}}, \tag{A18}$$

where m_{NGS} and m_{AL} are the fin efficiency m-factors defined in Equation A13 in Appendix D.

Appendix F - Video summary

Description:
Video files with a presentation-style summary of the research.

Filename:
01-Intro.mp4
02-Cooling systems, research motivation and goal.mp4
03-Material properties of NGS.mp4
04-Thermal performance of NGS heat sinks.mp4
05-Electromagnetic performance of NGS heat sinks.mp4
06-Energy efficiency and environmnental impact.mp4
07-Feasibility.mp4
08-Conclusions.mp4